Computational Studies of Plasma-Liquid Interactions

A Doctoral Thesis

Submitted in partial fulfilment of the requirements for the award of Doctor of Philosophy at Loughborough University

Wolfson School of Mechanical, Electrical and Manufacturing Engineering

Faraz Montazersadgh

October 2019

Abstract

By the introduction of modern power supplies capable of producing low-temperature plasma under atmospheric pressure, the interaction between plasmas and liquids have presented great potentials in many exciting applications in recent years. Cancer treatment, wound healing, nanomaterial production, water disinfection and chemical analysis are just a few examples of emerging applications of plasmas interacting with liquids.

Despite the large attention received in recent years, research in this area is still in its infancy. To take the current technologies further and develop practical solutions for these applications, many fundamental questions need to be answered first. Although reactive oxygen species (ROS) and reactive nitrogen species (RNS) are known to play a dominant role in these applications. The underlying physics of plasma-liquid interaction, the chemistry involved in the liquid phase, the interfacial effects governing the mass transfer between the plasma and the liquid, mass transfer quantities and the propagation mechanisms of the transferred species throughout the liquid media are just a few sample questions that remain unanswered.

A combination of computational modelling and experimental methods are used throughout this thesis to shine some light on some of these questions. New insights into the dynamics of the liquid phase chemistry as well as the physical effects of the plasma on the liquid bulk are addressed as part of this thesis. The developed computational model not only provides a better understanding of the system in general, but also predicts properties and quantities which are difficult or impossible to measure experimentally with current available apparatus and measurement techniques. The results are then employed to layout guidelines for optimized configurations of plasma-liquid systems in practical applications.

Since the gas phase computational study has been explored extensively in previous works, in this thesis our main focus will be the interaction between the plasma and the plasma effluent with the liquid phase and the subsequent physicochemical reactions.

The problem is broken down into three parts. In the first part, the plasma gas phase is studied independent of the liquid phase to clarify the kinetics of the plasma medium. The main chemical reaction pathways are studied as well as the effect of input power modulation on the chemical pathway variations and final gas composition.

The next part focuses on the transfer of heavy reactive species into the liquid and the subsequent chemical reactions. This is relevant in remote plasma systems in which the plasma is not in electric contact with the liquid. In particular we study an epoxidation reactor that relies on a He + O_2 to epoxidate alkenes in liquid phase.

In the third part, the focus is on the transfer of electrons into the liquid phase. In this case, the plasma is electrically connected to the liquid and electrons are delivered to the liquid to drive liquid phase reactions. The electrochemical properties of the liquid are studied along with the effect of the surface tension gradient caused by the plasma on the liquid phase mixing patterns.

Keywords: *plasma-liquid, computational model, numerical simulation, atmospheric pressure, pulse power.*

Acknowledgement

First and foremost, I would like to express my sincere gratitude to my supervisor Dr Felipe Iza for the continuous support of my PhD study and related research, for his patience, motivation, and immense knowledge. His guidance helped me in all the time of research and writing of this thesis. I could not have imagined having a better advisor and mentor for my PhD study.

Besides my first supervisor, I would like to thank Dr Hemaka Bandulasena for his insightful comments and support, but also for his life changing discussions during the group meetings which encouraged me to widen my research from various perspectives.

My sincere thanks also go to Dr Benjamin Buckley for his support in the chemical aspects of the research. I would also like to acknowledge my MSc and BSc supervisors at Sharif University of Technology, Prof Soheila Yaghmaei and Prof Mohammad Soltanieh who have unconditionally supported me throughout my studies.

I thank my fellow lab mates in the Plasma & Pulse Power Group (P3G) for the stimulating discussions, for their help and support, and for all the fun we have had in the last few years.

Last but not the least, I would like to express my deepest love to my family: my wonderful wife Maryam, my parents and my brother for supporting me spiritually throughout writing this thesis and my life in general.

Research Output

Journal Papers:

Peer-reviewed Publications:

[1] **Faraz Montazersadgh**, Alexander Wright, Junchen Ren, Alex Shaw, Hemaka Bandulasena, Felipe Iza, 'Influence of the On-time on the Ozone production in Pulsed Dielectric Barrier Discharges', *Plasma, pp. 39–50, 2019*

[2] Han Xu, Sui Wang, Muhammad Shaban, **Faraz Montazersadgh**, Anas Alkayal, Dingxin Liu, Micheal G Kong, Benjamin Buckley and Felipe Iza, 'Trans-Stilbene Epoxidation by He+O2 Atmospheric Pressure Plasma: Epoxidation Without Oxidant Waste-Stream', *Plasma Proc. & Polymers, DOI: 10.1002/ppap.201900162, 2019*

[3] Alexander Wright, Matteo Taglioli, **Faraz Montazersadgh**, Alex Shaw, Felipe Iza, H C Hemaka Bandulasena,'Microbubble-Enhanced DBD Plasma Reactor: Design and Modelling', *Chemical Engineering Research and Design, vol. 144. Pp. 159-173, 2019*

[4] Abdulkadir Hussein Sheik, **Faraz Montazersadgh**, Victor Starov, Anna Trybala, and H. C. Hemaka Bandulasena,'Procedures Used in Electrokinetic Investigations of Surfactant-Laden Interfaces, Liquid Films and Foam System', *Current Opinion in Colloid & Interface Science, vol. 37. pp. 128–135, 2018*

[5] Abdulkadir Hussein Sheik, **Faraz Montazersadgh**, Victor Starov, Anna Trybala, and H. C. Hemaka Bandulasena,'Electrokinetic investigation in a freely suspended liquid film using fluorescent dyes: experiments and Numerical Simulations', *Langmuir*, *DOI:* 10.1021/acs.langmuir.9b03852, 2020

In Preperation / Under review:

[6] **Faraz Montazersadgh**, Abdulkadir Hussein Sheik , Alexander Wright, Alex Shaw, H. C. Hemaka Bandulasena and Felipe Iza, 'The Importance of Surface Tension Gradient in Plasma-Liquid Treatment Systems', *Scientific Reports, 2020*

[7] **Faraz Montazersadgh**, Wang Sui, Alexander Wright, Benjamin Buckley, H. C. Hemaka Bandulasena, Felipe Iza, 'Estimation of Atomic O Henry's Constant: Numerical Simulations and Experiments', *JPhysics D, 2020*

Conference Contributions:

[1] **Faraz Montazersadgh**, Abdulkadir Hussein Sheik, Alexander Wright, Alex Shaw, H. C. Hemaka Bandulasena, Felipe Iza, 'The Importance of Surface Tension Gradients in Plasma-Liquid Treatments', Poster Presentation, 46th IOP Plasma Physics Conference, Loughborough, UK, April 2019

[2] **Faraz Montazersadgh**, Abdulkadir Hussein Sheik, Alexander Wright, Alex Shaw, Hemaka Bandulasena and Felipe Iza, 'Mixing in Liquid Treated by an Atmospheric Pressure Plasma Jet: The Importance of Surface Tension Gradient', Oral Presentation, 16th Technological Plasma Workshop, Coventry, UK, October 2018

[3] **Faraz Montazersadgh**, Abdulkadir Hussein Sheik, Alexander Wright, Alex Shaw, Hemaka Bandulasena and Felipe Iza, 'Mixing in Liquid Treated by an Atmospheric Pressure Plasma Jet: The Importance of Surface Tension Gradient', Oral Presentation, 7th Young Professionals Workshop on Plasma Medicine, Rostock, Germany, September 2018

[4] G. Colonna, M. Turner, M. Becker, D. Loffhagen, F. Sigeneger, F. Gordillo, A. Luque, F. Iza, **F. Montazersadgh**, J van Dijk, W. Graef, G. Kroesen, D. Mihailova, A. Bogaerts, S. Heijkers, L. Alves, M. Castela, V. Guerra, M. Lino da Silva, L. Marques, N. Pinhao, C. Pintassilgo, A. Tejero, T. Kozak, A. Derzsi, Z. Donko, P. Hartmann, K. Kutasi, S. Pancheshnyi, 'Plasma Chemistry Round Robin', Poster, 70th Annual Gaseous Electronics Conference, The American Physical Society, Pittsburgh, Pennsylvania, USA, November 2017

[5] **Faraz Montazersadgh**, Alexander Wright, Alex Shaw, H. C. Hemaka Bandulasena and Felipe Iza, 'Space Averaged Mathematical Model of Pulse Powered Atmospheric Pressure Air Plasma', Poster, Plasmas Surfaces and Thin Films Early Career Researchers Meeting, Institute of Physics, Loughborough, UK, June 2017

[6] **Faraz Montazersadgh**, Alexander Wright, Alex Shaw, H. C. Hemaka Bandulasena and Felipe Iza, 'Mathematical Model of an Atmospheric Pressure Air Plasma', Poster, Loughborough University Summer Showcase, Loughborough University, Loughborough, UK, June 2017

[7] **Faraz Montazersadgh**, H. C. Hemaka Bandulasena and Felipe Iza, 'Mathematical Modelling of Plasma Liquid Interactions', Abstract Presentation, Wolfson School Conference, Loughborough University, Loughborough, UK, June 2017

Symbols

Symbol	Description	Unit
$\boldsymbol{n}$	number density	$\frac{1}{m^3}$
$\boldsymbol{v}$	velocity	$\frac{m}{s}$
$\boldsymbol{a}$	acceleration	$\frac{m}{s^2}$
$\boldsymbol{R_k}$	reaction rate of species *k*	$\frac{mol}{s \cdot m^3}$
$\boldsymbol{k_j}$	reaction rate coefficient of reaction *j*	*
σ	collisional cross section	m^2
$\boldsymbol{\varepsilon}$	mean energy	eV
$\boldsymbol{G}$	volumetric mass generation rate	$\frac{mol}{m^3}$
$\boldsymbol{\Gamma}$	flux	$\frac{1}{m^2}$
$\boldsymbol{U}$	Internal energy	eV
$\boldsymbol{T}$	temperature	eV
$\boldsymbol{P}$	power	eV
$\boldsymbol{H}$	enthalpy	eV
$\boldsymbol{\nu_{mi}}$	momentum transfer electron collision frequency	Hz
$\boldsymbol{R}$	global gas constant	$\frac{eV}{mol \cdot K}$
$\mathbf{U}_r$	reactor heat capacity	$\frac{eV}{K}$
$\boldsymbol{C_p}$	specific heat capacity	$\frac{eV}{K \cdot kg}$
$\boldsymbol{k_b}$	Boltzmann constant	$\frac{eV}{K}$
$\boldsymbol{m_e}$	electron mass	kg
$\boldsymbol{M_i}$	heavy particles mass	kg
$\boldsymbol{\emptyset_l}$	liquid phase fraction	-
$\boldsymbol{K_l}$	mass transfer coefficient	$\frac{m}{s}$
$\boldsymbol{P_k}$	partial pressure in the gas phase of species *k*	Pa
$\boldsymbol{H_k}$	henry's constant of species *k*	$\frac{Pa \cdot m^3}{mol}$
$\boldsymbol{\overline{a_i^V}}$	bubble surface to volume ratio	$\frac{1}{m}$
$\boldsymbol{Sh}$	Sherwood number	-

Symbol	Description	Unit
Gr	Grashof number	-
Sc	Schmidt number	-
Me	mixing efficiency	-
γ	secondary electron emission coefficient	-
u	mean velocity	$\frac{m}{s}$
t	time	s
α_k	Bohm velocity reduction factor of species *k*	-
V	electric potential	V
m_{gl}	gas-liquid mass transfer rate	$\frac{kg}{s \cdot m^3}$
μ_k	mobility of species *k*	$\frac{m^2}{V \cdot s}$
E	electric field	$\frac{V}{m}$
D_k	diffusion coefficient of species *k*	$\frac{m^2}{s}$
$\boldsymbol{J}$	electric current density	$\frac{A}{m^2}$
σ_T	conductivity	$\frac{S}{m}$
ϵ	electric permeability	$\frac{F}{m}$
F	Faraday constant	$\frac{C}{mol}$
c_k	concentration of species k	$\frac{mol}{m^3}$
Q	heat energy per unit volume	$\frac{eV}{m^3}$
ρ	density	$\frac{kg}{m^3}$
$\boldsymbol{I}$	unit matrix	-
g	gravity acceleration	$\frac{m}{s^2}$
p	pressure	Pa
η	dynamic viscosity	$\frac{m^2}{s}$
$\boldsymbol{F_i}$	ionic volume force per unit volume	N
$\boldsymbol{F_c}$	surface tension force	N
ζ	surface tension coefficient	$\frac{N}{m}$

* zero order reaction: $\frac{mol}{s \cdot m^3}$, first order reaction: $\frac{1}{s}$, second order reaction: $\frac{m^3}{mol \cdot s}$,third order reaction: $\frac{m^6}{mol^2 \cdot s}$

Contents

1. Introduction

1.1. Plasma Discharges: From myth to reality

Plasma is sometimes referred to as the 'magic wand' of modern technology [1]. In many practical applications such as etching and coating in the semiconductor industry, plasma technology competes with other approaches and has been more successfully implemented over time [1]. The glowing nature of this process has also caught the attention of many science fiction producers and novelists as a futuristic technology.

But how is plasma explained from a scientific point of view? The word 'Plasma' was introduced in the 1920s to describe a conducting gas [2]. Plasma is the fourth state of matter and is created by adding enough energy to a gas so that some of the electrons leave their atoms. The interactions between free electrons and other particles create a series of physicochemical reactions, including photon releasing, excitation, dissociation and ionization processes, that lead to the high reactivity of plasmas. Ionization, which is a result of energetic electrons colliding with neutrals to produce free electrons and positive ions, is the required reaction to form a plasma.

Plasmas can generally be categorized into thermal and non-thermal plasmas [1]. In thermal plasmas, electrons are close to local thermodynamic equilibrium (LTE). This type of plasma is produced in the sun and the stars, where the gas temperature exceeds 10^7 K (about 1keV) [1]. These type of plasmas can theoretically be used for nuclear fusion of hydrogen isotopes to generate energy [3].

Numerous plasmas exist far from thermodynamic equilibrium (cold plasmas). In these plasmas, different particles can have different temperatures. Electron temperature often significantly exceeds that of the heavy particles. In many non-thermal plasma systems, the electron temperature is on the order of 10,000 K (about 1 eV) while the neutral gas temperature remains close to room temperature [1]. The lack of equilibrium between electrons and heavy species is the main feature of cold plasmas. This type of plasma has been used

in many technological applications for decades, such as energy efficient lighting, industrial coating and plasma etching [3]. The possibility to combine a reactive plasma generated by hot electrons and a cold surface at atmospheric pressure enables liquid treatment, which is the main focus of this study. As it is often the case in the literature, the term plasma, cold plasma and non-thermal plasma will be used interchangeably throughout this thesis.

To produce non-thermal plasma, electron heating is commonly achieved by the application of an electric field. Plasmas can be categorised based on the frequency of the applied electric field:

DC plasmas: In this type, the plasma is generated between two electrodes while a direct current is flowing through the system. Free electrons and ions carry the current throughout the plasma medium. Plasma density can be enhanced by using magnetic fields to confine charged species and reduce loss to the walls e.g. magnetron sputtering in low-pressure plasmas [4]. Magnetic confinement of the particles in atmospheric pressure plasmas is generally inefficient due to the high collisionality of the plasma medium [5].

To ignite a DC plasma discharge, electron avalanches must be formed. The very first free electrons in the gas are provided by cosmic rays, radioactivity or leftover charges from previous plasma activity. These electrons are accelerated towards the anode by the applied electric field, ionizing the gas and creating positive ions in particular. These ions are drifted towards the cathode and upon bombardment of the cathode by energetic ions (as well as metastables and photons), secondary electrons are emitted from the cathode. These electrons are accelerated towards the anode creating additional avalanches. If a sufficient number of electrons are produced to compensate for losses at the walls and the anode through the process, the plasma becomes self-sustained [6].

The minimum required voltage to create a plasma between two electrodes is called the breakdown voltage V_{br}, which mainly depends on the type of gas, the pressure and the gap size. Paschen's law was introduced in 1889 and states that the breakdown voltage is a function of the product of the gap length d and gas pressure p ($V_{br} = f(pd)$). Extensive experiments for different gases have been conducted to generate their

'Paschen curves'. Paschen curves show a minimum typically around pd = 1-10 Torr·cm. If pd is too large or too small, electrons undergo too many or too few collisions to effectively create avalanches. Too frequent collisions prevent electrons from reaching the ionization energy in between collisions, while too few collisions result in high energy electrons reaching the walls without undergoing collisions [1].

AC plasmas (kHz): The frequency of the applied electric field is low enough so that the electrons and ions can follow the oscillation of the electric field in this type of plasma. AC plasmas are frequently used for large-scale industrial applications. The electrons and the ions both contribute to the current transfer across the plasma.

The gas breakdown mechanism is generally the same as the DC discharge in this type of plasma i.e. the plasma is mainly sustained due to secondary electron emissions while the electrodes act alternatively as cathode and anode. The discharge may extinguish momentarily as the voltage drops below the breakdown voltage [1].

RF plasmas (MHz): The frequency of the applied electric field is in the range of radio waves in this type of plasma. This frequency is so high that only electrons are fast enough to follow the electric field, whereas the ions almost remain at rest due to their larger inertia [3]. Oscillating electron clouds create positive sheaths along the electrodes. As a result, a strong time-averaged electric field is formed within the sheaths that directs from the plasma towards the electrodes. Positive ions are accelerated within the sheath, bombarding the electrode over an rf cycle. To compensate for the loss of net positive charge, some electrons escape once the oscillating cloud approaches the electrode closely (sheath collapse). Except for such brief moments, the instantaneous potential of the discharge must always be positive with respect to the walls and electrode surface; otherwise, the electrons would quickly leak out extinguishing the discharge [7].

Wave heated plasmas (GHz and optical): In this type, the frequency of the applied electric field is so high that the electromagnetic wave cannot penetrate completely in the plasma. An additional magnetic field is often used to cause resonant heating of the electrons [3].

1.2. Plasma – Liquid Applications: Opportunities and Challenges

Plasma-liquid interaction has become an increasingly important topic in the field of plasma science and technology. While Cavendish's 'experiments on air' in 1785 might be the first attempt to report plasma-liquid interaction, up to 30 years ago the focus of plasma-liquid application was limited to electrolysis, e.g. production of dilute sulphuric acid [8]. These works were later followed by a strong emphasis on environmental driven studies exploring the plasmas as a rich source of reactive species. Due to the availability of modern power supplies with the capability of producing low temperature plasma under atmospheric pressure, interest in plasma-liquid applications has been renewed in the past couple of decades [9].

Plasmas applied on liquids range from DC plasmas [10] to AC plasmas with the frequency ranging from 50-60 Hz up to GHz [11]. The operating pressure can range from a few kPa (plasma application on ionic liquids) up to several MPa (e.g. supercritical liquids) [12].

As an example, plasma-liquid interactions are successfully exploited in water decontamination with various electrode configurations. These configurations range from bubbling the plasma effluent through the liquid phase to using the plasma-liquid interface as the electrode [13]. Micropollutants, such as pharmaceuticals and personal care products are a growing concern since traces have been found in drinking water. These micropollutants can be eliminated by cold (electrons not at equilibrium with heavy particles) atmospheric plasma (CAP) successfully [14]. Plasmas success in eliminating pollutants is mainly due to the production of reactive oxygen species such as O_3, OH, O, H_2O_2 and UV [15], [16].

Another exciting application of CAPs on liquids is anti-cancer therapy in medicine. Reactive oxygen and nitrogen species (RONS) have been shown to be effective in cancer tumour treatment [17]–[25]. Cancer treatment has been investigated *in-vitro* where the anti-cancer effects of CAP are studied on cultured cancer cells in Petri dishes as well as *in-vivo* where CAP or plasma-treated liquid is directly applied to tumours in animals/patients [26]. Chronic and non-healing wound treatment by CAP is another area where plasma-

liquid interaction is used in medicine. The direct interaction of CAP with the liquid layer of the tissue triggers a sequence of biological responses which speed tissue recovery [27]–[29]. Blood coagulation and tissue sterilization are among other medical applications of CAP [30]. This is most attractive because many multi-resistant germs can no longer be treated by standard antibiotics [31]. Tissue removal by electrosurgical plasmas [32], [33] and skin regeneration have also been explored [34].

Another example of plasma-liquid application is electrode replacement. Electrochemical reactions often require metal electrodes such as Pt, which is expensive and limited in supply. CAP has been used as a gaseous metal-free electrode to mediate electron transfer in the solution [35], [36]. In fact, a new branch of nanomaterial synthesis based on the interaction of plasma and liquids has also been developed in recent years. Plasma-liquid interaction systems trigger chemical reactions in the liquid due to the presence of reactive species, ions and electrons at the plasma-liquid interface [37]. To drive reduction reactions, the liquid is used as the anode while the plasma acts as the cathode. The key advantage of synthesis of nanomaterials by plasma-liquid interaction over conventional solution-based methods is that not only the chemical reactions can be controlled by the solution composition but also the discharge properties such as free electron energy and ion energies can be used to control the synthesis process, yielding nanoparticles with fewer impurities [38]–[41].

In more recent years, plasma-liquid applications have been extended to agriculture as well. Seeds produced commercially are commonly treated by fungicides and insecticides to enhance the survivability and germination. These chemicals introduce potential hazards to the environment. Plasma-activated water and plasma treatment of seeds have shown promising results in terms of seed germination and storability [42], [43] as well as plant stress response [44].

Plasma-liquid interactions are also utilized in analytical chemistry to analyse samples based on glow discharges with liquid electrodes [45], [46].

Despite all the new exciting opportunities enabled by plasma-liquid interactions, crucial information required to further improve their efficiency remains limited. As an example, the plasma species dose for cancer therapy must be quantitatively appropriate to damage the tumour cells without affecting healthy tissues. Precision plays a critical role in these applications and the window of operation is limited.

One of the most critical scientific questions is the chemical identity and the dose profile of plasma-induced reactive oxygen species (ROS) and reactive nitrogen species (RNS) inside a the treated liquid [47]. This may require quantification of plasma parameters, such as electric field, electron density and electron energy in close proximity to the liquid-gas interface, which is challenging to acquire experimentally [48]. Other aspects that require further investigation include the way the plasma species are transferred into the bulk liquid through the gas/liquid interface, the types of the reactions the species undergo, the dominating reactions in the liquid phase, the penetration depth of the plasma species, the effect of the electric field on the interface and the plasma hydrodynamic effects in the liquid phase [47].

Experimental diagnostic techniques (e.g. UV absorption and Fourier-transform infrared spectroscopy (FTIR), gas column for the gas phase and gas chromatography-mass spectrometry, chemical probes such as TEMPD and nuclear magnetic resonance spectroscopy (NMR) for the liquid phase) are often used to identify and quantify plasma-liquid interaction products. However, one challenge is that short-lived species, ions, metastables and electrons are difficult to track. While it is essential to determine the fate of these species in the gas and the liquid phase in order to design and optimize a plasma-liquid interaction reactor, experimental analysis is not always possible for the chemical species produced in the system with current diagnostics. This is either due to the short half-life of the plasma products or the lack of information about the nature of the products in the gas or the liquid phase.

Another challenge is that the effect of individual parameters in the mass transfer rate is difficult to determine. As an example, studies suggest that the shear stress induced by the jet gas flow has an important impact on the mass transfer rate [49]. The electric field induced by the plasma also can affect the ion

migration velocity and patterns in the liquid, which in turn will affect the mass transfer rate. But which effect is more important in a plasma-liquid reactor design? Are these effects contradicting one another? What is the effect of the heat dissipated in the gas and the liquid by the plasma? Are there any other important effects that are being ignored? And could these effects be used to enhance the mass transfer rate in a reactor? Answer to these questions would greatly influence the design of reactors for a specific plasma-liquid application [9].

While many of these questions are difficult to tackle with the currently available experimental diagnostics, computational modelling can provide complementary insights to improve our current understanding of physio-chemical processes in plasma-liquid systems.

1.3. Computational Modelling of Plasma-Liquid Interaction: State of the Art

Modelling plasma-liquid systems is typically divided into two parts. The first part is the gas phase chemistry model which deals with the chemical kinetics of the plasma in the gas phase. This typically involves the densities of various species and accounts for the losses on the walls and electrodes. The electron and ion fluxes determine the current density which in turn affects the electric field in the gas and the liquid phase. The results of this model are then used in a second model where the effect of mass transfer, electric field, heat transfer and other physical properties of the plasma are extended to the gas surrounding the plasma and the liquid phase. While a lot of work has been done in the simulation of plasmas in the gas phase, studies on the effects of the plasma on the liquid phase are scarce. This is mainly because while low-pressure plasmas have been used in industry for decades, atmospheric low-temperature plasma applications have only gained interest in recent years as power supplies capable of producing such plasmas have become more readily available. This has enabled plasma-liquid interactions not possible at low pressures due to vapour pressure limitation. Another reason is the complex nature of the interaction itself.

In this section, gas phase plasma models are introduced, and the advantages and disadvantages of different approaches are outlined. Plasma-liquid interaction models are described subsequently.

1.3.1. Gas Phase Plasma Models

The geometry and complex kinetics of the plasma medium challenge plasma diagnostic methods in terms of temporal and spatial resolution. Numerical simulation can provide additional information on the plasma dynamics and chemistry [50]–[52]. A combination of diagnostic methods and plasma modelling can also be used to study short-lived species [53], [54]. Various commonly used plasma modelling methods are introduced in this section. Despite the efforts made in computer simulation of plasmas over the last decades, a model capable of integrating all aspects of a plasma system in detail is computationally prohibitive. Instead, simpler models with appropriate assumptions are normally used [55].

DC Breakdown Model:

The simplest way to describe plasma ignition is by considering electron multiplication by electron impact ionisation as shown in figure 1.1.

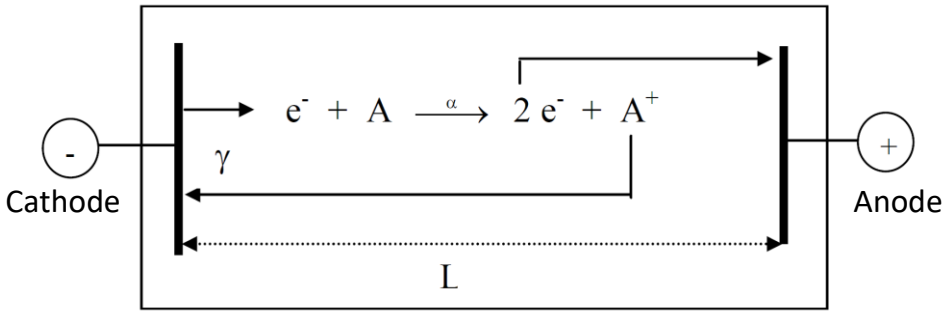

Figure 1.1. Analytical description of DC breakdown [56].

The electron balance equation yields $\frac{dn_e}{dx} = \alpha n_e$, where n_e is the electron density and α is the first Townsend ionisation coefficient. The analytical solution is $n_e = n_{e,0}\exp\left(\int_0^L \alpha\ dx\right)$, where $n_{e,0}$ is the electron density at the cathode and $n_{e,0}\exp\left(\alpha L\right)$ the density at the anode. Assuming a constant value for α

throughout the integration domain, for each electron released at the cathode $\exp(\alpha L)$ electrons reach the anode. This leaves $\exp(\alpha L) - 1$ positive ions formed in the discharge volume, which will drift to the cathode. The number of secondary electrons emitted due to the ions is given by $\gamma(\exp(\alpha L) - 1)$, where γ is the secondary electron emission coefficient. The number of electrons emitted must be equal to or larger than 1 to fulfil the self-sustaining discharge condition. Hence:

$$\alpha L = \ln\left(1 + \frac{1}{\gamma}\right) \quad (1.1)$$

This is a simple analytical equation to describe the conditions required for plasma ignition (or gas breakdown). More complicated terms accounting for the electron temperature, ambipolar diffusion, electrode and side-wall losses can be found in [7].

The advantage of this type of analytical model is its simplicity and low calculational cost. This type of model provides invaluable insights into the breakdown mechanism; however, it cannot be used to describe the plasma. This is because once the plasma forms the electric field in the discharge gap, it is no longer uniform and α is not constant throughout the discharge.

Direct Solving of Boltzmann Equation:

The gas phase plasma can be modelled by solving the Boltzmann equation. Let f be the distribution function that describes the number of particles at time t with velocity $\boldsymbol{v}$ and position $\boldsymbol{r}$. Each particle is hence pictured in a 6-dimensional space according to time. One of the dimensions is shown in figure 1.2.

If f is known, other properties of the plasma such as density n, mean velocity u and flux Γ can be calculated according to equations 1.2 to 1.4 [57][55].

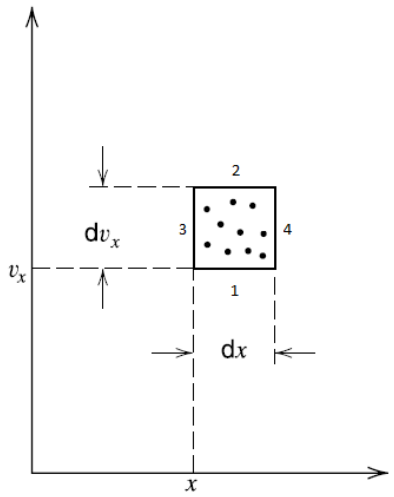

Figure 1.2. One dimensional v_x-x phase space [7].

$$n(\boldsymbol{r},t) = \int_{-\infty}^{+\infty} f d\boldsymbol{v} \tag{1.2}$$

$$\boldsymbol{u}(\boldsymbol{r},t) = \frac{1}{n}\int_{-\infty}^{+\infty} \boldsymbol{v} f d\boldsymbol{v} \tag{1.3}$$

$$\boldsymbol{\Gamma}(\boldsymbol{r},t) = n\boldsymbol{u} = \int_{-\infty}^{+\infty} \boldsymbol{v} f d\boldsymbol{v} \tag{1.4}$$

Particles drift in phase space, flowing into or out of the fixed volume. The continuity equation of f can be written by considering the particle flow across each face into or out of $dx\ dv_x$:

face 1: $f(x, v_x, t)dx\ a_x(x, v_x, t)dt$ (particles flow in)

face 2: $f(x, v_x + dv_x, t)dx\ a_x(x, v_x + dv_x, t)dt$ (particles flow out)

face 3: $f(x, v_x, t)dv_x v_x dt$ (particles flow in)

face 4: $f(x + dx, v_x, t)dv_x v_x dt$ (particles flow out)

where the flow velocities in the v_x and x directions are $a_x v dv_x/dt$ and $v_x \equiv dx/dt$. Hence:

$$\begin{aligned} f(x, v_x, t + dt)dx\ dv_x - \ & f(x, v_x, t)dx\ dv_x \\ &= [f(x, v_x, t)a_x(x, v_x, t) - f(x, v_x + dv_x, t)\ a_x(x, v_x + dv_x, t)]dxdt \\ &\quad + [f(x, v_x, t)v_x - f(x + dx, v_x, t)v_x]\ dt \end{aligned} \tag{1.5}$$

Dividing both sides by $dx\ dv_x\ dt$:

$$\frac{\partial f}{\partial t} = -\frac{\partial}{\partial x}(f v_x) - \frac{\partial}{\partial v_x}(f a_x) \qquad (1.6)$$

Since v_x is independent of x and assuming that a_x does not depend on v_x, then:

$$\frac{\partial f}{\partial t} = -v_x \frac{\partial}{\partial x}(f) - a_x \frac{\partial}{\partial v_x}(f) \qquad (1.7)$$

Taking all the terms to the left-hand side and three-dimensional generalization of equation 1.6 yields:

$$\frac{\partial f}{\partial t} + \boldsymbol{v}.\nabla_r f + \boldsymbol{a}.\nabla_v f = 0 \qquad (1.8)$$

where $\nabla_{\boldsymbol{r}} = (\frac{\hat{x}\partial}{\partial x} + \frac{\hat{y}\partial}{\partial y} + \frac{\hat{z}\partial}{\partial z})$ and $\nabla_{\boldsymbol{v}} = (\frac{\hat{x}\partial}{\partial v_x} + \frac{\hat{y}\partial}{\partial v_y} + \frac{\hat{z}\partial}{\partial v_x})$.

Equation 1.8 describes a collision-less plasma and is known as the Vlasov equation or the collisionless Boltzmann equation. To account for collisions that in very short timescale cause particles to "appear" or "disappear" in the box shown in figure 1.2, a term is added to the right-hand side of equation 1.8 [58]:

$$\frac{\partial f}{\partial t} + \boldsymbol{v}.\nabla_r f + \boldsymbol{a}.\nabla_v f = \frac{\partial f}{\partial t}|_c \qquad (1.9)$$

Equation 1.9 is known as the Boltzmann (BE) equation. BE contains all the information required to describe the plasma. However; direct solution of the BE is rarely attempted especially when collision and radiative processes within the plasma cannot be neglected. Direct solution is typically limited to simple scenarios such as uniform discharges [59].

Fluid Models:

Another strategy to model a plasma consists of solving a set of moments of the BE [60]. The zero-velocity moment of this equation $\int_{-\infty}^{+\infty}(BE)d\ \ \boldsymbol{v}$results in the continuity or particle preservation equation. The first velocity moment $m\int_{-\infty}^{+\infty} v(BE)d\ \ \boldsymbol{v}$ and second velocity moment $\frac{1}{2}m\int_{-\infty}^{+\infty}\boldsymbol{v}^2\,(BE)d\ \ \boldsymbol{v}$ result in the momentum and energy balance equations respectively, where m is the mass of the particle. These are the

fundamental equations of fluid models. Higher order moments of the Boltzmann equation can be calculated [61], but in order to reach a solution, this equation chain must be truncated at some point [57].

Fluid models describe plasma according to macroscopic quantities such as density, pressure, average velocity and temperature [62], [63]. Truncated moments of Vlasov or Boltzmann equations are used for each species present in the plasma and coupled with Poisson or Maxwell equations to evolve the electromagnetic fields and to calculate the force exerted on charged species [61].

In some studies, the motion of the charged particles is assumed to be in equilibrium with the electric field. This is known as the local field approximation (LFA), which reduces the computational cost as the mass balance equation will be the only remaining set of equations that needs to be solved. A good approximation of the plasma behaviour can be achieved even with LFA in some simple cases [55], [60], [64], [65].

A less restrictive simplification is the use of the drift-diffusion approximation. In this method, the particle fluxes are given as the sum of a diffusive term, which depends on particle density gradients, and a drift term for charged particles that depends on the electric field. Most often, ions are assumed to be at the same temperature as the background gas and therefore, only the energy balance equation is solved [66], [67].

The main advantage of fluid models is their fast computation with detailed chemistry. The disadvantage is that since the properties of the plasma are averaged, solving the system of equations requires assumptions for the velocity distribution function. These assumptions introduce the main limitation of fluid models as the velocity distribution functions may have limited reliability [68], particularly in low-pressure discharges [52], [69].

Global Models:

Global models or 0D models are simple fluid models that consider the plasma medium to be uniform. Although wall reactions and side-wall fluxes are accounted for in the mass balance, the spatial distribution

of the densities is ignored. This is to improve computational efficiency while generating results that can provide quick insight into experimental results [52], [70].

Global models solve a mass balance equation for each of the species in the plasma including the electrons:

$$\frac{\partial n_i}{\partial t} = \sum R_j \quad (1.10)$$

where n_i is the density of species i and R_j are the generation and loss rates due to reactions that produce or consume species *i.* These rates can be calculated as $R_j = k_j n_i n_k$ for two-body reactions where k_j is the reaction rate coefficient of reaction j and n_i and n_k the density of the reacting species. The reaction rate coefficient is often a function of the temperature of the particles involved in the reaction. To calculate the electron temperature, the electron energy balance is solved (see discussion in chapter 2). Similar expressions can be derived for 3-body collision processes (e.g. de-excitation of an excited state).

Although spatial evolution is not accounted for in global models, the spatial behaviour of various species and plasma properties can be deduced from the temporal behaviour based on the gas plug flow velocity in a steady state [71], [72].

Global models have been modified and enhanced in case studies to give a better approximation e.g. in electronegative discharges [73], [74]. Since extensive chemistry models are often used in global model simulations, efforts have also been made to generate chemical sets and identify possible chemical pathways automatically [75].

Several codes that solve global models have been made available. GlobalKin code solves a global model according to given reaction rate coefficients [76], [77]. Quantemol-P is a commercial code built around GlobalKin to provide a graphical user interface [78]. Another application is ZDPlasKin, which uses a user-defined reaction scheme to solve the global model equations for various species densities as well as bulk gas and electron temperatures [79]. GlobalKin and ZDPlasKin can be used in conjunction with Pumpkin

which analyses chemical pathways [80]. PLASIMO [81] and COMSOL [82] are also commercial products that provide users with a framework to create global models.

Advantages of global models include simple calculations with low computational cost. Large chemistry sets can be accounted for, including the study of the main chemical pathways. The main disadvantage is the lack of spatial resolution, which can be problematic in inhomogeneous discharges. Although not limited to global models, the sensitivity of the solution to the reaction rate data needs to be kept in mind. Since a relatively small number of the reactions can potentially dominate the behaviour of the system, small errors in the reaction rate data can drastically affect the results.

Particle In Cell - Monte Carlo Collisions (PIC - MCC) Models:

In particle in cell - Monte Carlo Collisions (PIC - MCC) models, ions and electrons are tracked as they move in magnetic and electric fields. The motion of each particle is obtained by solving the Newton-Lorentz

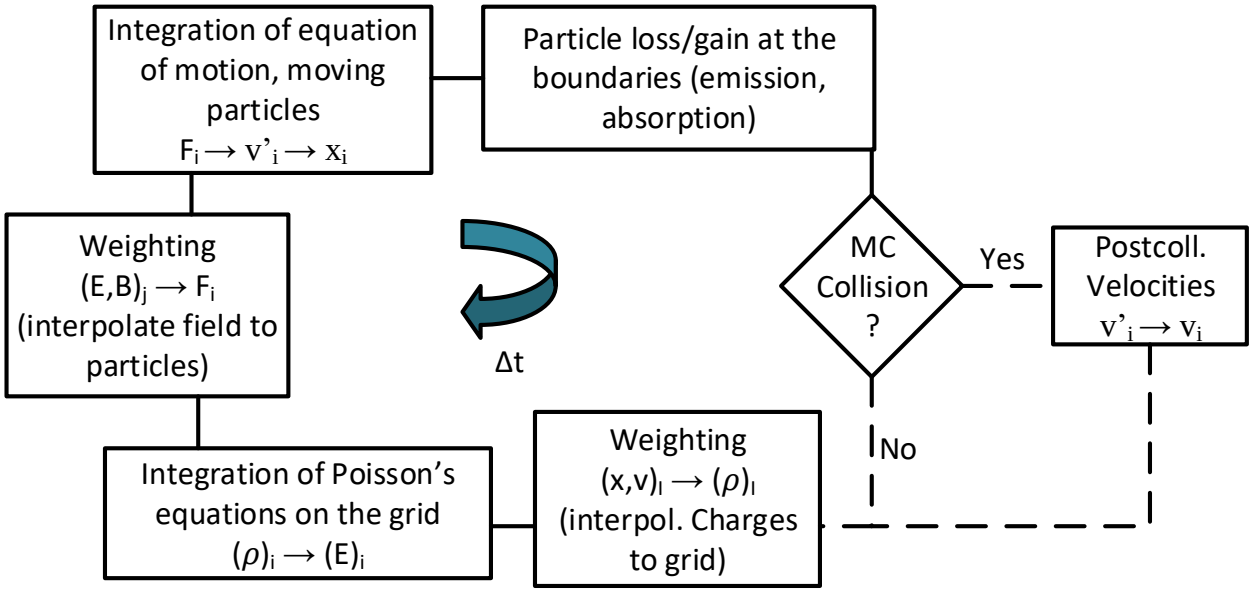

Figure 1.3. Flow diagram of the PIC model using super particles [56].

force equation. These models often require high computational intensity while accuracy relies on the physical description of the particles [61]. The electric field is calculated taking into account the applied

voltage and the position of the charged particles. Unlike fluid simulations, PIC-MCC simulations do not make any assumptions about the velocity distribution of the particles and are therefore self-consistent [83].

The results of PIC - MCC simulations can reliably predict experimental observations [69], [84]–[86] but a great number of particles are required to be simulated in order to reflect real plasma discharge behaviour. Due to the high computational cost, simulations are carried out using 'super particles' which represent a large number of particles collectively while chemistry of the model is limited to only a few species [86]. Figure 1.3 shows the flowchart of a PIC model where real plasma particles are replaced by superparticles (e.g. 1 super particle = 2×10^7 real particles).

The key advantage of PIC - MCC simulations is that the motion of the particles is solved without making any assumption on the velocity distribution. Non-local kinetics are hence captured accurately and the energy distribution can be derived from the simulation for each species [52], [55], [87]. PIC method is straightforward, simple to implement and has fewer assumptions than fluid models [52]. Drawbacks of PIC simulations include high computational cost and discrete particle noise. The discrete particle noise causes local numerical heating (increase in total local energy) which can affect simulation results. Choosing the correct ratio between the real particle number and super particles improves the result accuracy [88].

Hybrid Models:

Fluid models do not resolve the electron and ion energy distribution function (EEDF / IEDF) and assumptions need to be made in this regard. PIC - MCC simulations resolve EED and IED as a function of space and time but with high computational cost [89]. Hybrid methods have been developed to combine the best features of fluid and PIC - MCC approaches. These approaches preserve some of the accuracies of PIC – MCC simulations while reducing the computational load [68]. A common way of combining modelling aspects is to model the ions as a fluid while electrons are treated as particles [89], [90]. Other studies have used a PIC model for the pulse on-time while a fluid model during the pulse-off time [91]. Ions can also be modelled as particles while electrons are assumed to be fluid [92].

The complex algorithms and the cumbersome numerical implementation are often referred to as the disadvantages of this model. Besides, the modelling strategy must be tailored to the problem at hand as the chosen model combination can significantly affect the simulated plasma results[93].

1.3.2. Plasma-Liquid Interaction Models

Plasma-liquid interaction models have only emerged in the past few years. In addition to the complexity of modelling gas plasma, simulations of plasmas interacting with liquids need to account for processes in the liquid phase and challenging physio-chemical processes at the plasma-liquid interface. Often the chemical processes in the liquid phase are unknown, further complicating the task of modelling plasma-liquid systems. This is particularly true in systems with non-water solvents. The transfer of reactive species to the liquid through the plasma-liquid interface triggers chemical reactions in the liquid phase and this is often accounted for in plasma-liquid simulations. However, the vapour transferred from the liquid to the plasma can affect the plasma composition significantly (e.g. the effect of water vapour in an oxygen-helium plasma [94]) and should also be taken into consideration. While Henry's law provides some insight about the gas and the liquid phase species densities, information about short-lived species densities, electron concentration in the regions adjacent to the interface and non-equilibrium condition are limited to a very few studies [49], [95], [96]. It is often assumed that the sticking coefficient or surface loss of electrons reaching the liquid is equal to one [49] although there is no direct evidence of this. While it is proven experimentally that electrons can penetrate into the liquid phase at least a few nanometers [97], more in-depth studies are required to determine the spatiotemporal electron density and their energy distribution in the liquid medium [49]. In spite of the challenges, significant progress has been made in modelling plasma-liquid interaction in recent years [98]–[102].

Many reactor geometries have been proposed for plasma-liquid interaction [103]. Due to the variety of modelling techniques, different modelling softwares are used to model the reactors. A number of Multiphysics packages are often used e.g. VizGlow [104] and COMSOL [105] as well as author-developed

codes e.g. nonPDPSIM [99]. Plasma-liquid systems can be categorized into the following sub-categories for modelling purposes:

Direct discharges in liquids:

Direct discharges in liquids can be produced by a rapid breakdown process. This is often achieved by applying a strong nanosecond pulsed voltage [10] or by AC excitation of 50 Hz to GHz inside the liquid phase [11]. In-liquid plasma is produced in the liquid directly or in a transient vapour phase without relying on flowing gases. As a result, the reactive species are very different from typical gaseous plasmas with selected background gas mixtures [9].

Efforts have been made to explore plasmas produced directly in liquids using imaging and optical emission spectroscopy. These techniques enable basic plasma parameters measurements e.g. discharge morphology, bulk temperature and electron density[106], [107]. Ionization in atomic liquids have been explored for many years and the mechanisms are relatively well-understood [108]. However, plasmas produced in non-atomic liquids such as water are more challenging to understand [9]. The main unresolved questions are: (a) considering some studies suggest that breakdown can occur without a phase change [109], what is the breakdown mechanism in liquids? And (b) what physical and chemical processes occur during the process [110]? To bypass these issues, studies have been performed to simulate vapour layer formation in the liquid phase where less information is required about the chemical kinetics of the process [111].

Streamer-like plasma discharges in the liquids are formed in plasma filaments less than 10 μm. It is possible to model a plasma filament surrounded by water by dividing the plasma filament into two parts: the centre which dissociates water and produces radicals, and the surrounding plasma where the radicals are recombined producing long-lived species. Although processes at the plasma-liquid interface are not considered, a good agreement can be achieved between the model and measured densities in the liquid phase [112].

Direct discharge in the liquid may not be industrially feasible. As an example, to generate an underwater streamer discharge, the electric voltage difference required is typically between 50 to 400 kV with a current of more than 100 A. This configuration is difficult to achieve and maintain in steady state and is not efficient from an energy consumption standpoint [113]..

Discharges in the gas phase over a liquid:

A more practical approach of applying plasmas on liquids is to produce the plasma in the gas phase and bring it in contact with the liquid phase. Three typical configurations used in this method are (a) plasma produced in a plasma jet without electric contact with the liquid, (b) plasma electrolysis where the liquid is

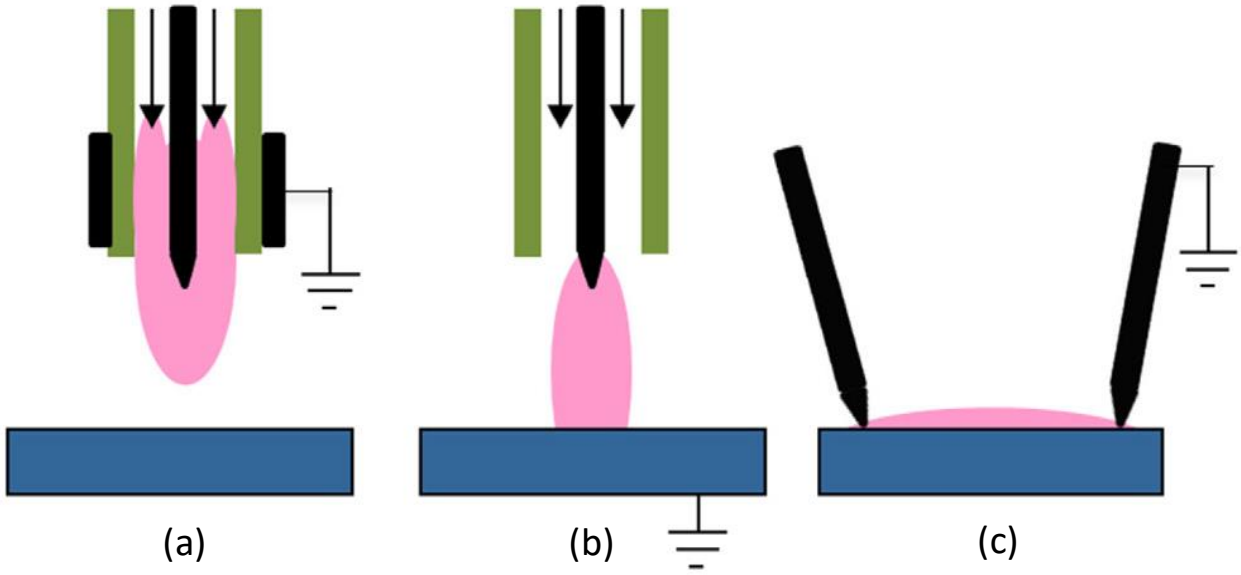

Figure 1.4. Schematic of various plasma over liquid configurations. (a) Plasma without electrical contact with the liquid. (b) Using the conductive liquid as an electrode. (c) Discharge formed at the liquid surface [9].

used as an electrode and (c) plasma discharge between two metal pins contacted with the surface of the liquid. The schematics of these concepts are shown in figure 1.4. These plasmas are typically sustained at atmospheric pressure, except for ionic liquids [114], [115].

The first configuration is shown in figure 1.4 (a). Plasma is applied on the liquid surface without direct electrical contact to the liquid phase. Reactive species are transferred by a convective flow through the plasma jet onto the liquid surface. Examples include a dielectric barrier discharge (DBD) between a central needle electrode and an electrode ring [116], two outer ring electrodes [117], [118], and a single electrode with capacitive coupling [119]. In all configurations, excitation frequencies can range from kHz to GHz [120], [121].

Plasma can also be produced between a metal pin and a conductive liquid electrode with various discharge geometries and system configurations [96], [122]–[124] as shown in figure 1.4 (b). This type of glow discharge can be produced even with a DC current in ambient air [125]. The large electric field produced between the needle and the liquid can cause instabilities at the interface which can lead to enhanced mass transfer between the plasma and the liquid [126]. Using liquid in both electrodes has also been explored in the context of two falling parallel conductive films [127]. A metal plate can be used instead of the pin to increase the plasma-liquid interaction interface. This configuration is also used in nanoparticle production [38].

The main difference between a plasma jet not in electric contact with the liquid and a jet using the conductive liquid as an electrode is the electric field orientation compared to the direction of the flowing gas. This causes the plasma jet without an electric contact to the liquid to be dominated by neutral species where in the case of the jet using the liquid as an electrode, the liquid is also exposed to electrons and ions [128].

The third configuration is to generate electric discharges along the liquid surface with two metal electrodes placed far from one another (e.g. 20 cm apart) while the electrode tips are close to the liquid [129] as shown in figure 1.4 (c). This configuration has gained more attention in recent years as the reactive species are produced at the plasma-liquid interface at a potentially larger surface area compared to the previous configurations [130].

All these configurations are typically modelled by solving the Navier-Stokes equations (continuity, momentum, energy) to obtain the flow field. In cases where the gas is static and the plasma is produced on the surface of a dielectric layer, the dominating mechanism transferring plasma reactive species into the liquid is diffusion and electrohydrodynamic (EHD) effects [131]. The shape of the liquid surface deformation can be determined according to experimental data [101], [132]. The plasma region is then resolved by either using experimental data [133] or computational modelling. Model results are obtained by solving Poison's equation, transport equations for charged and neutral species, the electron energy equation and radiation transport. Electron transport and rate coefficients are obtained by solving the Boltzmann equation for a given average electron energy [134]. The liquid phase is treated similarly to the gas phase with the proper dielectric and transport constants [98]–[100], [135]. Thermodynamic equilibrium is assumed at the gas-liquid interface and Henry's constants are used to determine the flux of species into the liquid phase [47], [71]. Caution must be exercised in this regard as Henry's equation assumption of liquid being in equilibrium with the gas phase may not always reflect an accurate image of the problem [49].

Multiphase environments with discharges in bubbles or droplets in plasma:

The mass transfer rate between the liquid and gas phase can significantly be improved by increasing the interfacial area. This concept has been extended to plasma-liquid interaction by using bubbles and droplets.

To increase the reaction interface area using bubbles, plasma-liquid interaction can be performed by injecting bubbles into the liquid while using the injection capillary as an electrode [136]. With sufficient power, plasma is ignited inside the bubble along the gas-liquid interface [137]. Although some liquid species are transferred into the plasma gas phase inevitably, the main concept is to transfer the plasma reactive species into the liquid phase. The electric field can locally affect the chemistry of the process through field-induced decomposition and charged particle acceleration [138]. Plasma can also be produced

while the bubble is detached from the capillary by microwave excitation [139] or in the inlet gas before interacting with the liquid [140], [141].

Another method to increase the plasma-liquid interface is using liquid droplets. For example, the feed solution can be injected perpendicularly to the plasma jet axis allowing droplets to be formed in the plasma medium. These droplets are subject to break-up and evaporation in contact with the hot gas flow. Here, the main concept is to transfer the liquid species into the gas phase e.g. to identify the compounds in the liquid by atomic emission spectroscopy (AES) and mass spectroscopy (MS). Aerosol droplets are typically expected to fully vaporize within the residence time in these applications [142]–[144]. Researches have been carried out to expand the knowledge of evaporating droplets in plasmas [145]. In industrial applications, aerosol droplets in plasmas often contain precursor material for plasma deposition [146], [147]. Droplets have also been studied in cases where the droplet is not fully evaporated e.g. to decontaminate water using plasma [148], [149]. These applications range from low-pressure [150] to atmospheric pressure [151] plasmas.

To model plasma produced in a single bubble attached to a capillary, simulations are often performed using a configuration where the liquid is grounded, and the bubble is attached to the high-voltage capillary. Poison's equation is coupled with transport equations for all charged and neutral species and electron energy equation. The system of equations is then solved for electrical potential, density, momentum and electron temperature. Reaction rate coefficients are a function of average electron energy which is obtained by solving Boltzmann's equation using a two-term spherical harmonic expansion. In this configuration, the plasma is sustained by secondary emissions from the surface[152], [153].

To simulate the plasma produced inside a swarm of bubbles rising in a liquid, charged and neutral species continuity equations are coupled with drift diffusion for the species flux terms, along with the electron energy balance to obtain the electron temperature. Poisson's equation is solved to obtain self-consistent

electrostatic potential in the bubbles. For a microwave plasma, the electron heating is assumed to purely result from wave Joule heating [154].

To model aerosol-plasma interaction, a fluid model is used for the gas phase where major discharge species e.g. electrons, metastables and positive ions are considered along with the gas phase plasma reactions. Mass, energy and momentum balances are written for the gas plasma phase and the liquid aerosol droplet. Empirical correlations i.e. generalized non-dimensional equations describing the multiphase system are used to describe the plasma-liquid interaction behaviour. The electric field is calculated by Poisson's equation in the gas phase and is then included in the momentum balance equation [155]–[158].

Recent investigations argue that the interactions between a droplet and the surrounding plasma differ from that of bulk liquid-plasma interface. Droplet charging and selective heating affect the diffusion of plasma species into aerosol droplets [159]. Although the effect of droplets on plasma properties has been extensively investigated [143], [160] the impact of plasma on physical and chemical properties of droplets is poorly understood [161].

1.4. Problem Description

Regardless of the size and nature of the transferred species, the main idea of contacting plasmas and liquids remains the same: to transfer reactive species into the liquid as efficiently as possible. These species can range from charged species (e.g. electrons and ions) to neutral species. Low mass transfer rates and the ambiguity involved in the governing mechanisms, often hinder the technology from being used in industrial and medical applications despite clear advantages over older conventional methods.

As a practical example of the problem, epoxides which are key building blocks in organic synthesis and important intermediates in the preparation of many natural products are typically prepared by reacting alkenes with sacrificial mono-oxygen donors, such as peracids or organic peroxyacid [162], [163]. While plasma-liquid epoxidation shows clear advantages over conventional chemical methods (e.g. reduction of

toxic by-products), the reaction yield in experimental configurations is so low that renders the method impractical in industrial applications [164].

1.5. Project Aim and Novelty

The aim of this project is to provide new insights into plasma-liquid interactions and where possible provide guidelines for the design of plasma-liquid reactors. While computational modelling should not be regarded as a perfect evaluation tool, it can be used to provide valuable insights into the plasma-liquid interaction phenomenon [47]. In addition, some experiments are conducted to validate the simulation results and to infer the value of unknown constants. For example, the value of Henry's constant for atomic O which plays an important role in epoxidation reactor design, and the local surface tension gradient which significantly affects the mixing patterns of the liquid phase have been estimated by comparing simulation and experimental results.

The developed computational model covers a wide range of multidisciplinary aspects such as plasma physics, heat transfer, mass transfer, electric current and charges, surface effects and chemical reactions, while still being computationally tractable.

As a result of the difference in time and spatial scale between plasma processes and liquid dynamics, two computational approaches have been investigated: models that describe the plasma-liquid interaction in detail, but are intensive computationally and do not account for the long timescales or the system geometry in detail, and models that describe the system time and dimensions realistically but lack the details about the plasma.

Simulation and experimental results have provided new insights into the effect of power modulation on the chemistry of DBD reactors, guidelines for the design of a plasma epoxidation reactor and the importance of surface tension on liquid treatments. These are discussed in chapters 4-6 of this thesis.

1.6. Thesis Structure

This thesis is structured as follows:

The introductory chapter describes the background of the project while underlining the new emerging opportunities as well as the challenges of plasma-liquid applications.

Chapter two describes the experimental methodology, including the measurement techniques as well as the materials, analytical tools and experimental conditions. The reason why an experiment or measurement strategy is chosen is also outlined in this chapter.

The third chapter describes the basics of the computational models used throughout this thesis. This includes the equations, initial and boundary conditions as well as the numerical strategy used to solve the system of equations. The reason behind choosing one strategy over another is also explained here.

The main triggering mechanism of the reactions occurring in the plasma-liquid interface or within the liquid medium is the reactive species transfer. This includes free electrons produced within the plasma as well as long-lived and short-lived neutral plasma products. To study transfer of these species, initially, the plasma in the gas phase needs to be understood. Therefore, chapter four is a study carried out on the gas phase plasma excluding the liquid medium. This chapter lays out the foundations of the kinetic plasma model used in the upcoming chapters as well as the plasma simulation results. The significance of power modulation on the plasma final gas composition for an air DBD is discussed in detail.

The fifth chapter focuses on the transfer of heavy particles reactive species as the key triggering mechanism for chemical reactions in the liquid phase. The computational model is used to understand the phenomenon as well as to enhance and optimize a plasma-liquid bubble reactor. A set of reactor design guidelines are outlined in this chapter, which not only explains the effect of various mechanisms on the reactor yield in the current configuration but also paves the way for a more optimized future reactor design.

The sixth chapter describes plasma-driven electrolysis in which the electrons are delivered to the liquid to drive reduction processes. In this setup, the plasma acts mainly as a source of electrons, although additional plasma effects on the liquid such as heating, electric fields, external gas flows and conductivity are taken into consideration. The importance of surface tension in the liquid mixing pattern is studied in detail in this chapter.

Finally, conclusions and future work are drawn in chapter seven.

2. Experimental Setups and Characterisation Methodology

Three experimental setups are used throughout this thesis. The first one consists of a DBD reactor without liquid to study the gas chemistry of an air plasma and how it is influenced by the modulation of the input power. The second setup is used to study the transport of neutral reactive species to a liquid in an AC epoxidation reactor. And the third one is a DC plasma electrolytic cell in which the plasma is in electrical contact with the liquid and acts as a source of electrons to drive reduction reactions.

2.1. Dielectric Barrier Discharge (DBD) Air Plasma

This experimental setup consists of an air DBD operating at atmospheric pressure. For a given background gas, one of the most important factors affecting the plasma gas composition is the input power and its modulation scheme. In particular, the effects of various on-times on the plasma gas composition are studied as part of this thesis.

Figure 2.1 shows a schematic of the plasma source used to analyse the air plasma in the gas phase. The reactor can be split into two parts. The lower part of the reactor is the plasma module which consists of 19 stainless steel rods with a hemispherical cap at the upper tip and the high voltage is applied to each electrode. Each steel rod is placed within a quartz dielectric crucible. At a gap of 1 mm above the tip of the crucibles is the nickel membrane which acts as the ground electrode. Compressed air is supplied to the bottom of the plasma module at 1 standard litre per minute (SLPM) from a mass flow controller (PR 4000B, MKS) and flows upwards through the discharge and the pores of the nickel membrane. Once the gas has passed through the membrane it enters the reaction tank. Further details of the reactor used can be found in [165].

2.1.1. Power Supply

The power supply used was built in-house and consisted of a full-bridge DC-AC inverter and a high turn ratio step-up resonant transformer. A sinusoidal voltage of 31 kV_{pp} and a frequency of 21.6 kHz was modulated with a 30% duty cycle. Three on-times were investigated in the study: 1 ms, 10 ms and 100 ms.

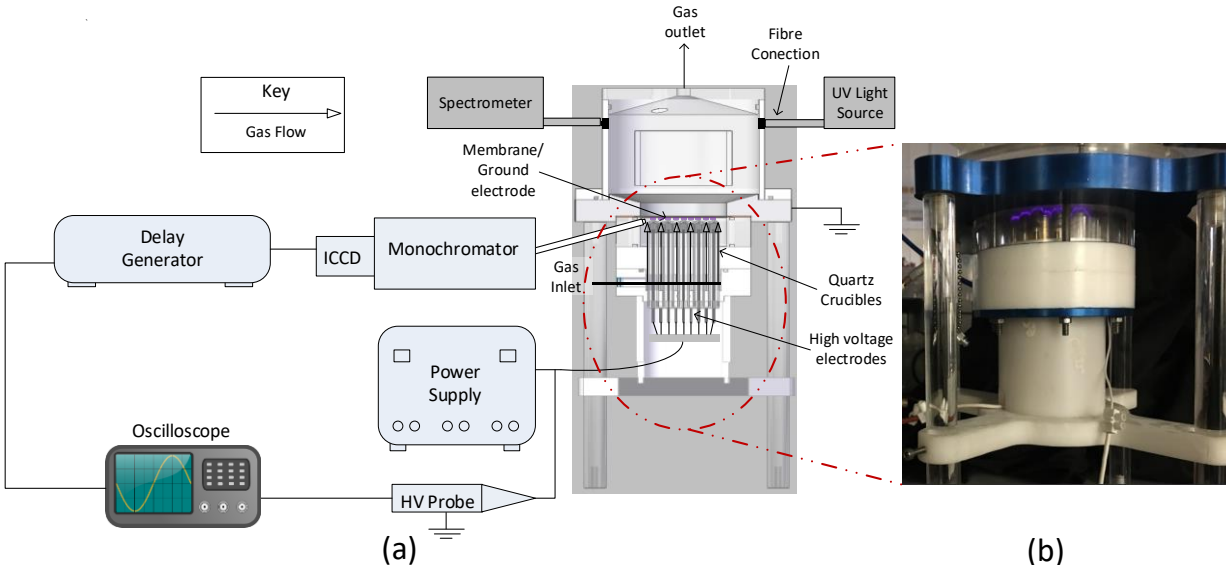

Figure 2.1. (a) Schematic of the DBD plasma reactor and (b) experimental setup [166].

2.1.2. Gas Phase Analysis

The concentration of reactive species were measured by a combination of UV absorption (for ozone) and Fourier-transform infrared spectroscopy (FTIR) (for RNS), both using the Beer-Lambert law. The ozone concentration was calculated by directing a 255 nm LED light source (LLS-255, Ocean Optics) with a fibre optic cable (QP600-1-XSR, Ocean Optics) and a collimating lens through the upper region of the reaction tank as shown in figure 2.1. A changing ozone concentration is reflected in the light intensity change measured from the light collected by the spectrometer (HR2000+, Ocean Optics). The concentration of NO_2, N_2O and NO_2 were measured in the exhaust gas which was passed through a gas cell (1-16m, Pike technologies) mounted in the FITR spectrometer (4700, Jasco). IR cross sections for each gas were taken from the HITRAN database [167].

2.1.3. Temperature Measurements

To measure the gas temperature between the electrodes a fibre optic thermometer (FOB102, Omega Inc.) was used. The fibre was directed through a sealable hole in the side of the plasma module with a thermometer connected to a PC that served as a data logger.

2.1.4. Electrical Measurements

The power delivered to the plasma, was calculated by averaging the instantaneous power over a period. This was obtained by multiplying the current and voltage signals, considering the different delays of the voltage and current probes. Power measurements were compared with that obtained with the Lissajous method and although both were comparable for continuous waveforms, the Lissajous method becomes questionable when the input signal is modulated due to transients when the plasma is switched on and off. A current probe (2877, Pearson) and high voltage probe (P6015, Tektronix) was used to capture the waveforms with an oscilloscope (DP4104B, Tektronix) operated with a sampling rate of at least 100 MHz. Figure 2.2 shows that a high sampling rate is essential to capture the current waveform accurately as low sample rates miss current spikes and therefore underestimate the power. The data was collected and post-processed off-line in a PC.

It was anticipated that the transient nature of the input power would result in the modulation of the optical emission of the plasma, providing an indirect measure of the instantaneous input power. Therefore, the optical emission intensity of the nitrogen second positive system (0-2) was tracked and averaged over time as a proxy of the input power. This was done using a fibre optic cable (QP600-1-XSR, Ocean Optics) inserted through a port in the plasma module side wall as shown in Figure 2.1 and a spectrometer (Andor SR-303i-A, 100 μm slit, grating 2400 l/mm). The angle of the hole and fibre's orientation ensured a direct line of sight of the discharge region. An iCCD camera (Andor iStar) was synchronized with the power supply and the oscilloscope, and a delay generator (7075, Berkeley Nucleonics) was used to trigger the iCCD camera (exposure time 5 μs) at different times within the plasma on-time.

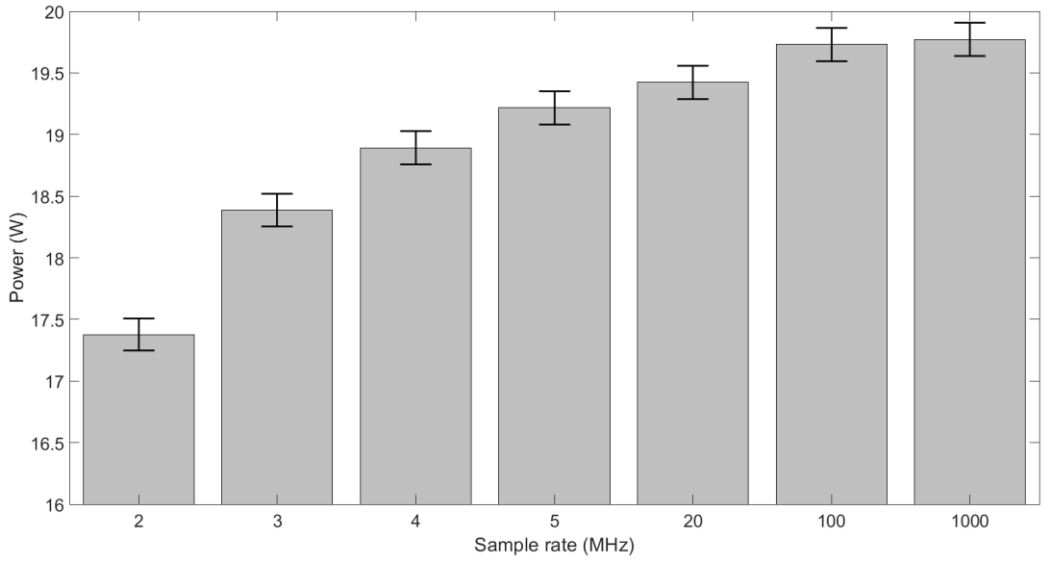

Figure 2.2. Dependence of the measured power on the sampling frequency of the oscilloscope [166].

Figure 2.3 shows that indeed the measured instantaneous power and the plasma emission intensity are correlated and transient in nature. Regardless of the on-time duration, at the beginning of the on-time pulse, the power and light intensity recorded in the experiments show a transient with an "overshoot" that oscillates and attenuates as time progresses. The cause of this damped oscillating overshoot is a combination of the topology of the resonant power supply and the time varying plasma impedance, which combined create an RLC equivalent load for the H-bridge.

This initial transient takes a significant portion of the on-time period when this is set to 1ms (Figure 2.3), but a much smaller fraction when the on-time period is 10 or 100 ms. The presence of this transient means that a different average power is delivered at different on-times, even when the power supply is set to deliver the same voltage. As a result of the increased power delivered at the beginning of the on-time period and the tailing off at the end of the on-time pulse (Figure 2.3), shorter on-times have a higher average power. Negative For the particular conditions of this study, the average power delivered to the plasma increases by 8% and 25% as the on-time is reduced from 100ms to 10ms and 1 ms, respectively. This draws attention to the care required when measuring power in pulsed sinusoidal DBDs.

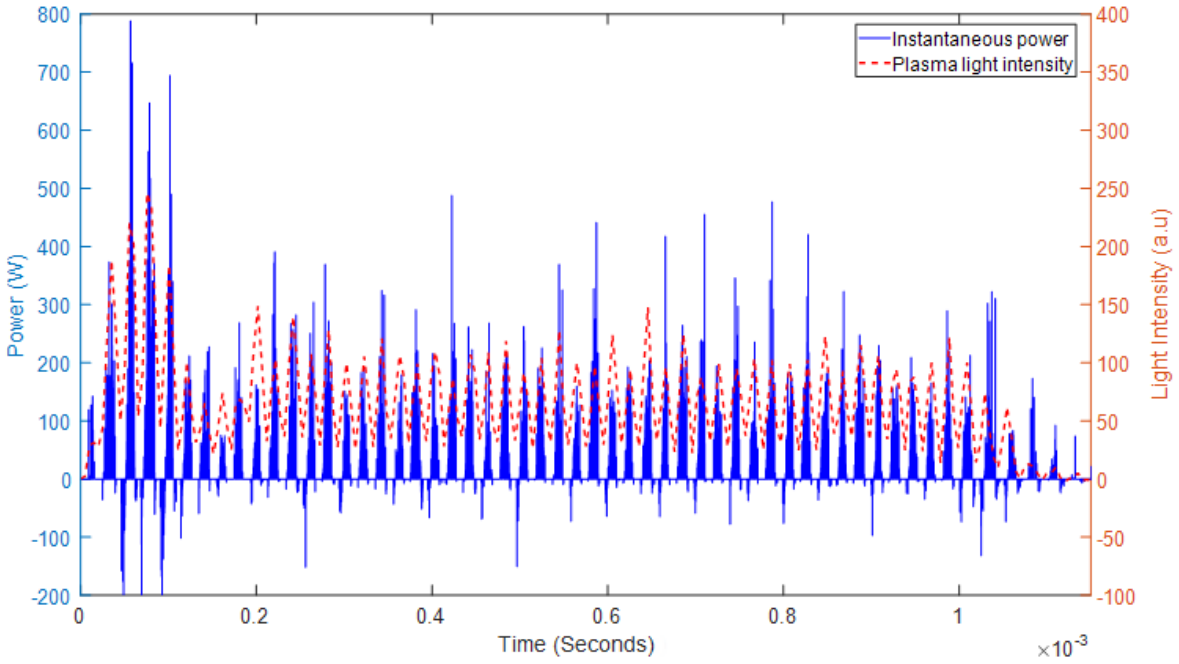

Figure 2.3. Instantaneous power and the nitrogen SPS emission intensity during a 1 ms on-time pulse (Sample rate: 1 GHz). Average nitrogen SPS emission intensity is used as an estimate to track power variation during the on-time [166].

2.2. Plasma Epoxidation Reactor

The second experiment focuses on the transfer of the reactive species from the plasma into the liquid. In particular a He + O_2 plasma is generated to produce atomic oxygen in the gas phase that is then delivered to the liquid where it oxidises an alkene to produce epoxide.

The batch reactor geometry is shown in figure 2.4. The plasma jet consists of three ring-electrodes and a quartz glass tube acting as a dielectric barrier. The high voltage electrode is positioned in the middle of two ground electrodes 10 mm apart from one another. This configuration limits the plasma plume to the distance between the electrodes, hence limiting the effects of the charged species on the liquid. The plasma effluent is then bubbled in a batch reactor open to ambient air. A bent glass tube was chosen to minimize the effect of the UV generated by the plasma on chemical compounds in the liquid. A water-cooled condenser was placed at the top of the reactor to reduce the evaporation of the solution throughout the experiment. The

feed gas consisted of 0.1 % to 1.5 % oxygen (by volume) and He. The initial solution consisted of 8.0 ml of 10 mM *trans*-stilbene (Thermo Fisher Scientific Ltd.) in acetonitrile (VWR Prolab Chemicals) as solvent.

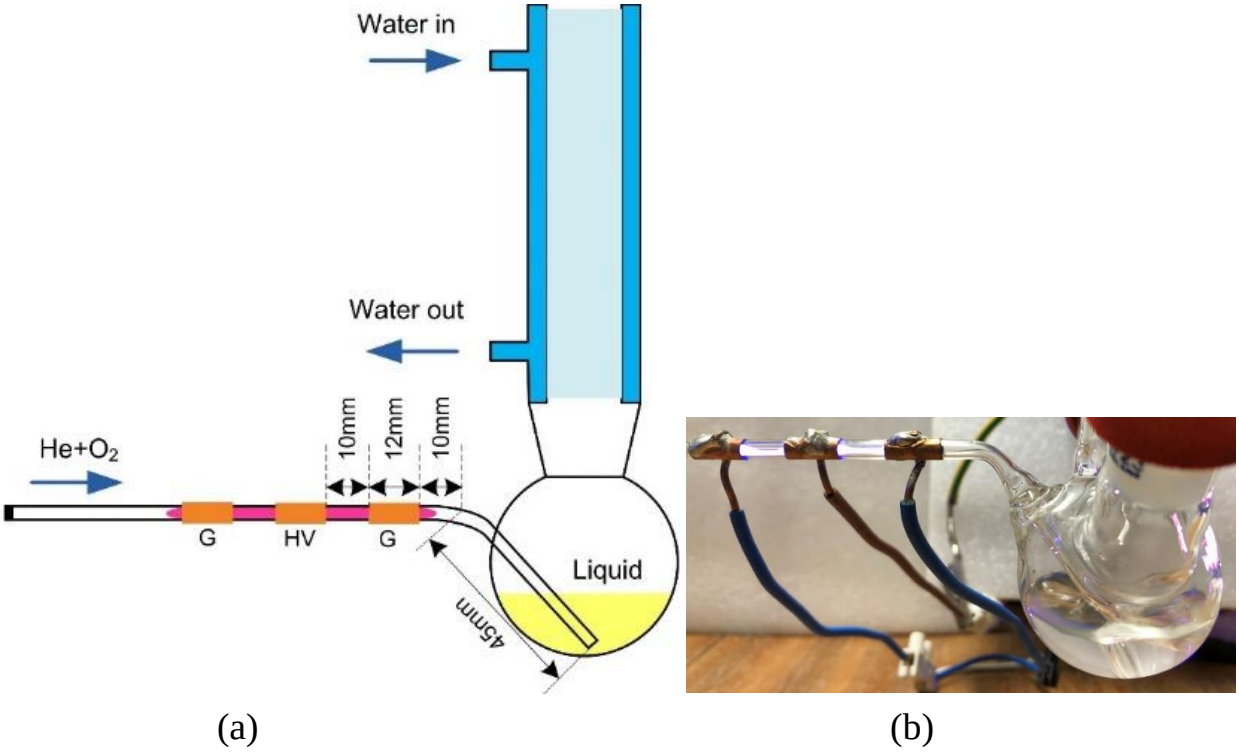

Figure 2.4 (a) A schematic of the experimental batch epoxidation setup and (b) the experimental setup open to the atmospheric air.

2.2.1. Gas Phase Analysis

Atomic oxygen, singlet oxygen, ozone, He^+ and He^* are the main species produced in He + O_2 plasmas. Of these, only ozone is readily measurable in the experimental setup. The ozone concentration in the plasma afterglow is measured using a 255 nm LED light source directed through the gas and collected by a collimating lens and a fibre optic cable (QP600-1-XSR, Ocean Optics). Ozone concentration was then calculated by Beer-Lambert law according to the light intensity change detected by the spectrometer (HR2000+ Ocean Optics).

Changing the O_2 fraction in the feed gases causes the variation of the length of the plasma plume [168], but this factor can be neglected in this work since the plasma plume near the ground electrode is very short [94].

2.2.2. Power Supply

The same in-house built AC power supply used in the previous experimental setup was used to generate the He + O_2 plasma. The tuning capacitor was adjusted to resonate with the new load and the power supply was operated in continuous mode, delivering 5W.

2.2.3. Liquid Analysis

The solutions were treated for 90 minutes in the batch reactor and then analysed by gas chromatography-mass spectrometry (GCMS) (Shimadzu QP2010 Ultra / SE). Naphthalene with a concentration of 50 mM was used as internal standard and calibration curves for the starting materials and the main products were prepared prior to the experiment.

2.2.4. Bubble Size Measurement

A high-speed camera (Photon Fastcam, M2.1) coupled with a long-distance lens (Infinity, KC) were placed level with the multi-neck flask to measure the bubble size. The bubble size distribution was determined by analysing acquired images with ImageJ software.

2.3. Plasma Electrolysis Reactor

The third experiment setup was used to study a plasma-liquid system in which the plasma is electrically connected to the liquid and acts as a source of electrons.

The reactor consisted of a cylindrical tank with a radius of 45 mm and a depth of 5 mm as shown in figure 2.5. A plasma jet which consisted of a glass tube with a radius of 2 mm and a metal rod placed in the centre acting as the ground electrode was used to generate the plasma. A high-voltage 8 mm × 8 mm nickel electrode was submerged into the liquid phase, biasing the liquid positively with respect to the plasma. The solution consisted of de-ionized water with 2 g/L KCl (Sigma Aldrich Ltd.) solvated to make the solution conductive. 1 SLPM helium was used as the background gas and the system was exposed to open atmospheric ambient air.

2.3.1. Power Supply

The power supply used in this experiment was a D.C. power supply (Brandenburg Alpha Series model 507A) and the output current was fixed at 2 mA. A resistor of 1 MΩ was used to ballast the circuit.

2.3.2. pH Analysis

Two of the main factors affecting the efficiency of an electrolysis reactor when water is used as the main solvent are the local pH and the liquid velocity field. These factors can be monitored collectively by using universal pH indicators. A universal pH indicator (Fisher Scientific Ltd.) was added to the solution to track the changes in the local pH and the solution mixing patterns.

2.3.3. Physical Characterisation

Surface temperatures were measured by thermal imaging (FLIR Model E64501). The average surface tension coefficient of the liquid samples was measured by the pendant drop method (Kruss Drop Shape Analyzer Model DSA 100). The dynamic viscosity was measured using a rheometer (Discovery Hybrid Rheometer Model HR-3).

2.3.4. Particle Image Velocimetry (PIV)

PIV was carried out using 4 µm latex particles with a density of 10^3 kg·m^{-3} (Invitrogen by Thermo Fisher Scientific Ltd) using a 2×2 mm window captured in 4000 fps by a highspeed camera (Photron Model MC1). A white light emitting diode (LED) light source was used to illuminate the system. The flow field was optically scanned at different vertical and horizontal distances 10 mm apart. For each distance, 1000 consecutive images were recorded. The analysis was performed by PIVlab v1.43 (open source) and Matlab™ with an interrogation area set to 128×128 pixels and 50% overlap.

2.3.5. Mixing Efficiency

To study the effect of the surface tension gradient on the mixing efficiency, 0.1 mM $AgNO_3$ (Sigma Aldrich Ltd.) was added to a solution of 1% mass polyvinyl alcohol (PVA) (Sigma Aldrich Ltd.) and 99% deionised water. The same amount of salt used previously was also added to pure deionized water and each solution was treated for 15 minutes.

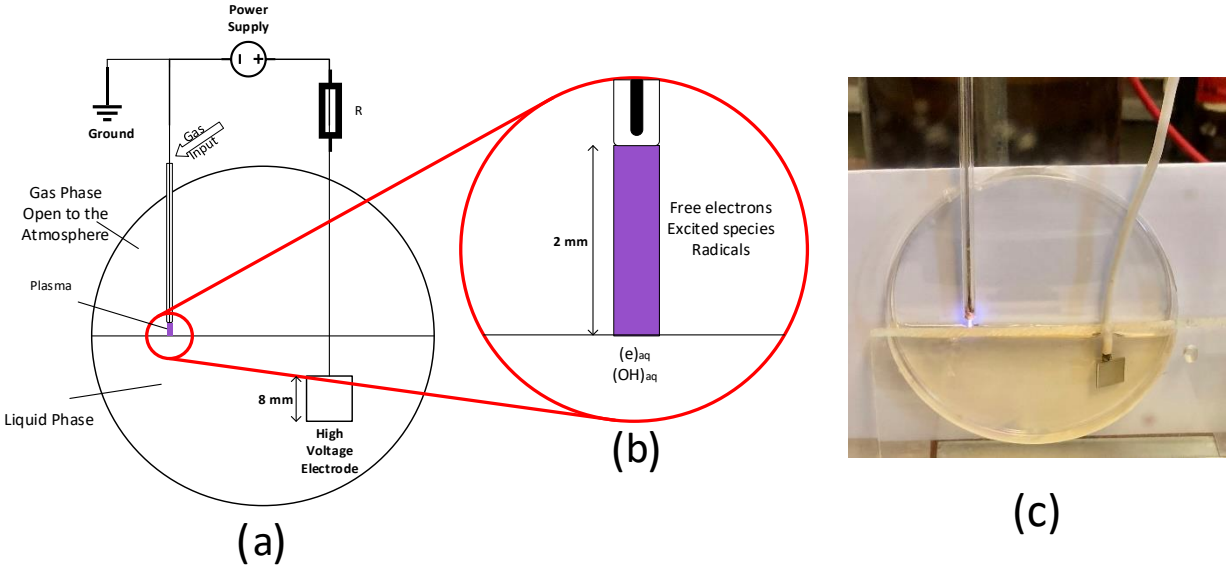

Figure 2.5 A schematic of direct plasma-liquid interaction (a) anticipated species in different phases included in the computational model (b). The experimental setup open to the atmospheric air (c).

2.4. Summary

The three experimental setups and the methods used to characterize the systems were introduced in this chapter. These include a DBD reactor for the study of the influence of the power modulation on the air plasma composition, a remote plasma jet used for the epoxidation of alkenes and a DC plasma electrolysis reactor in which the plasma acts as a source of electrons.

3. Computational Model

In this chapter we introduce the numerical models developed as part of this thesis. While plasmas interacting with liquids date back to 1785, modelling plasma-liquid interaction has attracted more attention in recent years due to exciting new applications and improved computational resources [1-8].

A computational model is a way of describing physical systems or phenomena through mathematical concepts and language. This description not only leads to a better understanding of the system but can also be utilized to improve an engineering method or predict the behaviour of a specific system under various conditions. The results of a well-defined and successful simulation can greatly reduce experiment costs and also the time spent on trials, while providing insights into the sensitivity of the system to various parameters and initial conditions. In addition, it can provide spatial-temporal information that cannot be measured accurately with current technologies.

Successful implementation of a mathematical model depends on how well the system is defined. Thus, the first step in developing a mathematical model is to know the system and the relevant physical phenomena as accurately as possible. Having a sense of what is happening in a system is one of the most crucial steps which will help in initially setting up a model as well as further development and verification.

To define a system mathematically, the governing equations need to be identified. These equations are often described in references for a generalized problem and need to be chosen, modified and simplified accurately to capture the main physio-chemical processes relevant to the problem at hand [7], [169].

Boundary and initial conditions should be added before achieving a practical system of equations. This may require further investigation and the addition of governing physical relations before proceeding to the next step.

Since most systems of equations will require being integrated and solved numerically rather than symbolically, all constants need to be non-dimentionalised, normalised and described in numerical values. These values can often be found in literature or obtained from experimental data.

Due to the nonlinear behaviour of plasma discharges, numerical models often lead to a stiff system of equations which needs to be evaluated by variable integration steps [170]. This is further discussed in a subsequent section.

An important step in any simulation study is to verify the results with experimental data; however, these data may not readily be available for comparison. A combination of available experimental observations and verified theoretical studies are often utilized in this regard.

The theoretical description of general two-phase liquid-gas interaction is well established. What separates plasma-liquid modelling from general fluid phase simulation is the assumption that the fluid is in local thermodynamic equilibrium (LTE) and their response to electromagnetic fields due to the presence of charged species.

The objective of the current chapter is to introduce the computational models used throughout this thesis. General modelling methodology is described in the next section and the reasons behind the selection of the chosen models are explained. The governing equations are described later, and the final section underlines the numerical implementation structure as well as enhancements and contributions incorporated as part of this thesis.

3.1. Modelling Methodology

One of the main challenges in modelling plasma-liquid interaction is the different geometrical scales involved in the problem. While spatial variation of plasma density and electron temperature occur within the plasma sheath in distances of a few micrometres, liquid flow variations occur within cm scales in practical applications. Resolving micrometre scales throughout the model is computationally costly and renders the model infeasible in practical problems where the reactor dimensions exceed several centimetres. Another challenge in modelling plasma-liquid interaction systems is the difference in time scales. Plasma dynamics occur in microsecond timescale due to the rapid transitions of the electrons while meaningful changes in the liquid phase typically require simulation up to several hundred minutes.

To overcome these challenges and model plasma-liquid interactions efficiently, the system is broken down into two separate sub-models. The first one consists of the plasma model which accounts for the electron collision reactions and the subsequent processes e.g. ionization, excitation and UV emission. Species densities and fluxes to the boundaries are calculated as well as the electron and gas temperature. The results are then coupled with a computational fluid dynamic (CFD) model that accounts for the gas and liquid flow dynamics, mass transfer, electric effects and temperature variations in the system. This decoupling of the plasma and liquid phases is reasonable given the large time scale difference in the two phases.

Breaking down the problem into sub-models may result in less resolution in the fluid dynamic model. While this does not affect the general long-lived and short-lived species mass transfer trends and liquid flow patterns which are the main topic of this study, caution must be exercised in cases where the plasma-liquid interaction area is specifically being studied. Examples include electron penetration depth estimation and short-lived species mass transfer calculations in the liquid phase.

It should be noted that although the focus of this study is the changes caused by the plasma in the liquid phase, the liquid phase can also cause changes in the plasma composition (e.g. through liquid evaporation into the plasma medium). These effects were neglected because for the system of interest, gas flows are perpendicular to the liquid surface.

Due to the differences in the relevant physical theories of each sub-model, the current section is divided into two sections explaining the fundamentals of each model separately.

3.2. Plasma Model Selection

The aim of our computational study is to provide new insights into the plasma-liquid interaction. As discussed above, a compromise between accuracy and computational feasibility needs to be struck to model such systems. Since we are particularly interested in the chemistry of the plasma and the transport of chemical species into the liquid phase and their subsequent fate, a global model was selected to model the plasma.

As discussed in section 1.3.1, global models are capable of simulating complex chemistry at the expense of neglecting spatial variations within the plasma. This is not critical as in our applications we are mostly interested in the afterglow chemistry.

The synthetic dry air model (80% N_2 and 20% O_2) used in this work includes 37 species including electrons, ions, metastables and excited species. This is based on the model used in [170].

3.3. Governing Equations of the Plasma Gas Phase

Before proceeding with the model development, there are a few concepts and definitions that need to be explained. These concepts are later utilized in deriving the governing equations and describing the case studies.

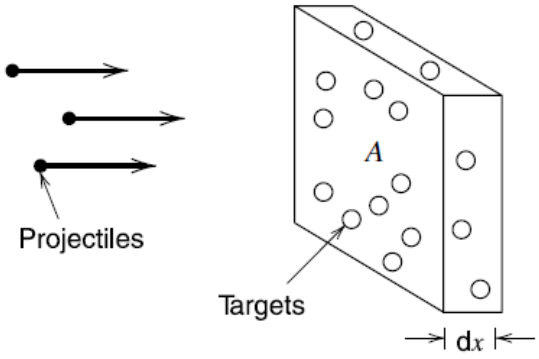

Figure 3.1. Collisional cross-section illustrated [7]

The collisional cross section is defined as an effective area that quantifies the likelihood of a scattering event occuring when an incident beam strikes a target object [7]. This is shown in figure 3.1. The particle removal from the beam is shown by equation 3.1.

$$dn = -\sigma n n_g dx \quad (3.1)$$

where n is the projectile particle density, n_g the target particle density and σ the collisional cross section of the interaction. To define a cross section, particle interaction must be specified. Multiplying 3.1 by v:

$$d\Gamma = -\sigma\Gamma n_g dx \qquad (3.2)$$

where Γ is the particle flux.

Assuming the particles are hard elastic spheres of radii a_1 and a_2, let the 'interaction' be the collision between the spheres. By drawing a circle of radius $a_{12} = a_1 + a_2$ in the $x = const$ plane, a collision occurs if the centres of the particles fall within this radius. The fraction of the unit area in which a collision occurs is $n_g dx\, \pi a_{12}^2$. The fraction of particles colliding within dx is:

$$\frac{d\Gamma}{\Gamma} = \frac{dn}{n} = -n_g \sigma dx \quad (3.3)$$

Where $\sigma = \pi a_{12}^2$ is the hard sphere cross section. In this case σ is independent of v. The collide flux is calculated by integrating equation 3.2:

$$\Gamma(x) = \Gamma_0(1 - e^{-\frac{x}{\lambda}}) \quad (3.4)$$

where the term $\Gamma_0 e^{-\frac{x}{\lambda}}$ is the uncollided flux. $\lambda = \frac{1}{n_g \sigma}$ is the mean free path or the decay of the beam which is the distance over which the uncollided flux decreases to 1/e of the initial value of Γ_0 at $x = 0$. The mean time between interactions is:

$$\tau = \frac{\lambda}{v} \qquad (3.5)$$

The interaction or collision frequency is the inverse of τ:

$$\omega \equiv \tau^{-1} = \sigma n_g v \qquad (3.6)$$

The rate constant can be defined as the collision frequency per unit density:

$$K = \sigma v \qquad (3.7)$$

As an example, the experimental and calculated cross sections for the elastic collision of electrons through helium gas as a function of the electron kinetic energy is shown in figure 3.2.

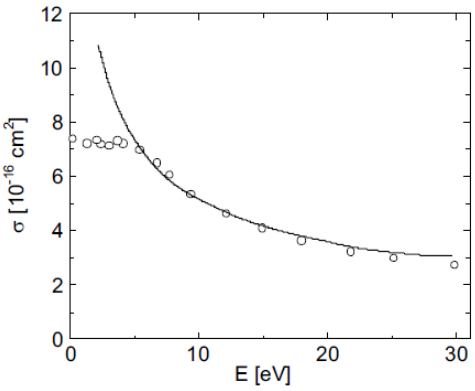

Figure 3.2. An example of the calculated (solid line) and experimental (dots) collisional cross section plot [7].

Another important concept is the concept of energy distribution function (EDF). The energy distribution function shows the probability of a particle having a specific speed (hence energy). The probability function spreads out more widely as the average energy of the system rises or as the particle mass is decreased.

In the case of a normal energy probability function, the function is called a Maxwellian distribution. When a system is not in equilibrium, non-normal energy distributions can be encountered (e.g. bi-Maxwellian distribution in which more energetic electrons are characterised by a higher temperature or Druyvesteyn distribution in which most energetic electrons fall rapidly with energy [7]) which are generally referred to as non-Maxwellian energy distribution functions.

The next definition that needs to be introduced is that of temperature. Temperature is the parameter that defines the Maxwell-Boltzmann distribution and is a measure of the kinetic energy in the system, i.e. how fast/slow particles are moving. Non-Maxwellian EDFs require more than one parameter and therefore temperature is ill-defined. In these cases, temperature refers to an ‘effective temperature’ that is defined as

2/3 of the average energy in the system. As an example, assuming the electron energy distribution (EEDF) is g_e, the effective energy can be calculated by [7]:

$$T_{eff} = \frac{2}{3}\langle\varepsilon\rangle = \frac{2}{3n_e}\int_0^\infty \varepsilon\, g_e(\varepsilon)\, d\varepsilon \qquad (3.8)$$

Given the EDF of the colliding particles and the cross section of a collisional process, and assuming that the target molecules are stationary, the reaction rate constant (K) can be calculated by averaging $\varepsilon\sigma$ over energy:

$$K = \sigma v = \gamma \int_0^\infty \varepsilon\sigma(\varepsilon) f(\varepsilon) d\varepsilon \qquad (3.9)$$

Where v is the velocity of the colliding particle, ε is the energy, γ a proportional constant and f the distribution function.

Although the integration starts from zero energy, some reactions will only occur once a threshold energy is reached (e.g. ionization), in which case the lower limit of the integration can be set to the threshold energy.

3.3.1. Mass Balance Equation

The particle balance for each species is described as:

$$\frac{dn_k}{dt} = {G_k}^v + \frac{S_1}{V}\sum_{i=1}^{N}\alpha_i\,\Gamma_{1i} - \frac{S_2}{V}\Gamma_{2k} - n_k\frac{F_v}{V} \qquad (3.10)$$

In this equation n_k represents the density of species k, ${G_k}^v$ the net volumetric generation/loss rate of species k, Γ_{1i} the flux of species i to the electrodes, S_1 the total electrode surface area, α_i the probability of species i generating species k in a surface reaction on the electrode, $\Gamma_{2\mathrm{i}}$ the flux of species i to the walls not in electric contact with the plasma (side-walls), S_2 the side-walls area, V the plasma volume and F_v the gas volumetric flowrate. The first RHS term accounts for volume processes which are listed in appendices B and C. The listed volumetric rates are typically a function of reactant species densities multiplied by the reaction rate coefficient. These coefficients are either available as a function of collisional cross sections,

as calculated in equation 3.7, or as a function of electron / heavy species temperature. The second term represents surface processes at the electrodes, the third term mass transfer across the side boundaries and the last term the loss of species due to the gas flow. Since the rates of the electron collision reactions depend on the electron temperature, equation 3.10 needs to be coupled with the electron energy balance equation.

3.3.2. Electron Energy Balance Equation

The energy conservation equation for the electrons is obtained by multiplying the Boltzmann equation by $\frac{1}{2}mv^2$ and integrating over velocity space. Neglecting spatial variations, the resulting equation is [7]:

$$\frac{d}{dt}\left(\frac{3}{2}n_eT_e\right) = \frac{(1-f)P_{in}}{\mathrm{V}} - \sum_{i=1}^{N_{er}}\varepsilon_i R_i - \frac{S_1}{V}\left(\varepsilon_{ew}\Gamma_{1e} + \sum_{j=1}^{N_i}\varepsilon_{iw}\Gamma_{1i}\right) \quad (3.11)$$

In this equation n_e is the electron density, T_e electron temperature, $(1-f)$ is the fraction of the input energy coupled to electrons, P_{in} the total input power as a function of time, N_{er} number of electron-impact reactions, ε_i the electron energy loss of each volumetric reaction and ε_{ew} and ε_{iw} the energy lost per electron and ion reaching the electrodes. The first RHS term accounts for the input power delivered to the electrons, the second term shows the electron energy consumed in reactions and the last term shows the energy lost at the electrodes.

3.3.3. Neutral Gas Energy Balance Equation

Equations 3.10 and 3.11 are sufficient to obtain the time evolution of densities in the plasma provided the gas temperature can be assumed to remain constant; However, once the bulk gas temperature variation becomes significant (e.g. 100 – 200º C in an atmospheric air plasma), temperature can play an important role in determining the plasma composition because it affects the heavy species reaction rates. To account for gas temperature variations, the neutral gas energy balance equation is solved [134]:

$$\frac{d}{dt}\left(\frac{3}{2}n_gC_pT_g\right) = fP_{in} - \sum_{i=1}^{N_r}\Delta H_iR_i + \sum_{i=1}^{N_{el}}\frac{3}{2}n_e\nu_{mi}\left(\frac{2m_e}{M_i}\right)k_b(T_e - T_i) - \mathrm{U}_r(T_g - T_w)$$

$$-F_v N_g C_p (T_g - T_a) \qquad (3.12)$$

where n_g is the total gas density, C_p the gas specific heat capacity, T_g the gas temperature, N_r the number of reactions, ΔH_i each reaction enthalpy change, ν_{mi} the momentum transfer electron collision frequency with species i, N_{el} the number of the elastic collision reactions, m_e the electron mass, M_i the heavy particles mass, k_b the Boltzmann constant, U_r the reactor overall heat capacity, T_a the ambient temperature and T_w the reactor wall temperature. The first RHS term corresponds to the input plasma power that is initially not coupled to the electrons and that leads to the eventual heating of the gas medium (e.g. through ion-neutral collisions), the second term reflects the temperature changes due to reactions, the third term represents gas heating due to elastic collisions between electrons and background species, the fourth term shows heat loss through the reactor walls and the last term shows the heat loss due to the gas flow.

3.3.4. Electrode Losses

Fluxes to the electrodes shown in equations 3.10 and 3.11 are calculated for different species according to the effect of the electric field on the particles. Neutrals, which are assumed to demonstrate a Maxwellian EDF, are not affected by the electric field so their flux to the electrode is assumed to be given by the thermal flux [94]:

$$\Gamma_i = 0.25\, n_i v_{th} = 0.25 n_i \sqrt{\frac{2RT_g}{M_i}} \qquad (3.13) \qquad (1)$$

where v_{th} is the particle thermal velocity and R is the global gas constant.

Unlike neutrals, positive ions are affected by electric fields and therefore will be accelerated against the electrodes by the voltage sustained across the plasma sheaths. The velocity that positive particles reach at the beginning of a collisionless sheath is known as the Bohm velocity [171]. This value can either be calculated in a gas mixture by calculating the velocity for each ion separately (u_{bj}), ignoring ion-ion effects (Coulomb collisions) as shown in equation 3.14, or by calculating an average velocity ($\overline{u_b}$) for all ions

which accounts for large ion-ion interaction (Coulomb collisions) as shown in equation 3.15. The latter is argued to be more precise for a high-pressure gas mixture [172].

$$\Gamma_{j+} = \alpha_j \, n_j u_{bj} = \alpha_j n_j \sqrt{\frac{k_b T_e}{M_j}} \qquad (3.14)$$

$$\Gamma_{j+} = \alpha_j n_j \overline{u_b} = \alpha_j n_j \sqrt{\frac{k_b \sum \frac{n_{i+}}{M_{i+}}}{\frac{n_e}{T_e} + \sum \frac{n_{i-}}{T_g}}} \qquad (3.15)$$

where α_j is the Bohm velocity reduction factor that accounts for collision in the sheath. This is calculated by [7]:

$$\alpha_j = \frac{1}{\sqrt{1 + \frac{\pi L_{ds}}{2L_i}}}$$

where $L_i = \frac{1}{\sigma n_g}$ and $L_{ds} = \frac{(L_{de}{}^2 \, d)^{\frac{1}{3}}}{\sqrt{2.2\pi}}$. d is the gap length and $L_{de}$is the Debye length.

Since electrons are several orders of magnitude lighter than negative ions, they mostly compensate for the positive ion flux to the electrodes while negative charged ions remain confined in the plasma by the ambipolar electric field. As a result, the flux of negative charged ions is typically assumed to be zero. However, negative ions can escape the bulk plasma when there is no energy applied to the system and hence they need to be considered during the off-time of pulsed plasmas.

Assuming that the negative ions have a Maxwellian energy distribution, the flux of negative ions to the electrode depends primarily on the ion temperature and the plasma potential. Once the positive ion flux is known, it can be shown that the flux of negative ions can be estimated as:

$$\Gamma_{j-} = 0.25 n_j v_{thj} \left(\frac{\sum \Gamma_+}{n_e v_{th\,e} + \sum n_- v_{th\,i}} \right) \qquad (3.16)$$

3.3.5. Side-wall Losses

Throughout this thesis, side-walls are defined as the boundaries with no electrical connection through which particles can diffuse away. Due to their electrostatic interaction, electrons and ions will diffuse together. For each species, the flux is given by equation 3.17 [7]:

$$\Gamma_i = \pm\mu_i n_i \boldsymbol{E} - D_i \nabla n_i \qquad (3.17)$$

where $\boldsymbol{E}$ is the ambipolar electric field, μ_i the mobility and D_i the diffusion coefficient of species i. The first RHS term shows the flux due to the electric field and the second term denotes the flux due to diffusion. By imposing quasi-neutrality in the plasma, the net charge leaving the plasma must be zero:

$$\Gamma_+ = \Gamma_e + \Gamma_- \qquad (3.18)$$

where Γ_+ is the total flux of positively charged ions, Γ_- the total flux of negatively charged ions and Γ_e the electron flux.

Substituting 3.17 into 3.18 and solving for the ambipolar diffusion coefficient of each species one obtains (appendix A):

$$D_{ai} = D_i\left(1 \pm \frac{\sum D_{j-} n_{j-} + D_e n_e - \sum D_{j+} n_{j+}}{\sum D_{j-} n_{j-} + D_e n_e \frac{T_g}{T_e} + \sum D_{j+} n_{j+}}\right) \qquad (3.19)$$

where the ambipolar flux of positive ions towards the side-walls is:

$$\Gamma_+ = -D_{ai} \nabla n_+ \qquad (3.20)$$

3.4. CFD Model Selection

A computational fluid dynamic (CFD) model is used to simulate the non-plasma gas phase and the liquid phase. Since this is a multiphase problem, a two-phase flow modelling strategy is chosen.

To track the interface between a plasma gas phase and a liquid surface, three multiphase tracking methods are commonly used: Level set, phase field and moving mesh.

Level set and phase field methods both use an auxiliary function (or colour function) on a fixed mesh to 'diffuse' the interface. Momentum balance and continuity equations are solved in conjunction with the auxiliary function(s). The auxiliary function(s) value varies between e.g. 0 and 1, representing the liquid and the gas phase respectively. The interface is centred on the centre value of these function(s) e.g. 0.5, and the material properties of both phases such as density and kinematic viscosity are scaled smoothly across the interface according to the auxiliary function value [173].

These two methods are different from a methodological point of view. Level set method is a numerical approach where the interface is approximated using artificial smoothing functions. The interface evolution is given by a numerical convection equation with an artificial compression and diffusion term to maintain the interface thickness[173]:

$$\frac{\partial \varphi_{LS}}{\partial t} + v \cdot \nabla \varphi_{LS} = \omega \nabla . (\varepsilon_{LS} \nabla \varphi_{LS} - \varphi_{LS}(1 - \varphi_{LS}) n) \qquad (3.21)$$

where φ_{LS} is the level set function, ω the re-initialization parameter with the dimension of velocity, ε_{LS} the interfacial thickness and n the interface normal vector ($n = \nabla \varphi_{LS} / |\nabla \varphi_{LS}|$).

On the other hand, the phase field method is based on a physical approach where the mixing energy is minimized. The mixing energy is defined as the sum of the surface energy and bulk energy of the flow.

Cahn-Hillard convection equation is used to evolve phase field interface [174]:

$$\frac{\partial \varphi_{PF}}{\partial t} + \boldsymbol{u} \cdot \nabla \varphi_{PF} = \nabla . (\mathrm{M} \nabla \mathrm{G}) \qquad (3.22)$$

where M is the diffusion coefficient (mobility), G the chemical potential of the system. Mobility is expressed as:

$$\mathrm{M} = M_c \varepsilon_{PF}^2 \qquad (3.23)$$

where M_c is the characteristic mobility ε_{PF} is the interface thickness. The chemical potential is defined as:

$$G = \lambda[\frac{1}{\varepsilon_{PF}^2}\varphi_{PF}\left(\varphi_{PF} - \frac{1}{2}\right)(\varphi_{PF} - 1) - \nabla^2\varphi_{PF}] \qquad (3.24)$$

where λ is the mixing energy density.

In both cases of level set or phase field methods, the interface equations are coupled with the following Naiver Stokes and continuity equations:

$$\rho(\varphi)\frac{\partial \boldsymbol{u}}{\partial t} + \rho(\varphi)\boldsymbol{u}\cdot\nabla\boldsymbol{u} = -\nabla p\boldsymbol{I} + \nabla\cdot\left[\mu(\varphi)\left(\nabla\boldsymbol{u} + \nabla\boldsymbol{u}^{\boldsymbol{T}}\right)\right] + \rho(\varphi)\boldsymbol{g} + \boldsymbol{F}_c \qquad (3.25)$$

$$\nabla.\boldsymbol{u} = 0 \qquad (3.26)$$

where p is pressure, $\boldsymbol{I}$ the unit matrix depending on the number of dimensions accounted for, ρ density, μ viscosity, $\boldsymbol{g}$ gravitational acceleration, F_c surface tension force and φ is either φ_{LS} or φ_{PF}. Density and viscosity can be defined as:

$$\rho(\varphi) = \rho_1 + (\rho_2 - \rho_1)\varphi \qquad (3.27)$$

$$\mu(\varphi) = \mu_1 + (\mu_2 - \mu_1)\varphi \qquad (3.28)$$

where subscripts 1 and 2 refer to different phases.

To apply finite element method in solving the system of equations, equation 3.21 can be solved directly while equation 3.22 needs to be solved using two auxiliary equations [175]. This adds to the computational cost and leads to two interface transport equations for the phase field method while only one interface transport equation is required for the level set method. Therefore, the phase field method tracks the interface more accurately while the level set method is less costly computationally [176]–[178].

In contrast to these two methods, the moving mesh method tracks the interface position with a moving mesh using an arbitrary Lagrangian-Eulerian (ALE) approach [179]. The physical interface is much thinner than the practical mesh resolution, leading to the most accurate representation of the physical interface [180].

The main advantage of the moving mesh method over phase field and level set methods is that mass transport across the interface can be defined accurately. Mass transport from the plasma to the liquid is one of the main topics of this study and is difficult to implement accurately with the phase field and level set methods. For this reason, the moving mesh method was used in this work. The sharp interface also allows for different physics to be solved on either side of the interface. A comparison between the 3 methods is presented in table 3.1.

Table 3.1. Comparison of two-phase interface tracking methods. Visualisation of level-set and phase field methods look identical because both methods similarly 'diffuse' the interface to track the gas-liquid boundary.

	Level Set	Phase Field	Moving Mesh
Equations Solved	- Momentum balance - Continuity - One interface transport equation	- Momentum balance - Continuity -Two interface transport equations	- Momentum balance - Continuity - ALE moving mesh
Degrees of Freedom	132580	282060	656812
Supported Regimes	Laminar, Turbulent	Laminar, Turbulent	Laminar
Computational time for a sample problem*	1 hr and 6 min	1 hr and 19 min	3 hr and 2 min
Sample Visualization	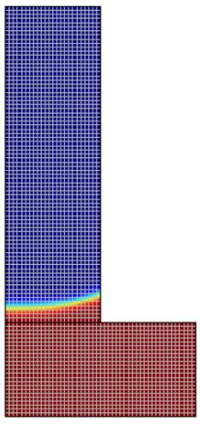	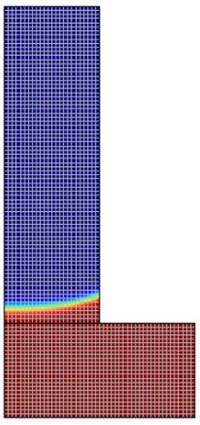	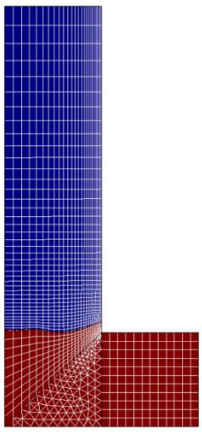

* Computations were performed using a PC with 16 GB of RAM and quad Core i-7 @ 2.8 GHz CPU.

3.5. Governing Equations of the non-Plasma Gas and the Liquid Phases

To track the physical and chemical changes in the gas and the liquid phases, electric current, mass, momentum and energy conservation equations are solved. Their formulation is discussed next.

3.5.1. Electric Current Conservation

To calculate the electric field and electric potentials in the system, the electrostatic approximation and electric current conservation are imposed:

$$\boldsymbol{J} = \sigma_T \boldsymbol{E} + \epsilon_r \epsilon_0 \frac{\partial \boldsymbol{E}}{\partial t} \qquad (3.29)$$

$$\boldsymbol{E} = -\nabla V - \frac{\partial \boldsymbol{A}}{\partial t} \qquad (3.30)$$

$$\boldsymbol{B} = \nabla \times \boldsymbol{A} \qquad (3.31)$$

where $\boldsymbol{J}$ is the total electric current density, σ_T the solution conductivity, $\boldsymbol{E}$ the local electric field, V the electric potential, $\boldsymbol{B}$ the magnetic field, $\boldsymbol{A}$ the magnetic field potential, ϵ_0 the electric permittivity of free space and ϵ_r the relative permittivity of the medium. In equation 3.29, the first right-hand term accounts for the conduction current and the second term for the displacement current. The displacement current and the subsequent electromagnetic forces are included in the simulations and the results are presented in 6.3.2.

When applied to the liquid phase, one needs to account not only for the conductivity due to the presence of dissolved salts (σ_{salt}) but also the conductivity arising from the arrival of electrons and ions from the plasma. Therefore, the conductivity of the solution (σ_{tot}) is given by:

$$\sigma_{tot} = \sigma_{salt} + F \sum c_i \mu_i \qquad (3.32)$$

where F is the Faraday constant, c_i the molar concentration of species i and μ_i the mobility of the charged species.

3.5.2. Energy Conservation

To account for the variation in temperature which determines the reaction rate coefficients and acts as the driving force of convection, the total energy balance of the system needs to be solved:

$$\dot{Q} = \rho C_p \frac{\partial T}{\partial t} + \rho C_p u \nabla \mathrm{T} + k \nabla \mathrm{T} \qquad (3.33)$$

where Q is the heat energy per unit volume, ρ the liquid or the gas phase density, C_p the heat capacity, u the velocity magnitude, T the temperature and k the thermal conductivity coefficient. The first right-hand term accounts for the energy accumulated in the volume due to the heat capacity of the medium, the second term for the heat transferred due to convection and the third term for the heat transferred due to conduction.

All simulations were conducted at atmospheric pressure and with the system open to ambient air.

3.5.3. Momentum Conservation

To determine the motion of the fluids, the momentum conservation equation is solved for gas, plasma and liquid separately with the relative boundary conditions:

$$\rho \frac{\partial}{\partial t}(\boldsymbol{u}) + \rho(\boldsymbol{u}.\nabla)\boldsymbol{u} = -\nabla.(p\boldsymbol{I} + \eta(\nabla \mathbf{u} + (\nabla \mathbf{u_i})^T) + \boldsymbol{F_i} - \rho \boldsymbol{g} + \boldsymbol{F_c} \qquad (3.34)$$

where p is the pressure, $\boldsymbol{I}$ the unit matrix, $\boldsymbol{g}$ the gravitational acceleration, η the dynamic viscosity, $\boldsymbol{F_i}$ the ionic volume force per unit volume and $\boldsymbol{F_c}$ the surface tension force per unit volume. In addition, the mass balance of the bulk fluid requires:

$$\frac{\partial \rho}{\partial t} + \nabla.(\rho \boldsymbol{u}) = 0 \qquad (3.35)$$

The ionic volume force $\boldsymbol{F_i}$ is the force exerted to the liquid by ions driven by the electric field. This is calculated as:

$$\boldsymbol{F_i} = e\boldsymbol{E}\sum(z_i c_i) \qquad (3.36)$$

where e is the unitary charge and z_i the charge number of the ion i.

The gravity term is to account for the natural convection caused by the temperature gradient in both the liquid and the gas phase. The changes in density due to temperature variation needs to be taken into account:

$$\rho = \rho_0(1 - \alpha_p(T - T_0)) \quad (3.37)$$

where ρ_0 is the reference density of the corresponding material at the reference temperature T_0 and α_p is the thermal expansion coefficient. Multiplying the above term by the gravitational acceleration results in the force per unit volume exerted on the bulk liquid that drives natural convection.

The surface tension $\boldsymbol{F_c}$ is the force in a direction tangential to the surface that is caused by the attraction of the particles in the surface layer and the bulk liquid. This can be written as:

$$\boldsymbol{F_c} = \boldsymbol{\nabla}.\boldsymbol{\tau} \quad (3.38)$$

$$\boldsymbol{\tau} = \zeta(\boldsymbol{I} - (\boldsymbol{nn^T}))\boldsymbol{\delta} \quad (3.39)$$

where $\boldsymbol{\tau}$ is the total stress tensor, ζ the surface tension coefficient, $\boldsymbol{I}$ the identity matrix, $\boldsymbol{n}$ the interface normal and $\boldsymbol{\delta}$ a Dirac delta function that is nonzero only at the fluid interface. Equation 3.38 and the divergence theorem show that if the surface tension is constant on the liquid surface then $\boldsymbol{F_c} = 0$, but if $\zeta = \zeta(l)$ then a net force results on the liquid surface where the direction of $\boldsymbol{F_c}$ is always from the lower ζ to the higher ζ. As it will be shown in chapter 6, the surface tension can play a very important role in plasma-liquid systems.

The fluid boundaries on the solid walls were assumed to be non-slip ($\boldsymbol{u_w} = 0$) while the fluid-fluid interface is assumed to have the following boundary condition due to momentum continuity:

$$\boldsymbol{n} \cdot (\boldsymbol{\tau_2} - \boldsymbol{\tau_1}) = -\nabla\zeta \quad (3.40)$$

where subscript 1 and 2 refer to each fluid phase and $\boldsymbol{\tau_i}$ is defined as:

$$\boldsymbol{\tau_i} = -p_i \boldsymbol{I} + \eta_i(\nabla \mathbf{u_i} + (\nabla \mathbf{u_i})^T) \qquad (3.41)$$

In the bubbling reactor used in chapter 5, the liquid is agitated by rising bubbles. To calculate the velocity induced by the bubbles in the reactor, the bulk liquid and the gas phase are treated as interpenetrating media where the bubble diameter is assumed to be constant.

In this case, by combining the momentum and the continuity equations for two phases, the liquid phase momentum balance is described by[181]:

$$\emptyset_l \rho_l \frac{\partial \boldsymbol{u}}{\partial t} + \emptyset_l \rho_l \boldsymbol{u}.\nabla \boldsymbol{u} = -\nabla p \boldsymbol{I} + \nabla.[\emptyset_l \mu_l (\nabla \boldsymbol{u} + (\nabla \boldsymbol{u})^T)] + \emptyset_l \rho_l \boldsymbol{g} \qquad (3.42)$$

where $\emptyset_l$ is the liquid phase fraction, ρ_l the liquid density, p pressure, I the unit matrix depending on the number of dimensions accounted for, μ_l the liquid dynamic viscosity and $\boldsymbol{g}$ the gravity acceleration. The assumptions of this model are:

- The gas phase density is negligible compared to the liquid phase.
- The motion of the bubbles is determined by a balance between pressure forces and viscous drag.
- The pressure field is shared between the two phases.

Ionic volume forces and surface tension are not considered in this case as they are meant to be negligible in this experimental setup.

3.5.4. Mass Conservation

Finally, the mass balance is solved to determine the spatiotemporal evolution of each species:

$$\frac{\partial c_i}{\partial t} = D_i \nabla^2 c_i + z_i c_i \mu_{\ i} \nabla^{\ 2} V + \sum R_i + \boldsymbol{u}.\nabla c_i + \left(\frac{m_{gl}}{M_w}\right)_i \qquad (3.43)$$

where c_i is the concentration, D_i the diffusion coefficient, z_i the charge number, μ_i the mobility of species i, V the electric potential, R_i the generation and loss due to the reactions involving species i, $\boldsymbol{u}$ the background liquid velocity field, M_w the molar mass and m_{gl} the mass transfer rate between the gas and the liquid calculated by the two-film theory [182]. The first right-hand term accounts for the mass transfer due to diffusion, the second term for the conduction due to the presence of an electric field, the third term for the mass loss or production in chemical reactions, the fourth term for the mass transfer due to convection and the last term for the transfer of species between bubbles and the liquid.

According to the two-film theory [183]:

$$m_{gli} = K_{li}\left(\frac{P_i}{H_i} - c_{li}\right) \times M_{wi} \times \overline{a_i^V} \qquad (3.44)$$

where K_{li} is the mass transfer coefficient, P_i the partial pressure in the gas phase, H_i Henry's constant and $\overline{a_i^V}$ the bubble surface to volume ratio. For a swarm of bubbles, the mass transfer coefficient K_{li} is estimated the following empirical correlation [184]:

$$Sh_i = K_{li}\frac{d_b}{D_i} = 0.45 \times Gr^{\frac{1}{3}} \times Sc^{\frac{1}{2}} \qquad (3.45)$$

where Sh_i is the Sherwood number, d_b the bubble diameter, Gr the Grashof number and Sc the Schmidt number.

3.6. Numerical Solution Strategy and Implementation

Combining the equations described in previous sections leads to a system of partial differential equations (PDEs). Several techniques can be used to solve this system of equations. The two most commonly used approaches are the finite volume method (FVM) and the finite element method (FEM). Although FVM requires less memory and the solution speed is generally higher, FEM is typically more stable numerically. Other solution approaches include the finite difference method, the spectral element method and the boundary element method. These methods have been extensively discussed and compared in [185]. In the

current study the air discharge is solved by MATLAB and the liquid CFD PDE system is solved by FEM using the commercial package COMSOL.

To describe this method, let u be a dependent variable in a PDE (e.g. temperature, pressure, electric potential, etc.). For a 1D geometry structure divided into several elements and nodes as shown in figure 3.3, u can be approximated by a linear combination of basis functions:

$$u_h = \sum_{i=1}^{N} u_i \psi_i \qquad (3.46)$$

where N is the total number of nodes, u_i the approximation coefficient and ψ_i the basis function.

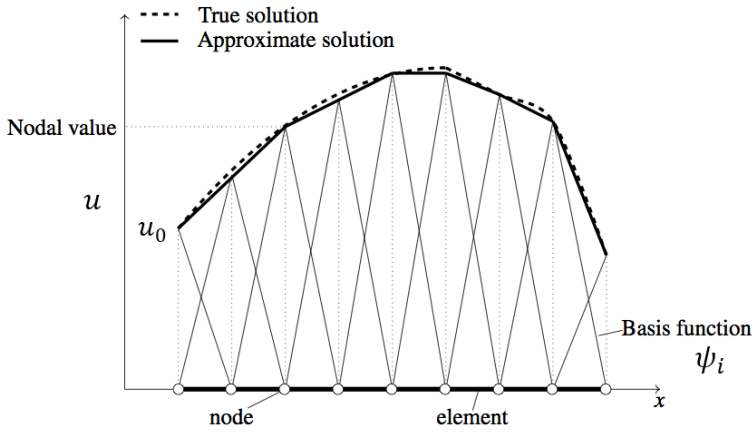

Figure 3.3. FEM basics explained.

To solve the problem given the boundary condition $u(x_0) = u_0$, first one must transform the original problem to its weak form and then discretize it. This yields a large but finite linear problem to solve [186].

The advantage of the FEM is that complex geometry can readily be handled. This also includes complex boundary constrains and initial values. Element size and geometry can be selected based on the physical knowledge of the problem at hand. Multidisciplinary problems involving several dependent variables e.g. temperature, electric field, mass transfer and fluid dynamics can readily be solved by this method.

Accuracy and resolution of the simulation results depend on the domain discretization and improper mesh selection can lead to fatal errors.

Due to the difference in timescales of the plasma and liquid phase, simply creating a system of equations with all the relevant equations and solving them simultaneously is not feasible. Instead, numerical strategies are required to reduce the computational demand by accounting for the unique physical and chemical characteristics of the system.

3.6.1. Pulsed Power Plasma Global Model

The structure of the global model used to study the effect of the input power modulation on the chemistry of an air DBD is shown in figure 3.4. A list of reactions is created according to the user input parameters (auto-rates) and a list of equations is created from the reaction rates (auto-ODE). These lists are created in the form of subroutines which not only can be solved by MATLAB internal ordinary differential equation (ODE) solvers, but also can later be referred to for debugging purposes. The problem often leads to a stiff system of equations as the reaction rates can differ several orders of magnitude due to the plasma nature. The atmospheric pressure air plasma was solved numerically by a stiff ODE solver (ode15s) using variable time steps.

The results of the simulation are then taken through an analysis sub-routine where the main reaction pathways are identified. The routine is repeated for each pulse period when the power is modulated. This helps to determine how the main reaction pathways change from pulse to pulse due to the accumulation of long-lived species and/or gas heating in the reactor.

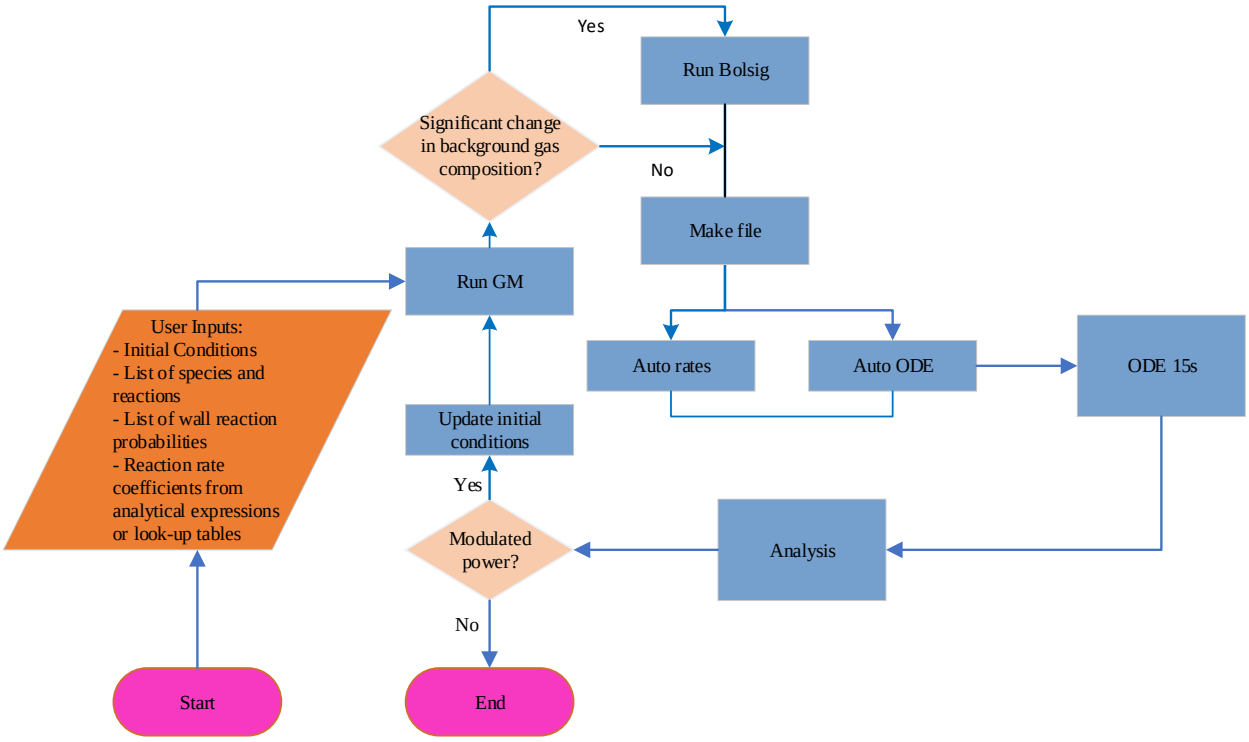

Figure 3.4. Structure diagram of the zero-dimensional global model. The process is repeated in case of modulated power input to track the main chemical pathways evolution.

Below is a list of features implemented in the global model:

Pulsed power input:

- Any mathematical function of time can be entered as the input power profile. This includes modulated waveforms.
- The model is can be run with zero input power to study the plasma evolution in afterglows and during the off-time of modulated signals.

Reaction rate calculation:

- Heavy particle reaction rate coefficients that are affected by the gas temperature and thus defined as a function of T_g.
- Reaction rate coefficients of electron-involved reactions can be expressed as a function of electron temperature T_e or the mean electron energy ε_e.

- A combination of the above where the reaction rate coefficient is affected by both the gas temperature and electron temperature.
- Constant reaction rates where the reaction rate is minimally affected by temperature within the defined operating condition.
- Where possible, reaction rates are determined from collisional cross sections according to equation 3.9. using Bolsig [59] to determine the electron EDF as shown in figure 3.5. The cross-section data were downloaded from LxCat [187] for the atmospheric pressure air and *He*-O_2 species. These calculations can be done as described in figure 3.5. The reaction rates are calculated at the beginning of each simulation run and whenever there is significant change in the composition of the background gas.

Bolsig was also integrated into the code to re-calculate reaction rates when the background gas composition or gas initial temperature change dramatically during the simulation. While this factor becomes important at lower pressures, the effect becomes less apparent at higher pressures as the background gas composition densities are more than 5 orders of magnitude larger than the density of species produced in the plasma in an atmospheric pressure air simulation.

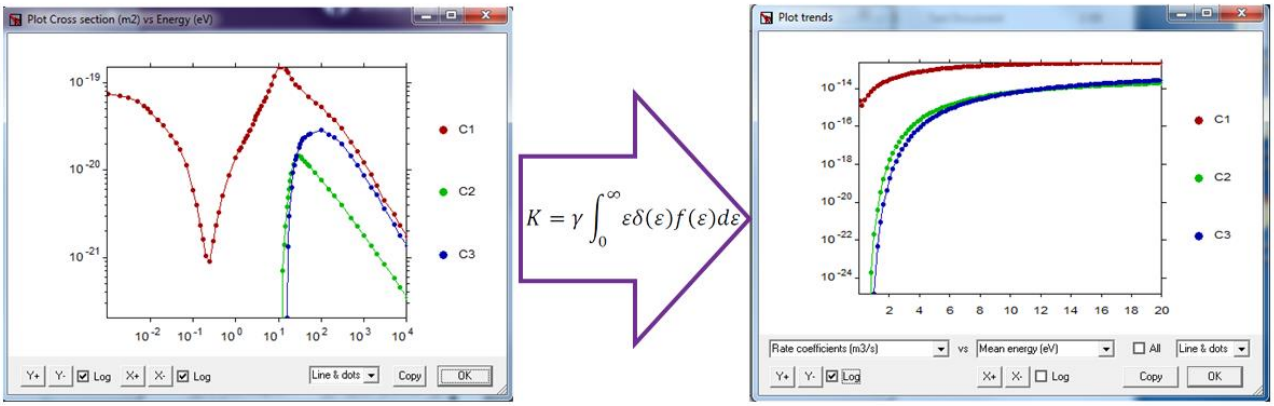

Figure 3.5. An example showing the calculation of reaction rate coefficients using Bolsig plus for some of the plasma species. Collisional cross-section data (left). Reaction rate coefficient (right)

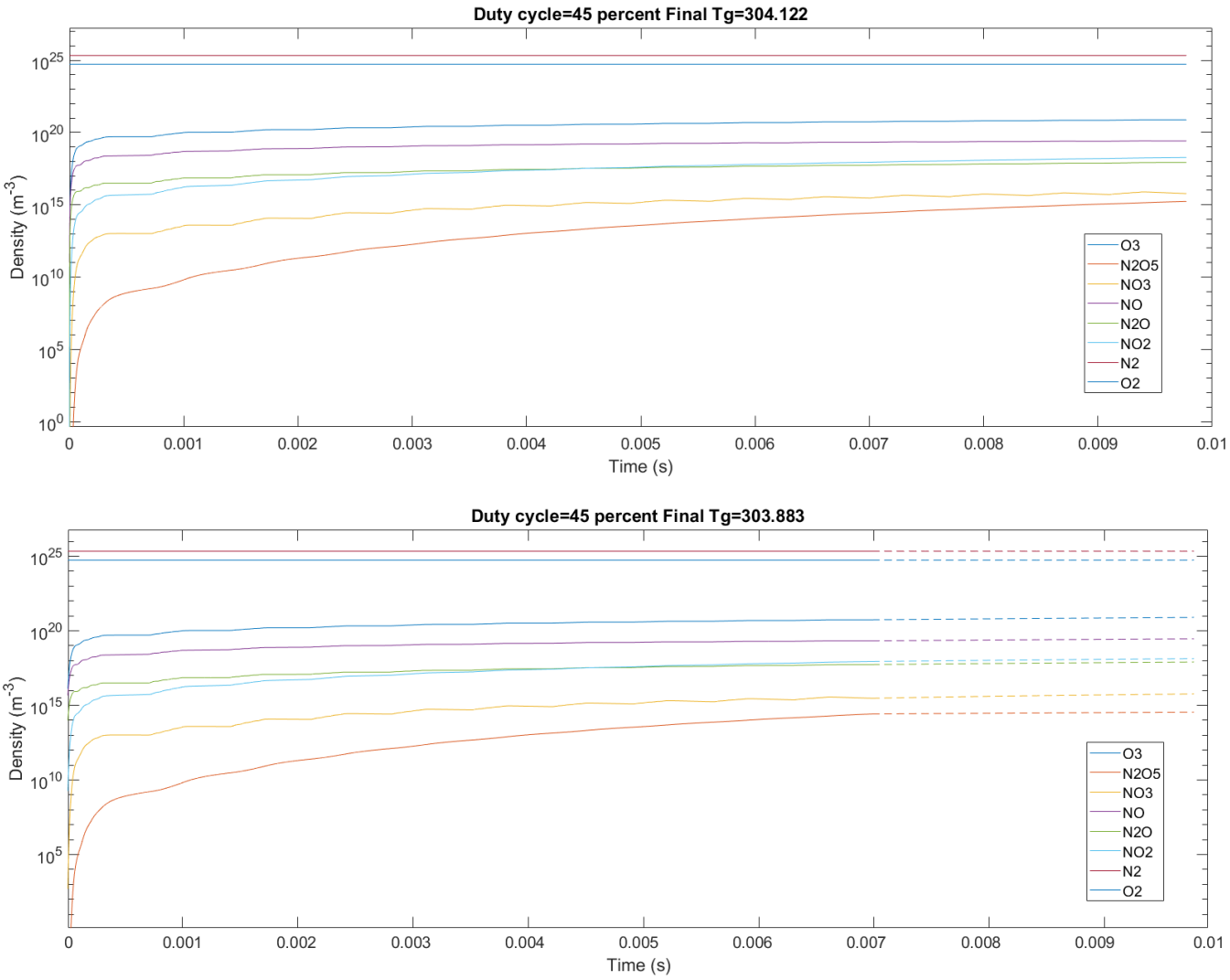

Figure 3.6. Time evolution of the key plasma long-lived species in an air plasma operated at 40 KHz with a 45% duty cycle and T_e ~ 5 eV. The gas temperature is evolving according as shown in figure 3.7. top: densities are calculated and bottom: densities are estimated.

Speed enhancement: Some general modifications are incorporated in the model to make the code run faster according to [188][189]. In general, it is time consuming to model chemistry changes in timescales of seconds or minutes while resolving input signals with millisecond timescale. When the input power is modulated, changes in the plasma occur slowly during the periods when power is not applied to the system. In this case, it is possible to increase the integration timestep by a factor of ~×1000 without compromising accuracy during these periods. This strategy can make the code run faster by 10 to 20 percent depending on the period length.

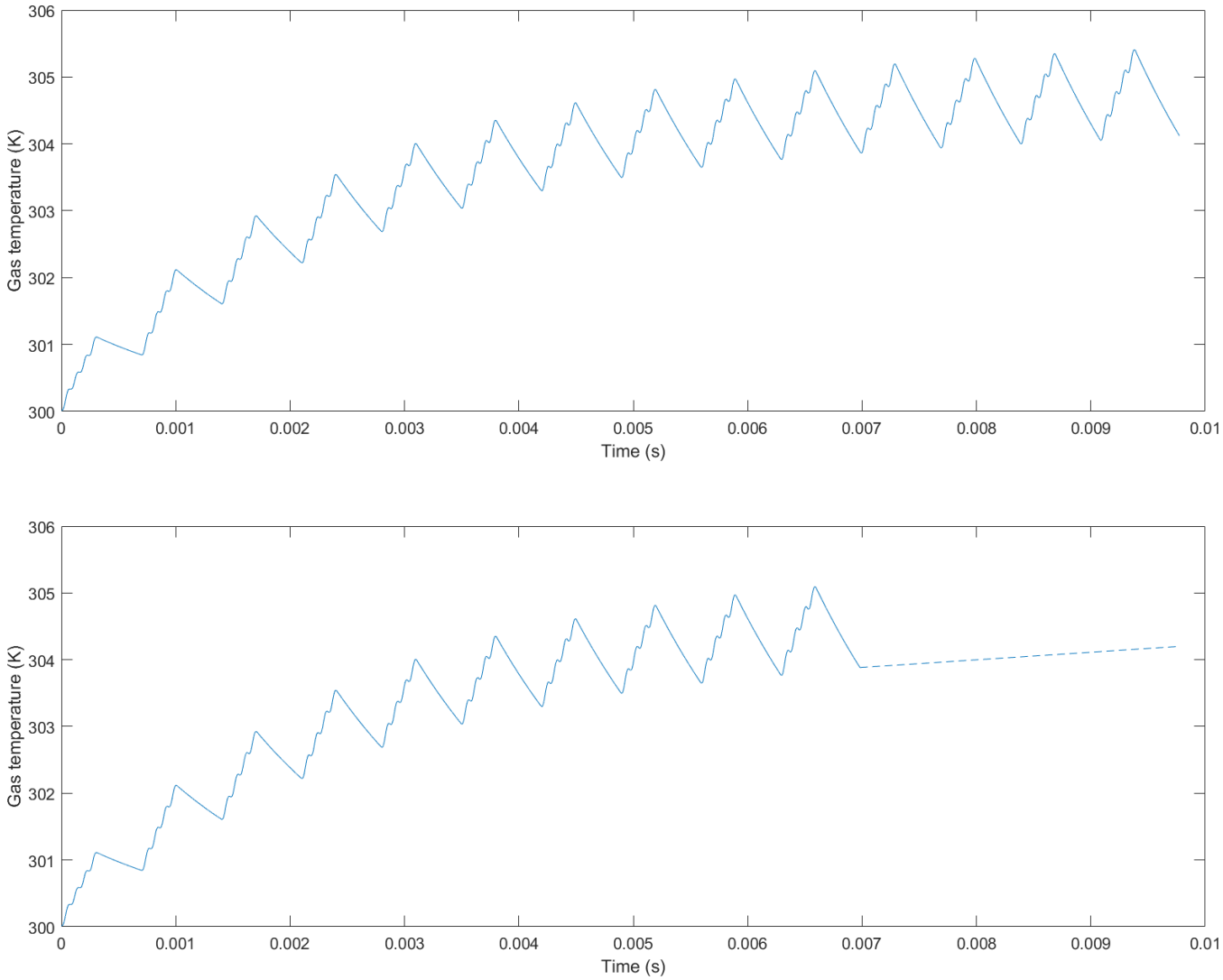

Figure 3.7. Gas temperature in an air plasma operated at 40 KHz with a 45% duty cycle. top: temperature is calculated and bottom: temperature is estimated.

In addition, multiscale simulation techniques are used to bridge between the disparate time scales. The code monitors the evolution of the densities and gas temperature while resolving the small timescale and extrapolates to predict the evolution in a larger timescale. This process is repeated multiple times until the required final simulation time is achieved. In the example shown in figure 3.6 and 3.7, the simulation time was reduced from 26 minutes and 50 seconds to 19 minutes and 5 seconds while estimated temperature and densities are less than 0.3 percent different. Since the final simulation time is achieved by adding a certain

number of 'complete cycles' throughout this study, the final temperature at the end of each cycle is chosen as a reference point to be extrapolated. The speed enhancement becomes more apparent in longer runs and for a 5-second simulation, the calculation time reduces from about 224 hours to 158 hours. The machine used for this study was a desktop PC with a quad-core Intel @ 3.4 GHz CPU and 16 GB installed memory (RAM). A similar study mentions 100 hours of calculation time for a single-pulse plasma using a computer with similar specifications [170]. Please note that although this technique reduced the time of simulation significantly with relatively little error, the final results presented in chapters 4 and 5 were derived without using extrapolation to preserve simulation accuracy.

Reaction rate visualisation: A graphical user interface (GUI) within the simulation code was designed and implemented in the global model to study the sensitivity of the simulation results to each reaction individually, hence identifying the potential key chemical pathways. A screenshot of the GUI is shown in figure 3.8. In this example, the reaction rates are derived according to appendices B throughout a single pulse. The bulk gas temperature and the electron temperature change throughout the pulse time, leading to changes in reaction rate coefficients. These changes are displayed in a graph as shown in figure 3.8. The list of reactions on the left side is automatically sorted according to their contribution to the generation/loss of a species of interest.

EEDF visualisation: The EEDF determines the reaction coefficients of electron-driven processes and this is calculated in the code by calling Bolsig [59]. The code then can visualize the time evolution of the EEDF in a 3D plot (Figure 3.9 (a) and (b)). For the non-Maxwellian case, T_{eff} = 5 eV.

At any given time, the area beneath the EEDF curve for energies larger than the excitation/ionization thresholds represents the number of electrons that have enough energy to take part in those specific reactions. As an example, the number of electrons with enough energy to take part in oxygen gas ionization with a threshold energy of 12.1 eV is always smaller in Maxwellian than in non-Maxwellian electron energy distribution function in the current study.

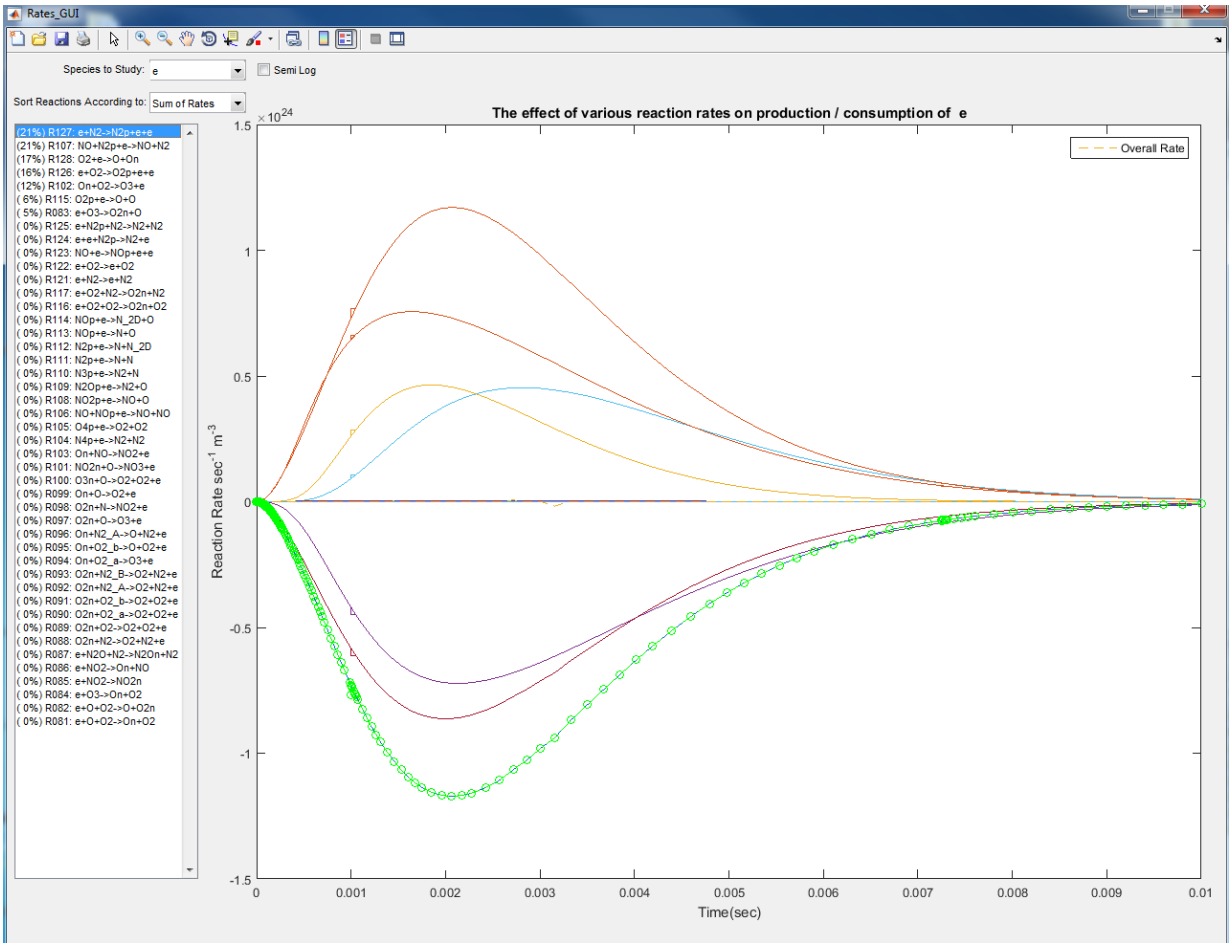

Figure 3.8. A screenshot of the GUI showing reaction rates vs time for the atmospheric air model with pulsed input power. The reactions are sorted according to the reaction rate in the left panel.

Other model features:

- **Reduced Electric Field (E/N) and mobility values:** While these values are not required to continue the integration process in the current model, they were obtained to compare the results with other models in which Boltzmann equation is solved directly for the electric field. These values are interpolated and extracted from Bolsig within the simulation. The comparison showed a good correlation between the current model and direct Boltzmann solvers results[190].

- **Model Accuracy:** To investigate simulation accuracy, the following factors were found to influence uncertainty in the results:

- Input data: This includes details about physical constants, e.g. collision cross section source and reaction rate coefficients especially at low electron temperatures.

- Numerical aspects: Interpolation and integration methods.

The effect of the above uncertainties was investigated in the atmospheric pressure plasma air model as presented in table 3.2. Final densities variance was calculated in each case and the average percentage is used to evaluate each factor's significance. Please note that the results of this study showed a good agreement (within 10%) with other similar studies as presented in [190].

Table 3.2. Factors influencing simulation result accuracy.

Factor		Investigation technique	Average final density variance percentage
Input data	Collisional cross section data source	The simulation was run for a range of available cross section data chosen from [187].	5.204 %
	Reaction rate coefficient	Reaction rate coefficients values was varied ±10% of appendix B.	3.429 %
Numerical aspects	Integration method	Spacing between integration points was changed by ±10%.	0.003 %
	Interpolation method	Interpolation method was changed from linear to nearest neighbour and cubic spline.	less than 0.001 %

- **Ion diffusion coefficients and correction factors:** Ion diffusion coefficients may not be readily available in references so these values are estimated when required according to [191]. These values are also corrected for various gas temperatures and pressures as described in [7].

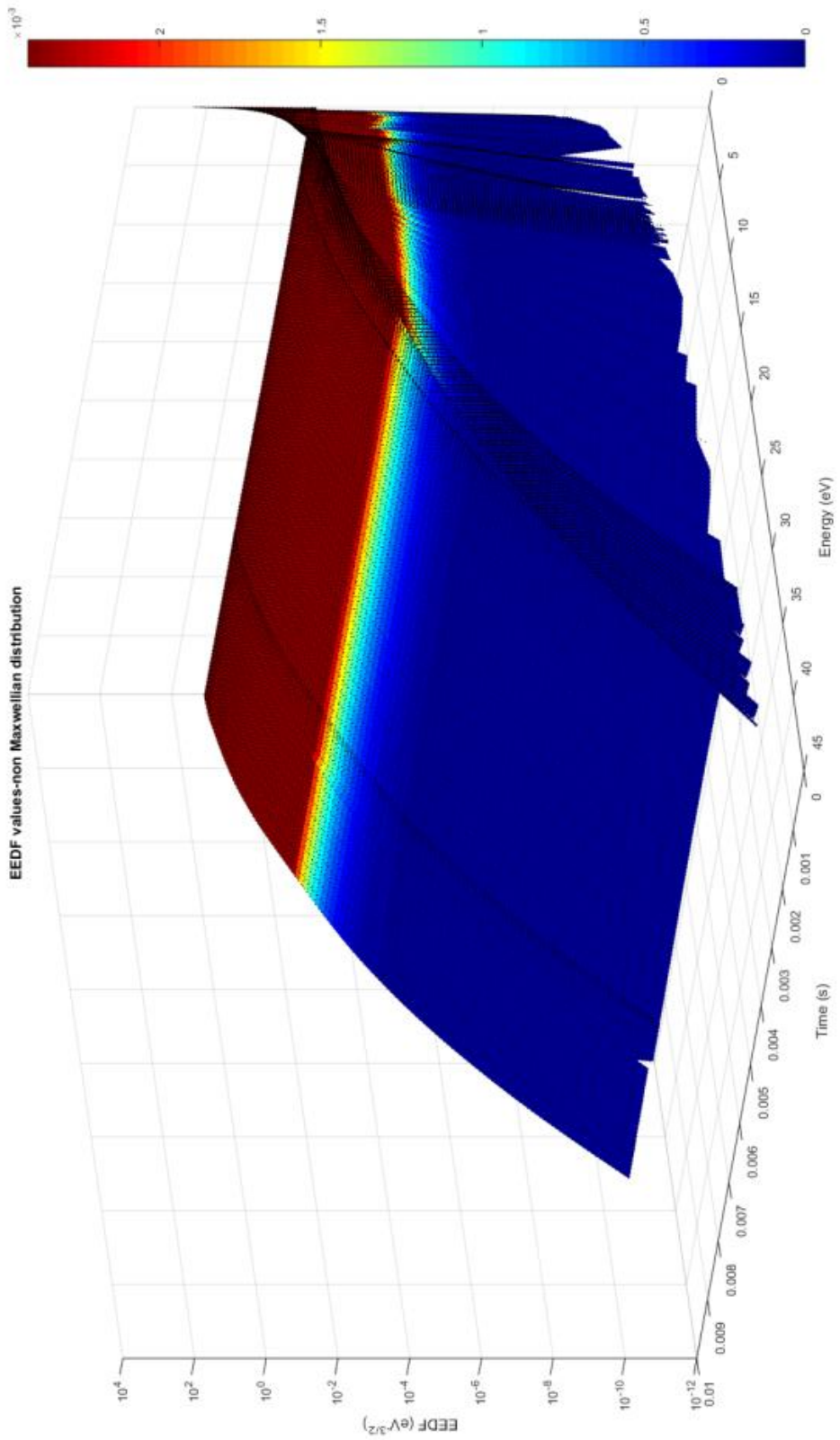

Figure 3.9.a Time evolution derived from the global model for non-Maxwellian EEDF of atmospheric air mixture. T_{eff} = 5eV.

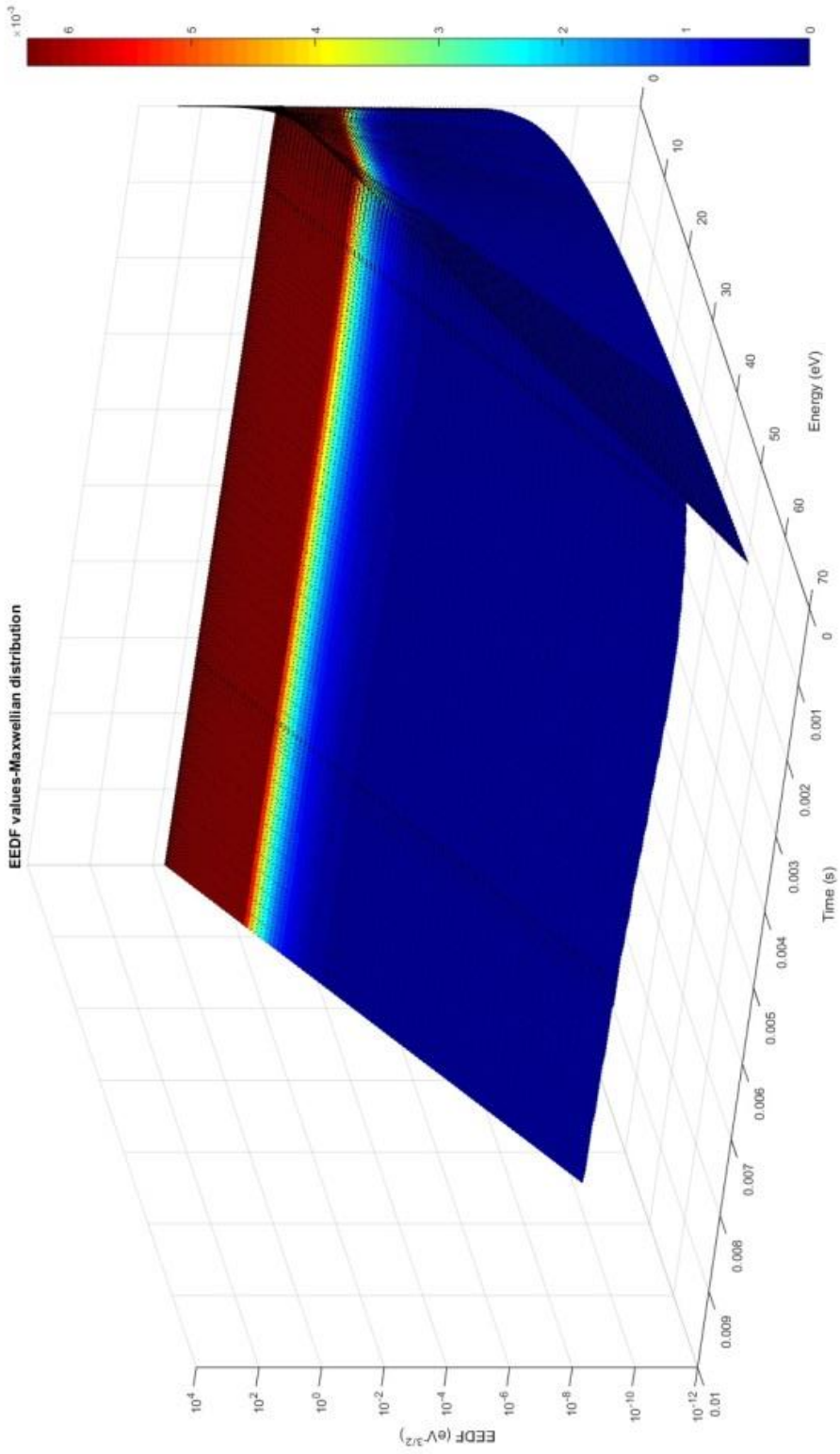

Figure 3.9.b Time evolution derived from the global model for Maxwellian EEDF of atmospheric air mixture.

3.6.2. Remote Epoxidation Reactor

To model the remote epoxidation reactor described in 2.2, the system is broken down into three sub-models as shown in figure 3.10. The first part consists of a *He-O_2* 0D plasma model where plasma gas composition is determined according to the input oxygen fraction and the input power. This sub-model accounts for 18 chemical species (O_2, O, O(1D), O_3, $O_2(a^1\Delta_g)$, O_2^+, O_2^-, O_3^-, O^-, O_4^+, O_2^+, O_4^-, He, He_2^+, He^+, He^*, He_2^+, He_2^*) with 176 bulk reactions and 10 surface reactions. The second part is a steady state 1D CFD model to simulate the transport of plasma species from the active plasma region to the liquid through the capillary tube (Fig 2.4). 6 key species (He, O_2, O_3, O, O(1D), $O_2(a^1\Delta_g)$), 20 bulk reactions and 3 surface reactions are used to predict the gas composition at the tip of the tube where the gas interacts with the liquid. The final sub-model is then used to calculate the velocity field in the liquid as well as the mass transfer and chemical reactions in the gas (bubbles) and liquid phase. The sub-model consists of a time-dependent 2D CFD model with the same species and reactions used in the previous part for the gas phase (bubbles) and 6 species with 7 reactions in the liquid phase. The gas phase and the liquid phase are formulated separately but inter-connected by the mass transferred from the bubble to the liquid as stated in equation 3.44 and the mass transferred from the liquid to the gas phase through evaporation. The liquid is assumed to be in equilibrium with the gas phase, hence the Henry's constant is used to determine the liquid vapour partial pressure.

The simulation results were compared to experimental observations as discussed in 5.2.1, to validate the simulation process, e.g. the ozone concentration of the plasma effluent was measured and compared with the 0D model results. Since for atomic oxygen (*O*), the Henry constant is not known accurately [192], the simulation results were matched to the experimental observations to eliminate it. Other reaction rates were obtained from the literature [193].

As the steps of the simulation need to be repeated several times as stated in figure 3.10, and the models are run in different software platforms with different output formats, several subroutines (e.g. a subroutine written under MATLAB to run the 0D plasma model and prepare the results in a format accessible by

COMSOL 1D plasma model) were designed to connect the models and automate the process in order to increase the simulation speed and prevent manual handling errors.

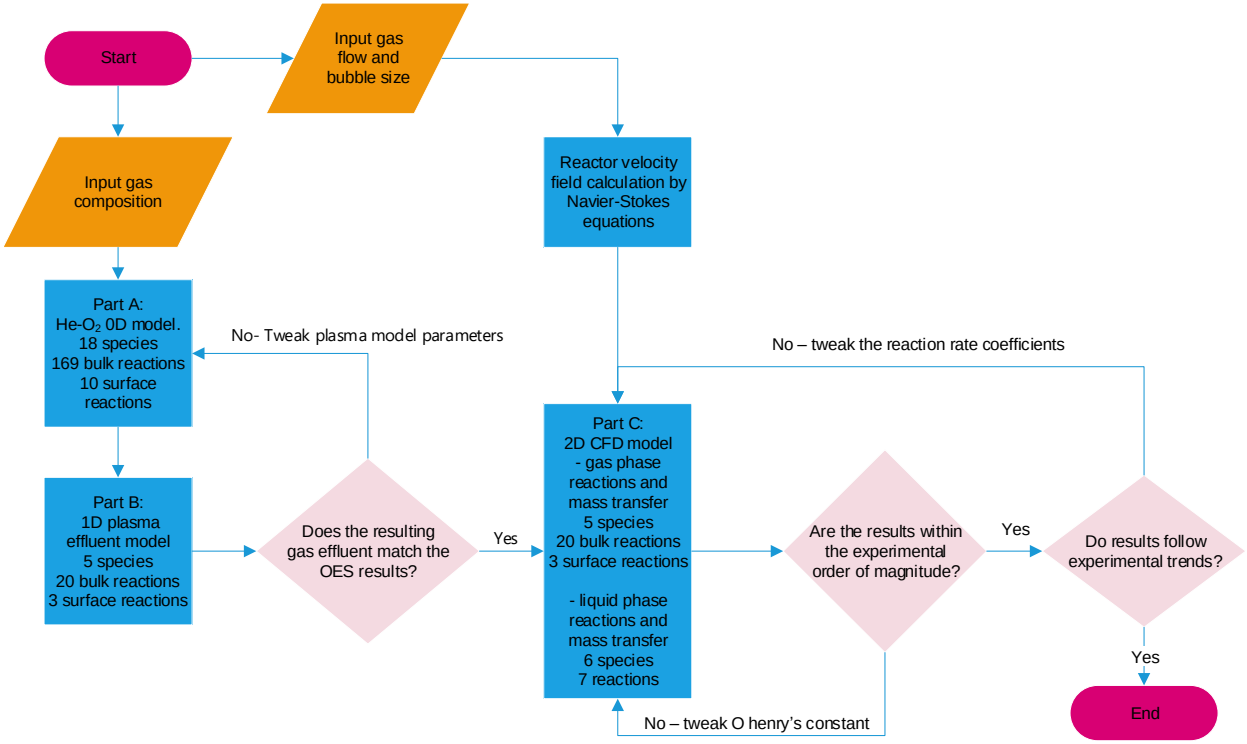

Figure 3.10. The structure of the model consists of part A: A 0D model to simulate the plasma produced between the electrodes according to the input gas composition. The results are then transferred to part B: A 1D model where the species depreciation is calculated according to plasma effluent reactions. The outcome is then set as the input gas composition of part C: A CFD model to calculate the reactor velocity field, the gas and liquid phase reactions and mass transfer. Model outcomes are verified with experimental results during the process.

3.6.3. Plasma-liquid Interaction with Electrical Connection

The main purpose of this computational model is the study of the spatial and temporal evolution of reactive species concentration in the liquid phase and the mixing efficiency under various conditions. Additionally, the model is used to determine the local surface tension coefficient under the plasma.

The structure of the CFD model is shown in figure 3.11. Simulation results depend strongly on the value of the surface tension of the liquid under the plasma. However, this value cannot be measured experimentally and therefore an iterative procedure is adopted to estimate this value by comparing simulation and

experimental results. The surface tension is iterated between the experimentally measured initial (before treatment) and final (after treatment) surface tension values e.g between 68.03 mN/m to 45.39 mN/m changing -0.01 mN/m at each iteration. This is independently accurate as the PIV and the CFD results for a laminar flow without the Marangoni effect show a good agreement (less than 2% error) and the only source of difference is local surface tension variation beneath the plasma.

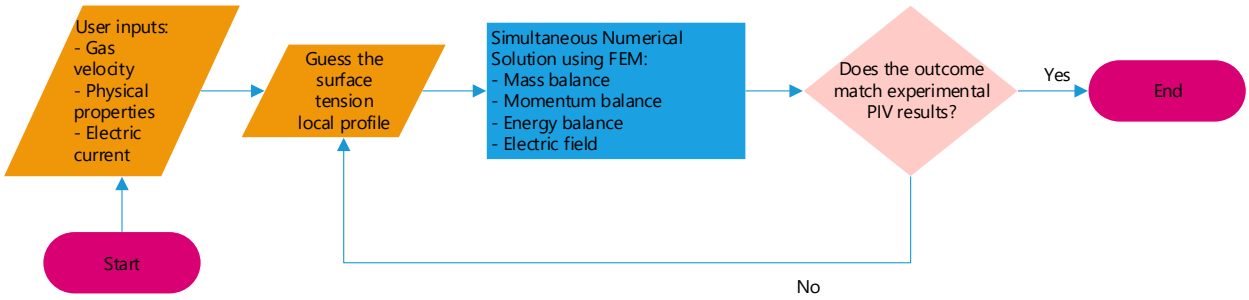

Figure 3.11. Structure of the CFD model. The local surface tension profile is guessed, and the results are compared to experimental outcomes during the simulation.

CFD Model Segregation and Mesh Reconfiguration: The 2-D model requires a large amount of computational resources and is infeasible with typically available computer system configurations. This can be overcome by solving momentum balance, current balance, energy balance and mass balance equations separately to reach a pseudo steady state that is then used as an initial condition for the next balance equation. Chemical and surface electrochemical reactions are included in the mass balance equation.

It is important to note that the moving mesh changes the geometry of the boundaries in all equations. While this doesn't cause a problem where the equations are solved simultaneously, it may cause inconsistencies if the equations are solved separately. This can be overcome by either using a fixed mesh in cases where the liquid surface deformation is negligible or by remeshing according to the new boundary geometry in each segregated stage.

3.7. Summary

Due to differences in simulation geometry scales and time-stepping requirements, the plasma-liquid interaction model was broken down into sub-models: the plasma model which accounts for electron impact reactions and the subsequent processes in the gas phase, and the CFD model which includes fluid dynamics, electric field, heat transfer, mass transfer, chemical and electrochemical reactions in the gas and the liquid phases.

A space-averaged 0D model was selected for the gas phase plasma because of its capability to handle complex chemistry sets and reduced computational cost.

Mass transfer from the plasma to the liquid is one of the most important aspects of the plasma-liquid interaction. A moving mesh method was used to model the two-phase flow because compared to the other available two-phase flow simulation methods, mass transfer through the liquid-gas interface could be implemented more accurately. FEM was chosen as the numerical method because complicated geometry along with a moving mesh can be handled by this method more readily.

The governing equations for the plasma and CFD model were introduced along with advanced features implemented to overcome the challenges of plasma-liquid systems.

Plasma chemistry has been explored in many studies in the literature in the past but the liquid phase chemistry reactions are relatively unknown. The model is structured so that when used in conjunction with experimental observations, the liquid phase chemistry and necessary unknown physical constants can be determined.

4. The Effects of the On-time on the Ozone Production in Pulsed DBDs[1]

As a first step to study systems, here we identify the key species produced and consumed in the gas phase of an atmospheric pressure plasma and investigate the effect of the on-time on the ozone production when the power is modulated. Short-lived and long-lived species not only trigger the liquid phase reactions but also contribute to the interface chemistry, which as shown in chapter six, play a vital role in the determination of the mass transfer throughout the system. Ozone is one of the most widely used products of atmospheric pressure plasmas. Due to ozone's high oxidation potential (2.07 V) compared to that of chlorine (1.36 V) and its availability to be produced on demand, it is now seen as a viable alternative for water treatment with widespread use across Europe and North America [194]. However, the cost associated with the production of ozone means its economic viability is low in many cases. This has led to extensive development into efficiency improvements of ozone generators [195]. To reduce the cost of ozone production, parameters of ozone generators can be manipulated in such a way as to change the characteristics of the plasma discharge to maximize ozone production efficiency. Parameters widely explored in the literature include feed gas composition and temperature [196], electrode size and shape [197], and cooling [198].

How the voltage is applied to the electrodes is also highly influential. Sinusoidal voltages are the most commonly used with an operating frequency typically between 1-50 kHz [199]. Higher frequencies can generate an increased concentration of ozone, but due to the increased power density, active cooling is essential to keep the gas temperature and prevent thermal breakdown of ozone [200]. Low temperature can also be favoured by use of helium or argon in the feed gas [201], [202]. However, the increase in cost associated with these gases means large-scale use is not economically viable.

[1] Computational simulations throughout this chapter were performed by the author. The experiments were carried out in collaboration with Plasma and Pulsed Power Group, Loughborough University [166].

Minimizing heat build-up around electrodes and thus the gas temperature is essential for ozone production as it enhances the conversion of ozone to reactive nitrogen species (RNS) such as NO_2 and NO_3 [203], [204]. This can be achieved through intelligent reactor design and with liquid cooling systems integrated with the reactor. However, the cost of cooling can be high, increasing the cost of ozone generation [198]. An alternative method to reduce the temperature is to modulate the input power to the plasma discharge. The ratio between the on-time and the off-time is known as the duty cycle [200]. Changing the duty cycle and the on-time can both influence the ozone density in the plasma. Low duty cycles have low average power which limits thermal degradation but also the average ozone production rate [205], [206]. The optimal duty cycle varies between reactors with the cooling efficiency of the electrodes being the most influential parameter.

While changing the modulation on-time for a fixed duty cycle and power influences the ozone density, a combination of the lack of literature in this field and little correlation between studies means the true effect of the on-time is not well defined. Olszewski *et al*. compared the ozone production of three different on-time periods and found that a period of 20 ms is marginally more effective than 2 ms but significantly more effective than a 2 minute period [207]. On the other hand, Barni et *al.* show a slightly different result where 0.5 ms is more efficient than 2.8 ms in ozone production [208].

The influence of the on-time on the ozone production has also been studied by Seri *et al.*, who showed that shorter on-times can increase the ozone concentration, but if they become too short, the efficiency will begin to decrease [209]. They cited the diffusion-time of the ozone away of the plasma active region as a key factor. During the modulation off-time air replenishes the ozone produced allowing the discharge to form in a higher concentration of oxygen. If this off-time is not long enough to allow ozone to diffuse away from the discharge region, subsequent discharges break down the ozone that has just been produced. Whilst this begins to explain the effects of the modulation on-time, further work is required to understand the chemistry occurring during the on and off-time of the plasma.

In this chapter, the direct effect of changing the modulation on-time for a fixed duty cycle is explored with attention paid to the air chemistry. The plasma reactor used for this study has been introduced in section 2.2 and has been used for the pre-treatment of biomass [140], [210] and wastewater [211].

The global model used to study the chemistry of the air discharge was introduced in section 3.3. In the model, the reactor is considered to be a cylindrical DBD reactor with circular electrodes of radius 60 mm. This gives an electrode surface area equal to that of the experimental DBD reactor. The gap between the electrodes is 2 mm and the gas flow rate of 1 SLPM. The reactor overall heat capacity was determined to be 0.015 W/K. The ambient air temperature and the initial gas temperature were set to 300 K.

4.1. Atmospheric Pressure Air Plasma Chemistry

The number of reactions in an air plasma is dramatically larger in noble gas plasmas (e.g. Argon plasma) due to roto-vibrational excitation, molecular variety and the need to account for the interaction between each species with all the other species present in the medium. Three-body reactions also may need to be studied, depending on the chemical nature of the mixture and the system pressure. Some studies have attempted to populate the reaction list automatically [75] while other studies focus on limiting the reaction list to the most effective ones [94].

It is important to bear in mind that the reactions cannot simply be ignored or prioritized due to the reaction rate coefficients. Each reaction leads to the production/consumption of certain species thus creating a unique pathway to intermediate and final products. Since these pathways often cross other reactions, elimination of a certain reaction may lead to the deletion of an entire group of consequent pathways. On the same note, reaction rates not only are determined by the reaction coefficient but also are mainly dependent on the reactant's densities. A reaction with a small reaction rate coefficient but largely available reactants may prove to be more effective on the entire process than a reaction with large reaction rate coefficient but less available reactants.

Prioritizing and utilizing a limited number of reactions is not only a matter of time spent on each simulation run or the volume of the calculations but also the accuracy of the results. One important fact that needs to

be considered is that although adding reactions makes a simulation more realistic by including additional chemical pathways, it can also have a negative effect on the overall accuracy of the simulation results as some reaction rate coefficients have large uncertainties. The addition of a certain reaction or species to a system may introduce a significant error without any meaningful contribution to the reaction pathways. It is, however, important to note that while not all reactions are equally important under all conditions, any particular reduced reaction set might no longer be valid due to the highly non-linear nature of plasma chemistry [170].

The chemistry of nitrogen-oxygen mixtures and with and without admixtures have been widely studied [170], [212]–[218]. In this thesis, a combination of dry air reactions was chosen from the literature based on the reactions involving main species in an air plasma according to previous similar works and experimental observations. The result is a dry air chemistry set database consisting of 37 species and 375 reactions as listed in appendix B.

Numerical values were handled in MATLAB, normalised and non-denationalised where applicable. To evaluate the error, the following cases were taken into consideration:

a) Most of the differences spotted in the reaction rate coefficients are due to the difference between two-body and three-body reaction rates (e.g. *R342*[2]*: $O + NO_2 + M \rightarrow NO_3 + M$* with a reaction rate coefficient of 9e-44×(300/Tg)^2 cm^6/s vs *R343: $O + NO_3 \rightarrow O_2 + NO_2$* with a reaction rate coefficient of 1.7e-17 cm^3/s. The background gas (M) density remains constant throughout the experiment with a value of ~1020 cm^{-3}. This can be integrated into the reaction rate coefficient, making the three-body reaction rate coefficient closer to that of two-body reactions.

b) Another method of validating the current number of reactions vs the uncertainty resulted from the reaction rate coefficients is to evaluate the results with the omission of the reactions with low

[2] Stating the reaction number according to appendix B, e.g. *R342* refers to reaction number 342 on the reaction list.

reaction rate coefficient. As an example, the simulation was run by omitting *R367:* $NO_2 + NO_3 + M \rightleftharpoons M + N_2O_5$ with the reaction rate coefficient of 2.8e-42×(300/Tg)$^{3.5}$ cm^6/s. As discussed later in 4.2.2, this reaction is one of the main pathways in production/destruction of N_2O_5 and omitting it causes major issues (e.g. NO_2 and NO_3 densities exceed NO density in contrast with experimental observations).

It is important to note that while every measure was taken to ensure the precision of the used reaction rate coefficients (e.g. checking reaction rate coefficient values through multiple references), in general, the uncertainty in reaction rate coefficients is counted as an inherent limitation of global models [219].

4.2. Main Chemical Pathways - Single Nanosecond Pulse

In this section, the main reaction pathways are discussed when a single square 2 ns pulse is applied at t= 1e-9 s to the system. These pathways may change when multiple pulses are applied as the background gas composition and temperature may evolve in time. Here, important ROS and RNS pathways are identified to provide an overall view of the system chemistry.

4.2.1. Reactive Oxygen Species (ROS)

Ozone is the most abandon ROS and it is mainly produced by atomic oxygen reacting with molecular oxygen in a three-body reaction as shown in equation 4.1. During the power-off time after the pulse, ozone is slowly quenched by NO (eq. 4.2).

R338: $O + O_2 + M \longrightarrow M + O_3$ (4.1)

R361: $O_3 + NO \longrightarrow NO_2 + O_2$ (4.2)

where M is a background gas such as N_2 or O_2.

At the beginning of the simulation, as can be seen in figure 4.1, atomic oxygen is produced rapidly via electron-impact dissociation of molecular oxygen. This results in rapid ozone production in the first 100 ns. As the input power declines, the atomic oxygen production rate declines due to the lack of energetic electrons. Ozone production, however, continues by consumption of the remaining atomic oxygen at a

lower rate. After 100 μs, atomic oxygen density begins to decline which results in a stall in ozone production. The decline in atomic oxygen concentration is temporarily (10^{-4}-10^{-3}s) halted due to the production of atomic oxygen via reaction 4.3:

R315: $N + O_2 \longrightarrow NO + O$ (4.3)

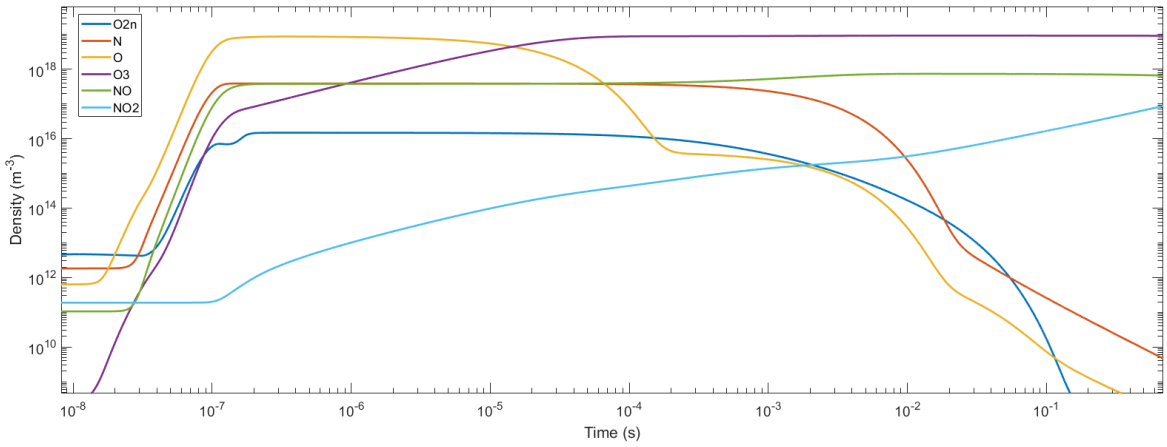

Figure 4.1. Time evolution of ozone and related ROS and RNS species. $\varepsilon_e = 5.5\ eV$

4.2.2. Reactive Nitrogen Species (RNS)

Initially, there are two main reactions producing NO_2. This compound not only is produced by the reaction between atomic oxygen and *NO*, but also is generated by the reaction between atomic oxygen and O_2^- as shown in equations 4.4 and 4.5.

R340: $NO + O + M \longrightarrow NO_2 + M$ (4.4)

R59: $N + O_2^- \longrightarrow NO_2 + e$ (4.5)

Both atomic oxygen and atomic nitrogen are consumed in reactions with larger reaction rates. This leads to a gradual but steady production of NO_2 up to about 1 ms. After that, as shown in figure 4.2, these species densities decline rapidly and then NO_2 production is governed by the reaction between ozone and *NO* as shown in equation 4.6.

R361: $O_3 + NO \longrightarrow NO_2 + O_2$ (4.6)

As the rate of this reaction is considered large compared to other reactions at 1ms (2.1e17 $m^{-3}s^{-1}$), NO_2 production rate keeps on accumulating at a larger rate as can be seen in figure 4.2.

NO_3 only starts to be produced when enough ozone and NO_2 are available in the mixture and the main production mechanism is according to equation 4.7.

R362: $NO_2 + O_3 \longrightarrow NO_3 + O_2$ (4.7)

After 10 ms, NO_3 starts decomposing to NO_2 by reacting with NO via equation 4.8. This is because enough NO and NO_3 becomes available for this reaction to occur.

R365: $NO + NO_3 \longrightarrow NO_2 + NO_2$ (4.8)

The main reaction governing production and consumption of N_2O_5 throughout the simulation period is:

R367: $NO_2 + NO_3 + M \rightleftharpoons M + N_2O_5$ (4.9)

The overall reaction rate in the first instances of the simulation is 1.6e6 m^{-3} and rises to 2.5e6 m^{-3} as time approaches 0.01 sec due to the rise of nitrogen dioxide and nitrogen trioxide in the gas composition. A decline is then detected in the overall reaction rate because of a sharper decline in NO_3 compared to the slighter rise in NO_2 density. NO_3 is less stable than NO_2 or even N_2O_5 [220] and it is prone to decomposition according to equation 4.8.

This results in the dynamic equilibrium 4.9 shifting to the LHS after 0.1 sec, hence reducing the amount of N_2O_5 and increasing that of NO_2.

N_2O is mainly produced by the reaction between atomic nitrogen and nitrogen oxide as shown in equation 4.10:

R310: $N + NO_2 \longrightarrow N_2O + O$ (4.10)

As the density of N declines, less N_2O is produced. N_2O is mainly decomposed according to equation 4.11 as shown in figure 4.4. O_2^- density is limited and declining, leading to slow decomposition of N_2O.

R157: $O_2^- + N_2O \longrightarrow O_3^- + N_2$ (4.11)

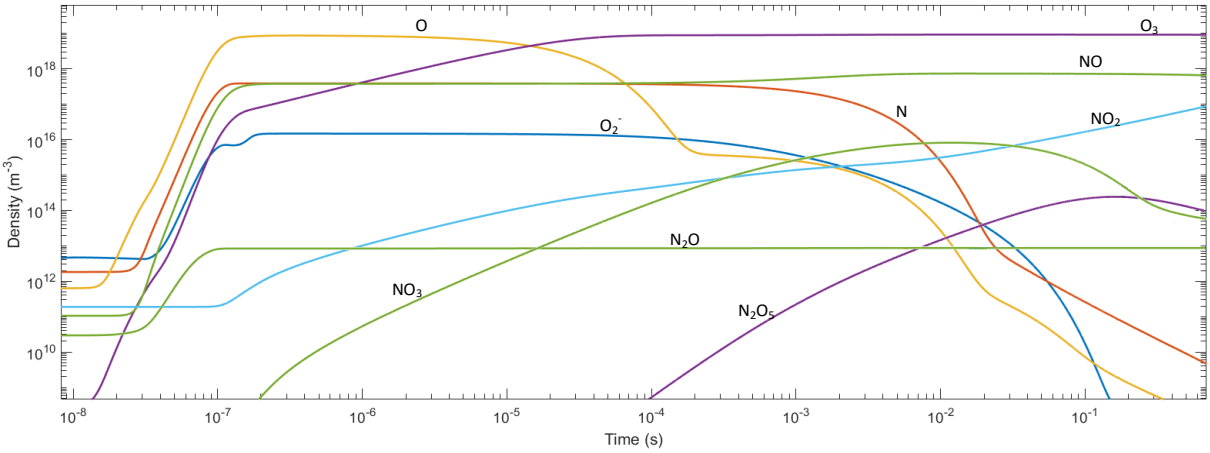

Figure 4.2. Time evolution of NO_x and related species densities.

To acquire a better overall understanding of the main chemical pathways, reactions discussed here are summarized in figures 4.3 to 4.5 with the reactions listed in appendix B. These flowcharts show the main chemical pathways including reaction rates for various main species at the designated time. The following results can be derived from these flowcharts:

- Electrons, as the main species initiating plasma reactions, play an important role at the beginning of the simulation as suggested in figure 4.3 and 4.4. The significance of electron-involved reactions declines in favour of longer-lived species reactions as shown in figure 4.5. The main source of electrons is oxygen and nitrogen undergoing ionisation processes.
- Time evolution of each species is a result of multiple reactions, where the dominating reaction(s) and pathway(s) may vary according to varying conditions throughout the simulation.
- Chemical pathways of each species must be studied in relation with all the other main chemical pathways. Simply just because the density of a species is higher in a mixture doesn't justify the availability of that species to all chemical pathways. Competitive and reversible reactions must be considered.
- Although gas temperature can be important in determining main chemical pathways, main chemical pathways can change for each species without much variation of gas temperature.

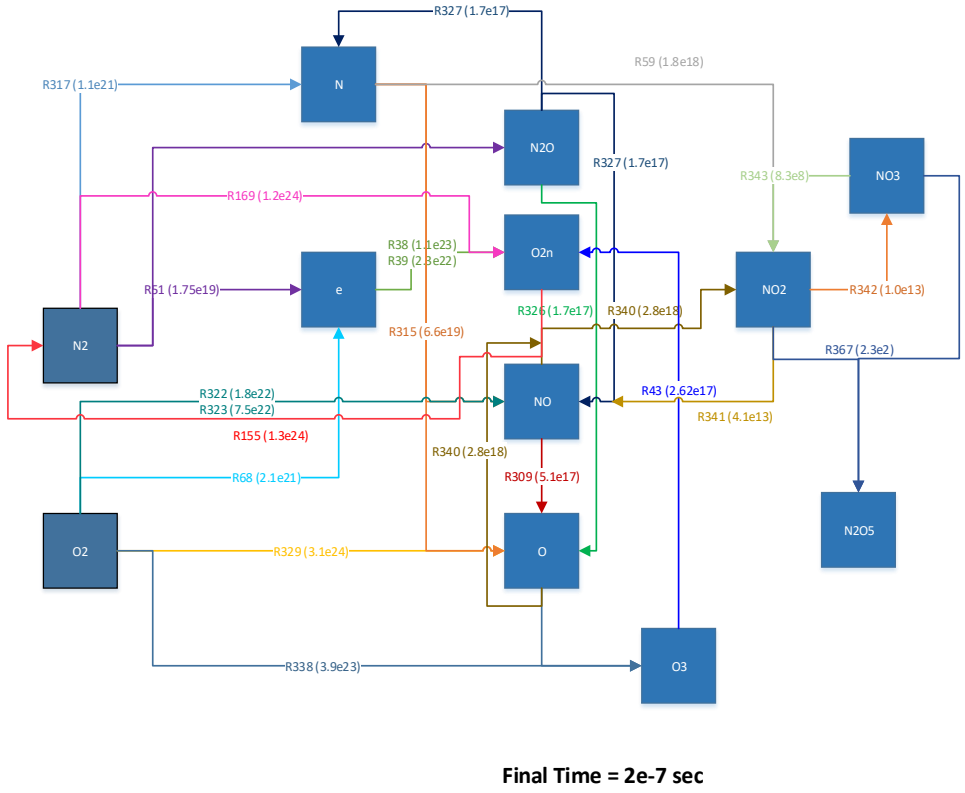

Figure 4.3. Main governing chemical reactions at t=2e-7 sec. Different colours are used to differentiate between reactions.

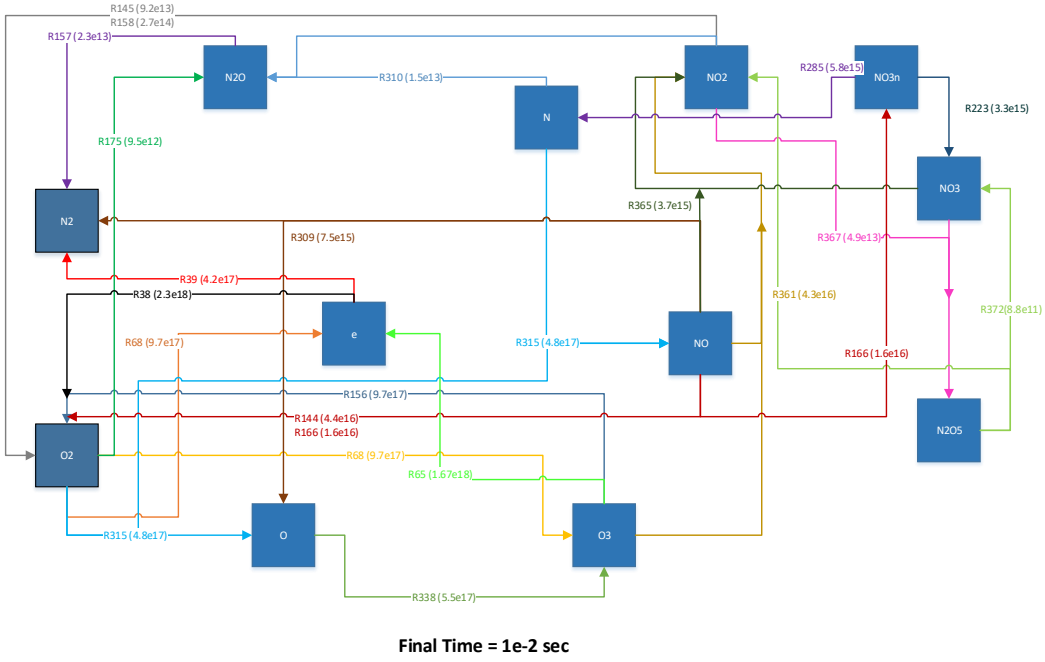

Figure 4.4. Main governing chemical reactions at t=1e-2 sec.

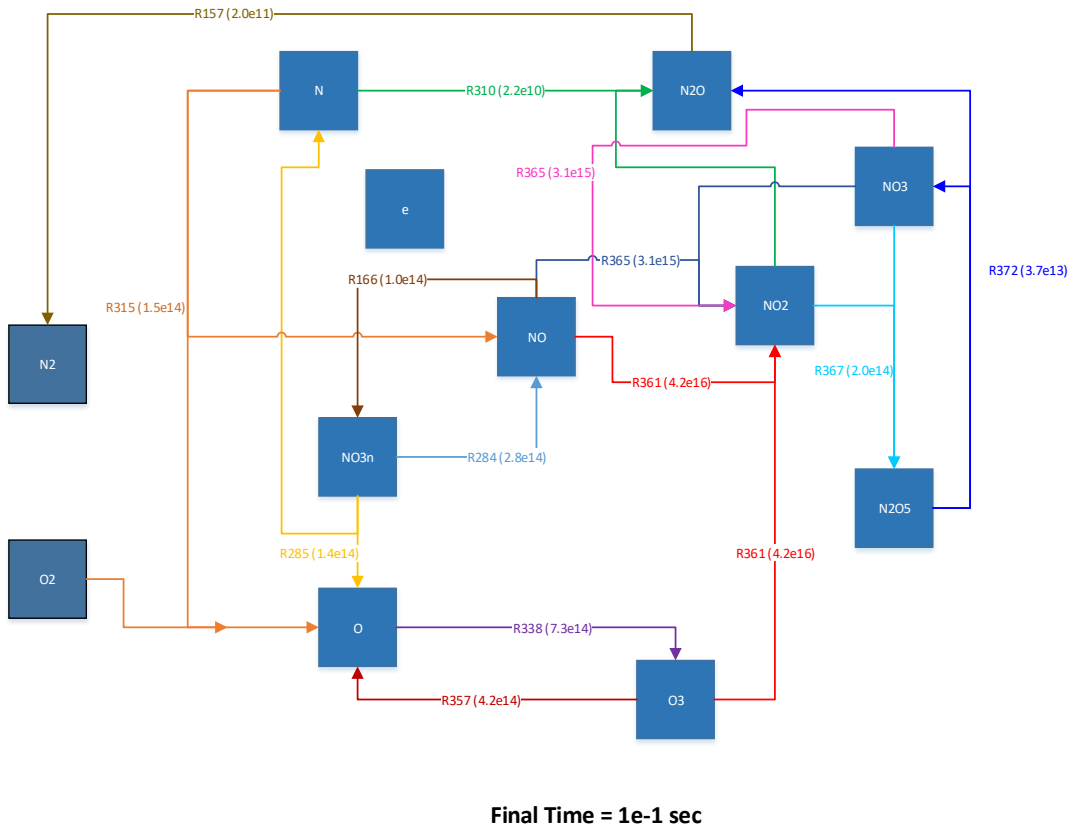

Figure 4.5. Main governing chemical reactions at t=1e-1 sec.

The gas temperature evolution is often ignored as it is argued that the variation was negligible [170]. To confirm this, the gas temperature was calculated and plotted against time. It can be concluded that in this case study, gas temperature variation for a single pulse is less than 0.5 K as shown in figure 4.6, which has an insignificant impact on volumetric reaction rates in general. However, the gas temperature effect is not

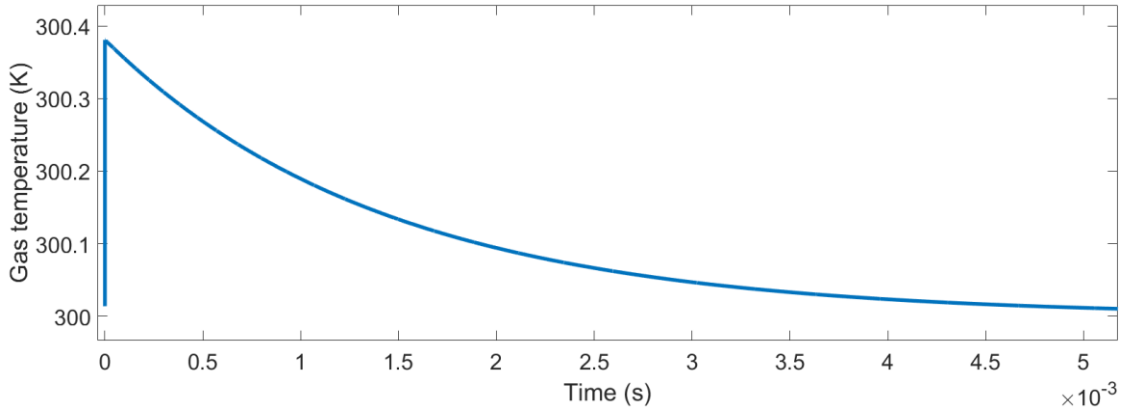

Figure 4.6. Gas temperature time evolution.

necessarily negligible when multiple pulses are introduced to the system as shown in figure 3.7. This is discussed in more detail in 4.3.2.

4.3. Main Chemical Pathways – Multiple Pulses

The analysis of the chemistry of the single-phase discharge reveals a complex interplay between different species and chemical pathways that depends on the gas background composition. As a result, it is anticipated that the plasma chemistry of a modulated plasma system will evolve over time and the simulation of an input power pulse will need to account for changes in the background gas composition due to power pulses.

Here we consider the simulation of the experimental setup described in section 2.1, where the power is modulated ON and OFF. During the on-time, power is delivered by a 21.6 KHz signal and the off-time is adjusted to keep the cycle at 30%. The analytical expression of the input power during the on-time is given by 4.12. and accounts for the transient damped oscillation observed in experiments (see Fig 2.3).

The dampening sinusoidal waveform was characterized experimentally and used as an input for the model described by equation 4.12:

$$P = P_m(1 + d_{overshoot} \cdot \exp(-t \cdot d_{freq} \cdot d_{factor}) * \sin(\pi \cdot d_{freq} \cdot t) * \sin(4t\pi n_c f)) \quad (4.12)$$

where P_m is the pulse magnitude, $d_{overshoot}$, d_{freq} and d_{factor} the properties of the damped oscillation, t the time with respect to the beginning of the pulse, n_c the number of cycles and f the frequency. Typical values are duty cycle of 30%, frequency 21.6 kHz, $d_{overshoot}$ 1.1767, d_{freq} 8 kHz and d_{factor} 0.5. The pulse magnitude was chosen so that the average power was the same as in the experimental reactor (34.740 W). The resulting power function is shown in Figure 4.7 (a). Figure 4.7 (b) shows a constant sinusoidal waveform with the same frequency duty cycle, total energy and average power to study the effect of the transient damped oscillation. Since the energy balance is written according to equations 3.11 and 3.12, the total input power during the experiment time is kept constant throughout the simulation.

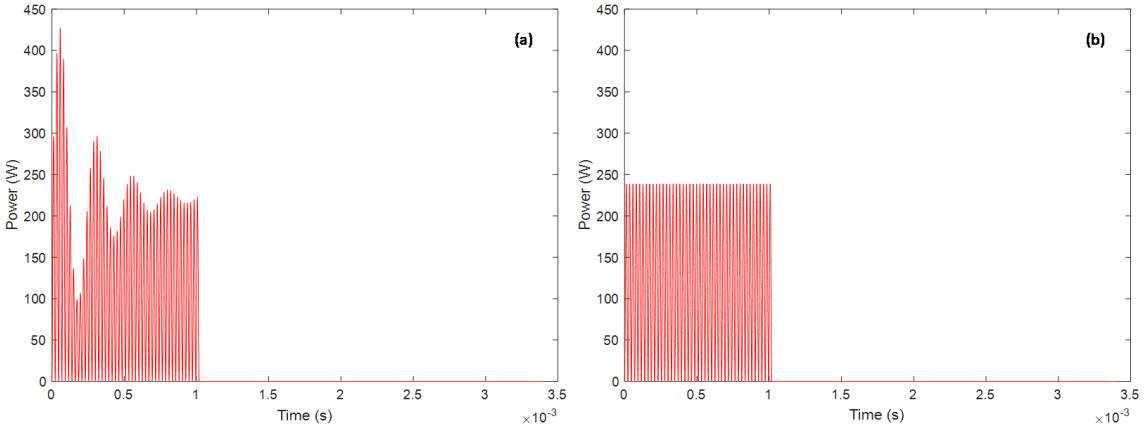

Figure 4.7. (a) Power waveform incorporating the overshoot and damping observed in experiments. (b) Theoretical pulsed sinusoidal power waveform. Both signals deliver the same average power [166].

4.3.1. Ozone Concentration

Figure 4.8 shows the time evolution of the ozone concentration generated in the reactor when the on-times are 1, 10 and 100 ms, respectively. Experimental and computational results agree qualitatively, and both show that 1 ms on-time is more efficient in generating ozone than longer on-time periods and that the ozone concentration initially increases, reaches a maximum after ~20 seconds and then decreases, becoming negligible after ~80 seconds. This non-monotonous trend has been observed in other DBD systems and is attributed to increasing poisoning of the background gas by NO_x species[221]. Indeed, as NO_x species accumulate in the reactor, the model shows that the catalytic action of NO and NO_2 quenches ozone and atomic oxygen:

R361: $NO + O_3 \rightarrow NO_2 + O_2$ (4.13)

R341: $NO_2 + O \rightarrow NO + O_2$ (4.14)

Net: *R66:* $O + O_3 \rightarrow 2O_2$ (4.15)

The simulations overestimate the amount of ozone generated in the system due to the limitations of the zero-dimensional model to capture the actual geometry of the real device. In the actual reactor (Fig 2.1), not all the gas flowing through the system becomes ionized. As a result, in experiments, the reactive species generated in the plasma are diluted in background gas before they are actually measured in the tank. This

contributes to the lower ozone concentrations observed in experiments. Nevertheless, the zero-dimensional model captures the general trends observed in experiments and provides valuable insights into the chemical pathways at play during the on- and off-time periods. Another source of the discrepancy can be attributed to the UV spectrometer cable being placed at the top of the reactor while the simulations are performed for the plasma region, between the two crucibles.

The better efficacy of the shorter on-time (Figure 4.8a) could be erroneously attributed to the higher input power delivered to the plasma due to the transient oscillation induced at the beginning of each pulse However, Figure 4.8b allows us to assess the effect of the power overshoot at the beginning of the pulse on the ozone production. For the two largest on-times (10 ms and 100 ms), there are virtually no difference between the "damped" (Figure 4.7a) and "constant" (Figure 4.7b) sinusoidal waveforms. This is expected as the overshoot at the beginning of each pulse lasts for a very short time when compared to the total duration of the on-time pulse. For the 1 ms on-time, a difference between the two waveforms is observed because the transient at the beginning of the pulse takes a significant fraction of the on-time of the pulse. However, this difference is negligible when compared with the difference caused by the change in on-time. Since the simulation results capture the same trend even when no oscillation is incorporated in the input power waveform (Figure 4.8b), it follows that the increased power delivered with the shorter on-times is not the main factor contributing to the enhanced ozone production. The underpinning mechanism is discussed in section 4.3.3 below.

4.3.2. Temperature Evolution

Figure 4.9 shows the temporal evolution of the discharge gas temperature for the three on-times. Shorter on-times result in higher gas temperature, with 1 ms reaching 398 K after 1200 seconds, 10 ms 385 K and 100 ms 375 K. The temperature rise is faster over the first 20 seconds for all cases.

The fast rise in temperature quickly turns the system from one where ozone is predominantly generated to one in which it is effectively destroyed [221], [222]. This explains the trends seen in Figure 4.8 where the ozone density rises and then falls back to zero again. Simulation results in which the gas temperature is

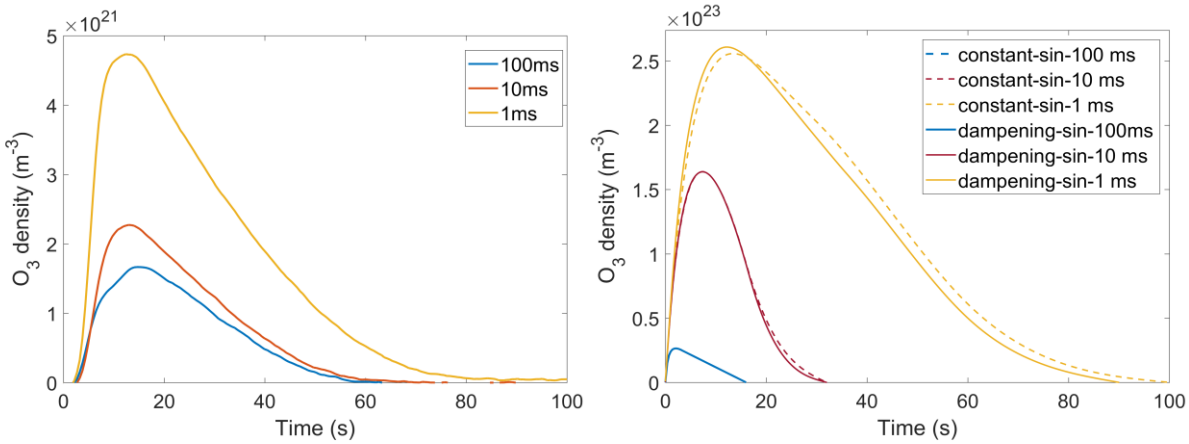

(a) (b)

Figure 4.8. Time evolution of the ozone concentration (a) experimental measurements and (b) computational results [166]. While simulation and experimental results show the same trends, the numerical values are different mainly due to the use of 0D geometry vs the actual geometry of the system. Another source of discrepancy can be attributed to the location of the UV spectrometer. While the optical cable is placed on top of the reactor as shown in figure 2.1, the simulation calculates ozone concentration inside the plasm, between the crucibles.

kept constant do not show the decrease in ozone concentration. It is interesting to note that 1 ms on-time results in the hottest discharge, yet 1 ms on-time is also the one that produces most ozone. Therefore, the transition from an ozone-producing to an ozone-destroying regime although triggered by temperature, must also rely on the actual discharge composition. In particular, the dissociation of N_2O_5 into NO_2 and NO_3 is favoured at higher temperature, and, as will be discussed in the next section, NO_2 plays a critical role in determining the ozone production/destruction efficacy.

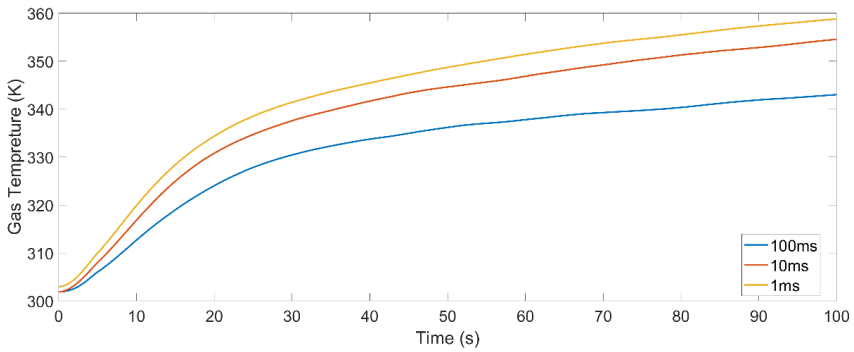

Figure 4.9. Time evolution of the gas temperature as measured by the optical fibre thermometer [166]. The tip of the optical fibre was pushed inside the tube and placed as close as possible to the plasma centre.

4.3.3. The Effect of Power Modulation on System Chemistry

The fact that the three on-time cases result in different ozone concentrations indicates that the net ozone generation rate during the on-times, the net ozone destruction rate during the off-times, or both are different (Fig 4.8). In fact, the enhanced ozone production with the 1 ms on-time is somewhat surprising, as this on-time is obtained at the highest gas temperature. Although it is not possible to fully resolve the temporal evolution of the ozone concentration in our experimental setup, simulation results indicate that the main difference can be attributed to the faster net production rate of ozone during the on-time of shorter on-time periods.

Ozone generation during the on-time is driven by the three-body reaction *R338:* $O + O_2 + M \rightarrow O_3 + M$, but during the on-time, other competing reactions destroy ozone. In the first seconds of the discharge, ozone is quenched by collisions with electrons (*R22:* $e + O_3 \rightarrow O_2^- + O$) and singlet oxygen (*R74:* $O_2a + O_3 \rightarrow 2O_2 + O$), primarily. Since singlet oxygen builds-up relatively slowly during the on-time pulse and decreases relatively quickly during the off-time, longer on-time pulses favour the accumulation of higher concentrations of singlet oxygen in the discharge during the on-time, which leads to enhanced ozone destruction. The ozone destruction rates associated with these reactions, however, are typically two orders of magnitude smaller than the generation rates and hence have little bearing on the net generation rate of ozone.

Instead the main mechanism affecting the net generation rate of ozone in the first seconds of the discharge is the availability of atomic oxygen. Longer on-times result in lower concentrations of atomic oxygen, which leads to the slower ozone production (*R78:* $O + O_2 + M \rightarrow O_3 + M$). This is the case because longer on-times favour the accumulation of NO_2, which, besides reacting with ozone directly (*R362:* $O_3 + NO_2 \rightarrow O_2 + NO_3$), quenches atomic oxygen (*R341:* $O + NO_2 \rightarrow NO + O_2$). Although during the first 10−20 s there is a net positive production of ozone, eventually, the accumulation of both NO and NO_2 leads to the catalytic destruction of O and O_3.

Therefore, the ozone production efficacy is dependent on the generation/destruction of NO_2, as this affects the balance of atomic oxygen. NO_2 is involved in the catalytic reaction with O and in the formation of N_2O_5. These reactions change the composition of the NO_x cocktail in the discharge but retain the total amount of nitrogen, and subsequently, other NO_x species lead to the formation of NO_2. Significantly, however, NO_2 also reacts with atomic nitrogen (*R310:* $N + NO_2 \rightarrow N_2O + O$). This is an important reaction because, on one hand, it releases O, which can subsequently lead to ozone production, and on the other, it produces N_2O. Unlike other NO_x species, N_2O is fairly stable and escapes the plasma removing nitrogen from the system, thereby preventing it from becoming NO_2 again. Short on-times are found to produce a higher average density of atomic nitrogen and, therefore, are more efficient in converting NO_2 into N_2O, thereby favouring ozone production. This occurs because atomic nitrogen is generated during the on-time and consumed during the off-time. For long on/off-times, atomic nitrogen is completely depleted for the most part of the off time, whereas in short on/off-time atomic nitrogen is present during the whole period.

Therefore, shorter on-times produce more ozone from a combination of effects. Previous studies have found that more frequent off-time periods allow for ozone to escape the discharge region and the discharge to form in the replenished gas between the electrodes [209]. In addition, the current study has found that shorter on-time periods favour a higher concentration of atomic oxygen and lower concentration of singlet oxygen, which contribute to a more efficient net production of ozone.

The higher atomic oxygen concentration is a direct consequence of the lower NO_2 accumulation in discharges with short on-times, as these discharges present larger concentrations of atomic nitrogen (N) that converts NO_2 into long-lived N_2O.

4.4. Summary

In this chapter, we have used a global model to study the chemistry of an atmospheric pressure air plasma air discharge when the input power is modulated. The model is capable of reproducing the trends observed in experiments, providing new insights into the underlying mechanisms.

In particular, we show that for fixed average power and duty-cycle, the on-time duration can have a marked influence on the performance of the DBD. Care must be exercised when measuring power in modulated DBD systems, as the varying plasma impedance and the output stage of the power supply can cause transients that become increasingly important in short on-time pulses.

The experimental and computational results presented here show that shorter on-time pulses lead to enhanced ozone production, even despite their operation at slightly higher temperature. The key underpinning mechanism that causes this important observation is the more efficient net generation rate of ozone during the plasma on-time due to the lower accumulation of NO_2 in the discharge, as this leads to a lower competing quenching rate of ozone and atomic oxygen. The lower accumulation of NO_2 is favoured by the larger average density of atomic nitrogen that converts NO_2 into the less reactive, longer-lived N_2O. Therefore, applications that rely on ozone production using DBDs should consider short on-times as a means of enhancing their efficiency.

5. Epoxidation of *trans*-Stilbene by *He-O_2* Atmospheric Pressure Plasma[3]

In this chapter, we use the global model discussed in the previous chapter and extend it to study the transport of reactive species into a liquid. As a practical example, atomic oxygen produced in the plasma can directly be used to epoxidate alkenes in solution. Epoxides are key building blocks in organic synthesis and are important intermediates in the preparation of many natural products. Epoxides are typically prepared by reacting alkenes with sacrificial mono-oxygen donors, such as peracids [223], [224]. A large number of catalysts has been developed to achieve high conversion and selectivity [225]–[228]. However, the sacrificial donor usually becomes a waste stream, which can damage the reaction equipment and cause pollution. Besides, catalysts are costly and require cumbersome preparation procedures. The ultimate scheme for synthesizing epoxides would be the direct reaction of alkenes with atomic oxygen as this method would eliminate the waste stream [224], [229], [230].

As shown in the previous chapter, atomic oxygen can be generated in oxygen containing plasmas, and therefore, if delivered to the liquid, it can drive epoxidation reaction of alkenes in solution [231]. A few recent studies show that atmospheric pressure plasma-driven epoxidation promises a novel approach in the epoxide production process [164]. While the main by-products such as benzaldehyde are environmental-friendly and non-toxic, [232] the industrialization of the process has been held back mainly by low production yields [233].

5.1. System Chemistry

The experimental setup used for the epoxidation study is discussed in section 2.2 and consists of a *He-O_2* DBD capillary discharge with the end of the tube submerged in the solution being treated. The alkene used

[3] Computational simulations throughout this chapter were performed by the author. The experiments were carried out in collaboration with Plasma and Pulsed Power Group and the School of Chemistry, Loughborough University [231].

in this study was *trans*-stilbene which was selected its non-volatility and product stability. Acetonitrile was used as the solvent.

5.1.1. Gas phase

The chemistry reaction set for the atmospheric pressure *He-O_2* plasma was determined according to [94]. Water-involved reactions were excluded from the reaction set as the experiment did not involve water. The resulting reaction set consists of 18 species and 176 reactions (see appendix C).

He-O_2 plasma generates both *O* and O_3 and normally the amount of *O* is higher than O_3 when the O_2 fraction in the feed gases is relatively low [234]. However, in this work, the concentration of *O* at the end of the tube is several orders of magnitude smaller than O_3 because, in the afterglow region, *O* is converted to O_3 [170].

5.1.2. Liquid Phase

Chromatographic analysis of plasma treated liquids reveal that *O* is the key species contributing to the formation of *trans*-stilbene epoxide [235], [236] where O_3 leads to the formation of benzaldehyde [168], [231]. In the presence of oxidants (*O*, O_2 and O_3) and moisture, benzaldehyde readily converts to benzoic acid [237]. The main reactions in the liquid phase are shown in scheme 5.1 to 5.3:

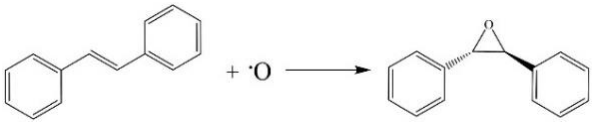

(5.1)

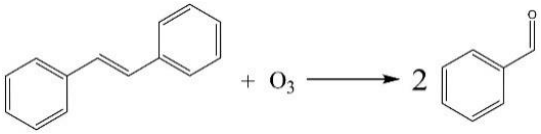

(5.2)

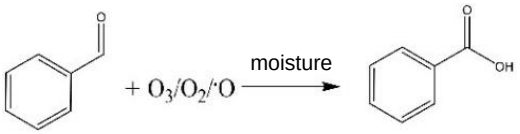

(5.3)

Since O_2 has a relatively high solubility in acetonitrile [238], [239], the alkene solution was bubbled with argon for 30 minutes before treatment to prevent the formation of ozone ($O + O_2 \rightarrow O_3$) in the liquid phase. Therefore, the key species taking part in the liquid phase reactions are *trans*-stilbene, benzaldehyde, *trans*-stilbene epoxide, benzoic acid, O, O_2 and O_3.

A list of the liquid phase reactions and physical constants used in the simulation of the liquid phase are shown in tables 5.1 and 5.2.

Table 5.1. Liquid phase reactions.

No.	Reaction Equation	Reaction Rate Coefficient*	Uncertainty***	Ref.
1	$(C_6H_5CH = CHC_6H_5) + O_3 \rightarrow 2(C_6H_5CHO) + \frac{1}{2}O_2$	3.9×10^9	$\pm 1.8 \times 10^9$	**
2	$(C_6H_5CH = CHC_6H_5) + O \rightarrow C_6H_5CHOCHC_6H_5$	1×10^{10}	$\pm 1.2 \times 10^9$	**
3	$O(1D) + O_2 \rightarrow O_3$	4.0×10^9	$\pm 8.4 \times 10^8$	[240]
4	$2O \rightarrow O_2$	2.8×10^{10}	$\pm 3.1 \times 10^9$	[241]
5	$C_6H_5CHO + O \rightarrow C_6H_5COOH$	3.0×10^6	$\pm 7.2 \times 10^4$	[242]
6	$C_6H_5CHO + O_2 \rightarrow C_6H_5COOH + \frac{1}{2}O_2$	1.0×10^6	$\pm 1.2 \times 10^4$	[242]
7	$C_6H_5CHO + O_3 \rightarrow C_6H_5COOH + O_2$	2.0×10^6	$\pm 2.5 \times 10^4$	[242]
8	$C_6H_5CHOCHC_6H_5 + O_3 \rightarrow C_6H_5CH = CHC_6H_5$	1.0×10^5	$\pm 1.4 \times 10^3$	**

* The reaction rate coefficient units are $M^{-1}s^{-1}$ for two-body reactions.

** Estimated by comparing experimental and computational results according to the algorithm described in figure 3.10. Estimates in agreement with Ref. [193].

*** The uncertainty column presents the range from the stated reaction rate coefficient in which the simulation results are within the reference ranges and agree with experimental observations.

5.2. Experimental and Computational Results

To validate the computational model (section 3.6.2), the simulation results were compared with experimental observations. Ozone density is used to correct the plasma 0D and 1D models while trans-stilbene, trans-stilbene epoxide and benzaldehyde concentrations are used to correct the 2D CFD model as described by the algorithm shown in figure 3.10Densities measured by OES are initially compared with the 1D plasma model to assure simulation accuracy. These results are then combined with the reactor velocity field and tested against GSMS outcomes to obtain an estimate for O Henry's constant. This value is then used to determine the reaction rate coefficients.

5.2.1. Ozone Density

Figure 5.1 shows the simulated spatial evolution of the plasma effluent gas composition across the tube. *O* degradation is rapid in the first 14 mm of the tube length but then slows down and the density decreases with a slower rate in the remaining distance. The reason is that although the main *O* consumption mechanisms which are $O + \text{wall} \rightarrow O_2$ and $O_2 + O + He \rightarrow He + O_3$ remain the same throughout the tube length, the main mechanism that generate *O* switches from $O_2(a^1\Delta_g) + O_3 \rightarrow 2O_2 + O$ to $He + O_3 \rightarrow He + O + O_2$ once $O_2(a^1\Delta_g)$ becomes scarce in the system. Since the density of atomic oxygen and singlet oxygen are several orders of magnitude smaller than ozone, the effect of the changes caused by these species' production/destruction in total ozone density is less apparent in figure 5.1.

Table 5.2. Physical constants used in the simulations.

Property	Symbol	Unit	Value	Ref.
Bubble diameter	d_b	m	4.00×10^{-3} – 6.00×10^{-3}	measured and averaged as described in 2.2.4
Liquid density	ρ_l	kg/m^3	768.00	[243]
Liquid viscosity	μ_l	Pa·s	3.41×10^{-3}	[243]
Diffusion coefficient of *O* in the liquid phase	$D_{O(l)}$	m^2/s	2.00×10^{-9}	[244]*
Diffusion coefficient of O_2 in the liquid phase	$D_{O_2(l)}$	m^2/s	2.00×10^{-9}	[244]*
Diffusion coefficient of O_3 in the liquid phase	$D_{O_3(l)}$	m^2/s	1.75×10^{-9}	[244]*
Diffusion coefficient of *O* in the gas phase	$D_{O(g)}$	m^2/s	7.20×10^{-3}	[245]
Diffusion coefficient of O_2 in the gas phase	$D_{O_2(g)}$	m^2/s	6.98×10^{-3}	[245]
Diffusion coefficient of O_3 in the gas phase	$D_{O_3(g)}$	m^2/s	6.98×10^{-3}	[245]
Diffusion coefficient of 'O_2 in the gas phase	$D_{\prime O_2(g)}$	m^2/s	6.98×10^{-3}	[245]
Diffusion coefficient of *O* in the gas phase	$D_{O1D(g)}$	m^2/s	7.20×10^{-3}	[245]
Henry's constant of *O*	H_O	mol/Pa·m^3	7.48×10^{-5} – 9.39×10^{-5}	[246]*,**
Henry's constant of O_2	H_{O_2}	mol/Pa·m^3	1.28×10^{-5}	[246]*
Henry's constant of O_3	H_{O_3}	mol/Pa·m^3	1.09×10^{-4}***	[246]*

* estimated by values in water.
** prediction based on simulation results.
*** numerical values were based on experimental values with the least number of significant figures.

Figure 5.2 shows the ozone density measured by *UV* absorption for different input gas compositions at the tip of the tube. The measured ozone concentration during steady state changes from bellow 5 ppm for 0.1 % O_2 gas fraction to 85 ppm for 1.5 % O_2 gas fraction which conforms with simulated fractions of 6.5 ppm to 149.9 ppm respectively (figure 5.6). The reason of the discrepancy can mainly be attributed to the 0D-1D geometry compared to the experimental setup.

5.2.2. Species Bulk Concentrations

To correct and verify the 2D CFD model, the average species concentrations were compared with the experimental results as shown in figure 5.3 (a-c). The samples were taken from the bulk liquid and analysed by GCMS. A good correlation between simulations and experiments can be seen. Please note that although the model was calibrated as explained in figure 3.10, the reaction rate coefficients and the O henry's constant are kept within a valid range which result in an acceptable overall solution for the system.

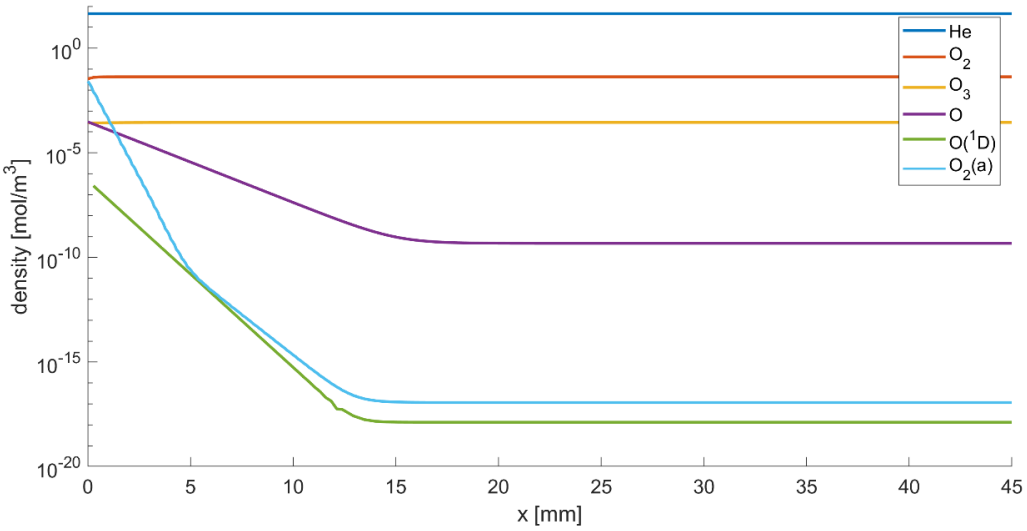

Figure 5.1. The density of plasma effluent main species as a function of tube length. *O* degradation is rapid in the first 14 mm and then slows down within the length of the tube.

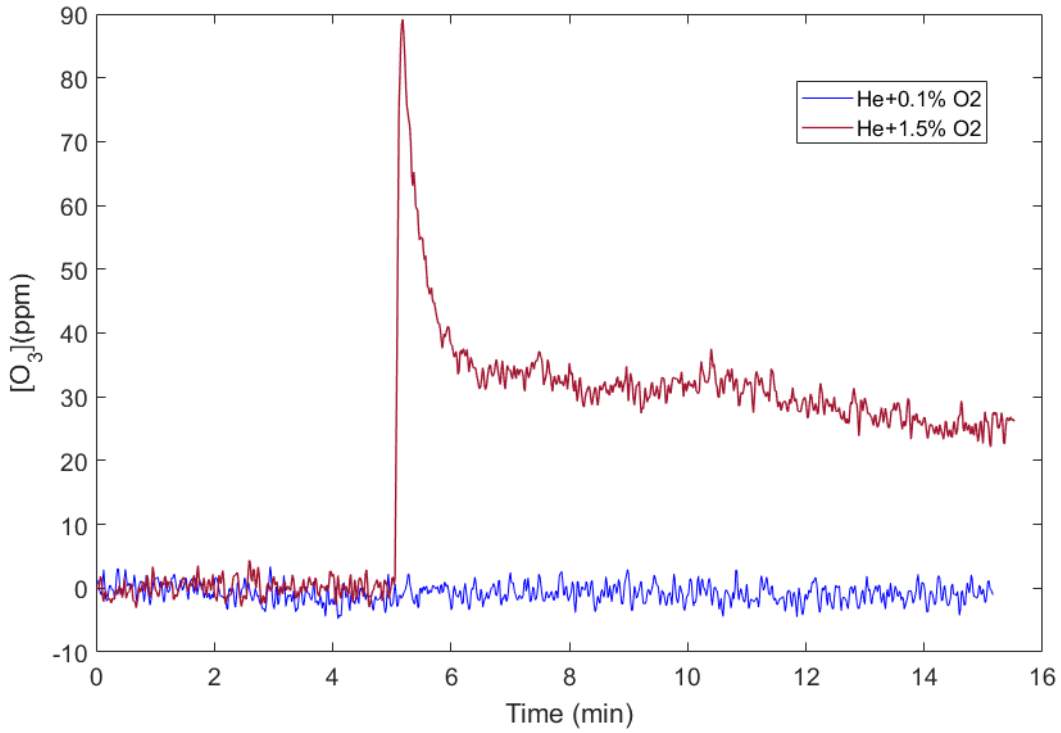

Figure 5.2. OES results taken at the tip of the tube show ozone density as a function of time. The spike at the beginning of the higher oxygen concentration can be attributed to the residual moisture in the tube before the plasma is ignited. The reported values are calculated by averaging OES results from t = 8.0 s to t= 14 s of the above figure.

The concentration of *trans*-stilbene decreases over time as it reacts with *O* and O_3 generated in the plasma to form epoxide and benzaldehyde. The decrease is faster when larger oxygen concentrations is present in the background gas as this leads to higher concentration of ROS in the plasma discharge.

As shown in Fig. 5.3c, *trans*-stilbene epoxide starts to degrade in the absence of *trans*-stilbene as suggested by the experimental curve. The degradation (highlighted by experimental observation at t=90 min for the case with 1.5% O_2) suggests that at least one more reaction exists that consumes *trans*-stilbene epoxide as shown in reaction 8 of table 5.1. The reaction is probably between trans-stilbene epoxide and *O* or O_3 with a lower reaction rate coefficient compared to that of trans-stilbene and *O*, breaking down the desired product into benzaldehyde.

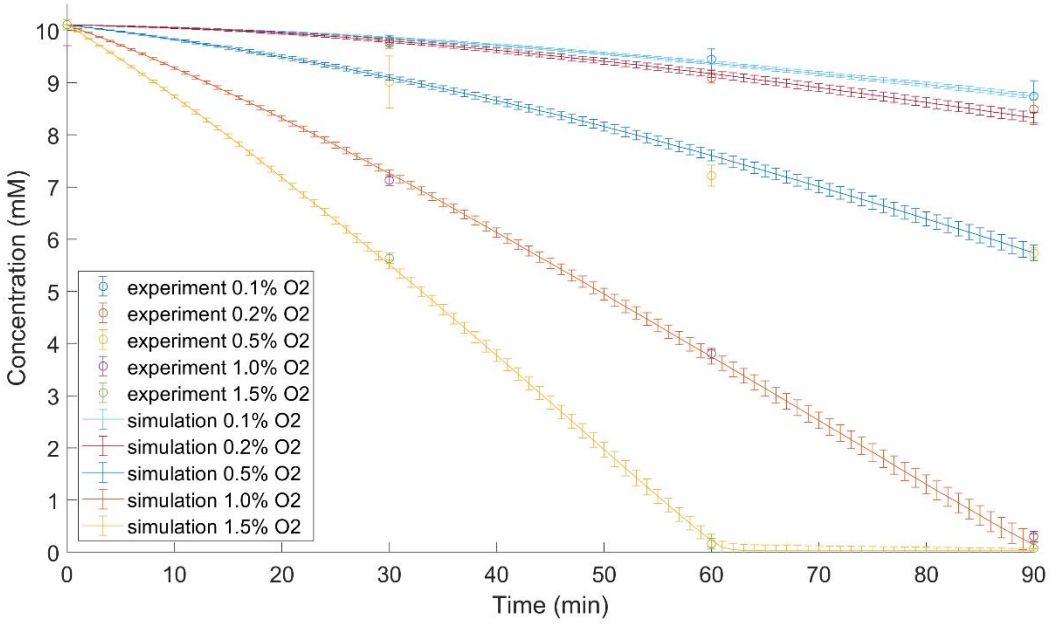

Figure 5.3a. Average concentration of trans-stilbene (reactant). Experimental results: samples were taken from the well-mixed glass flask and analysed by GCMS. Simulation results: averaged values of the 2D model. Simulation and experimental results show a good correlation.

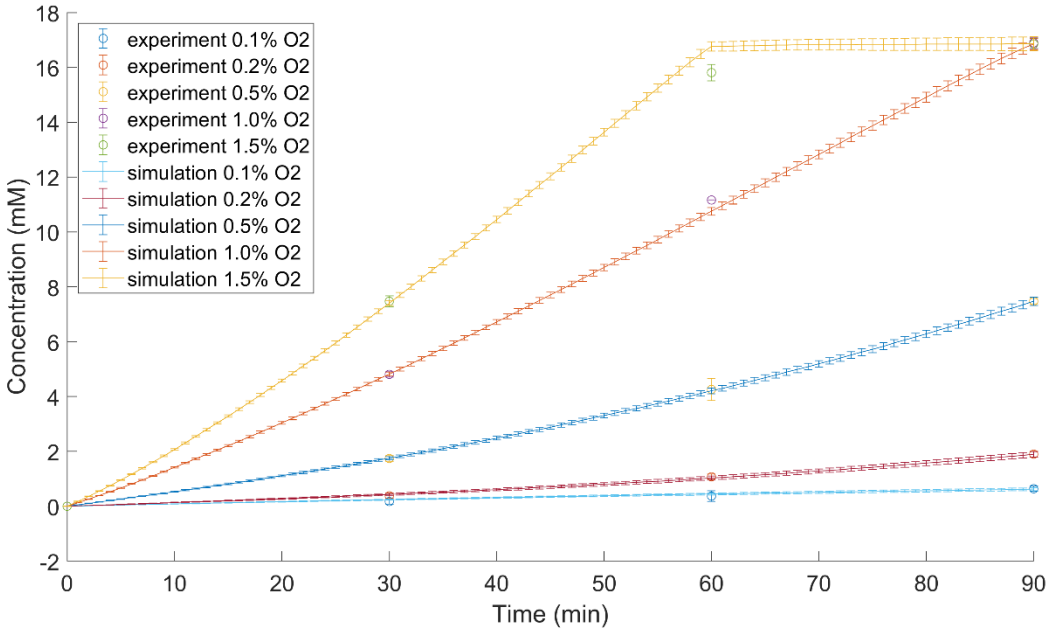

Figure 5.3b. Mean average concentration of benzaldehyde (by-product), simulation and experimental results show a good correlation.

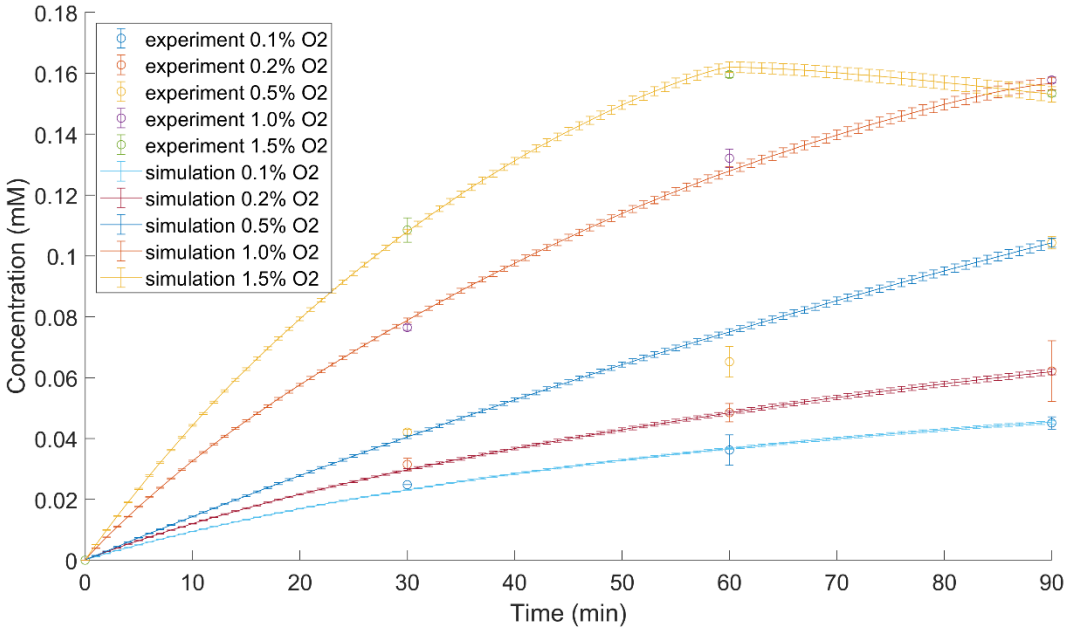

Figure 5.3c. Average concentration of *trans*-stilbene epoxide (product), simulation and experimental results show a good correlation.

5.3. Reactor Optimization and Design Guidelines

5.3.1. Plasma-Liquid Distance

To maximize the *trans*-stilbene epoxide production, the plasma should be placed closer than 14 mm to the liquid to prevent a significant drop in *O* density (figure 5.1). Figure 5.4 (a) shows the simulated *trans*-stilbene epoxide production once the tube length is decreased from 45 mm to 10 mm with 0.1% O_2 fraction in the input gas. While the product concentration increases from 0.021 mM to 0.145 mM after 90 minutes, benzaldehyde production does not change significantly as shown in figure 5.4 (b). This is because epoxide is produced by *trans*-stilbene reacting with *O* and as shown in figure 5.1, for the tube lengths bellow 14 mm *O* density becomes significantly higher (5e-7 mol/m^3) at the tip of the tube. Ozone density does not change significantly in this case; therefore, the concentration of benzaldehyde remains the same.

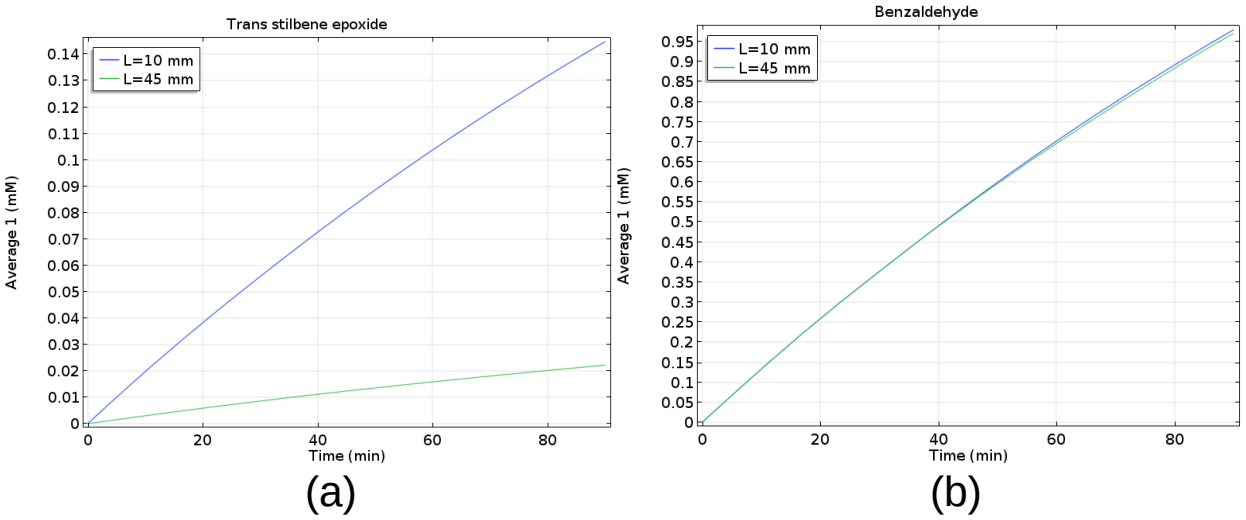

Figure 5.4. (a) *trans*-stilbene epoxide production is increased from 0.02 mM to 0.14 mM by reducing the tube length from 45 mm to 10 mm while 0.1% O_2 is used as the input gas fraction. (b) Benzaldehyde production remains the same because although *O* density has increased at the gas-liquid interface, ozone concentration remains the same.

While the plasma being placed closer than 14 mm from the liquid surface will increase the production of *trans*-stilbene epoxide, the plasma touching the liquid will cause ions to be transferred into the liquid, triggering potentially unwanted reactions. The *UV* generated by the plasma can also initiate side reactions, which could reduce the efficiency of the reactor.

5.3.2. Gas-Liquid Interfacial Area

The reactor design can vary significantly once the main gas-liquid mass transfer surface is identified. As shown in figure 5.5 (a), the transfer of *O* from gas to the liquid mainly occurs at the tube output interface in the case of the plasma being placed further than 14 mm to the liquid. This suggests that a larger gas-liquid interfacial area increases the mass transfer rate, however, as shown in figure 5.5 (b), by decreasing the plasma distance from 45 mm to 10 mm, significant *O* transfer continues in the bubbles, making the total bubble swarm surface area and the bubble rise time more important to consider in the reactor design. In this case, a significant fraction of *O* escapes the system without reacting with trans-stilbene.

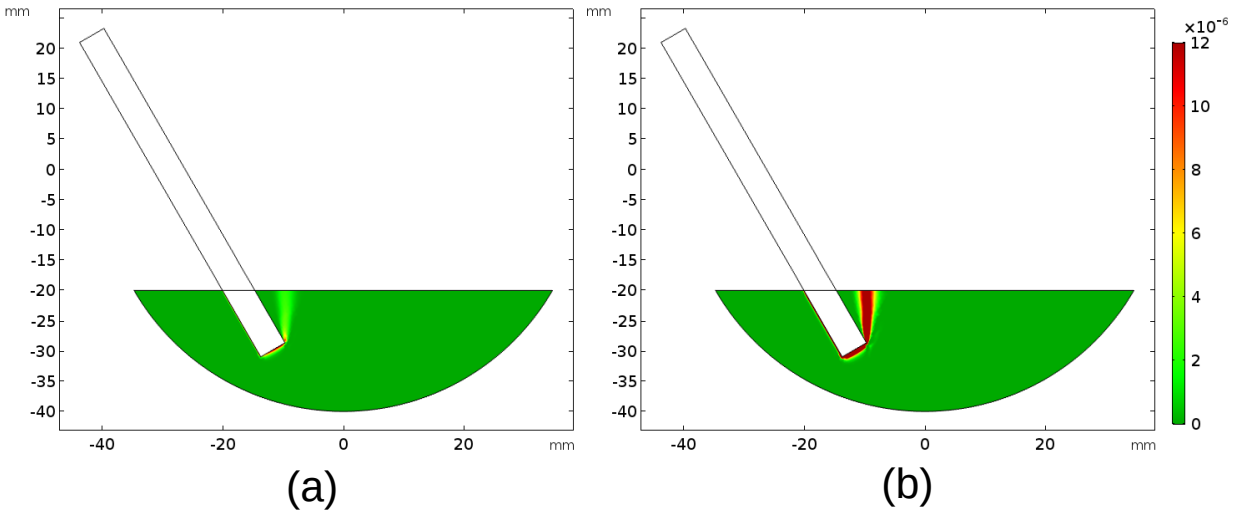

Figure 5.5. Local mass transfer of *O* for different plasma to liquid distances. In case (a) where the plasma is far from the liquid, the main mass transfer occurs at the tip of the tube where *O* is quenched into the liquid. In this case, the plasma-liquid interfacial area is the most important factor in determining the mass transfer rate between the gas and the liquid. In case (b) where the plasma is placed closer to the liquid before *O* is degraded by the gas phase chemical reactions, the mass transfer continues during the bubble rise. In this case, the total bubble swarm surface area and the bubble rise time become more important.

5.3.3. Input Gas Composition

O_2 fraction in the input gas contributes to ozone and *O* production. In O_2 fractions below 6%, *O* density is proportional to the O_2 density. In higher O_2 gas fractions, *O* is quenched by reacting with ozone. The maximum *O* production at the plasma does not necessarily translate to maximum trans-stilbene epoxide production because e.g. at 8% O_2 gas fraction, high ozone density leads to loss of *O* in the tube and the bubbles. Higher ozone density also reacts more readily with trans-stilbene and less reactant is left to form trans-stilbene benzaldehyde.

To find the most optimized input gas composition with the current configuration, the O_2 fraction was changed from 0.1 % to 10 % in the simulations. The results show that for an O_2 fraction of 1%, the maximum trans-stilbene epoxide is produced as shown in figure 5.7. It is, however, important to note that the optimized gas composition needs to be re-checked each time the reactor configuration has changed.

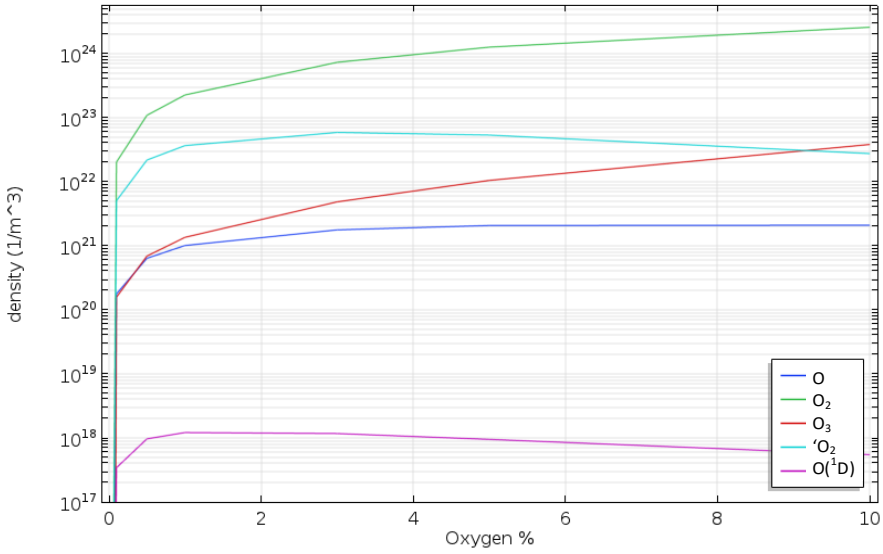

Figure 5.6. Oxygen species densities in the plasma effluent as a function of oxygen fraction in the feed gas. O production reaches maximum at ~6 % O_2 gas fraction.

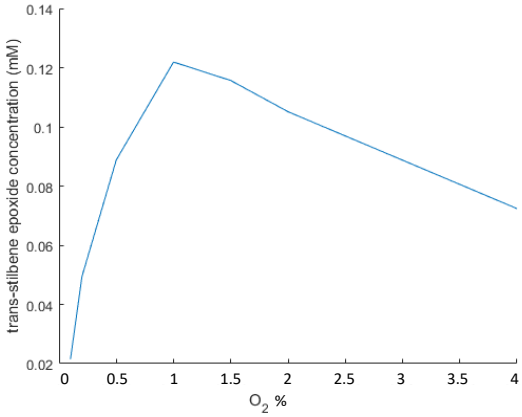

Figure 5.7. Trans-stilbene epoxide as a function of oxygen at t = 90 min volume fraction in the gas feed. Trans-stilbene epoxide concentration increases with oxygen fraction up to 1% mainly because more *O* is present in the gas phase. The concentration then drops in higher oxygen fractions because trans-stilbene is used by ozone producing benzaldehyde before reacting with *O*.

5.3.4. Input Power

A radio frequency (RF) input, with a frequency of 13.56 MHz equal to that of a COST reference jet [247], increases the production of *O* significantly [248]. This is observed experimentally where the ratio of *O* to O_3 becomes greater than 6 at low oxygen concentrations using an RF power supply [248].

To simulate utilizing a COST reference jet as the plasma source and compare it to a constant voltage, plasma densities were set to observed COST jet experimental densities according to [248] while using a 45 mm tube length. As shown in figure 5.8a and 5.8b, using a COST jet makes the epoxidation process more selective.

It is important to note that while the results are derived by fixing L=45 mm, *trans*-stilbene epoxide production can be increased up to 7.0 mM by setting L=10 mm and using an RF power supply combined.

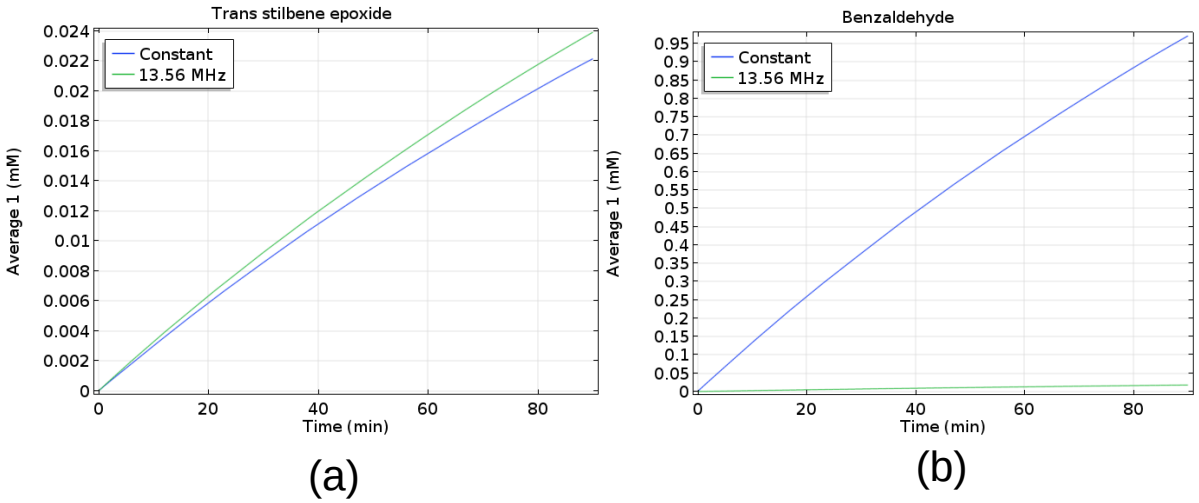

Figure 5.8. Simulation results (a) *trans*-stilbene epoxide and (b) benzaldehyde vs time. *Trans*-stilbene epoxide production is more selective by using an RF power supply due to higher *O* density in the plasma discharge. *O* to ozone ratio in the plasma was fixed to 6 and L to 45mm.

5.4. Proposed Reactor Design

Based on the reactor analysis, a new design is proposed to improve the production of *trans*-stilbene epoxide from *trans*-stilbene by plasma treatment. The proposed design follows the following criteria:

- **Production enhancement:** The liquid should be placed as close as possible to the plasma without directly touching it. The bubbles buoyancy force can be used as the mixing drive depending on the reactor geometry and the gas retention time should be long enough for the atomic oxygen to react with the *trans*-stilbene. To maximize *O* to ozone production, an RF plasma jet is required to produce

the plasma. Smaller bubble size is desirable to increase the surface to volume ratio. To increase the production yield, the reactor needs to be cooled down to 5-8º C as suggested by [164].

- **Practicality:** Product sampling ports must be designed to enhance the sampling process. A transparent window must be placed to map the velocity field, measure the bubble size and the reactor mixing patterns. The reactor geometry should minimize the solvent evaporation.

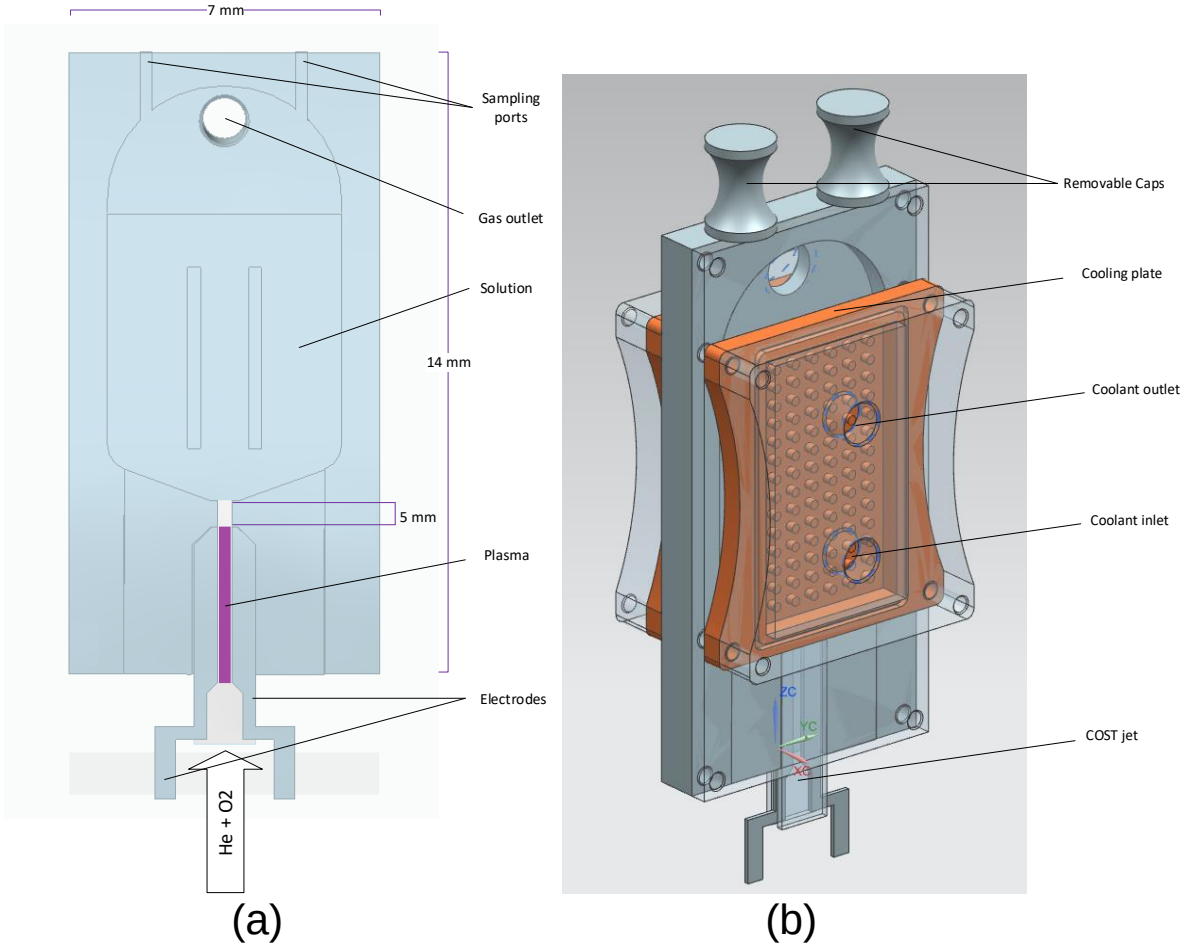

Figure 5.9. (a) The proposed reactor design schematic and (b) the 3D design with the cooling plates in place[4]. A COST jet is used as the plasma source while the solution is bubbled with the plasma discharge. The plasma is placed as close as possible to the liquid without direct contact.

[4] Device schematic and 3D model produced within Plasma and Pulsed Power Group, Loughborough University.

A COST jet is proposed as the reactor plasma source as shown in figure 5.9. The reactor back panel is made of polytetrafluoroethylene (PTFE) by computer numerical control (CNC) machining with baffles in place to enhance the mixing regime. The reactor front panel is made of glass, fixed by PTFE bolts. The cooling plates are made of copper with a machined fin pattern to increase the coolant liquid interface with the heat exchanger wall. A glass panel was placed on top of the cooling plate to map the coolant flow pattern. The top of the reactor was designed as a semi-circle to return some of the evaporated liquid into the reactor. To control the liquid and the gas outlet temperatures separately, the cooling plate was not extended to the top of the reactor, instead, another condenser (not shown in the figure) is used in the gas outlet to minimize the solvent evaporation.

5.5. Summary

trans-stilbene epoxidation by plasma was investigated experimentally by bubbling a *He*-O_2 plasma effluent through the *trans*-stilbene solution. A computational model was created describing the process in three stages. The first stage consisted of a 0D plasma model to determine the production of ROS in the active plasma region. The second stage was a 1D CFD model where the gas spatial evolution was studied to determine the input concentration for the third stage. The final model was a 2D CFD model which accounted for the gas-liquid velocity field as well as the gas and liquid chemical reactions and mass transfer.

The plasma model was corrected and verified by comparing the model results with the ozone concentration measured in the plasma effluent. The 2D CFD model results were verified by comparing the GCMS results against the simulation average final concentrations.

Several results and reactor design guidelines were derived from the simulations. Henry's constant of *O* was estimated by the model as well as the reaction rate coefficients of *trans*-stilbene with *O* to produce *trans*-stilbene epoxide and *trans*-stilbene with ozone to produce benzaldehyde as shown in table 5.1. The distance between the plasma and the gas outlet in the liquid phase should not exceed 14 mm to maintain a high *O* density in the gas phase. The plasma should not touch the liquid directly to prevent unwanted reactions due

to charged species or *UV*. The main *O* mass transfer occurs at the tip of the tube if the plasma effluent travel distance exceeds 14mm. Bubble surface to volume ratio become important in cases where enough *O* is present in the gas phase. *O* to ozone density fraction in the gas phase plays an important role in determining the product yield. This can be determined by changing the oxygen fraction in the gas phase. Although the *O* density increases with the oxygen content in the background gas, the epoxide yield drops at high oxygen concentration due to the presence of ozone. Ozone not only quenches *O* in the tube and the bubbles reducing the available reactant directly but it also competes with *O* in the liquid phase to react with *trans*-stilbene, producing benzaldehyde as a by-product. An RF plasma enhances the *trans*-stilbene epoxide production selectivity by increasing *O* to ozone ratio.

The results of this study are used to design a more efficient plasma epoxidation system. The generated model also can be used in a separate study to estimate Henry's constant of short-lived species (e.g. Henry's constant of *O*, described in table 5.2) of plasma effluents.

6. The Importance of Surface Tension Gradient in Plasma-Liquid Treatment Systems

In the previous chapter we studied a plasma-liquid system that exploited neutral reactive species to drive chemical reactions in the liquid phase. Plasma, however, also produces charged species which can be used to drive electrochemical reactions in liquids. As an example, in this chapter, we consider the experimental setup discussed in section 2.3 in which the plasma is used as a source of electrons, thereby creating an electrolytic cell where one electrode is replaced by a DC plasma. Plasma-driven electrochemical processes find application in medicine [23], [30], [249], bio-disinfection [15], [16], polymer surface modification [250] and analytical chemistry [251]. These applications often rely on natural convection liquid mixing, which determines the mass transfer between the plasma and the liquid. To better understand this process, a comprehensive study is undertaken to identify the key factors contributing to the mass transfer in such systems.

6.1. Model Chemistry

Deionised water is used as the solvent with salt (KCl) added to increase the conductivity of the solution. The liquid acts as the high-voltage electrode and therefore, the plasma is a source of electrons for liquid phase reactions[35], [36], [97]. Solvated electrons (free electrons surrounded by the liquid phase solution) react with water molecules producing OH^- in the plasma-liquid interaction region as shown by reaction 1 in table 6.1. This causes the pH to increase beneath the plasma as described in chapter 6.3.1. In the submerged electrode (anode) Cl^- is oxidised producing Cl_2. The Cl_2 then reacts with water in the anode region (reaction 3 in table 6.1) and a flux of H^+ is formed that causes the high voltage electrode region to become acidic [252]. Other chemical reactions include water dissociation and electron-proton recombination (see table 6.1).

Since the plasma is sustained in a noble gas, the generation of reactive species is limited and the plasma acts as a source of electrons. Therefore, in the model, a flux of electrons is introduced at the plasma-liquid

interface [35] and a corresponding flux of H^+ is released at the high voltage electrode to maintain current continuity.

The diffusion coefficients of the liquid phase species are listed in table 6.2 and the drift coefficients of charged species were obtained from the Einstein relation.

The initial conductivity of the solution was measured to be 33.28×10^{-4} S/m and the reference temperature is 300 K. A list of other physical properties used in the simulation is shown in table 6.3.

Table 6.1. Chemical reactions affecting the local pH of the liquid phase.

Reaction Number	Reaction Equation	Reaction Rate Coefficient	Ref.
1	$2e + H_2O \rightarrow 2\ OH^- + H_2$	1.9×10^{1} [m^3/(mol·s)]	[253]
2	$2Cl^- \rightarrow\ Cl_2 + 2e$	Anodic reaction	[252]
3	$Cl_2 + 2H_2O \rightarrow\ \ 2H^+ + 2HClO + \ 2e$	Anodic reaction	[252]
4	$H_2O \rightarrow H^+ + OH^-$	1.0×10^{-14} [1/s]	[253]
5	$H^+ + e \rightarrow H$	2.3×10^{10} [m^3/(mol·s)]	[253]
6	$H + H \rightarrow H_2$	7.8×10^{9} [m^3/(mol·s)]	[253]
7	$OH^- + H \rightarrow H_2O + \ e^-$	2.2×10^{7} [m^3/(mol·s)]	[253]
8	$H_2O + OH^- \rightarrow H_2O + \ {O_2}^-$	5.0×10^{9} [m^3/(mol·s)]	[253]

Table 6.2. Diffusivity of aqueous ions.

Species	D_i [m^2/s]	Ref.
OH^-	5.26×10^{-9}	[252]
H^+	9.312×10^{-9}	[252]
Cl^-	2.03×10^{-9}	[254]

Table 6.3. Thermodynamic and physical properties of the liquid and gas phase.

Property	Unit	Liquid phase	Gas phase		Ref.
			Air	He	
ϵ_r	1	80.1	1.000	1.000	[243]
ρ_0	kg/m^3	995	1	0.138	[243]
α_p	1/K	0.247×10^{-3}	3.4×10^{-3}	12.21×10^{-3}	[243]
C_p	J/kg·K	4.183×10^{-3}	1.007×10^{-3}	5.193×10^{-3}	[243], [169]
k	W/ m·K	0.6089	2.624×10^{-2}	0.149	[243], [169]
η	Pa·s	8.90×10^{-4}	1.81×10^{-5}	1.96×10^{-5}	[243], [169]

6.2. Model Verification

Simulation results are compared with the experimental observations to verify and validate the model before using it to study the underlying mechanisms governing the mass transfer in the system.

To minimize the effect of surface deformation on the flow patterns inside the liquid, the gas flow was set to 1 SLPM, a value for which the liquid surface was not visibly deformed. This value depends on the gas composition as heavier gases such as air or argon would introduce higher deformation to the surface. Please note that although the device is exposed to ambient air, the jet gas composition is dominated by the inlet gas (e.g. helium) which reduces the surface deformation.

6.2.1. pH Profile

Figure 6.1 shows the local pH in the liquid after 300s of plasma exposure (I = 2.0 mA). The electron flux creates a swarm of OH^- beneath the plasma region where the pH increases to ~10. Local changes of the pH in this region depend on the initial pH of the solution and the electron flux magnitude. Hydrolysis around the high voltage electrode creates an acidic region where the observed pH drops to ~4.

There is a good qualitative agreement between the model and the experimental pH profile, with some discrepancies around the high voltage electrode. These are due to the limited number of anodic reactions in the model and the limitation of modelling a plasma electrode in a 2D model.

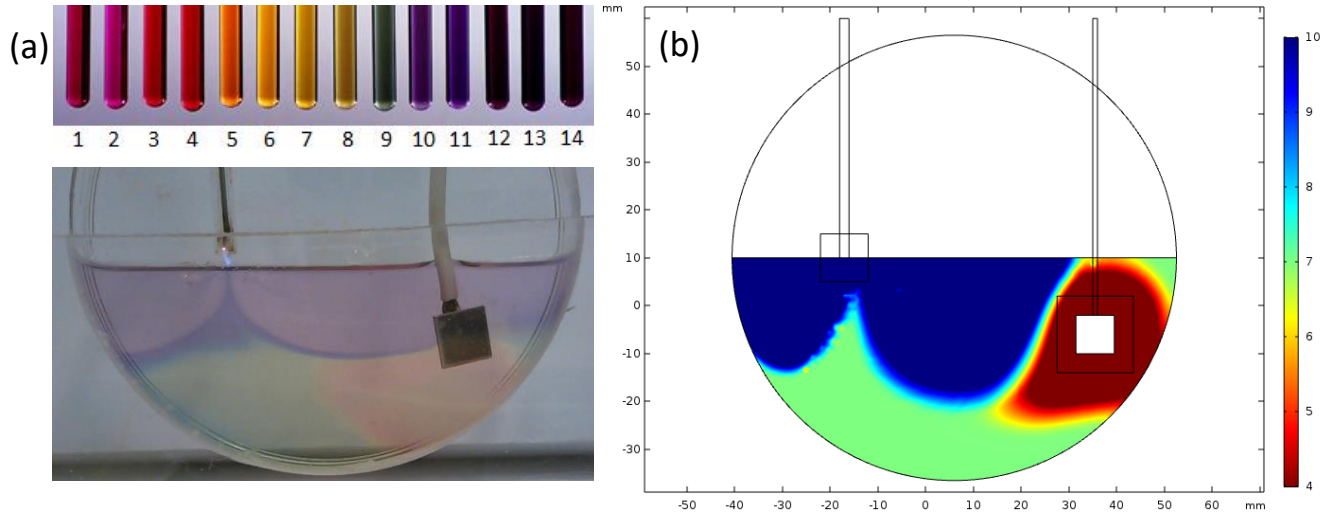

Figure 6.1. (a) Experimental local pH profile after 300 s. (b) Simulated pH profile after 300 s.

6.2.2. Particle Image Velocimetry (PIV)

Experimental time-averaged local velocity profiles were acquired by PIV and compared with the simulation as shown in figure 6.7 (a-I) and (a-II). The acquired raw data consisted of 1000 consecutive images for each scanned area. Each image was compared to the next image in PIVLab to determine the direction and the distance travelled by each particle. By accounting for the time between each image taken, the velocity vector was determined. Velocity vectors were averaged in x and y directions to give a velocity vector for each recorded image sequence. The values were then compared with the average velocity vectors calculated by the model at the same location. The maximum absolute deviation was 3.4×10^{-5} m/s in the x-direction and 1.2×10^{-5} m/s in the y-direction, which corresponds to a relative error of 5.2% and 4.0%, respectively. The model was also validated by comparing the liquid velocity field when the plasma was turned off and the impinging gas flow was the only factor inducing the liquid flow. In this case, the absolute deviation was 1.4×10^{-5} m/s in the x-direction and 1.1×10^{-5} m/s in the y-direction, which corresponds to a 2.1% and 3.6% relative error, respectively. The size of the latex particles (4 μm) represent the limiting scanning resolution.

6.3. Factors Affecting the Treated Liquid Mixing Patterns

The most significant factors affecting the mixing patterns are introduced and compared in this section. This is to gain an understanding of the importance of each factor and identify the key underlying physics at play. Natural convection, hydrodynamic and electrohydrodynamic effects and Marangoni forces are considered in the study.

6.3.1. Temperature

Since the plasma is the only heat source present in the system, the generated heat causes a natural convection flow in both the gas and the liquid phase. Figure 6.2 demonstrates the effect of the temperature on the velocity field while all the other mechanisms are ‘turned off’ in the simulation. The plasma edge temperature was kept constant while the electric field, gas flow and the electron flux were set to zero. Natural convection causes a velocity field of magnitude around 10^{-3} m/s in the gas phase while similarly

creating a velocity field of around 10^{-4} m/s in the liquid phase. While the flow pattern of the liquid can be slightly affected by the gas flow, the effect is negligible compared to the liquid natural convection velocity field.

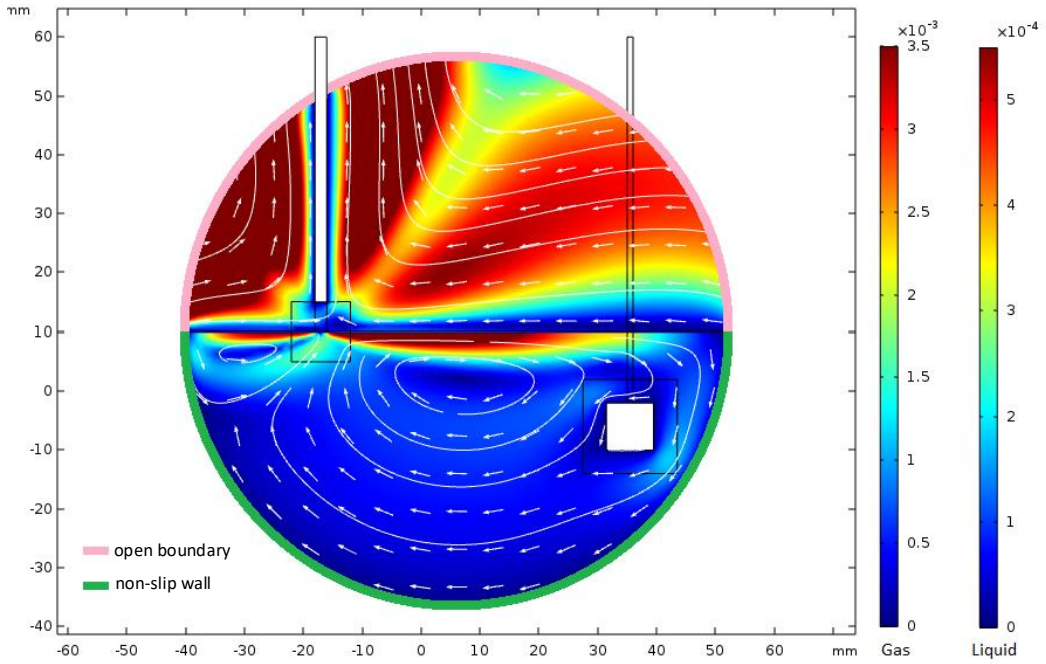

Figure 6.2. Simulated local velocity field (m/s) of the natural convection due to the temperature gradient after 300 s. All the other mechanisms are turned off in the simulation.

6.3.2. Electric Field

The electric field in the system depends on the applied voltage difference and the conductivity of the media. Since the conductivity of the gas phase is several orders of magnitude lower than that of the liquid phase, the electric field is larger in the gas phase (figure 6.3). The electric field affects the local pH profile in three different ways:

The electric force on the ions causes the positively and negatively charged species (OH^- and H^+) to drift opposite the direction of the electric field, with a velocity that depends on the field magnitude and the particle mobility. As ions collide with background molecules, they exert an ionic volume force that induce

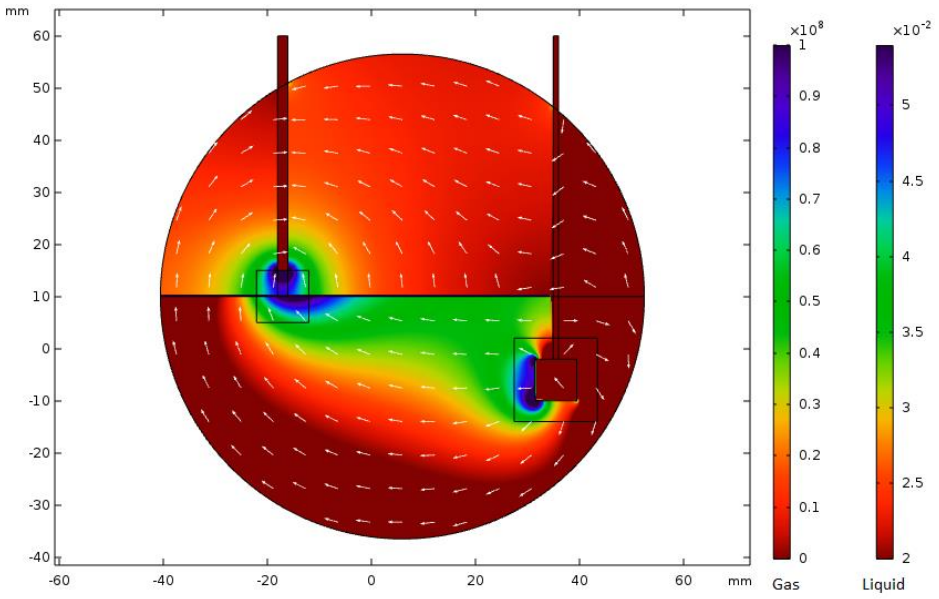

Figure 6.3. The simulated local electric field (V/m) after 300s.

flows in the liquid. This will affect the liquid velocity field which in time will affect the pH profile. The ionic volume force has a higher magnitude in the regions where the ions are present. The direction is towards the high voltage electrode in the basic regions and directed towards the plasma jet in the acidic region. As the OH^- and H^+ ions meet and react, a neutral zone is created where the ionic volume force is minimized. In this study, the velocity field generated by the electric field is less than 10^{-8} m/s, i.e. much smaller than the flows induced by natural convection.

Changes in the local conductivity due to generation/loss of ions (OH^- and H^+) also have the potential to change the electric field distribution and thereby the force acting on ions. These changes, however, are negligible in our case because the liquid conductivity is set by the large concentration of salt ions (K^+ and Cl^-).

6.3.3. Hydrodynamic Effect

It was observed in experiments and in simulations that the gas flow rate plays a major role in the determination of the mixing patterns in the liquid, especially when the gas velocity exceeds 1 m/s. As the input gas velocity was 5 m/s, hydrodynamic effects are important in the system. For velocities higher than

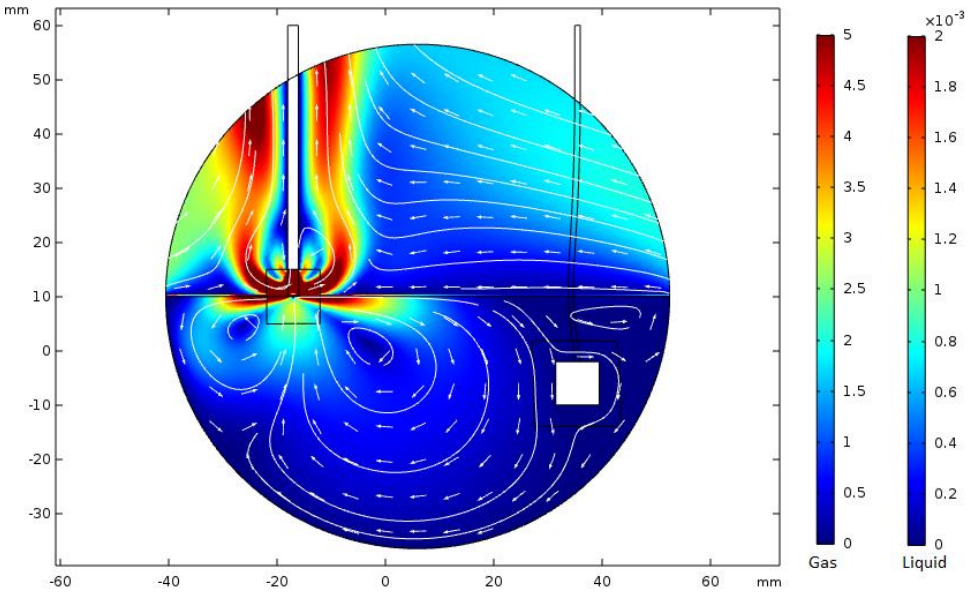

Figure 6.4. Simulation result of the local velocity field (m/s) as a result of the external gas flow after 300 s. Boundary conditions are described in figure 6.2.

10 m/s, the gas causes major surface deformations which complicate the liquid flow [255][256]. As shown in figure 6.4, for a 5 m/s flow, the gas creates an outward pattern on the liquid surface that is similar to the pattern caused by natural convection. In the gas phase, the gas is pulled upwards by the buoyancy force while the liquid flow pattern is mainly dictated by the system geometry.

6.3.4. Local Surface Tension – Marangoni Force

Since the plasma triggers chemical reactions at the plasma-liquid interface, these can lead to changes in the local surface tension that can be attributed to Marangoni forces.

The main factors that affect local surface tension are temperature, the liquid phase composition and the electric field[257]–[261]. A high electric field can cause a surface tension reduction, but this is small, typically < 2% in polar liquids at most [259] and is regarded negligible in this study. Local surface tension variation due to temperature is derived from [261] and accounted for in the simulation. Since the local surface tension decreases with increasing temperature, the surface tension force that results from plasma heating has the same direction as the velocity field caused by the external gas flow and the natural

convection. Simulation results show that the local surface tension decrease does not cause a major variation in the mixing patterns in the liquid and the pH spatiotemporal evolution remains qualitatively the same.

To examine the effect of the local surface tension change on the mixing patterns, PVA was added to the solution. A 1% PVA concentration was used in the experiments. This concentration is below the Critical Micelle Concentration (CMC) of PVA but it reduces the overall surface tension of the solution from 68.03 ± 0.58 mN/m to 45.39 ± 0.65 mN/m. This surface tension value is comparable of that of liquid media and organic solutions encountered in many plasma-liquid applications. Plasma treatment of the solution increases the average surface tension of the liquid to 49.29 ± 0.54 mN/m after 1.5 hours (5400 s) of treatment. This suggests that the local surface tension underneath the plasma is increased compared to that of the rest of the liquid, which would result in flow in the opposite direction to those induced by natural convection.

Introduction of PVA also changes the dynamic viscosity, which increases from 8.9×10^{-4} Pa·s to 1.2×10^{-3} Pa·s. While varying the dynamic viscosity may cause the velocity gradient to change, the direction of the flows would remain the same.

The simulation results show that just changing the surface tension and the dynamic viscosity does not affect the flow patterns and the local pH profile. Moreover, a small increase in the local interface surface tension coefficient underneath the plasma can drastically affect the flow patterns of the liquid phase. An increase in the local surface tension causes a shear force tangent to the liquid surface towards the plasma-liquid interaction point. This force creates a velocity field in the opposite direction of the velocity field created by the gas flow and the natural convection. This is known as the Marangoni effect [262], [263], which in this case reverses the entire liquid phase flow direction and the local pH profile as shown in figures 6.5 and 6.7. Simulation and experimental results qualitatively agree with each other. More information about the plasma-PVA reaction nature is required to further improve the computational model.

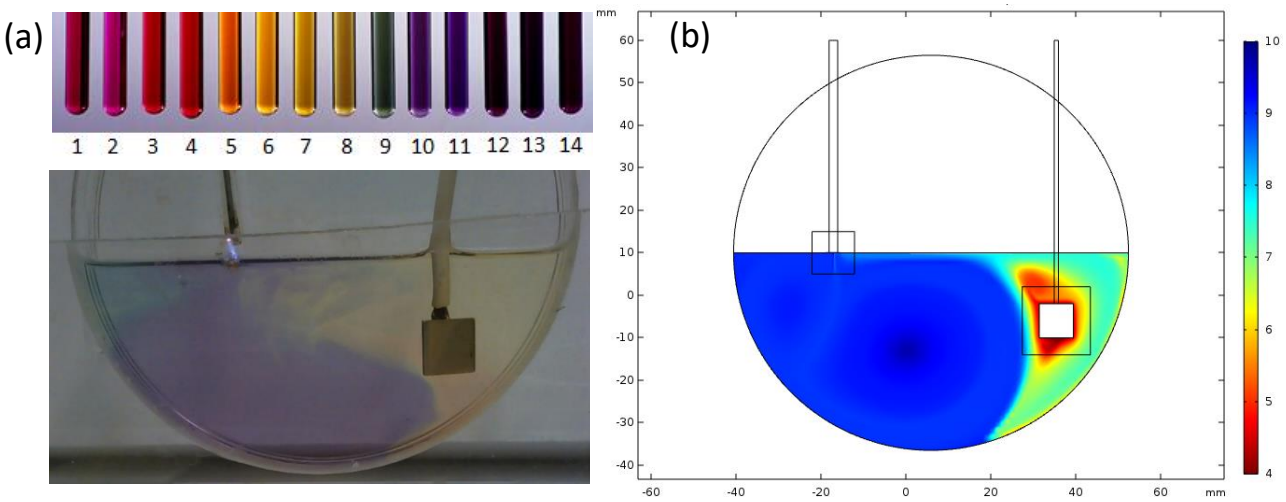

Figure 6.5. (a) Experimental local pH profile after 300s with 1% PVA solution. (b) Simulated pH profile after 300s with 1% PVA.

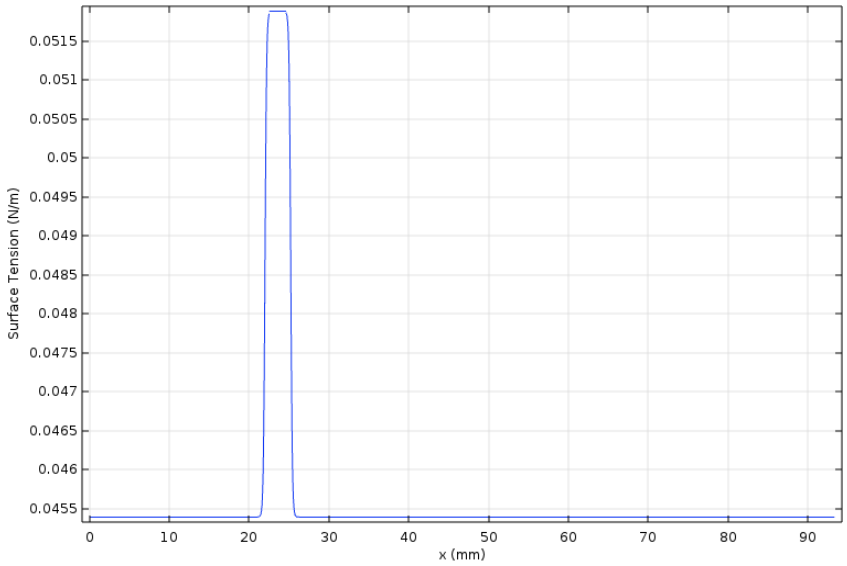

Figure 6.6. Calculated average local surface tension curve of the system with 1% PVA.

Measuring the local surface tension beneath the plasma is not possible using conventional methods, however, a rough estimate can be calculated by comparing simulation and experimental results of the velocity field and the pH profile patterns. The velocity of the Marangoni stream right beneath the plasma region was measured to be 6.49×10^{-3} m/s using PIV. While the absolute value of the local surface tension coefficient plays an important role in the determination of the surface tension shear force and the liquid phase velocity field, other properties such as the gradient around the plasma region and the effective radius

of the plasma on the liquid surface also affect the result. A range of local surface tension curves were applied to the model and the resulting pH profile and velocity field were compared with experimental data. In this way, the local surface tension coefficient was estimated to be 51.9 mN/m in the plasma-liquid interaction region with the actual profile shown in figure 6.6. The obtained curve represents an average local surface tension coefficient value throughout the simulation.

Figure 6.7 (a-I) and (b-I) show the simulated velocity field with figures 6.7 (a-II) and (b-II) showing a 2 mm by 2 mm window of the PIV analysis. This confirms the reversal of the liquid velocity field against the gas flow direction on the liquid surface by Marangoni flows formed beneath the plasma-liquid interaction interface. The induced Marangoni flow not only changes the direction of the flow, but also is greater in magnitude than any other forces. This will cause a better mixing efficiency in the batch reactor as explained in the next section.

6.4. Mixing Efficiency

Marangoni forces are normally neglected in plasma-liquid systems but can have a profound effect on the flow patterns in the liquid, thereby affecting the overall efficiency of the process.

6.4.1. Experimental Analysis

The experimental setup considered in this chapter is often used for formation of nanoparticles. Here, we consider *Ag* nanoparticle formation by introducing 0.1 mM $AgNO_3$ in the solution. The dissolved metal ions can be neutralized by electrons from the plasma by the following half-cell reaction [264]:

$$Ag^+ + e^-{}_{(aq)} \rightarrow Ag_{(s)} \quad (6.1)$$

$AgNO_3$ solutions were treated for 15 minutes with and without PVA (1%) to quantify the effect of the Marangoni flow. The mixing patterns after 5 minutes of treatment are compared in figure 6.8 (a-I) and (b-I).

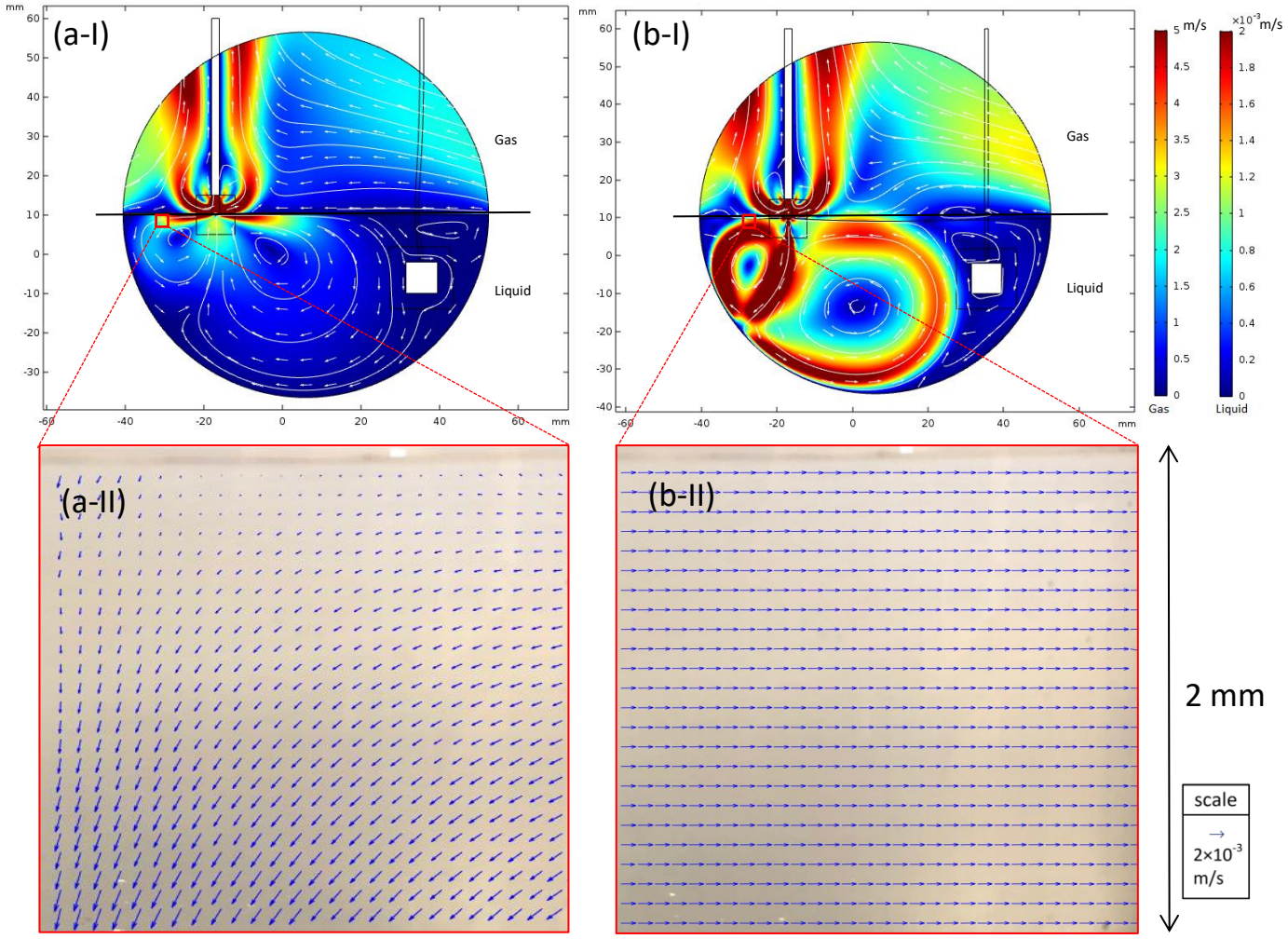

Figure 6.7. (a-I) Simulated velocity field during plasma treatment for de-ionized water-salt and (b-I) for de-ionized water-salt and 1% mass PVA after 300 s. The local velocity direction is reversed, and the magnitude is increased as confirmed by PIV analysis plotted in (a-II) and (b-II).

After the 15-minute treatment, the solutions were left for 24 hours and the precipitated silver was compared as shown in figure (a-II) and (b-II). The measurements show that silver production was increased by ~15 times by the presence of enhanced mixing due to Marangoni forces.

6.4.2. Computational Analysis

The mixing efficiency (Me) of the reactor is defined by equation 6.2 [265]–[267]:

$$Me = 1 - \sqrt{\frac{\sum_0^N (c - c_\infty)^2}{\sum_0^N (c_0 - c_\infty)^2}} \quad (6.2)$$

where c is the concentration of a tracer substance at a specific point and time, c_0 the maximum concentration at the plasma-liquid interaction boundary, c_∞ the homogeneous mixing concentration value and N the number of points on the surface. Since H_2O_2 is often regarded as one of the main air plasma long-lived species transferred to the liquid phase, c is assumed to be the concentration of a tracer substance with similar properties to H_2O_2. The tracer species is initially confined in a 5mm×10mm rectangle beneath the plasma and is assumed not to react with the solution and other chemical products.

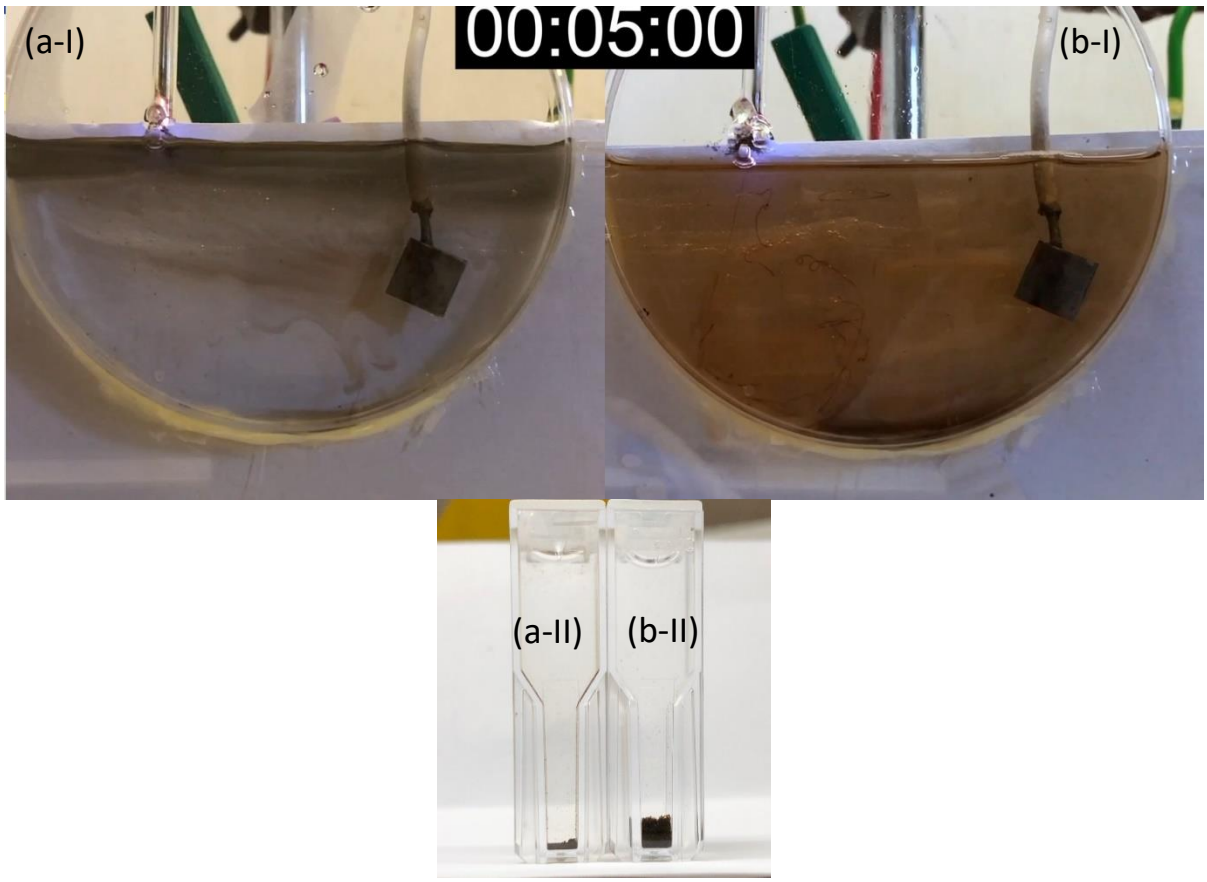

Figure 6.8. Comparing the effect of mixing due to surface tension gradient. (a-I) the mixing pattern of the solution without PVA and (b-I) the mixing pattern of the solution with 1% mass PVA after 5 minutes. Each solution was treated for 15 minutes. (a-II) coagulated silver of the solution without PVA and (b-II) coagulated silver from the solution with 1% PVA after 24 h. By the addition of 1% PVA mass to the solution, the mixing efficiency increases, leading to 15.1 ± 0.08 times more silver production.

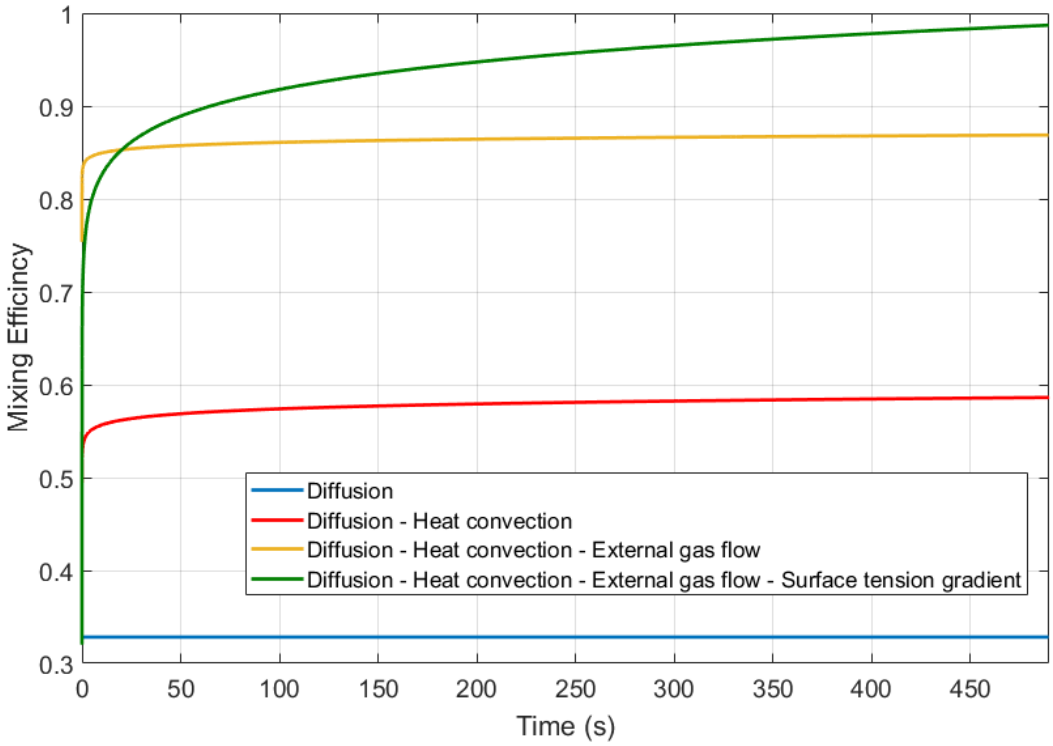

Figure 6.9. Mixing efficiency evolution derived from simulation with different mixing mechanisms: diffusion only while the plasma is turned off, diffusion and heat convection while the plasma is turned on without a gas flow, diffusion, heat convection and external gas flow while the plasma is produced with the gas flowing through the jet, and diffusion, heat convection, external gas flow and surface tension gradient while 1% PVA is added to the system.

The effect of different mechanisms in mixing efficiency is shown in figure 6.9. Mixing efficiency for the solution with 1% PVA is mainly governed by diffusion, heat convection, external gas flow and surface tension gradient when the solution contains PVA. The sheer force on the liquid surface created by the surface tension gradient is in the opposite direction of that of the velocity induced by the gas flow and heat convection. This causes the mixing efficiency to rise slower at the beginning of the mixing process when 1% PVA is added to the solution.

The addition of 1% PVA to the solution increases the mixing efficiency by up to 15% during the treatment period. The time for all the points in the reactor to reach within ±5 % of the homogeneous mixing

concentration is decreased from several hours to 510 s. This is mainly due to the higher reverse velocity field created by the surface tension gradient in the plasma-liquid interaction region.

The change in direction also favours the transport of short-lived reactive species to the bottom of the reactor. This can be relevant, for example, in the context of treating cells at the bottom of a Petri dish through liquid medium. For deep vessels (with a diameter to depth ratio less than one) enhanced mass transfer is favoured in cases where the surface tension is increased by the plasma. Shallow containers (with a diameter to depth ratio more than one) on the other hand, are more suitable when the liquid flow is driven by the gas flow. This mainly ensures that the short-lived species are transferred as rapidly as possible to the liquid instead of being trapped in low-velocity areas such as the reactor walls.

In cases where the external gas flow is not present, e.g. DBD reactors with liquid between the top and bottom electrodes, the reactor efficiency can greatly be improved by the introduction of a similar surfactant and creation of a surface tension gradient on the liquid surface. However; it should be noted that in reactors where the entire surface of the liquid is exposed to the plasma, little room is left for the liquid with lower surface tension to create a surface tension gradient across the surface. This can be improved by leaving unexposed areas on the liquid surface in the reactor design.

The gas flow shear stress tangent to the liquid surface is a competing effect against the surface tension gradient shear force if the liquid local surface tension is increased by the plasma. This suggests that in such cases, minimizing the gas velocity by either reducing the gas flow or increasing the jet inner diameter will result in a better mixture throughout the liquid as fewer conflicting forces are in place. Replacing the gas with a substance with less density where possible, e.g. when the plasma is used as a source of electrons, will result in the liquid velocity field being less influenced by the gas phase, hence enhancing the overall mixing efficiency. In cases where the liquid is not a surfactant, increasing the gas flow increases the mixing efficiency to the point that the velocity field penetration depth covers the entire reactor. Replacing the gas with a heavier gas substance or replacing the surrounding air with the input gas in open atmospheric plasmas

where the input gas is lighter than air and the buoyancy force prevents the gas from touching the liquid completely, will improve the mixing efficiency.

6.5. Summary

Various factors affecting the mass transfer in a plasma jet impinging the liquid surface were investigated experimentally and computationally. It was found that while the external gas phase velocity field and the natural convection due to temperature gradient play a major role in shaping the liquid phase mixing patterns, the surface tension gradient across the liquid surface may completely reverse the liquid phase flow with a higher average velocity hence significantly affecting the mixing efficiency and treatment time. The effect of other factors such as the ionic volume force, the mass diffusion and the ion migration within the electric field on the mixing pattern were found to be several orders of magnitude smaller than the dominant mechanisms.

The findings of this study can be used to improve the mass transfer in non-externally forced plasma-liquid systems. This can be done by changing the reactor design to enhance the local surface tension variation imposed by the plasma, or by modifying the liquid substrate, provided the modification does not affect other chemical reaction mechanisms significantly. As the local surface tension coefficient underneath the plasma cannot be measured by conventional apparatus, the computational model developed in this study can be used to estimate the local surface tension changes caused by plasma treatments.

7. Conclusions

Plasma-liquid interaction was studied with the aid of computational simulations and experimental methods. As a first step, a gas plasma model was studied and the effects of various parameters such as input power modulation and temperature variation on the chemistry of the discharge. An atmospheric pressure air plasma produced in a DBD reactor was used as an example. It was found that for fixed average power and duty-cycle, the on-time duration can have a significant influence on the performance of the DBD reactor. The experimental and computational results showed that shorter on-time pulses lead to enhanced ozone production despite their operation at slightly higher temperature. This is mainly due to more atomic nitrogen being produced in shorter on-times. Atomic nitrogen abandonment leads to more N_2O being produced in the system which, in turn, leads to less NO_2 density in the gas composition. Since NO_2 is the main species quenching atomic oxygen, more atomic oxygen is left to react with the background oxygen resulting in higher ozone production.

The plasma model was then extended to account for delivering neutral reactive species from the plasma active region to the liquid, where chemical reactions took place. An experimental epoxidation setup was used as an example. Here, atomic oxygen produced in the plasma was used to directly react with an alkene in the solution. It was showed that changing the plasma-liquid distance from 45 mm to 10 mm increases *trans*-Stilbene epoxide production from 0.021 mM to 0.145 mM while benzaldehyde production remains the same. This is due to rapid degradation of atomic oxygen compared to ozone. Considering gas phase simulated densities, tube lengths bellow 14 mm massively enhanced *trans*-stilbene production. Another important factor is the inlet gas composition. Oxygen fraction of 1% maximises *trans*-stilbene epoxide production because lower oxygen fractions lead to less atomic oxygen production and higher oxygen percentages result in higher ozone and higher benzaldehyde concentrations. The reaction can be made more selective by using an RF input power due to the increase in atomic oxygen to ozone ratio.

Finally, we undertake the study of a plasma-liquid system in which electrons were used to drive electrochemical processes. The study outlined mass transfer in such systems and the role of different forces

in the resulting flow patterns. It was found that plasma treatment of a 1% PVA solution decreases the surface tension from 68.03 ± 0.58 mN/m to 45.39 ± 0.65 mN/m. This suggests that the local surface tension at the plasma-liquid interface is increased, changing the direction and the velocity of the velocity field induced by the plasma in the liquid phase.

7.1. Key Findings and Knowledge Contribution

The key findings of this study contributing to science, engineering and technology are outlined bellow:

7.1.1. Science

Plasma-driven epoxidation: The main reactions in the liquid phase of the epoxidation process were identified by combining experimental and computational results. Specifically, the reaction rate coefficients were found by comparing simulation results with experimental data.

Atomic O Henry's constant: This value was calculated by adjusting the value in the simulation to match experimental results. Atomic *O* Henry's constant was found to be $7.48 \times 10^{-5} – 9.39 \times 10^{-5}$..

The surface tension spatial evolution: It was shown that the surface tension gradient induced by the plasma on the liquid surface plays a vital role in the determination of the liquid mixing regime. The spatial surface tension evolution was calculated by assuming a spatial variation profile and comparing the resulting mixing patterns and velocity fields in the liquid to that in experiments.

7.1.2. Engineering

Reactor design guidelines: A set of reactor design guidelines were derived from the reactor simulation results. These guidelines were then combined with practical aspects to design a reactor to increase the production yield for epoxidation application.

The importance of surface tension gradient in small-scale plasma-liquid treatment: It was shown that the surface tension gradient can completely change the reactor mixing pattern which in turn could increase

the production rate (e.g. 15.1 ± 0.08 times increase in *Ag* nanoparticle formation). This information can also be used to design a more optimized reactor geometry.

7.1.3. Technology

Modelling methodology: The method used throughout this study to model plasma-liquid interaction overcomes some of the most challenging aspects of plasma-liquid interaction. Coupling a typical CFD model with a plasma simulation configuration arises practical complexities due to temporal and spatial scale differences. The computational methodology selection and the general model structure layout a practical technique to simulate this phenomenon efficiently.

Numerical enhancements: Several sub-procedures and numerical implementation enhancements methods were used throughout this thesis which could pave the way for a more convenient and accurate plasma-liquid interaction modelling.

7.2. Outlook

Advances in plasma-liquid applications are hindered by the complex physio-chemical processes at play. Modelling has been shown to be a promising method to provide new insights into this interaction. Challenges involved in modelling such systems include differences in spatiotemporal scales of plasmas compared to the liquids. Changes in plasma properties typically occur within a few times the Debye length in timescales smaller than milliseconds while meaningful changes in the liquid phase can involve reactor dimensions exceed several centimetres in several hundred seconds. The method introduced in the current thesis resolves this issue by combining a plasma global model with CFD calculations. This method needs to be expanded to provide insights into other plasma-liquid systems, e.g. plasma and aerosols which recently have offered new potential opportunities in a wide range of applications such as nanotechnology, agriculture, medicine, combustion control and cosmetics. Uncertainties in physicochemical plasma-droplet

interactions can be addressed by the methods described within this thesis, opening the plasma community to the scientists from other fields due to the multidisciplinary nature of the problem.

As plasma-liquid applications continue to grow, the lack of information about the process becomes more apparent. More specifically, the physicochemical nature of the interaction between the gas phase short-lived species and the liquid phase has remained unknown. The method used in the current study to estimate atomic oxygen Henry's constant presents a new opportunity to tackle this issue without relying on experimentally challenging and costly direct measurements. The views of this study can be used to develop a rather simple experimental setup, capable of measuring short-lived species Henry's constants when combined with computational modelling analysis.

Epoxidation without a waste stream and costly catalyst material introduced in chapter 5 shows the great potential that lies within plasma epoxidation process. While the reactor design guidelines provided in this chapter layout an insight to the future industrialisation of the process, a step further is to design a continuous-flow reactor which will be more viable in practical industrial scenarios. Extra care must be taken into consideration at this stage as the continuous-flow system may introduce new challenges, e.g. formation of a layer of products and by-products in the vicinity of the submerged electrode which may potentially slow down or stop epoxidation when long retention times is required.

The proposed design presented at the end of chapter 5 not only lays out new opportunities for the processes relying on direct atomic oxygen interaction with the liquid phase, but also pave the way for a new generation of reactors capable of transferring short-lived species from a COST jet into the liquid phase while taking advantage of the enhanced surface of the bubbles. This design can be taken a step further by using surface enhancement methods (e.g. using a microfluidic oscillator before the jet inlet), producing microbubbles in the liquid phase which provide massive improvements in the mass transfer interface over traditional methods.

The results presented in chapter 6 denote that by introducing a surfactant in the liquid phase, mass transfer between the plasma and the liquid can greatly be enhanced. This is due to the Marangoni effect, improving mixing efficiency in the system. The effect of a surfactant in increasing mixing efficiency is particularly of interest in nano-particle production and biological systems. More extensive investigation is required within these applications to take advantage of this effect as a mass-transfer improving mechanism in future reactor designs.

While the studies presented in this thesis are still at their initial stages of development, hopefully, the techniques and the guidelines presented in this work will help readers not only to develop a better understanding of the phenomenon, but also to improve the current engineering applications of plasma-liquid interactions.

Appendix A – Ambipolar Diffusion Coefficient Calculation

quasi-neutrality of the side-walls for single component system:

$$\Gamma_+ = \Gamma_e + \Gamma_-$$

the flux of each ion:

$$\Gamma_i = \pm\mu_i n_i E - D_i \nabla n_i$$

thus:

$$-\mu_+ n_+ E - D_+ \nabla n_+ = \mu_- n_- E - D_- \nabla n_- + \mu_e n_e E - D_e \nabla n_e$$

$$E = \frac{D_+ \nabla n_+ - D_- \nabla n_- - D_e \nabla n_e}{-\mu_{i+} n_+ - \mu_- n_- - \mu_e n_e}$$

hence for the positive ion:

$$\Gamma_+ = -\mu_+ n_+ \left(\frac{-D_+ \nabla n_+ + D_- \nabla n_- + D_e \nabla n_e}{\mu_{i+} n_+ + \mu_- n_- + \mu_e n_e}\right) - D_+ \nabla n_+$$

by assuming

$$\frac{\nabla n_e}{\nabla n_+} = \frac{n_e}{n_+}$$

and

$$\frac{\nabla n_-}{\nabla n_+} = \frac{n_-}{n_+}$$

hence

$$\Gamma_+ = -\mu_+ n_+ \left(\frac{-D_+ + D_- \frac{n_-}{n_+} + D_e \frac{n_e}{n_+}}{\mu_{i+} n_+ + \mu_- n_- + \mu_e n_e}\right) \nabla n_+ - D_+ \nabla n_+$$

$$= \left(-\mu_+ n_+ \left(\frac{-D_+ + D_- \frac{n_-}{n_+} + D_e \frac{n_e}{n_+}}{\mu_{i+} n_+ + \mu_- n_- + \mu_e n_e}\right) - D_+ \right) \nabla n_+$$

since

$$\mu = \frac{T}{D}$$

For a multi-component system:

$$D_{ai} = D_i \left(1 \pm \frac{\sum D_{j-} n_{j-} + D_e n_e - \sum D_{j+} n_{j+}}{\sum D_{j-} n_{j-} + D_e n_e \frac{T_g}{T_e} + \sum D_{j+} n_{j+}}\right)$$

Appendix B – Dry Air Reaction List and Rate Constants

Number	formula	Rate[5]	Ref.
1	e+N_2→N_2D+N+e	K(1)=3.99e-17*engy^2.24*exp(-9.10/ε)	[170]
2	e+N_2→N_2_A3sigma+e	K(2)=LUT[6]_interp(Te)	[187]
3	e+N_2→N_2_B3pi+e	K(3)=LUT_interp(Te)	[187]
4	e+N_2→N_2p+e+e	K(4)=LUT_interp(Te)	[187]
5	e+N→N_2D+e	K(5)=5.06e-15*exp(-10.8/ε^3.95)	[170]
6	e+N→N^++e+e	K(6)=LUT_interp(Te)	[187]
7	e+O_2→O+O+e	K(7)=2.03e-14*ε^-0.10*exp(-8.47/ε)	[170]
8	e+O_2→O_1D+O+e	K(8)=1.82e-14*ε^-0.13*exp(-10.7/ε)	[170]
9	e+O_2→O_2_a1delta+e	K(9)=1.04e-15*exp(-2.59/ε)	[170]
10	e+O_2→O_2p+e+e	K(10)=LUT_interp(Te)	[187]
11	e+O_3→O+O_2+e	K(11)=1.78e-12*ε^-0.614*exp(-11.5/ε)	[170]
12	e+O→O_1D+e	K(12)=7.46e-15*exp(-5.58/ε^1.47)	[170]
13	e+O→Op+e+e	K(13)=LUT_interp(Te)	[187]
14	e+N_2O_5→NO_2^++NO_3+e+e	K(14)=2.43e-17*ε^2.77*exp(-5.62/ε)	[170]
15	e+N^++M→N+M	K(15)=3.12e-35/Te^1.5	[170]
16	e+N_2^+→N+N	K(16)=1.66e-12/Te^0.7	[170]
17	e+N_2^+→N_2D+N	K(17)=1.5e-12/Te^0.7	[170]
18	e+N_2^++M→N_2+M	K(18)=3.12e-35/Te^1.5	[170]
19	e+N3$^+$→N_2+N	K(19)=3.46e-12/Te^0.5	[170]
20	e+N4$^+$→N_2+N_2	K(20)=4.73e-11/Te^0.53	[170]
21	e+O^++M→O+M	K(21)=3.12e-35/Te^1.5	[170]
22	e+O_2^+→O+O	K(22)=1.68e-11/Te^0.7	[170]
23	e+O_2^+→O+O_1D	K(23)=1.24e-11/Te^0.7	[170]
24	e+O_2^++M→O_2+M	K(24)=3.12e-35/Te^1.5	[170]
25	e+O4$^+$→O_2+O_2	K(25)=2.42e-11/Te^0.5	[170]
26	e+N_2O^+→N2+O	K(26)=3.46e-12/Te^0.5	[170]
27	e+NO^+→N+O	K(27)=1.07e-11/Te^0.85	[170]
28	e+NO^+→N_2D+O	K(28)=4.28e-11/Te^0.85	[170]
29	e+NO^++M→NO+M	K(29)=3.12e-35/Te^1.5	[170]
30	e+NO_2^+→NO+O	K(30)=3.46e-12/Te^0.5	[170]
31	e+e+N^+→N+e	K(31)=1e-31*(Tg/Te)^4.5	[170]
32	e+e+N_2^+→N_2+e	K(32)=1e-31*(Tg/Te)^4.5	[170]
33	e+e+O^+→O+e	K(33)=1e-31*(Tg/Te)^4.5	[170]
34	e+e+O_2^+→O_2+e	K(34)=1e-31*(Tg/Te)^4.5	[170]
35	e+e+NO^+→NO+e	K(35)=1e-31*(Tg/Te)^4.5	[170]
36	e+O+O_2→O^-+O_2	K(36)=1e-43	[170]
37	e+O+O_2→O_2^-+O	K(37)=1e-43	[170]
38	e+O_2+O_2→O_2^-+O_2	K(38)=1.4e-41*(Tg/Te)*exp(-600/Tg)*exp(700*(Te-Tg)/(Te*Tg))	[170]
39	e+O_2+N_2→O_2^-+N_2	K(39)=1.1e-43*(Tg/Te)^2*exp(-70/Tg)*exp(1500*(Te-Tg)/(Te*Tg))	[170]
40	e+O_2→O^-+O	K(40)=2.63e-16*ε^-0.495*exp(-5.65/ε)	[170]
41	e+O_2→O_2^-	K(41)=LUT_interp(Te)	[187]
42	e+O_3→O^-+O_2	K(42)=1e-17	[170]
43	e+O_3→O_2^-+O	K(43)=1e-15	[170]
44	e+O_3+M→O_3^-+M	K(44)=1e-43	[170]
45	e+N_2O→On+N_2	K(45)=2e-16	[170]

[5] *cm^3/s, cm^6/s. T_g and T_e are in Kelvins. ε is given in electron volts.*

[6] *Values are interpolated from a look up table created based on collisional cross section data of dry air gas mixture.*

46	$e+NO+M \rightarrow NO^- +M$	K(46)=8e-43	[170]
47	$e+NO_2 \rightarrow O^- +NO$	K(47)=1e-17	[170]
48	$e+NO_2+M \rightarrow NO_2^- +M$	K(48)=1.5e-42	[170]
49	$e+NO_3+M \rightarrow NO_3^- +M$	K(49)=1e-42	[170]
50	$O^- +N \rightarrow NO+e$	K(50)=2.6e-16	[170]
51	$O^- +N_2 \rightarrow N_2O+e$	K(51)=1e-18	[170]
52	$O^- +N_2\_A3sigma \rightarrow N_2+O+e$	K(52)=2.2e-15	[170]
53	$O^- +N_2\_B3pi \rightarrow N_2+O+e$	K(53)=1.9e-15	[170]
54	$O^- +O \rightarrow O_2+e$	K(54)=1.4e-16	[170]
55	$O^- +O_2 \rightarrow O_3+e$	K(55)=1e-18	[170]
56	$O^- +O_2\_a1delta \rightarrow O_3+e$	K(56)=3e-16	[170]
57	$O^- +O_3 \rightarrow O_2+O_2+e$	K(57)=3e-16	[170]
58	$O^- +NO \rightarrow NO_2+e$	K(58)=2.6e-16	[170]
59	$O_2^- +N \rightarrow NO_2+e$	K(59)=5e-16	[170]
60	$O_2^- +N_2 \rightarrow N_2+O_2+e$	K(60)=1.9e-18*(Tg/300)^0.5*exp(-4990/Tg)	[170]
61	$O_2^- +N_2\_A3sigma \rightarrow N_2+O_2+e$	K(61)=2.1e-15	[170]
62	$O_2^- +N_2\_B3pi \rightarrow N_2+O_2+e$	K(62)=2.5e-15	[170]
63	$O_2^- +O \rightarrow O3+e$	K(63)=1.5e-16	[170]
64	$O_2^- +O_2 \rightarrow O_2+O_2+e$	K(64)=2.7e-16*(Tg/300)^0.5*exp(-5590/Tg)	[170]
65	$O_2^- +O_3 \rightarrow O_3+O_2+e$	K(65)=6e-16	[170]
66	$O_2^- +O_2\_a1delta \rightarrow O_2+O_2+e$	K(66)=2e-16	[170]
67	$O_3^- +O \rightarrow O_2+O_2+e$	K(67)=3e-16	[170]
68	$O_3^- +O_2 \rightarrow O_3+O_2+e$	K(68)=2.3e-17	[170]
69	$O_3^- +O3 \rightarrow O_2+O_2+O_2+e$	K(69)=3e-16	[170]
70	$NO^- +M \rightarrow NO+M+e$	K(70)=2.40e-19	[170]
71	$NO^- +NO \rightarrow NO+NO+e$	K(71)=5e-18	[170]
72	$NO^- +N_2O \rightarrow NO+N_2O+e$	K(72)=5.1e-18	[170]
73	$NO_2^- +O \rightarrow NO_3+e$	K(73)=1e-18	[170]
74	$NO_2^- +N \rightarrow N_2+O_2+e$	K(74)=1e-18	[170]
75	$NO_3^- +O \rightarrow NO_2+O_2+e$	K(75)=1e-18	[170]
76	$NO_3^- +N \rightarrow N_2+O_3+e$	K(76)=1e-18	[170]
77	$N^+ +N+M \rightarrow N_2^+ +M$	K(77)=1e-41	[170]
78	$N^+ +N_2+M \rightarrow N_3^+ +M$	K(78)=4.6e-41	[170]
79	$N^+ +N_2O \rightarrow NO^+ +N_2$	K(79)=5.5e-16	[170]
80	$N^+ +NO \rightarrow NO^+ +N$	K(80)=4.72e-16	[170]
81	$N^+ +NO \rightarrow N_2^+ +O$	K(81)=8.33e-17	[170]
82	$N^+ +NO \rightarrow O^+ +N_2$	K(82)=1e-18	[170]
83	$N^+ +NO_2 \rightarrow NO_2^+ +N$	K(83)=3e-16	[170]
84	$N^+ +NO_2 \rightarrow NO^+ +NO$	K(84)=5e-16	[170]
85	$N^+ +O \rightarrow O^+ +N$	K(85)=1e-18	[170]
86	$N^+ +O+M \rightarrow NO^+ +M$	K(86)=1e-41	[170]
87	$N^+ +O_2 \rightarrow NO^+ +O$	K(87)=2.7e-16	[170]
88	$N^+ +O_2 \rightarrow O^+ +NO$	K(88)=2.8e-17	[170]
89	$N^+ +O_2 \rightarrow O_2^+ +N$	K(89)=3e-16	[170]
90	$N^+ +O3 \rightarrow NO^+ +O_2$	K(90)=5e-16	[170]
91	$N_2^+ +N \rightarrow N^+ +N_2$	K(91)=1e-18	[170]
92	$N_2^+ +N+M \rightarrow N_3^+ +M$	K(92)=1e-41*(300/Tg)	[170]
93	$N_2^+ +N_2+M \rightarrow N4^+ +M$	K(93)=1e-41*(300/Tg)	[170]
94	$N_2^+ +N_2\_A3sigma \rightarrow N_3^+ +N$	K(94)=3e-16	[170]
95	$N_2^+ +N_2O \rightarrow N_2O^+ +N_2$	K(95)=6e-16	[170]
96	$N_2^+ +N_2O \rightarrow NO^+ +N+N_2$	K(96)=4e-16	[170]
97	$N_2^+ +NO \rightarrow NO^+ +N_2$	K(97)=3.9e-16	[170]
98	$N_2^+ +NO_2 \rightarrow NO^+ +N_2O$	K(98)=5e-17	[170]

99	$N_2^+ + NO_2 \rightarrow NO_2^+ + N_2$	K(99)=3e-16	[170]
100	$N_2^+ + O \rightarrow NO^+ + N$	K(100)=1.4e-16	[170]
101	$N_2^+ + O \rightarrow NO^+ + N\_2D$	K(101)=1.8e-16*(300/Tg)	[170]
102	$N_2^+ + O \rightarrow O^+ + N_2$	K(102)=1e-17*(300/Tg)^0.5	[170]
103	$N_2^+ + O_2 \rightarrow O_2^+ + N_2$	K(103)=5e-17	[170]
104	$N_2^+ + O_3 \rightarrow O_2^+ + O + N_2$	K(104)=1e-16	[170]
105	$N_3^+ + N \rightarrow N_2^+ + N_2$	K(105)=6.6e-17	[170]
106	$N_3^+ + O_2 \rightarrow O_2^+ + N + N_2$	K(106)=2.3e-17	[170]
107	$N_3^+ + O_2 \rightarrow NO^+ + O + N_2$	K(107)=2e-17	[170]
108	$N_3^+ + O_2 \rightarrow NO_2^+ + N_2$	K(108)=4.4e-17	[170]
109	$N_3^+ + NO \rightarrow NO^+ + N_2 + N$	K(109)=7e-17	[170]
110	$N_3^+ + NO \rightarrow N_2O^+ + N_2$	K(110)=7e-17	[170]
111	$N_3^+ + N_2O \rightarrow NO^+ + N_2 + N_2$	K(111)=5e-17	[170]
112	$N_3^+ + NO_2 \rightarrow NO^+ + NO + N_2$	K(112)=7e-17*(1e6)	[170]
113	$N_3^+ + NO_2 \rightarrow NO_2^+ + N + N_2$	K(113)=7e-17	[170]
114	$N_4^+ + N_2 \rightarrow N_2^+ + N_2 + N_2$	K(114)=2.1e-16*exp(Tg/121)	[170]
115	$N_4^+ + N_2O \rightarrow N_2O^+ + N_2 + N_2$	K(115)=3e-16	[170]
116	$N_4^+ + N \rightarrow N^+ + N_2 + N_2$	K(116)=1e-17	[170]
117	$N_4^+ + NO \rightarrow NO^+ + N_2 + N_2$	K(117)=3.9e-16	[170]
118	$N_4^+ + NO_2 \rightarrow NO_2^+ + N_2 + N_2$	K(118)=2.5e-16	[170]
119	$N_4^+ + NO_2 \rightarrow NO^+ + N_2O + N_2$	K(119)=5e-17	[170]
120	$N_4^+ + O \rightarrow O^+ + N_2 + N_2$	K(120)=2.5e-16	[170]
121	$N_4^+ + O_2 \rightarrow O_2^+ + N_2 + N_2$	K(121)=2.4e-16	[170]
122	$O^+ + N + M \rightarrow NO^+ + M$	K(122)=1e-41	[170]
123	$O^+ + N_2 + M \rightarrow NO^+ + N + M$	K(123)=6e-41*(300/Tg)^2	[170]
124	$O^+ + O + M \rightarrow O_2^+ + M$	K(124)=1e-41	[170]
125	$O^+ + O_2 \rightarrow O_2^+ + O$	K(125)=2.1e-17*(300/Tg)^0.5	[170]
126	$O^+ + O_3 \rightarrow O_2^+ + O2$	K(126)=1e-16	[170]
127	$O^+ + N\_2D \rightarrow N^+ + O$	K(127)=1.3e-16	[170]
128	$O^+ + NO \rightarrow NO^+ + O$	K(128)=1e-18	[170]
129	$O^+ + NO \rightarrow O_2^+ + N$	K(129)=3e-18	[170]
130	$O^+ + N_2O \rightarrow N_2O^+ + O$	K(130)=6.3e-16	[170]
131	$O^+ + N_2O \rightarrow NO^+ + NO$	K(131)=2.3e-16	[170]
132	$O^+ + N_2O \rightarrow O_2^+ + N_2$	K(132)=2e-17	[170]
133	$O^+ + NO_2 \rightarrow NO^+ + O_2$	K(133)=5e-16	[170]
134	$O^+ + NO_2 \rightarrow NO_2^+ + O$	K(134)=1.6e-15	[170]
135	$O_2^+ + O_2 + M \rightarrow O_4^+ + M$	K(135)=5.5e-43*(300/Tg)^2.7	[170]
136	$O_2^+ + N \rightarrow NO^+ + O$	K(136)=1.5e-16	[170]
137	$O_2^+ + N_2 \rightarrow NO^+ + NO$	K(137)=1e-23	[170]
138	$O_2^+ + N_2O_5 \rightarrow NO_2^+ + NO_3 + O_2$	K(138)=8.8e-16	[170]
139	$O_2^+ + NO \rightarrow NO^+ + O_2$	K(139)=4.6e-16	[170]
140	$O_2^+ + NO_2 \rightarrow NO_2^+ + O_2$	K(140)=6.6e-16	[170]
141	$O_2^+ + NO_2 \rightarrow NO^+ + O_3$	K(141)=1e-17	[170]
142	$O_4^+ + O \rightarrow O_2^+ + O_3$	K(142)=3e-16	[170]
143	$O_4^+ + O_2 \rightarrow O_2^+ + O_2 + O_2$	K(143)=3.3e-12*(300/Tg)^4*exp(-5030/Tg)	[170]
144	$O_4p + NO \rightarrow NO^+ + O_2 + O_2$	K(144)=6.80e-16	[170]
145	$O_4p + NO_2 \rightarrow NO_2^+ + O_2 + O_2$	K(145)=3e-16	[170]
146	$O^- + O_2 + M \rightarrow O_3^- + M$	K(146)=1.1e-42*(300/Tg)	[170]
147	$O^- + O_2\_a1delta \rightarrow O_2^- + O$	K(147)=1e-16	[170]
148	$O^- + O_3 \rightarrow O_3^- + O$	K(148)=8e-16	[170]
149	$O^- + N_2O \rightarrow NO^- + NO$	K(149)=2e-16	[170]
150	$O^- + N_2O \rightarrow N_2O^- + O$	K(150)=2e-18	[170]
151	$O^- + NO + M \rightarrow NO_2^- + M$	K(151)=1e-41	[170]

152	$O^-+NO_2 \rightarrow NO_2^-+O$	K(152)=1.2e-15	[170]
153	$O^-+NO_3 \rightarrow NO_3^-+O$	K(153)=3e-16	[170]
154	$O_2^-+O \rightarrow O^-+O_2$	K(154)=3.3e-16	[170]
155	$O_2^-+O_2+M \rightarrow O_4^-+M$	K(155)=3.5e-43*(300/Tg)	[170]
156	$O_2^-+O_3 \rightarrow O_3^-+O_2$	K(156)=3.5e-16	[170]
157	$O_2^-+N_2O \rightarrow O_3^-+N_2$	K(157)=1e-17	[170]
158	$O_2^-+NO_2 \rightarrow NO_2^-+O_2$	K(158)=7e-16	[170]
159	$O_2^-+NO_3 \rightarrow NO_3^-+O_2$	K(159)=5e-16	[170]
160	$O_3^-+O \rightarrow O_2^-+O_2$	K(160)=1e-17	[170]
161	$O_3^-+NO \rightarrow NO_2^-+O_2$	K(161)=1e-17	[170]
162	$O_3^-+NO \rightarrow NO_3^-+O$	K(162)=1e-17	[170]
163	$O_3^-+NO_2 \rightarrow NO_3^-+O_2$	K(163)=2e-17	[170]
164	$O_3^-+NO_2 \rightarrow NO_2^-+O_3$	K(164)=7e-17	[170]
165	$O_3^-+NO_3 \rightarrow NO_3^-+O_3$	K(165)=5e-16	[170]
166	$O_4^-+NO \rightarrow NO_3^-+O_2$	K(166)=2.5e-16	[170]
167	$O_4^-+O \rightarrow O^-+O_2+O_2$	K(167)=3e-16	[170]
168	$O_4^-+O \rightarrow O_3^-+O_2$	K(168)=4e-16	[170]
169	$O_4^-+N_2 \rightarrow O_2^-+O_2+N_2$	K(169)=1e-16*exp(-1044/Tg)	[170]
170	$N_2O^++NO \rightarrow NO^++N_2O$	K(170)=2.3e-16	[170]
171	$N_2O^++N_2O \rightarrow NO^++NO+N_2$	K(171)=1.2e-17	[170]
172	$N_2O^++NO_2 \rightarrow NO^++N_2+O_2$	K(172)=4.29e-16	[170]
173	$N_2O^++NO_2 \rightarrow NO_2^++N_2O$	K(173)=2.21e-16	[170]
174	$N_2O^++O_2 \rightarrow NO^++NO_2$	K(174)=4.59e-17	[170]
175	$N_2O^++O_2 \rightarrow O_2^++N_2O$	K(175)=2.24e-16	[170]
176	$NO^++N_2O_5 \rightarrow NO_2^++NO_2+NO_2$	K(176)=5.9e-16	[170]
177	$NO^++O_3 \rightarrow NO_2^++O_2$	K(177)=1e-21	[170]
178	$NO^++N+M \rightarrow N_2O^++M$	K(178)=1e-41*(300/Tg)	[170]
179	$NO^-+N_2O \rightarrow NO_2^-+N_2$	K(179)=2.8e-20	[170]
180	$NO^-+NO_2 \rightarrow NO_2^-+NO$	K(180)=3e-16	[170]
181	$NO^-+NO_3 \rightarrow NO_3^-+NO$	K(181)=3e-16	[170]
182	$NO^-+O_2 \rightarrow O_2^-+NO$	K(182)=5e-16	[170]
183	$NO^-+O_3 \rightarrow O_3^-+NO$	K(183)=3e-16	[170]
184	$NO^-+O \rightarrow O^-+NO$	K(184)=3e-16	[170]
185	$NO_2^++NO \rightarrow NO^++NO_2$	K(185)=2.75e-16	[170]
186	$NO_2^-+N_2O_5 \rightarrow NO_3^-+NO_3+NO$	K(186)=7e-16	[170]
187	$NO_2^-+NO \rightarrow NO^-+NO_2$	K(187)=2.75e-16	[170]
188	$NO_2^-+NO_2 \rightarrow NO_3^-+NO$	K(188)=4e-18	[170]
189	$NO_2^-+NO_3 \rightarrow NO_3^-+NO_2$	K(189)=5e-16	[170]
190	$NO_2^-+O_3 \rightarrow NO_3^-+O_2$	K(190)=1.8e-17	[170]
191	$NO_2^-+N_2O \rightarrow NO_3^-+N_2$	K(191)=5e-19	[170]
192	$NO_3^-+NO \rightarrow NO_2^-+NO_2$	K(192)=3e-21	[170]
193	$O^++O^- \rightarrow O+O$	K(193)=2e-13*(300/Tg)^0.5	[170]
194	$O^++O_2^- \rightarrow O_2+O$	K(194)=2e-13*(300/Tg)^0.5	[170]
195	$O^++O3^- \rightarrow O3+O$	K(195)=2e-13*(300/Tg)^0.5	[170]
196	$O^++O4^- \rightarrow O2+O2+O$	K(196)=1e-13	[170]
197	$O^++N2O^- \rightarrow N2O+O$	K(197)=2e-13*(300/Tg)^0.5	[170]
198	$O^++NO^- \rightarrow NO+O$	K(198)=2e-13*(300/Tg)^0.5	[170]
199	$O^++NO_2^- \rightarrow NO_2+O$	K(199)=2e-13*(300/Tg)^0.5	[170]
200	$O^++NO_3^- \rightarrow NO_3+O$	K(200)=2e-13*(300/Tg)^0.5	[170]
201	$O_2^++O^- \rightarrow O+O+O$	K(201)=1e-13	[170]
202	$O_2^++O^- \rightarrow O+O_2$	K(202)=2e-13*(300/Tg)^0.5	[170]
203	$O_2^++O_2^- \rightarrow O_2+O_2$	K(203)=2e-13*(300/Tg)^0.5	[170]
204	$O_2^++O_2^- \rightarrow O_2+O+O$	K(204)=1e-13	[170]

205	$O_2^+ + O_3^- \rightarrow O_3 + O_2$	K(205)=2e-13*(300/Tg)^0.5	[170]
206	$O_2^+ + O_3^- \rightarrow O_3 + O + O$	K(206)=1e-13	[170]
207	$O_2^+ + O_4^- \rightarrow O_2 + O_2 + O_2$	K(207)=1e-13	[170]
208	$O_2^+ + N_2O^- \rightarrow N_2O + O_2$	K(208)=2e-13*(300/Tg)^0.5	[170]
209	$O_2^+ + N_2O^- \rightarrow N_2O + O + O$	K(209)=1e-13	[170]
210	$O_2^+ + NO^- \rightarrow NO + O_2$	K(210)=2e-13*(300/Tg)^0.5	[170]
211	$O_2^+ + NO^- \rightarrow NO + O + O$	K(211)=1e-13	[170]
212	$O_2^+ + NO_2^- \rightarrow NO_2 + O_2$	K(212)=2e-13*(300/Tg)^0.5	[170]
213	$O_2^+ + NO_2^- \rightarrow NO_2 + O + O$	K(213)=1e-13	[170]
214	$O_2^+ + NO_3^- \rightarrow NO_3 + O_2$	K(214)=2e-13*(300/Tg)^0.5	[170]
215	$O_2^+ + NO_3^- \rightarrow NO_3 + O + O$	K(215)=1e-13	[170]
216	$O_4^+ + O^- \rightarrow O + O_2 + O_2$	K(216)=1e-13	[170]
217	$O_4^+ + O_2^- \rightarrow O_2 + O_2 + O_2$	K(217)=1e-13	[170]
218	$O_4^+ + O_3^- \rightarrow O_3 + O_2 + O_2$	K(218)=1e-13	[170]
219	$O_4^+ + O_4^- \rightarrow O_2 + O_2 + O_2 + O_2$	K(219)=1e-13	[170]
220	$O_4^+ + N_2O^- \rightarrow N_2O + O_2 + O_2$	K(220)=1e-13	[170]
221	$O_4^+ + NO^- \rightarrow NO + O_2 + O_2$	K(221)=1e-13	[170]
222	$O_4^+ + NO_2^- \rightarrow NO_2 + O_2 + O_2$	K(222)=1e-13	[170]
223	$O_4^+ + NO_3^- \rightarrow NO_3 + O_2 + O_2$	K(223)=1e-13	[170]
224	$N^+ + N_2O^- \rightarrow N_2O + N$	K(224)=2e-13*(300/Tg)^0.5	[170]
225	$N^+ + NO^- \rightarrow NO + N$	K(225)=2e-13*(300/Tg)^0.5	[170]
226	$N^+ + NO_2^- \rightarrow NO_2 + N$	K(226)=2e-13*(300/Tg)^0.5	[170]
227	$N^+ + NO_3^- \rightarrow NO_3 + N$	K(227)=2e-13*(300/Tg)^0.5	[170]
228	$N^+ + O^- \rightarrow O + N$	K(228)=2e-13*(300/Tg)^0.5	[170]
229	$N^+ + O_2^- \rightarrow O_2 + N$	K(229)=2e-13*(300/Tg)^0.5	[170]
230	$N^+ + O_3^- \rightarrow O_3 + N$	K(230)=2e-13*(300/Tg)^0.5	[170]
231	$N^+ + O_4^- \rightarrow O_2 + O_2 + N$	K(231)=1e-13	[170]
232	$N_2^+ + N_2O^- \rightarrow N_2O + N_2$	K(232)=2e-13*(300/Tg)^0.5	[170]
233	$N_2^+ + N_2O^- \rightarrow N_2O + N + N$	K(233)=1e-13	[170]
234	$N_2^+ + NO^- \rightarrow NO + N_2$	K(234)=2e-13*(300/Tg)^0.5	[170]
235	$N_2^+ + NO^- \rightarrow NO + N + N$	K(235)=1e-13	[170]
236	$N_2^+ + NO_2^- \rightarrow NO_2 + N_2$	K(236)=2e-13*(300/Tg)^0.5	[170]
237	$N_2^+ + NO_2n \rightarrow NO_2 + N + N$	K(237)=1e-13	[170]
238	$N_2^+ + NO_3n \rightarrow NO_3 + N_2$	K(238)=2e-13*(300/Tg)^0.5	[170]
239	$N_2^+ + NO_3n \rightarrow NO_3 + N + N$	K(239)=1e-13	[170]
240	$N_2^+ + O^- \rightarrow O + N + N$	K(240)=1e-13	[170]
241	$N_2^+ + O^- \rightarrow O + N_2$	K(241)=2e-13*(300/Tg)^0.5	[170]
242	$N_2^+ + O_2^- \rightarrow O_2 + N + N$	K(242)=1e-13	[170]
243	$N_2^+ + O_2^- \rightarrow O_2 + N_2$	K(243)=2e-13*(300/Tg)^0.5	[170]
244	$N_2^+ + O_3^- \rightarrow O_3 + N + N$	K(244)=1e-13	[170]
245	$N_2^+ + O_3^- \rightarrow O_3 + N_2$	K(245)=2e-13*(300/Tg)^0.5	[170]
246	$N_2^+ + O_4^- \rightarrow O_2 + O_2 + N_2$	K(246)=1e-13	[170]
247	$N_2O^+ + N_2O^- \rightarrow N_2O + N_2O$	K(247)=2e-13*(300/Tg)^0.5	[170]
248	$N_2O^+ + N_2O^- \rightarrow N_2O + N_2 + O$	K(248)=1e-13	[170]
249	$N_2O^+ + NO^- \rightarrow NO + N_2O$	K(249)=2e-13*(300/Tg)^0.5	[170]
250	$N_2O^+ + NO^- \rightarrow NO + N_2 + O$	K(250)=1e-13	[170]
251	$N_2O^+ + NO_2^- \rightarrow NO_2 + N_2O$	K(251)=2e-13*(300/Tg)^0.5	[170]
252	$N_2O^+ + NO_2^- \rightarrow NO_2 + N_2 + O$	K(252)=1e-13	[170]
253	$N_2O^+ + NO_3^- \rightarrow NO_3 + N_2O$	K(253)=2e-13*(300/Tg)^0.5	[170]
254	$N_2O^+ + NO_3^- \rightarrow NO_3 + N_2 + O$	K(254)=1e-13	[170]
255	$N_2O^+ + O^- \rightarrow O + N_2O$	K(255)=2e-13*(300/Tg)^0.5	[170]
256	$N_2O^+ + O^- \rightarrow O + N_2 + O$	K(256)=1e-13	[170]
257	$N_2O^+ + O_2^- \rightarrow O_2 + N_2O$	K(257)=2e-13*(300/Tg)^0.5	[170]

258	$N_2O^+ + O_2^- \rightarrow O_2 + N_2 + O$	K(258)=1e-13	[170]
259	$N_2O^+ + O_3^- \rightarrow O_3 + N_2O$	K(259)=2e-13*(300/Tg)^0.5	[170]
260	$N_2O^+ + O_3^- \rightarrow O_3 + N_2 + O$	K(260)=1e-13	[170]
261	$N_2O^+ + O_4^- \rightarrow O_2 + O_2 + N_2O$	K(261)=1e-13	[170]
262	$N_3^+ + N_2O^- \rightarrow N_2O + N_2 + N$	K(262)=1e-13	[170]
263	$N_3^+ + NO^- \rightarrow NO + N_2 + N$	K(263)=1e-13	[170]
264	$N_3^+ + NO_2^- \rightarrow NO_2 + N_2 + N$	K(264)=1e-13	[170]
265	$N_3^+ + NO_3^- \rightarrow NO_3 + N_2 + N$	K(265)=1e-13	[170]
266	$N_3^+ + O^- \rightarrow O + N_2 + N$	K(266)=1e-13	[170]
267	$N_3^+ + O_2^- \rightarrow O_2 + N_2 + N$	K(267)=1e-13	[170]
268	$N_3^+ + O_3^- \rightarrow O_3 + N_2 + N$	K(268)=1e-13	[170]
269	$N_3^+ + O_4^- \rightarrow O_2 + O_2 + N + N_2$	K(269)=1e-13	[170]
270	$N_4^+ + N_2O^- \rightarrow N_2O + N_2 + N_2$	K(270)=1e-13	[170]
271	$N_4^+ + NO^- \rightarrow NO + N_2 + N_2$	K(271)=1e-13	[170]
272	$N_4^+ + NO_2^- \rightarrow NO_2 + N_2 + N_2$	K(272)=1e-13	[170]
273	$N_4^+ + NO_3^- \rightarrow NO_3 + N_2 + N_2$	K(273)=1e-13	[170]
274	$N_4^+ + O^- \rightarrow O + N_2 + N_2$	K(274)=1e-13	[170]
275	$N_4^+ + O_2^- \rightarrow O_2 + N_2 + N_2$	K(275)=1e-13	[170]
276	$N_4^+ + O_3^- \rightarrow O_3 + N_2 + N_2$	K(276)=1e-13	[170]
277	$N_4^+ + O_4^- \rightarrow O_2 + O_2 + N_2 + N_2$	K(277)=1e-13	[170]
278	$NO^+ + N_2O^- \rightarrow N_2O + NO$	K(278)=2e-13*(300/Tg)^0.5	[170]
279	$NO^+ + N_2O^- \rightarrow N_2O + N + O$	K(279)=1e-13	[170]
280	$NO^+ + NO^- \rightarrow NO + NO$	K(280)=2e-13*(300/Tg)^0.5	[170]
281	$NO^+ + NO^- \rightarrow NO + N + O$	K(281)=1e-13	[170]
282	$NO^+ + NO_2^- \rightarrow NO_2 + NO$	K(282)=2e-13*(300/Tg)^0.5	[170]
283	$NO^+ + NO_2^- \rightarrow NO_2 + N + O$	K(283)=1e-13	[170]
284	$NO^+ + NO_3^- \rightarrow NO_3 + NO$	K(284)=2e-13*(300/Tg)^0.5	[170]
285	$NO^+ + NO_3^- \rightarrow NO_3 + N + O$	K(285)=1e-13	[170]
286	$NO^+ + O^- \rightarrow O + N + O$	K(286)=1e-13	[170]
287	$NO^+ + O^- \rightarrow O + NO$	K(287)=2e-13*(300/Tg)^0.5	[170]
288	$NO^+ + O2^- \rightarrow O_2 + N + O$	K(288)=1e-13	[170]
289	$NO^+ + O2^- \rightarrow O_2 + NO$	K(289)=2e-13*(300/Tg)^0.5	[170]
290	$NO^+ + O3^- \rightarrow O_3 + N + O$	K(290)=1e-13	[170]
291	$NO^+ + O_3^- \rightarrow O_3 + NO$	K(291)=2e-13*(300/Tg)^0.5	[170]
292	$NO^+ + O_4^- \rightarrow O_2 + O2 + NO$	K(292)=1e-13	[170]
293	$NO_2^+ + N_2O^- \rightarrow N_2O + NO_2$	K(293)=2e-13*(300/Tg)^0.5	[170]
294	$NO_2^+ + N_2O^- \rightarrow N_2O + N + O_2$	K(294)=1e-13	[170]
295	$NO_2^+ + NO^- \rightarrow NO + NO_2$	K(295)=2e-13*(300/Tg)^0.5	[170]
296	$NO_2^+ + NO^- \rightarrow NO + N + O_2$	K(296)=1e-13	[170]
297	$NO_2^+ + NO2^- \rightarrow NO2 + NO_2$	K(297)=2e-13*(300/Tg)^0.5	[170]
298	$NO_2^+ + NO2^- \rightarrow NO2 + N + O_2$	K(298)=1e-13	[170]
299	$NO_2^+ + NO_3^- \rightarrow NO3 + NO_2$	K(299)=2e-13*(300/Tg)^0.5	[170]
300	$NO_2^+ + NO_3^- \rightarrow NO_3 + N + O_2$	K(300)=1e-13	[170]
301	$NO_2^+ + O^- \rightarrow O + NO_2$	K(301)=2e-13*(300/Tg)^0.5	[170]
302	$NO_2^+ + O^- \rightarrow O + N + O_2$	K(302)=1e-13	[170]
303	$NO_2^+ + O_2^- \rightarrow O_2 + NO_2$	K(303)=2e-13*(300/Tg)^0.5	[170]
304	$NO_2^+ + O2^- \rightarrow O_2 + N + O_2$	K(304)=1e-13	[170]
305	$NO_2^+ + O_3^- \rightarrow O_3 + NO_2$	K(305)=2e-13*(300/Tg)^0.5	[170]
306	$NO_2^+ + O_3^- \rightarrow O_3 + N + O_2$	K(306)=1e-13	[170]
307	$NO_2^+ + O_4^- \rightarrow O_2 + O_2 + NO_2$	K(307)=1e-13	[170]
308	$N + N + M \rightarrow N_2 + M$	K(308)=8.3e-46*exp(500/Tg)	[170]
309	$N + NO \rightarrow N_2 + O$	K(309)=2.1e-17*exp(100/Tg)	[170]
310	$N + NO_2 \rightarrow N_2O + O$	K(310)=5.8e-18*exp(220/Tg)	[170]

311	$N+NO_2 \rightarrow N_2+O+O$	K(311)=9.1e-19	[170]
312	$N+NO_2 \rightarrow NO+NO$	K(312)=6e-19	[170]
313	$N+NO_2 \rightarrow N_2+O_2$	K(313)=7e-19	[170]
314	$N+O+M \rightarrow NO+M$	K(314)=6.3e-45*exp(140/Tg)	[170]
315	$N+O_2 \rightarrow NO+O$	K(315)=1.5e-17*exp(-3600/Tg)	[170]
316	$N+O_3 \rightarrow NO+O_2$	K(316)=5e-22	[170]
317	$N\_2D+N_2 \rightarrow N+N_2$	K(317)=5e-18*exp(-1620/Tg)	[170]
318	$N\_2D+N_2O \rightarrow N_2+NO$	K(318)=1.5e-17*exp(-570/Tg)	[170]
319	$N\_2D+NO \rightarrow N_2O$	K(319)=6e-17	[170]
320	$N\_2D+NO \rightarrow O+N_2$	K(320)=4.5e-17	[170]
321	$N\_2D+O \rightarrow N+O$	K(321)=7e-19	[170]
322	N_2D+O2→NO+O	K(322)=1.5e-18*(Tg/300)^0.5	[170]
323	N_2D+O2→NO+O_1D	K(323)=6e-18*(Tg/300)^0.5	[170]
324	$N_2\_A3sigma+N_2 \rightarrow N_2+N_2$	K(324)=2.2e-20	[170]
325	$N_2\_A3sigma+N_2\_A3sigma \rightarrow N_2\_B3pi+N_2$	K(325)=4e-16	[170]
326	$N_2\_A3sigma+N_2O \rightarrow O+N_2+N_2$	K(326)=8e-17	[170]
327	$N_2\_A3sigma+N_2O \rightarrow NO+N+N_2$	K(327)=8e-17	[170]
328	$N_2\_A3sigma+NO_2 \rightarrow N_2+NO+O$	K(328)=1.3e-17	[170]
329	$N_2\_A3sigma+O_2 \rightarrow N_2+O+O$	K(329)=5e-18*exp(-210/Tg)	[170]
330	$N_2\_A3sigma+O_2 \rightarrow O_2\_a1delta+N_2$	K(330)=1e-18	[170]
331	$N_2\_A3sigma+N \rightarrow N+N_2$	K(331)=5e-17	[170]
332	$N_2\_A3sigma+O \rightarrow NO+N\_2D$	K(332)=7e-18	[170]
333	$N_2\_A3sigma+O \rightarrow O\_1D+N_2$	K(333)=2.3e-17	[170]
334	$N_2\_B3pi+N_2 \rightarrow N_2\_A3sigma+N_2$	K(334)=5e-17	[170]
335	$N_2\_B3pi+NO \rightarrow N_2\_A3sigma+NO$	K(335)=2.4e-16	[170]
336	$N_2\_B3pi+O2 \rightarrow N_2+O+O$	K(336)=3e-16	[170]
337	$O+O+M \rightarrow O_2+M$	K(337)=3.2e-47*exp(900/Tg)	[170]
338	$O+O_2+M \rightarrow O_3+M$	K(338)=3.4e-46*(300/Tg)^1.2	[170]
339	$O+O_3 \rightarrow O_2+O_2$	K(339)=8e-18*exp(-2060/Tg)	[170]
340	$O+NO+M \rightarrow NO_2+M$	K(340)=1e-43*(300/Tg)^1.6	[170]
341	$O+NO_2 \rightarrow NO+O_2$	K(341)=6.5e-18*exp(120/Tg)	[170]
342	$O+NO_2+M \rightarrow NO_3+M$	K(342)=9e-44*(300/Tg)^2	[170]
343	$O+NO_3 \rightarrow O_2+NO_2$	K(343)=1.7e-17	[170]
344	$O\_1D+O_2 \rightarrow O+O_2$	K(344)=6.4e-18*exp(67/Tg)	[170]
345	$O\_1D+O \rightarrow O+O$	K(345)=8e-18	[170]
346	$O\_1D+O_2\_a1delta \rightarrow O+O_2$	K(346)=1e-17	[170]
347	$O\_1D+O_2 \rightarrow O+O_2\_a1delta$	K(347)=1e-18	[170]
348	$O\_1D+O_3 \rightarrow O+O+O_2$	K(348)=1.2e-16	[170]
349	$O\_1D+O_3 \rightarrow O_2+O_2$	K(349)=1.2e-16	[170]
350	$O\_1D+N_2 \rightarrow O+N_2$	K(350)=1.8e-17*exp(107/Tg)	[170]
351	$O\_1D+N_2+M \rightarrow N_2O+M$	K(351)=9e-49	[170]
352	$O\_1D+N_2O \rightarrow N_2+O_2$	K(352)=4.4e-17	[170]
353	$O\_1D+N_2O \rightarrow NO+NO$	K(353)=7.2e-17	[170]
354	$O\_1D+NO \rightarrow O+NO$	K(354)=4e-17	[170]
355	$O\_1D+NO_2 \rightarrow NO+O_2$	K(355)=1.4e-16	[170]
356	$O_2\_a1delta+O_2 \rightarrow O_2+O_2$	K(356)=3.8e-24*exp(-205/Tg)	[170]
357	$O_2\_a1delta+O_3 \rightarrow O+O_2+O_2$	K(357)=5.2e-17*exp(-2840/Tg)	[170]
358	$O_2\_a1delta+M \rightarrow O_2+M$	K(358)=8e-27	[170]
359	$O_2\_a1delta+NO \rightarrow O_2+NO$	K(359)=2.5e-17	[170]
360	$O_2\_a1delta+N2 \rightarrow O_2+N_2$	K(360)=1.5e-24	[170]
361	$O_3+NO \rightarrow NO_2+O_2$	K(361)=1.8e-18*exp(-1370/Tg)	[170]
362	$O_3+NO_2 \rightarrow NO_3+O_2$	K(362)=1.4e-19*exp(-2470/Tg)	[170]
363	$O_3+M \rightarrow O+O_2+M$	K(363)=3.92e-16*exp(-11400/Tg)	[170]

364	$NO+NO_2+M \rightarrow N_2O_3+M$	K(364)=3.09e-46*(300/Tg)^7.7	[170]
365	$NO+NO_3 \rightarrow NO_2+NO_2$	K(365)=1.8e-17*exp(110/Tg)	[170]
366	$NO_2+NO_2+M \rightarrow N_2O_4+M$	K(366)=1.17e-45*(300/Tg)^3.8	[170]
367	$NO_2+NO_3+M \rightarrow N_2O_5+M$	K(367)=2.8e-42*(300/Tg)^3.5	[170]
368	$NO_2+NO_3 \rightarrow NO_2+NO+O_2$	K(368)=2.3e-19*exp(-1600/Tg)	[170]
369	$NO_3+NO_3 \rightarrow NO_2+NO_2+O_2$	K(369)=5e-18*exp(-3000/Tg)	[170]
370	$N_2O_3+M \rightarrow NO+NO_2+M$	K(370)=1.03e-16*exp(-2628/Tg)	[170]
371	$N_2O_4+M \rightarrow NO_2+NO_2+M$	K(371)=1.09e-13*exp(-4952/Tg)	[170]
372	$N_2O_5+M \rightarrow NO_2+NO_3+M$	K(372)=1e-9*(300/Tg)^3.5*exp(-11000/Tg)	[170]
373	$e+N_2 \rightarrow e+N_2$	K(373)=LUT_interp(Te)	[187]
374	$e+O_2 \rightarrow e+O_2$	K(374)=LUT_interp(Te)	[187]
375	$NO+e \rightarrow NOp+e+e$	K(375)=LUT_interp(Te)	[187]

Appendix C – He-O_2 Reaction List and Rate Constants

Number	formula	Rate	Ref.
1	$e+O_2 \rightarrow 2O+e$	LUT_interp(Te)	[187]
2	$e+O_2 \rightarrow O1D+O+e$	LUT_interp(Te)	[187]
3	$e+O_2 \rightarrow O2a+e$	LUT_interp(Te)	[187]
4	$e+O_2 \rightarrow O_2^+ +2e$	LUT_interp(Te)	[187]
5	$e+O_3 \rightarrow O+O_2+e$	LUT_interp(Te)	[187]
6	$e+O \rightarrow O1D+e$	LUT_interp(Te)	[187]
7	$e+O \rightarrow O^{++}+2e$	LUT_interp(Te)	[187]
8	$e+O^+ +M \rightarrow O+M$	3.12e-35/Te^1.5	[94]
9	$e+O_2+ \rightarrow 2O$	1.68e-11/Te^0.7	[94]
10	$e+O_2+ \rightarrow O+O1D$	1.24e-11/Te^0.7	[94]
11	$e+O_2^+ +M \rightarrow O_2+M$	3.12e-35/Te^1.5	[94]
12	$e+O_4^+ \rightarrow 2O_2$	2.42e-11/Te^0.5	[94]
13	$2e+O^+ \rightarrow O+e$	1e-31*(Tg/Te)^4.5	[94]
14	$2e+O_2^+ \rightarrow O_2+e$	1e-31*(Tg/Te)^4.5	[94]
15	$e+O+O_2 \rightarrow O-+O_2$	1e-43	[94]
16	$e+O+O_2 \rightarrow O_2^- +O$	1e-43	[94]
17	$e+2O_2 \rightarrow O_2^- +O_2$	1.4e-41*Tg/Te*exp(-600/Tg)*exp(700*(Te-Tg)/(Te*Tg))	[94]
18	$e+O_2+N_2 \rightarrow O_2^- +N_2$	1.1e-43*(Tg/Te)^2*exp(-70/Tg)*exp(1500*(Te-Tg)/(Te*Tg))	[94]
19	$e+O_2 \rightarrow O^- +O$	LUT_interp(Te)	[94] [94]
20	$e+O_2 \rightarrow O_2^-$	LUT_interp(Te)	[94]
21	$e+O_3 \rightarrow O^- +O_2$	1e-17	[94]
22	$e+O_3 \rightarrow O_2^- +O$	1e-15	[94]
23	$e+O_3+M \rightarrow O_3^- +M$	1e-43	[94]
24	$O^- +O \rightarrow O_2+e$	1.4e-16	[94]
25	$O^- +O_2 \rightarrow O_3+e$	1e-18	[94]
26	$O^- +O_2a \rightarrow O_3+e$	3e-16	[94]
27	$O-+O_3 \rightarrow 2O_2+e$	3e-16	[94]
28	$O_2^- +O \rightarrow O_3+e$	1.5e-16	[94]
29	$O_2^- +O_2 \rightarrow 2O_2+e$	2.7e-16*(Tg/300)^0.5*exp(-5590/Tg)	[94]
30	$O_2^- +O_3 \rightarrow O_3+O_2+e$	6e-16	[94]
31	$O_2^- +O_2a \rightarrow 2O_2+e$	2e-16	[94]
32	$O_3^- +O \rightarrow 2O_2+e$	3e-16	[94]
33	$O_3^- +O_2 \rightarrow O_3+O_2+e$	2.3e-17	[94]
34	$O_3^- +O_3 \rightarrow 3O_2+e$	3e-16	[94]
35	$O^+ +O+M \rightarrow O_2^+ +M$	1e-41	[94]
36	$O^+ +O_2 \rightarrow O_2^+ +O$	2.1e-17*(300/Tg)^0.5	[94]
37	$O^+ +O_3 \rightarrow O_2^+ +O_2$	1e-16	[94]
38	$O_2^+ +O_2+M \rightarrow O_4^+ +M$	5.5e-43*(300/Tg)^2.7	[94]
39	$O_4^+ +O \rightarrow O_2^+ +O_3$	3e-16	[94]
40	$O_4^+ +O_2 \rightarrow O_2^+ +2O_2$	3.3e-12*(300/Tg)^4*exp(-5030/Tg)	[94]
41	$O^- +O_2+M \rightarrow O_3^- +M$	1.1e-42*(300/Tg)	[94]
42	$O^- +O_2a \rightarrow O_2^- +O$	1e-16	[94]
43	$O^- +O_3 \rightarrow O_3^- +O$	8e-16	[94]
44	$O_2^- +O \rightarrow O^- +O_2$	3.3e-16	[94]
45	$O_2^- +O_2+M \rightarrow O_4^- +M$	3.5e-43*(300/Tg)	[94]
46	$O_3^- +O \rightarrow O_2^- +O_2$	1e-17	[94]
47	$O_4^- +O \rightarrow O^- +2O_2$	3e-16	[94]

48	$O_4^-+O \rightarrow O_3^-+O_2$	4e-16	[94]
49	$O^++O^- \rightarrow 2O$	2E-13*(300/Tg)^0.5	[94]
50	$O^++O_2^- \rightarrow O_2+O$	2E-13*(300/Tg)^0.5	[94]
51	$O^++O_3^- \rightarrow O_3+O$	2E-13*(300/Tg)^0.5	[94]
52	$O^++O_4^- \rightarrow 2O_2+O$	1E-13	[94]
53	$O_2^++O^- \rightarrow 3O$	1E-13	[94]
54	$O_2^++O^- \rightarrow O+O_2$	2E-13*(300/Tg)^0.5	[94]
55	$O_2^++O_2^- \rightarrow 2O_2$	2E-13*(300/Tg)^0.5	[94]
56	$O_2^++O_2^- \rightarrow O_2+2O$	1E-13	[94]
57	$O_2^++O_3^- \rightarrow O_3+O_2$	2E-13*(300/Tg)^0.5	[94]
58	$O_2^++O3^- \rightarrow O_3+2O$	1E-13	[94]
59	$O_2^++O_4^- \rightarrow 3O_2$	1E-13	[94]
60	$O_4^++O^- \rightarrow O+2O_2$	1E-13	[94]
61	$O_4^++O_2^- \rightarrow 3O_2$	1E-13	[94]
62	$O_4^++O_3^- \rightarrow O_3+2O_2$	1E-13	[94]
63	$O_4^++O_4^- \rightarrow 4O_2$	1E-13	[94]
64	$O+O+M \rightarrow O_2+M$	3.2E-47*exp(900/Tg)	[94]
65	$O+O_2+M \rightarrow O_3+M$	3.4E-46*(300/Tg)^1.2	[94]
66	$O+O_3 \rightarrow 2O_2$	8E-18*exp(-2060/Tg)	[94]
67	$O1D+O_2 \rightarrow O+O_2$	6.4E-18*exp(67/Tg)	[94]
68	$O1D+O \rightarrow 2O$	8E-18	[94]
69	$O1D+O_2a \rightarrow O+O_2$	1E-17	[94]
70	$O1D+O_2 \rightarrow O+O_2a$	1E-18	[94]
71	$O1D+O_3 \rightarrow 2O+O_2$	1.2E-16	[94]
72	$O1D+O_3 \rightarrow 2O2$	1.2E-16	[94]
73	$O2a+O2 \rightarrow 2O2$	3.8E-24*exp(-205/Tg)	[94]
74	$O2a+O3 \rightarrow O+2O2$	5.2E-17*exp(-2840/Tg)	[94]
75	$O2a+M \rightarrow O2+M$	8E-27	[94]
76	$O3+M \rightarrow O+O2+M$	3.92E-16*exp(-11400/Tg)	[94]
77	$O+O+M \rightarrow O2+M$	3.2E-47*exp(900/Tg)	[94]
78	$O+O_2+M \rightarrow O3+M$	3.4E-46*(300/Tg)^1.2	[94]
79	$O+O_3 \rightarrow 2O_2$	8E-18*exp(-2060/Tg)	[94]
80	$O1D+O_2 \rightarrow O+O_2$	6.4E-18*exp(67/Tg)	[94]
81	$e+He \rightarrow e+He$	LUT_interp(Te)	[94]
82	$e+He \rightarrow 2e+He^+$	1.5e-15*Te^0.68*exp(-24.6/Te)	[94]
83	$e+Hem \rightarrow 2e+He^+$	1.28e-13*Te^0.6*exp(-4.78/Tg)	[94]
84	$e+He_2m \rightarrow He_2^++2e$	9.75e-16*Te^0.71*exp(-3.4/Te)	[94]
85	$e+He \rightarrow Hem+e$	LUT_interp(Te)	[94]
86	$e+Hem \rightarrow He+e$	7e-16*(Te/300)^0.5	[94]
87	$e+He_2m \rightarrow e+2He$	3.8e-15	[94]
88	$He^++e \rightarrow He$	2e-18	[94]
89	$e+He+ \rightarrow Hem$	6.76e-19*Te^-0.5	[94]
90	$2e+He^+ \rightarrow Hem+e$	7.8e-50*(Te/Tg)^-4.4	[94]
91	$2e+He^+ \rightarrow He+e$	7e-32*(Te/Tg)^-4.5	[94]
92	$e+He^++He \rightarrow Hem+He$	1e-39	[94]
93	$He_2^++e \rightarrow 2He$	1e-14	[94]
94	$He_2^++e \rightarrow He_2m$	1.5e-22	[94]
95	$e+He_2^+ \rightarrow Hem+He$	8.9e-21*(Te/Tg)^-1.5	[94]
96	$He_2^++e+e \rightarrow 2He+e$	7e-42*(Te/Tg)^-4.5	[94]
97	$2e+He_2+ \rightarrow Hem+He+e$	2.8e-42	[94]
98	$He_2++He+e \rightarrow 3He$	2e-39*(Te/Tg)^-2.5	[94]
99	$e+He_2^++He \rightarrow Hem+2He$	3.5e-39	[94]

100	$e+He_{2+}+He \rightarrow He_2m+He$	1.5e-39	[94]
101	$He^+ + O^- \rightarrow He+O$	2e-15*(Tg/300)^-0.5	[94]
102	$He^+ + O_2^- \rightarrow He+O_2$	2e-15*(Tg/300)^-0.5	[94]
103	$He^+ + O_3^- \rightarrow He+O_3$	2e-15*(Tg/300)^-0.5	[94]
104	$He^+ + O_2^- \rightarrow He+O+O$	1e-15	[94]
105	$He^+ + O_3^- \rightarrow He+O_2+O$	1e-15	[94]
106	$He^+ + O_4^- \rightarrow He+O_2+O_2$	1e-15	[94]
107	$He2^+ + O^- \rightarrow 2He+O$	1e-15	[94]
108	$He_2^+ + O_2^- \rightarrow 2He+O_2$	1e-15	[94]
109	$He_2^+ + O_3^- \rightarrow 2He+O_3$	1e-15	[94]
110	$He_2^+ + O_2^- \rightarrow 2He+O+O$	1e-15	[94]
111	$He_2^+ + O_3^- \rightarrow 2He+O_2+O$	1e-15	[94]
112	$He_2^+ + O_4^- \rightarrow 2He+O_2+O_2$	1e-15	[94]
113	$He^+ + O \rightarrow He+O^+$	5e-17*(Tg/300)^0.5	[94]
114	$He^+ + O1D \rightarrow He+O^+$	5e-17*(Tg/300)^0.5	[94]
115	$He^+ + O2 \rightarrow He+O2^+$	3.3e-17*(Tg/300)^0.5	[94]
116	$He^+ + O2 \rightarrow He+O+O^+$	1.07e-15*(Tg/300)^0.5	[94]
117	$He^+ + O2a \rightarrow He+O2+$	3.3e-17*(Tg/300)^0.5	[94]
118	$He^+ + O2a \rightarrow He+O+O^+$	1.07e-15*(Tg/300)^0.5	[94]
119	$He^+ + O3 \rightarrow He+O2+O^+$	1.07e-15*(Tg/300)^0.5	[94]
120	$He_2^+ + O \rightarrow 2He+O^+$	1e-15*(Tg/300)^0.5	[94]
121	$He_2^+ + O1D \rightarrow 2He+O^+$	1e-15*(Tg/300)^0.5	[94]
122	$He_2^+ + O_2 \rightarrow 2He+O_2^+$	1e-15*(Tg/300)^0.5	[94]
123	$He_2^+ + O_2a \rightarrow 2He+O_2^+$	1e-15*(Tg/300)^0.5	[94]
124	$He_2^+ + O_2 \rightarrow 2He+O+O^+$	1.05e-15	[94]
125	$He_2^+ + O_3 \rightarrow 2He+O_2+O^+$	1e-15*(Tg/300)^0.5	[94]
126	$He+Hem \rightarrow 2He$	5.8e-21	[94]
127	$He+He_2m \rightarrow 3He$	4.9e-22	[94]
128	$He+O1D \rightarrow He+O$	1e-19	[94]
129	$He+O_2a \rightarrow He+O_2$	8e-27*(Tg/300)^0.5	[94]
130	$M+He_2m \rightarrow 2He+M$	1.5e-21	[94]
131	$He+O- \rightarrow He+O+e$	2.5e-24*(Tg/300)^0.6	[94]
132	$He+O2- \rightarrow He+O2+e$	3.9e-16*exp(-7400/Tg)	[94]
133	$O3-+He \rightarrow He+O2+O+e$	3e-16	[94]
134	$Hem+O- \rightarrow He+O+e$	3e-16	[94]
135	$O_2^- + Hem \rightarrow He+O_2+e$	3e-16	[94]
136	$O_3^- + Hem \rightarrow He+O_3+e$	3e-16	[94]
137	$O_4^- + Hem \rightarrow He+O_2+O_2+e$	3e-16	[94]
138	$He_2m+O- \rightarrow 2He+O+e$	3e-16	[94]
139	$O_2^- + He_2m \rightarrow 2He+O_2+e$	3e-16	[94]
140	$O_3^- + He_2m \rightarrow 2He+O_3+e$	3e-16	[94]
141	$O_4^- + He_2m \rightarrow 2He+O_2+O_2+e$	3e-16	[94]
142	$2Hem \rightarrow He^+ + He+e$	8.7e-16*(Tg/300)^0.5	[94]
143	$2Hem \rightarrow He_2^+ + e$	2.03e-15*(Tg/300)^0.5	[94]
144	$Hem+He_2m \rightarrow He^+ + 2He+e$	5e-16	[94]
145	$Hem+He_2m \rightarrow He2^+ + He+e$	2e-15	[94]
146	$2He_2m \rightarrow He++3He+e$	3e-16	[94]
147	$2He_2m \rightarrow He_2^+ + 2He+e$	1.2e-15	[94]
148	$Hem+O \rightarrow He+O^+ + e$	3.96e-16*(Tg/300)^0.17	[94]
149	$Hem+O1D \rightarrow He+O^+ + e$	3.96e-16*(Tg/300)^0.17	[94]
150	$Hem+O2 \rightarrow He+O2++e$	2.54e-16*(Tg/300)^0.5	[94]
151	$Hem+O_3 \rightarrow He+O_2^+ + O+e$	2.6e-16	[94]
152	$He_2m+O \rightarrow 2He+O^+ + e$	3.6e-16	[94]

153	$He_2m+O1D \rightarrow 2He+O^+ +e$	3.6e-16	[94]
154	$He_2m+O_2 \rightarrow 2He+O_2 ++e$	3.6e-16	[94]
155	$He_2m+O_3 \rightarrow 2He+O_2^+ +O+e$	3.6e-16	[94]
156	$He+O_3 \rightarrow He+O+O_2$	1.56e-15*exp(-11140/Tg)	[94]
157	$Hem+He_2^+ \rightarrow He^+ +2He$	1e-16	[94]
158	$O_2^+ +Hem \rightarrow He+O+O^+$	1e-16	[94]
159	$O_4^+ +Hem \rightarrow He+O_2+O_2^+$	1e-16	[94]
160	$O_2^+ +He2m \rightarrow 2He+O+O^+$	1e-16	[94]
161	$O_4^+ +He_2m \rightarrow 2He+O_2^+ +O_2$	1e-16	[94]
162	$He_2^+ +2e \rightarrow He_2m+e$	1.2e-33	[94]
163	$e+O^+ +He \rightarrow O+He$	6.45e-43*(Te/Tg)^-2.5	[94]
164	$e+O+He \rightarrow O^- +He$	1e-43	[94]
165	$e+O_2 ++He \rightarrow O2+He$	3.12e-35*(Te/Tg)^-1.5	[94]
166	$e+O_2+He \rightarrow O_2^- +He$	1e-43	[94]
167	$e+O_3+He \rightarrow O_3^- +He$	1e-43	[94]
168	$He^+ +2He \rightarrow He_2^+ +He$	1.4e-43*(Tg/300)^-0.6	[94]
169	$He+O^- +O_2 \rightarrow He+O_3^-$	1.1e-42*(Tg/300)^-1	[94]
170	$He+O_2^- +O_2 \rightarrow He+O_4^-$	3.5e-43*(Tg/300)^-1	[94]
171	$He+O^+ +O \rightarrow O_2^+ +He$	1e-41*(Tg/300)^0.5	[94]
172	$He+O_2^+ +O_2 \rightarrow O_4^+ +He$	3.9e-42*(Tg/300)^-3.2	[94]
173	$He+2O \rightarrow O_2+He$	1.3e-44*(Tg/300)^-1*exp(-170/Tg)	[94]
174	$He+O+O_2 \rightarrow O_3+He$	3.4e-46*(Tg/300)^-1.2	[94]
175	$He+2O \rightarrow O_2a+He$	9.88e-47	[94]
176	$Hem+2He \rightarrow He_2m+He$	1.5e-46	[94]

References

[1] A. Fridman, *Plasma Chemistry*. Cambridge: Cambridge University Press, 2008.

[2] B. M. Smirnov, *Physics of Ionized Gases*. Weinheim, Germany: Wiley-VCH Verlag GmbH, 2001.

[3] A. von Keudell and V. Schulz-von der Gathen, “Foundations of low-temperature plasma physics—an introduction,” *Plasma Sources Sci. Technol.*, vol. 26, no. 11, p. 113001, 2017.

[4] S. Gopikishan, I. Banerjee, and S. K. Mahapatra, “Influence of magnetic field on plasma parameters and thin film deposition along axial and radial distances in DC magnetron,” in *arXiv:1704.06503 [physics.plasm-ph]*, 2017, pp. 1–8.

[5] F. Iza, J. K. Lee, and M. G. Kong, “Electron kinetics in radio-frequency atmospheric-pressure microplasmas,” *Phys. Rev. Lett.*, vol. 99, no. 7, pp. 2–5, 2007.

[6] P. J. Bruggeman, F. Iza, and R. Brandenburg, “Foundations of atmospheric pressure non-equilibrium plasmas,” *Plasma Sources Science and Technology*, vol. 26, no. 12. p. 123002, 23-Nov-2017.

[7] M. A. Lieberman and A. J. Lichtenberg, *Principles of Plasma Discharges and Materials Processing*. Hoboken, NJ, USA: John Wiley & Sons, Inc., 2005.

[8] A. Hickling and M. D. Ingram, “Contact glow-discharge electrolysis,” *Trans. Faraday Soc.*, vol. 60, pp. 783–793, 1964.

[9] P. J. Bruggeman *et al.*, “Plasma–liquid interactions: a review and roadmap,” *Plasma Sources Sci. Technol.*, vol. 25, no. 5, p. 053002, 2016.

[10] P. Bruggeman and C. Leys, “Non-thermal plasmas in and in contact with liquids,” *J. Phys. D. Appl. Phys.*, vol. 42, no. 5, p. 053001, Mar. 2009.

[11] M. T. Elford, “The Ratio DT/μ for Electrons in Water Vapour at 294 K,” *J. Phys.*, vol. 48, no. 37, pp. 427–437, 1995.

[12] R. N. Barnett, R. Giniger, O. Cheshnovsky, and U. Landman, “Dielectron attachment and hydrogen evolution reaction in water clusters,” *J. Phys. Chem. A*, vol. 115, no. 25, pp. 7378–7391, 2011.

[13] M. Magureanu, C. Bradu, and V. I. Parvulescu, “Plasma processes for the treatment of water contaminated with harmful organic compounds,” *J. Phys. D. Appl. Phys.*, vol. 51, no. 31, p. 313002, Aug. 2018.

[14] J. E. Foster, “Plasma-based water purification: Challenges and prospects for the future,” *Phys. Plasmas*, vol. 24, no. 5, p. 055501, May 2017.

[15] M. Sato, “IJPEST_Vol3_No1_02_pp008-014,” *Int. J. Plasma Environ. Sci. Technol.*, vol. 3, no. 1, pp. 8–14, 2009.

[16] S. Ikawa, A. Tani, Y. Nakashima, and K. Kitano, “Physicochemical properties of bactericidal plasma-treated water,” *J. Phys. D. Appl. Phys.*, vol. 49, no. 42, p. 425401, 2016.

[17] A. M. Hirst, F. M. Frame, M. Arya, N. J. Maitland, and D. O’Connell, “Low temperature plasmas as emerging cancer therapeutics: the state of play and thoughts for the future,” *Tumor Biol.*, vol. 37, no. 6, pp. 7021–7031, 2016.

[18] M. Ishaq, M. Evans, and K. Ostrikov, “Effect of atmospheric gas plasmas on cancer cell signaling,” *Int. J. Cancer*, vol. 134, no. 7, pp. 1517–1528, 2014.

[19] S. Mashayekh, H. Rajaee, M. Akhlaghi, B. Shokri, and Z. M. Hassan, “Atmospheric-pressure plasma jet characterization and applications on melanoma cancer treatment (B/16-F10),” *Phys. Plasmas*, vol. 22, no. 9, p. 093508, Sep. 2015.

[20] D. Yan *et al.*, “Principles of using Cold Atmospheric Plasma Stimulated Media for Cancer Treatment,” *Sci. Rep.*, vol. 5, no. June, pp. 1–17, 2015.

[21] Z. Chen, L. Lin, X. Cheng, E. Gjika, and M. Keidar, “Treatment of gastric cancer cells with nonthermal atmospheric plasma generated in water,” *Biointerphases*, vol. 11, no. 3, p. 031010, 2016.

[22] D. Xu *et al.*, “Cold atmospheric plasma as a potential tool for multiple myeloma treatment,” *Oncotarget*, vol. 9, no. 26, pp. 18002–18017, 2018.

[23] H. J. Ahn *et al.*, “Targeting Cancer Cells with Reactive Oxygen and Nitrogen Species Generated by Atmospheric-Pressure Air Plasma,” *PLoS One*, vol. 9, no. 1, p. e86173, Jan. 2014.

[24] S. Ikawa, K. Kitano, and S. Hamaguchi, “Effects of pH on Bacterial Inactivation in Aqueous Solutions due to Low-Temperature Atmospheric Pressure Plasma Application,” *Plasma Process. Polym.*, vol. 7, no. 1, pp. 33–42, Jan. 2010.

[25] A. M. Hirst, F. M. Frame, N. J. Maitland, and D. O’Connell, “Low Temperature Plasma: A Novel Focal Therapy for Localized Prostate Cancer?,” *Biomed Res. Int.*, vol. 2014, no. March, pp. 1–15, 2014.

[26] D. Yan, J. H. Sherman, and M. Keidar, “Cold atmospheric plasma, a novel promising anti-cancer treatment modality,” *Oncotarget*, vol. 8, no. 9, pp. 15977–15995, 2017.

[27] P. L. Shao, J. Der Liao, T. W. Wong, Y. C. Wang, S. Leu, and H. K. Yip, “Enhancement of

wound healing by non-thermal N2/Ar micro-plasma exposure in mice with fractional-CO2-laser-induced wounds," *PLoS One*, vol. 11, no. 6, pp. 1–15, 2016.

[28] Fridman, "Investigation on the effects of the atmospheric pressure plasma on wound healing in diabetic rats.," *Sci. Rep.*, vol. 6, p. 19144, 2016.

[29] N. Y. Babaeva, N. Ning, D. B. Graves, and M. J. Kushner, "Ion activation energy delivered to wounds by atmospheric pressure dielectric-barrier discharges: sputtering of lipid-like surfaces," *J. Phys. D. Appl. Phys.*, vol. 45, no. 11, p. 115203, Mar. 2012.

[30] G. Fridman *et al.*, "Blood coagulation and living tissue sterilization by floating-electrode dielectric barrier discharge in air," *Plasma Chem. Plasma Process.*, vol. 26, no. 4, pp. 425–442, 2006.

[31] M. G. Kong *et al.*, "Plasma medicine: an introductory review," *New J. Phys.*, vol. 11, no. 11, p. 115012, Nov. 2009.

[32] K. McKay, D. X. Liu, F. Iza, M. Z. Rong, and M. G. Kong, "Double-layer structures in low-temperature atmospheric-pressure electronegative RF microplasmas: Separation of electrons and anions," *IEEE Trans. Plasma Sci.*, vol. 39, no. 11 PART 1, pp. 2138–2139, 2011.

[33] K. R. Stalder, D. F. McMillen, and J. Woloszko, "Electrosurgical plasmas," *J. Phys. D. Appl. Phys.*, vol. 38, no. 11, pp. 1728–1738, 2005.

[34] G. Fridman, G. Friedman, A. Gutsol, A. B. Shekhter, V. N. Vasilets, and A. Fridman, "Applied plasma medicine," *Plasma Process. Polym.*, vol. 5, no. 6, pp. 503–533, 2008.

[35] M. Witzke, P. Rumbach, D. B. Go, and R. M. Sankaran, "Evidence for the electrolysis of water by atmospheric-pressure plasmas formed at the surface of aqueous solutions," *J.*

Phys. D. Appl. Phys., vol. 45, no. 44, p. 442001, Nov. 2012.

[36] C. Richmonds *et al.*, “Electron-transfer reactions at the plasma-liquid interface,” *J. Am. Chem. Soc.*, vol. 133, no. 44, pp. 17582–17585, 2011.

[37] A. R. Denaro and A. Hickling, “Glow-Discharge Electrolysis in Aqueous Solutions,” *J. Electrochem. Soc.*, vol. 105, no. 5, p. 265, 1958.

[38] Q. Chen, J. Li, and Y. Li, “A review of plasma–liquid interactions for nanomaterial synthesis,” *J. Phys. D. Appl. Phys.*, vol. 48, no. 42, p. 424005, Oct. 2015.

[39] C. Richmonds and R. M. Sankaran, “Plasma-liquid electrochemistry: Rapid synthesis of colloidal metal nanoparticles by microplasma reduction of aqueous cations,” *Appl. Phys. Lett.*, vol. 93, no. 13, pp. 91–94, 2008.

[40] Q. Chen, T. Kaneko, and R. Hatakeyama, “Reductants in gold nanoparticle synthesis using gas-liquid interfacial discharge plasmas,” *Appl. Phys. Express*, vol. 5, no. 8, pp. 10–12, 2012.

[41] D. Mariotti, J. Patel, V. Švrček, and P. Maguire, “Plasma-liquid interactions at atmospheric pressure for nanomaterials synthesis and surface engineering,” *Plasma Process. Polym.*, vol. 9, no. 11–12, pp. 1074–1085, 2012.

[42] L. Sivachandiran and A. Khacef, “Enhanced seed germination and plant growth by atmospheric pressure cold air plasma: combined effect of seed and water treatment,” *RSC Adv.*, vol. 7, no. 4, pp. 1822–1832, 2017.

[43] R. Zhou *et al.*, “Effects of Atmospheric-Pressure N2, He, Air, and O2 Microplasmas on Mung Bean Seed Germination and Seedling Growth,” *Sci. Rep.*, vol. 6, no. 1, p. 32603, 2016.

[44] X. Zhang *et al.*, “Atmospheric cold plasma jet for plant disease treatment,” *Appl. Phys. Lett.*, vol. 104, no. 4, p. 043702, Jan. 2014.

[45] M. R. Webb and G. M. Hieftje, “Spectrochemical analysis by using discharge devices with solution electrodes,” *Anal. Chem.*, vol. 81, no. 3, pp. 862–867, 2009.

[46] J. F. Bruch, O. Guilbaud, and C. Bor, “Mise en correspondance de l’hystéroscopie et de l’anatomo-cyto- pathologie endométriale: Vers une nouvelle sémiologie dynamique endoscopique et microscopique»,” *Reprod. Hum. Horm.*, vol. 20, no. 3, pp. 133–138, 2014.

[47] Z. C. Liu *et al.*, “Physicochemical processes in the indirect interaction between surface air plasma and deionized water,” *J. Phys. D. Appl. Phys.*, vol. 48, no. 49, p. 495201, 2015.

[48] M. S. Simeni, A. Roettgen, V. Petrishchev, K. Frederickson, and I. V Adamovich, “Electron density and electron temperature measurements in nanosecond pulse discharges over liquid water surface,” *Plasma Sources Sci. Technol.*, vol. 25, no. 6, p. 064005, 2016.

[49] A. D. Lindsay, D. B. Graves, and S. C. Shannon, “Fully coupled simulation of the plasma liquid interface and interfacial coefficient effects,” *J. Phys. D. Appl. Phys.*, vol. 49, no. 23, p. 235204, Jun. 2016.

[50] K. Niemi, T. Gans, and D. O’Connell, “Comparison of a global model to semi-kinetic fluid simulations for atmospheric pressure radio-frequency plasmas,” *Plasma Sources Sci. Technol.*, vol. 22, no. 3, p. 032001, May 2013.

[51] T. Hemke *et al.*, “Ionization by bulk heating of electrons in capacitive radio frequency atmospheric pressure microplasmas,” *Plasma Sources Sci. Technol.*, vol. 22, no. 1, p.

015012, Dec. 2012.

[52] H. W. Lee, G. Y. Park, Y. S. Seo, Y. H. Im, S. B. Shim, and H. J. Lee, “Modelling of atmospheric pressure plasmas for biomedical applications,” *J. Phys. D. Appl. Phys.*, vol. 44, no. 5, p. 053001, Feb. 2011.

[53] K. Niemi *et al.*, “Absolute atomic oxygen and nitrogen densities in radio-frequency driven atmospheric pressure cold plasmas: Synchrotron vacuum ultra-violet high-resolution Fourier-transform absorption measurements,” *Appl. Phys. Lett.*, vol. 103, no. 3, pp. 1–5, 2013.

[54] K. Niemi *et al.*, “Diagnostic based modelling of radio-frequency driven atmospheric pressure plasmas,” *J. Phys. D. Appl. Phys.*, vol. 43, no. 12, p. 124006, Mar. 2010.

[55] W. Benstâali and A. Belasri, “Comparison of particle in cell and fluid models in plasma display panels simulation,” *EPJ Web Conf.*, vol. 44, p. 04006, Mar. 2013.

[56] A. Bogaerts, “Plasma Modeling I : Modeling of Plasmas,” in *20th International School on “Low Temperature Plasma Physics,”* 2016, pp. 1–36.

[57] E. Havlıcková, “Fluid model of plasma and computational methods for solution,” *WDS’06 Proc. Contrib. Pap. Part III*, no. 4, pp. 180–186, 2006.

[58] a J. Lichtenberg, I. G. Kouznetsov, Y. T. Lee, M. a Lieberman, I. D. Kaganovich, and L. D. Tsendin, “Modelling plasma discharges at high electronegativity,” *Plasma Sources Sci. Technol.*, vol. 6, no. 3, pp. 437–449, 1999.

[59] G. J. M. Hagelaar and L. C. Pitchford, “Solving the Boltzmann equation to obtain electron transport coefficients and rate coefficients for fluid models,” *Plasma Sources Sci. Technol.*, vol. 14, no. 14, pp. 722–733, 2005.

[60] Z. L. P. Toshiaki Makabe, *Plasma Electronics: Applications in Microelectronic Device Fabrication*. Taylor & Francis Group, 2016.

[61] L. Wang, A. H. Hakim, A. Bhattacharjee, and K. Germaschewski, “Comparison of multi-fluid moment models with particle-in-cell simulations of collisionless magnetic reconnection,” *Phys. Plasmas*, vol. 22, no. 1, pp. 1–15, 2015.

[62] A. K. Gain, W. W. Immerzeel, F. C. Sperna Weiland, and M. F. P. Bierkens, “Impact of climate change on the stream flow of the lower Brahmaputra: trends in high and low flows based on discharge-weighted ensemble modelling,” *Hydrol. Earth Syst. Sci.*, vol. 15, no. 5, pp. 1537–1545, May 2011.

[63] G. Chen and L. L. Raja, “Fluid modeling of electron heating in low-pressure, high-frequency capacitively coupled plasma discharges,” *J. Appl. Phys.*, vol. 96, no. 11, pp. 6073–6081, 2004.

[64] J.-P. Boeuf, Y. Lagmich, T. Callegari, L. Pitchford, and T. Unfer, “New Insights in the Physics of DBD Plasma Actuators for Flow Control,” in *46th AIAA Aerospace Sciences Meeting and Exhibit*, 2008, pp. 18–46.

[65] G. E. Georghiou, A. P. Papadakis, R. Morrow, and A. C. Metaxas, “Numerical modelling of atmospheric pressure gas discharges leading to plasma production,” *J. Phys. D. Appl. Phys.*, vol. 38, no. 20, pp. R303–R328, Oct. 2005.

[66] Y. J. Hong, M. Yoon, F. Iza, G. C. Kim, and J. K. Lee, “Comparison of fluid and particle-in-cell simulations on atmospheric pressure helium microdischarges,” *J. Phys. D. Appl. Phys.*, vol. 41, no. 24, p. 245208, Dec. 2008.

[67] H. C. Kim, F. Iza, S. S. Yang, M. Radmilović-Radjenović, and J. K. Lee, “Particle and fluid

simulations of low-temperature plasma discharges: benchmarks and kinetic effects," *J. Phys. D. Appl. Phys.*, vol. 38, no. 19, pp. R283–R301, Oct. 2005.

[68] F. Iza, S. H. Lee, and J. K. Lee, "Computer modeling of low-temperature plasmas," *Gas Discharges - Fundam. Appl.*, vol. 661, no. 2, pp. 1–31, 2007.

[69] S. H. Lee, F. Iza, and J. K. Lee, "Particle-in-cell Monte Carlo and fluid simulations of argon-oxygen plasma: Comparisons with experiments and validations," *Phys. Plasmas*, vol. 13, no. 5, p. 057102, May 2006.

[70] E. Kemaneci, E. Carbone, J.-P. Booth, W. Graef, J. van Dijk, and G. Kroesen, "Global (volume-averaged) model of inductively coupled chlorine plasma: Influence of Cl wall recombination and external heating on continuous and pulse-modulated plasmas," *Plasma Sources Sci. Technol.*, vol. 23, no. 4, p. 045002, 2014.

[71] D. X. Liu *et al.*, "Aqueous reactive species induced by a surface air discharge: Heterogeneous mass transfer and liquid chemistry pathways," *Sci. Rep.*, vol. 6, no. December 2015, p. 23737, 2016.

[72] W. Van Gaens and A. Bogaerts, "Kinetic modelling for an atmospheric pressure argon plasma jet in humid air," *J. Phys. D. Appl. Phys.*, vol. 46, no. 27, p. 275201, Jul. 2013.

[73] S. Kim, M. A. Lieberman, A. J. Lichtenberg, and J. T. Gudmundsson, "Improved volume-averaged model for steady and pulsed-power electronegative discharges," *J. Vac. Sci. Technol. A Vacuum, Surfaces, Film.*, vol. 24, no. 6, pp. 2025–2040, Nov. 2006.

[74] D. D. Monahan and M. M. Turner, "Global models of electronegative discharges: critical evaluation and practical recommendations," *Plasma Sources Sci. Technol.*, vol. 17, no. 4, p. 045003, 2008.

[75] J. J. Munro and J. Tennyson, “Global plasma simulations using dynamically generated chemical models,” *J. Vac. Sci. Technol. A Vacuum, Surfaces, Film.*, vol. 26, no. 4, pp. 865–869, Jul. 2008.

[76] R. Dorai and M. J. Kushner, “A model for plasma modification of polypropylene using atmospheric pressure discharges,” *J. Phys. D. Appl. Phys.*, vol. 36, no. 6, pp. 666–685, Mar. 2003.

[77] D. S. Stafford and M. J. Kushner, “O2(1Δ) production in He/O2mixtures in flowing low pressure plasmas,” *J. Appl. Phys.*, vol. 96, no. 5, pp. 2451–2465, 2004.

[78] S. Lopez-Lopez, J. J. Munro, D. Brown, and J. Tennyson, “Simulations of SF<inf>6</inf> plasma etching in the GEC Reference Cell,” in *2011 Semiconductor Conference Dresden*, 2011, no. June 2015, pp. 1–3.

[79] L. C. P. S. Pancheshnyi, B. Eismann, G. J. M. Hagelaar, “Computer code ZDPlasKin,” 2008. [Online]. Available: https://www.zdplaskin.laplace.univ-tlse.fr/. [Accessed: 16-Oct-2018].

[80] A. H. Markosyan, A. Luque, F. J. Gordillo-Vázquez, and U. Ebert, “PumpKin: A tool to find principal pathways in plasma chemical models,” *Comput. Phys. Commun.*, vol. 185, no. 10, pp. 2697–2702, 2014.

[81] M. Jimenez-Diaz, E. A. D. Carbone, J. van Dijk, and J. J. A. M. van der Mullen, “A two-dimensional Plasimo multiphysics model for the plasma–electromagnetic interaction in surface wave discharges: the surfatron source,” *J. Phys. D. Appl. Phys.*, vol. 45, no. 33, p. 335204, Aug. 2012.

[82] P. Roger W. Pryor, *Multiphysics Modeling Using COMSOL®: A First Principles Approach*.

Jones and Bartlett Publishers, LLC, 2009.

[83] V. Vahedi and M. Surendra, “A Monte Carlo collision model for the particle-in-cell method: applications to argon and oxygen discharges,” *Comput. Phys. Commun.*, vol. 87, no. 1–2, pp. 179–198, 1995.

[84] G. J. Kim, F. Iza, and J. K. Lee, “Field emission and lifetime of microcavity plasma,” *Phys. Plasmas*, vol. 16, no. 1, p. 013502, Jan. 2009.

[85] V. A. Godyak and R. B. Piejak, “Abnormally low electron energy and heating-mode transition in a low-pressure argon rf discharge at 13.56 MHz,” *Phys. Rev. Lett.*, vol. 65, no. 8, pp. 996–999, 1990.

[86] H. C. Kim, O. Manuilenko, and J. K. Lee, “Particle-in-cell Monte-Carlo simulation of capacitive RF discharges: Comparison with experimental data,” *Japanese J. Appl. Physics, Part 1 Regul. Pap. Short Notes Rev. Pap.*, vol. 44, no. 4 A, pp. 1957–1958, 2005.

[87] M. Surendra and D. B. Graves, “Particle Simulations of Radio-Frequency Glow Discharges,” *IEEE Trans. Plasma Sci.*, vol. 19, no. 2, pp. 144–157, 1991.

[88] W. Jiang, H. Wang, Z. Bi, and Y. Wang, “Implicit and electrostatic particle-in-cell/Monte Carlo model in two-dimensional and axisymmetric geometry: II. Self-bias voltage effects in capacitively coupled plasmas,” *Plasma Sources Sci. Technol.*, vol. 20, no. 3, p. 035013, Jun. 2011.

[89] T. J. Sommerer and M. J. Kushner, “Numerical investigation of the kinetics and chemistry of rf glow discharge plasmas sustained in He, N2, O2, He/N2/O2, He/CF4/O2, and SiH4/NH3using a Monte Carlo-fluid hybrid model,” *J. Appl. Phys.*, vol. 71, no. 4, pp.

1654–1673, 1992.

[90] S. Fatemi, A. R. Poppe, G. T. Delory, and W. M. Farrell, “AMITIS: A 3D GPU-Based Hybrid-PIC Model for Space and Plasma Physics,” *J. Phys. Conf. Ser.*, vol. 837, no. 1, pp. 0–27, 2017.

[91] F. Iza, J. L. Walsh, and M. G. Kong, “From submicrosecond- to nanosecond-pulsed atmospheric-pressure plasmas,” *IEEE Trans. Plasma Sci.*, vol. 37, no. 7 PART 2, pp. 1289–1296, 2009.

[92] R. K. Porteous and D. B. Graves, “Modeling and Simulation of Magnetically Confined Low-Pressure Plasmas in Two Dimensions,” *IEEE Trans. Plasma Sci.*, vol. 19, no. 2, pp. 204–213, 1991.

[93] A. S. Lipatov, *The Hybrid Multiscale Simulation Technology: An Introduction with Application to Astrophysical and Laboratory Plasmas*. Springer Science & Business Media, 2002.

[94] D. X. Liu, M. Z. Rong, X. H. Wang, F. Iza, M. G. Kong, and P. Bruggeman, “Main species and physicochemical processes in cold atmospheric-pressure He + O2 Plasmas,” *Plasma Process. Polym.*, vol. 7, no. 9–10, pp. 846–865, 2010.

[95] A. V Marenich, C. J. Cramer, and D. G. Truhlar, “Universal Solvation Model Based on Solute Electron Density and on a Continuum Model of the Solvent Defined by the Bulk Dielectric Constant and Atomic Surface Tensions Aleksandr,” *J. Phys. Chem. B*, vol. 113, no. 18, pp. 6378–6396, 2009.

[96] P. Rumbach, D. M. Bartels, R. M. Sankaran, and D. B. Go, “The effect of air on solvated electron chemistry at a plasma/liquid interface,” *J. Phys. D. Appl. Phys.*, vol. 48, no. 42, p.

424001, Oct. 2015.

[97] P. Rumbach, D. M. Bartels, R. M. Sankaran, and D. B. Go, “The solvation of electrons by an atmospheric-pressure plasma,” *Nat. Commun.*, vol. 6, no. 1, p. 7248, Nov. 2015.

[98] S. A. Norberg, W. Tian, E. Johnsen, and M. J. Kushner, “Atmospheric pressure plasma jets interacting with liquid covered tissue: touching and not-touching the liquid,” *J. Phys. D. Appl. Phys.*, vol. 47, no. 47, p. 475203, 2014.

[99] W. Tian and M. J. Kushner, “Atmospheric pressure dielectric barrier discharges interacting with liquid covered tissue,” *J. Phys. D. Appl. Phys.*, vol. 47, no. 16, p. 165201, 2014.

[100] C. Chen *et al.*, “A Model of Plasma-Biofilm and Plasma-Tissue Interactions at Ambient Pressure,” *Plasma Chem. Plasma Process.*, vol. 34, no. 3, pp. 403–441, May 2014.

[101] A. Lindsay, C. Anderson, E. Slikboer, S. Shannon, and D. Graves, “Momentum, heat, and neutral mass transport in convective atmospheric pressure plasma-liquid systems and implications for aqueous targets,” *J. Phys. D. Appl. Phys.*, vol. 48, no. 42, p. 424007, Oct. 2015.

[102] I. S. Djakaou, R. M. Ghezzar, M. E. M. Zekri, F. Abdelmalek, S. Cavadias, and S. Ognier, “Removal of Model Pollutants in Aqueous Solution by Gliding Arc Discharge. Part II: Modeling and Simulation Study,” *Plasma Chem. Plasma Process.*, vol. 35, no. 1, pp. 143–157, 2015.

[103] P. Vanraes, A. Y. Nikiforov, and C. Leys, “Electrical Discharge in Water Treatment Technology for Micropollutant Decomposition,” in *Plasma Science and Technology - Progress in Physical States and Chemical Reactions*, InTech, 2016, pp. 457–506.

[104] E. T. Inc., “VizGlow: Plasma Modeling Software for Multi- Dimensional Simulations of Non-Equilibrium Glow Discharge Systems.” Esgee Technologies, Inc., 2015.

[105] J. O. Wilkes, *Introduction to COMSOL Multiphysics*. COMSOL Inc, 2009.

[106] A. F. Yong Yang, Young I. Cho, *Plasma Discharge in Liquid: Water Treatment and Applications*. CRC Press, 2012.

[107] N. Bonifaci, A. Denat, and V. Atrazhev, “Ionization phenomenon in high-density gaseous and liquid argon in corona discharge experiments,” *J. Phys. D. Appl. Phys.*, vol. 30, no. 19, pp. 2717–2725, 1997.

[108] N. Bonifaci, A. Denat, and V. Atrazhev, “Ionization phenomenon in high-density gaseous and liquid argon in corona discharge experiments,” *J. Phys. D. Appl. Phys.*, vol. 30, no. 19, pp. 2717–2725, 1997.

[109] A. Starikovskiy, Y. Yang, Y. I. Cho, and A. Fridman, “Non-equilibrium plasma in liquid water: dynamics of generation and quenching,” *Plasma Sources Sci. Technol.*, vol. 20, no. 2, p. 024003, Apr. 2011.

[110] S. Samukawa *et al.*, “The 2012 Plasma Roadmap,” *J. Phys. D. Appl. Phys.*, vol. 45, no. 25, p. 253001, Jun. 2012.

[111] L. Schaper, W. G. Graham, and K. R. Stalder, “Vapour layer formation by electrical discharges through electrically conducting liquids—modelling and experiment,” *Plasma Sources Sci. Technol.*, vol. 20, no. 3, p. 034003, Jun. 2011.

[112] B. R. Locke and S. M. Thagard, “Analysis and review of chemical reactions and transport processes in pulsed electrical discharge plasma formed directly in liquid water,” *Plasma Chem. Plasma Process.*, vol. 32, no. 5, pp. 875–917, 2012.

[113] S. Horikoshi and N. Serpone, “In-liquid plasma: a novel tool in the fabrication of nanomaterials and in the treatment of wastewaters,” *RSC Adv.*, vol. 7, no. 75, pp. 47196–47218, 2017.

[114] K. Baba, T. Kaneko, and R. Hatakeyama, “Ion irradiation effects on ionic liquids interfaced with rf discharge plasmas,” *Appl. Phys. Lett.*, vol. 90, no. 20, pp. 1–4, 2007.

[115] S. A. Meiss, M. Rohnke, L. Kienle, S. Zein El Abedin, F. Endres, and J. Janek, “Employing plasmas as gaseous electrodes at the free surface of ionic liquids: Deposition of nanocrystalline silver particles,” *ChemPhysChem*, vol. 8, no. 1, pp. 50–53, 2007.

[116] O. Binazon, A. Dubois-Gaché, R. M. Nanau, and M. G. Neuman, “Efficacy and safety of platelet inhibitors,” *J. Pharm. Pharm. Sci.*, vol. 16, no. 1, pp. 1–39, 2012.

[117] R. Foest, E. Kindel, A. Ohl, M. Stieber, and K.-D. Weltmann, “Non-thermal atmospheric pressure discharges for surface modification,” *Plasma Phys. Control. Fusion*, vol. 47, no. 12B, pp. B525–B536, Dec. 2005.

[118] Q. T. Algwari and D. O’Connell, “Electron dynamics and plasma jet formation in a helium atmospheric pressure dielectric barrier discharge jet,” *Appl. Phys. Lett.*, vol. 99, no. 12, p. 121501, Sep. 2011.

[119] E. Stoffels, A. J. Flikweert, W. W. Stoffels, and G. M. W. Kroesen, “Plasma needle: A non-destructive atmospheric plasma source for fine surface treatment of (bio)materials,” *Plasma Sources Sci. Technol.*, vol. 11, no. 4, pp. 383–388, 2002.

[120] J. F. Kolb *et al.*, “Cold atmospheric pressure air plasma jet for medical applications,” *Appl. Phys. Lett.*, vol. 92, no. 24, pp. 1–3, 2008.

[121] M. L. and V. P. X Lu, “On atmospheric-pressure non-equilibrium plasma jets and plasma

bullets,” *Plasma Sources Sci. Technol.*, vol. 16, no. 1, pp. 1–39, 2012.

[122] P. Mezei and T. Cserfalvi, “Electrolyte cathode atmospheric glow discharges for direct solution analysis,” *Appl. Spectrosc. Rev.*, vol. 42, no. 6, pp. 573–604, 2007.

[123] P. Rumbach, J. P. Clarke, and D. B. Go, “Electrostatic Debye layer formed at a plasma-liquid interface,” *Phys. Rev. E*, vol. 95, no. 5, pp. 1–8, 2017.

[124] P. Rumbach, R. Xu, and D. B. Go, “Electrochemical Production of Oxalate and Formate from CO 2 by Solvated Electrons Produced Using an Atmospheric-Pressure Plasma,” *J. Electrochem. Soc.*, vol. 163, no. 10, pp. F1157–F1161, 2016.

[125] Z. Machala, I. Jedlovský, and V. Martišovitš, “DC Discharges in Atmospheric Air and Their Transitions,” vol. 36, no. 4, pp. 918–919, 2008.

[126] N. Shirai, S. Uchida, and F. Tochikubo, “Influence of oxygen gas on characteristics of self-organized luminous pattern formation observed in an atmospheric dc glow discharge using a liquid electrode,” *Plasma Sources Sci. Technol.*, vol. 23, no. 5, p. 054010, Sep. 2014.

[127] P. Andre *et al.*, “Experimental study of discharge with liquid non-metallic (tap-water) electrodes in air at atmospheric pressure,” *J. Phys. D*, vol. 34, no. December 2001, pp. 3456–3465, 2001.

[128] J. L. Walsh and M. G. Kong, “Contrasting characteristics of linear-field and cross-field atmospheric plasma jets,” *Appl. Phys. Lett.*, vol. 93, no. 11, pp. 2006–2009, 2008.

[129] A. Rumeli and M. Hizal, “Calculation of Impulse Flashover Voltage of a Water Column,” *IEEE Trans. Electr. Insul.*, vol. EI-21, no. 4, pp. 591–598, Aug. 1986.

[130] V. Petrishchev, S. Leonov, and I. V Adamovich, “Studies of nanosecond pulse surface ionization wave discharges over solid and liquid dielectric surfaces,” *Plasma Sources Sci. Technol.*, vol. 23, no. 6, p. 065022, Sep. 2014.

[131] H. Kawamoto and S. Umezu, “Electrohydrodynamic deformation of water surface in a metal pin to water plate corona discharge system,” *J. Phys. D. Appl. Phys.*, vol. 38, no. 6, pp. 887–894, 2005.

[132] C. C. W. Verlackt, W. Van Boxem, and A. Bogaerts, “Transport and accumulation of plasma generated species in aqueous solution,” *Phys. Chem. Chem. Phys.*, vol. 20, no. 10, pp. 6845–6859, 2018.

[133] C. A. J. van Gils, S. Hofmann, B. K. H. L. Boekema, R. Brandenburg, and P. J. Bruggeman, “Mechanisms of bacterial inactivation in the liquid phase induced by a remote RF cold atmospheric pressure plasma jet,” *J. Phys. D. Appl. Phys.*, vol. 46, no. 17, p. 175203, May 2013.

[134] A. M. Lietz and M. J. Kushner, “Air plasma treatment of liquid covered tissue: long timescale chemistry,” *J. Phys. D. Appl. Phys.*, vol. 49, no. 42, p. 425204, Oct. 2016.

[135] N. Y. Babaeva, W. Tian, and M. J. Kushner, “The interaction between plasma filaments in dielectric barrier discharges and liquid covered wounds: electric fields delivered to model platelets and cells,” *J. Phys. D. Appl. Phys.*, vol. 47, no. 23, p. 235201, Jun. 2014.

[136] H. Aoki, K. Kitano, and S. Hamaguchi, “Plasma generation inside externally supplied Ar bubbles in water,” *Plasma Sources Sci. Technol.*, vol. 17, no. 2, p. 025006, May 2008.

[137] K. Tachibana, Y. Takekata, Y. Mizumoto, H. Motomura, and M. Jinno, “Analysis of a pulsed discharge within single bubbles in water under synchronized conditions,” *Plasma*

Sources Sci. Technol., vol. 20, no. 3, p. 034005, Jun. 2011.

[138] A. M. Saitta, F. Saija, and P. V. Giaquinta, “Ab Initio Molecular Dynamics Study of Dissociation of Water under an Electric Field,” *Phys. Rev. Lett.*, vol. 108, no. 20, p. 207801, May 2012.

[139] S. N. Gucker, B. S. Sommers, and J. E. Foster, “Plasma Production in Isolated Bubbles,” *IEEE Trans. Plasma Sci.*, vol. 42, no. 10, pp. 2636–2637, Oct. 2014.

[140] A. Wright *et al.*, “Dielectric barrier discharge plasma microbubble reactor for pretreatment of lignocellulosic biomass,” *AIChE J.*, vol. 64, no. 11, pp. 3803–3816, Nov. 2018.

[141] A. Wright *et al.*, “Microbubble-enhanced dielectric barrier discharge pretreatment of microcrystalline cellulose,” *Biomass and Bioenergy*, vol. 118, no. May, pp. 46–54, 2018.

[142] K. Kahen, K. Jorabchi, C. Gray, and A. Montaser, “Spatial mapping of droplet velocity and size for direct and indirect nebulization in plasma spectrometry,” *Anal. Chem.*, vol. 76, no. 24, pp. 7194–7201, 2004.

[143] G. C. Y. Chan, Z. Zhu, and G. M. Hieftje, “Effect of single aerosol droplets on plasma impedance in the inductively coupled plasma,” *Spectrochim. Acta Part B At. Spectrosc.*, vol. 76, pp. 87–95, Oct. 2012.

[144] S. Groh, C. C. Garcia, A. Murtazin, V. Horvatic, and K. Niemax, “Local effects of atomizing analyte droplets on the plasma parameters of the inductively coupled plasma,” *Spectrochim. Acta Part B At. Spectrosc.*, vol. 64, no. 3, pp. 247–254, Mar. 2009.

[145] P. Fauchais *et al.*, “Suspension and solution plasma spraying,” *J. Phys. D. Appl. Phys.*, vol. 46, no. 22, p. 224015, Jun. 2013.

[146] F. Fanelli, A. M. Mastrangelo, and F. Fracassi, “Aerosol-Assisted Atmospheric Cold Plasma Deposition and Characterization of Superhydrophobic Organic–Inorganic Nanocomposite Thin Films,” *Langmuir*, vol. 30, no. 3, pp. 857–865, Jan. 2014.

[147] E. Sardella, F. Palumbo, G. Camporeale, and P. Favia, “Non-Equilibrium Plasma Processing for the Preparation of Antibacterial Surfaces,” *Materials (Basel).*, vol. 9, no. 7, p. 515, Jun. 2016.

[148] Z. Machala, B. Tarabova, K. Hensel, E. Spetlikova, L. Sikurova, and P. Lukes, “Formation of ROS and RNS in water electro-sprayed through transient spark discharge in air and their bactericidal effects,” *Plasma Process. Polym.*, vol. 10, no. 7, pp. 649–659, 2013.

[149] Z. Machala, L. Chládeková, and M. Pelach, “Plasma agents in bio-decontamination by dc discharges in atmospheric air,” *J. Phys. D. Appl. Phys.*, vol. 43, no. 22, p. 222001, Jun. 2010.

[150] M. Goeckner, D. Ogawa, I. Saraf, and L. Overzet, “Progress report: Direct injection of liquids into low-pressure plasmas,” *J. Phys. Conf. Ser.*, vol. 162, p. 012014, Apr. 2009.

[151] C. P. Stallard, M. M. Iqbal, M. M. Turner, and D. P. Dowling, “Investigation of the formation mechanism of aligned nano-structured siloxane coatings deposited using an atmospheric plasma jet,” *Plasma Process. Polym.*, vol. 10, no. 10, pp. 888–903, Jul. 2013.

[152] W. Tian, K. Tachibana, and M. J. Kushner, “Plasmas sustained in bubbles in water: optical emission and excitation mechanisms,” *J. Phys. D. Appl. Phys.*, vol. 47, no. 5, p. 055202, Feb. 2014.

[153] N. Y. Babaeva, D. V Tereshonok, and G. V Naidis, “Initiation of breakdown in bubbles

immersed in liquids: pre-existed charges versus bubble size," *J. Phys. D. Appl. Phys.*, vol. 48, no. 35, p. 355201, Sep. 2015.

[154] D. Levko, A. Sharma, and L. L. Raja, "Microwave plasmas generated in bubbles immersed in liquids for hydrocarbons reforming," *J. Phys. D. Appl. Phys.*, vol. 49, no. 22, p. 22LT01, Jun. 2016.

[155] M. M. Iqbal and M. M. Turner, "Investigations of Droplet-Plasma Interaction using Multi-Dimensional Coupled Model," *Contrib. to Plasma Phys.*, vol. 55, no. 9, pp. 627–642, Oct. 2015.

[156] X. ming Shao, K. Zhang, and H. bing Xiong, "Modeling of Micro- and Nanoparticle Characteristics in DC Suspension Plasma Spray," *J. Therm. Spray Technol.*, vol. 24, no. 3, pp. 309–317, 2014.

[157] M. M. Iqbal, C. P. Stallard, D. P. Dowling, and M. M. Turner, "Three-dimensional coupled fluid-droplet model for atmospheric pressure Plasmas," *Plasma Process. Polym.*, vol. 12, no. 3, pp. 201–213, 2015.

[158] C. Marchand, C. Chazelas, G. Mariaux, and A. Vardelle, "Liquid precursor plasma spraying: Modeling the interactions between the transient plasma jet and the droplets," *J. Therm. Spray Technol.*, vol. 16, no. 5–6, pp. 705–712, 2007.

[159] P. D. Maguire *et al.*, "Controlled microdroplet transport in an atmospheric pressure microplasma," *Appl. Phys. Lett.*, vol. 106, no. 22, p. 224101, Jun. 2015.

[160] D. Ogawa, C. W. Chung, M. Goeckner, and L. Overzet, "Transient effects caused by pulsed gas and liquid injections into low pressure plasmas," *Plasma Sources Sci. Technol.*, vol. 19, no. 3, p. 034013, Jun. 2010.

[161] Y. Shan and Y. Hu, “Heat and Mass transfer within an evaporating solution droplet in a plasma jet,” in *Journal of Thermal Spray Technology*, 2012, vol. 21, no. 3–4, pp. 676–688.

[162] J. Rudolph, K. L. Reddy, J. P. Chiang, and B. K. Sharpless, “Highly efficient epoxidation of olefins using aqueous H2O2 and catalytic methyltrioxorhenium/pyridine: Pyridine-mediated ligand acceleration,” *J. Am. Chem. Soc.*, vol. 119, no. 26, pp. 6189–6190, 1997.

[163] Y. Zhu, Q. Wang, R. G. Cornwall, and Y. Shi, “Organocatalytic Asymmetric Epoxidation and Aziridination of Olefins and Their Synthetic Applications,” *Chem. Rev.*, vol. 114, no. 16, pp. 8199–8256, 2014.

[164] Y. Suga and H. Sekiguchi, “Epoxidation of carbon double bond using atmospheric non-equilibrium oxygen plasma,” *Thin Solid Films*, vol. 506–507, pp. 427–431, May 2006.

[165] A. Wright, M. Taglioli, F. Montazersadgh, A. Shaw, F. Iza, and H. C. H. Bandulasena, “Microbubble-enhanced DBD plasma reactor: Design, characterisation and modelling,” *Chem. Eng. Res. Des.*, vol. 144, pp. 159–173, Apr. 2019.

[166] F. Montazersadgh *et al.*, “Influence of the On-time on the Ozone Production in Pulsed Dielectric Barrier Discharges,” *Plasma*, vol. 2, no. 1, pp. 39–50, Mar. 2019.

[167] I. E. Gordon *et al.*, “The HITRAN2016 molecular spectroscopic database,” *J. Quant. Spectrosc. Radiat. Transf.*, vol. 203, pp. 3–69, Dec. 2017.

[168] E. C. Tuazon, J. Arey, R. Atkinson, and S. M. Aschmann, “Gas-phase reactions of 2-vinylpyridine and styrene with hydroxyl and NO3 radicals and ozone,” *Environ. Sci. Technol.*, vol. 27, no. 9, pp. 1832–1841, Sep. 1993.

[169] R. B. Bird, W. E. Stewart, and E. N. Lightfoot, *Transport Phenomena*. John Wiley & Sons

Ltd, 2002.

[170] Y. Sakiyama, D. B. Graves, H.-W. Chang, T. Shimizu, and G. E. Morfill, “Plasma chemistry model of surface microdischarge in humid air and dynamics of reactive neutral species,” *J. Phys. D. Appl. Phys.*, vol. 45, no. 42, p. 425201, 2012.

[171] K.-U. Riemann, “The Bohm criterion and sheath formation,” *J. Phys. D. Appl. Phys.*, vol. 24, no. 4, pp. 493–518, Apr. 1991.

[172] M. KHORAMABADI, H. GHOMI, and P. K. SHUKLA, “The Bohm-sheath criterion in plasmas containing electrons and multiply charged ions,” *J. Plasma Phys.*, vol. 79, no. 3, pp. 267–271, Jun. 2013.

[173] H. A. Akhlaghi Amiri and A. A. Hamouda, “Evaluation of level set and phase field methods in modeling two phase flow with viscosity contrast through dual-permeability porous medium,” *Int. J. Multiph. Flow*, vol. 52, pp. 22–34, 2013.

[174] V. E. Badalassi, H. D. Ceniceros, and S. Banerjee, “Computation of multiphase systems with phase field models,” *J. Comput. Phys.*, vol. 190, no. 2, pp. 371–397, 2003.

[175] P. Yue, C. Zhou, J. J. Feng, C. F. Ollivier-Gooch, and H. H. Hu, “Phase-field simulations of interfacial dynamics in viscoelastic fluids using finite elements with adaptive meshing,” *J. Comput. Phys.*, vol. 219, no. 1, pp. 47–67, 2006.

[176] H. Hua, J. Shin, and J. Kim, “Level Set, Phase-Field, and Immersed Boundary Methods for Two-Phase Fluid Flows,” *J. Fluids Eng.*, vol. 136, no. 2, p. 021301, 2013.

[177] M. Ismail, *Level Set and Phase Field Methods : Application to Moving Interfaces and Two-Phase Fluid Flows*. Claremont: Claremont Graduate University, 2007.

[178] E. Maitre, C. Misbah, P. Peyla, and A. Raoult, “Comparison between advected-field and level-set methods in the study of vesicle dynamics,” *Phys. D Nonlinear Phenom.*, vol. 241, no. 13, pp. 1146–1157, Jul. 2012.

[179] M. J. Baines, M. E. Hubbard, P. K. Jimack, and R. Mahmood, “A moving-mesh finite element method and its application to the numerical solution of phase-change problems,” *Commun. Comput. Phys.*, vol. 6, no. 3, pp. 595–624, 2009.

[180] V. Bruyere, C. Touvrey, and P. Namy, “Comparison between Phase Field and ALE Methods to model the Keyhole Digging during Spot Laser Welding,” in *COMSOL Conference*, 2013, pp. 1–7.

[181] M. K. H. Al-Mashhadani, H. C. H. Bandulasena, and W. B. Zimmerman, “CO 2 Mass Transfer Induced through an Airlift Loop by a Microbubble Cloud Generated by Fluidic Oscillation,” *Ind. Eng. Chem. Res.*, vol. 51, no. 4, pp. 1864–1877, Feb. 2012.

[182] H. Langemann, “Accompanied Model for By Chemical Mass Transfer,” *Chem. Eng. Sci.*, vol. 49, no. 3, pp. 3457–3463, 1994.

[183] P. Luis, Ed., *Fundamental Modelling of Membrane Systems*. Elsevier, 2018.

[184] P. H. Calderbank and M. B. Moo-Young, “The continuous phase heat and mass transfer properties of dispersions,” *Chem. Eng. Sci.*, vol. 50, no. 24, pp. 3921–3934, Dec. 1995.

[185] R. P. Dwight and H. Bijl, *Solution methods and acceleration techniques in CFD*. John Wiley & Sons, Ltd., 2010.

[186] E. L. Gouri Dhatt, Gilbert Touzot, *Finite Element Method*. London: ISTE Ltd, 2012.

[187] “LxCat.net. Data for Modeling Plasmas – exchange of fundamental data and numerical

tools for modeling plasmas.," 2018. [Online]. Available: Assoc.lxcat.net. [Accessed: 18-Jul-2018].

[188] N. Van Riel, *Speeding up simulations of ODE models in Matlab using CVode and MEX files*. Eindhoven University of Technology, 2012.

[189] W. J. Palm, "Appendix A : MATLAB Basics MATLAB numbers and numeric formats," in *Introduction to MATLAB 7 for Engineers*, New York: McGraw-Hill, 2005, pp. 1–19.

[190] F. G. G. Colonna, CNR-Nanotec, M. Turner, M. Becker, D. Loffhagen, F. Sigeneger and S. P. A. Luque, F. Iza, F. Montazersadgh, J van Dijk, W. Graef, G. Kroesen, D. Mihailova, A. Bogaerts, S. Heijkers L. Alves, M. Castela, V. Guerra, M. Lino da Silva, L. Marques, N. Pinhao, C. Pintassilgo, A. Tejero, T. Kozak, A. Derzsi, Z. Donko, P. Hartmann, K, "Plasma chemistry round robin," in *GEC17 Meeting of The American Physical Society*, 2017, p. 10.

[191] D. B. Go, *GASEOUS IONIZATION AND ION TRANSPORT: An Introduction to Gas Discharges*. Notre Dame: Department of Aerospace and Mechanical Engineering University of Notre Dame, 2012.

[192] C. C. W. Verlackt, W. Van Boxem, and A. Bogaerts, "Transport and accumulation of plasma generated species in aqueous solution," *Phys. Chem. Chem. Phys.*, vol. 20, no. 10, pp. 6845–6859, 2018.

[193] G. E. Zaikov, J. A. Howard, and K. U. Ingold, "Absolute rate constants for hydrocarbon autoxidation. XIII. Aldehydes: photo-oxidation, co-oxidation, and inhibition," *Can. J. Chem.*, vol. 47, no. 16, pp. 3017–3029, Aug. 1969.

[194] M. G. Nagarkatti, "Ozone in Water Treatment: Application and Engineering," *J. Environ.*

Qual., vol. 20, no. 4, pp. 881–882, Oct. 1991.

[195] G. Vezzu, J. L. Lopez, A. Freilich, and K. H. Becker, “Optimization of large-scale ozone generators,” *IEEE Trans. Plasma Sci.*, vol. 37, no. 6 PART 1, pp. 890–896, 2009.

[196] N. Brueggemann, T. Puehmeier, R. Fiekens, F. J. Richardt, and M. Salvermoser, “Cooling Conditions of Ozone Generators,” *Ozone Sci. Eng.*, vol. 39, no. 3, pp. 196–201, 2017.

[197] T. Murata, Y. Okita, M. Noguchi, and I. Takase, “Basic parameters of coplanar discharge ozone generator,” *Ozone Sci. Eng.*, vol. 26, no. 5, pp. 429–442, 2004.

[198] M. H. Panjeshahi and A. Ataei, “Application of an environmentally optimum cooling water system design to water and energy conservation,” *Int. J. Environ. Sci. Technol.*, vol. 5, no. 2, pp. 251–262, Mar. 2008.

[199] A. Suksri, K. Karnchanalekha, K. Tonmitra, and P. Apiratikul, “A comparative study on suitable high voltage sources for ozone generation,” in *2009 6th International Conference on Electrical Engineering/Electronics, Computer, Telecommunications and Information Technology, ECTI-CON 2009*, 2009, vol. 1, pp. 296–299.

[200] M. Šimek, S. Pekárek, and V. Prukner, “Influence of power modulation on ozone production using an AC surface dielectric barrier discharge in oxygen,” *Plasma Chem. Plasma Process.*, vol. 30, no. 5, pp. 607–617, 2010.

[201] S. Zhang, A. Sobota, E. M. van Veldhuizen, and P. J. Bruggeman, “Temporally resolved ozone distribution of a time modulated RF atmospheric pressure argon plasma jet: flow, chemical reaction, and transient vortex,” *Plasma Sources Sci. Technol.*, vol. 24, no. 4, p. 045015, Jul. 2015.

[202] J. Park *et al.*, “An atmospheric pressure plasma source,” *Appl. Phys. Lett.*, vol. 76, no. 3, pp. 288–290, Jan. 2000.

[203] Y. M. Sung and T. Sakoda, “Optimum conditions for ozone formation in a micro dielectric barrier discharge,” *Surf. Coatings Technol.*, vol. 197, no. 2–3, pp. 148–153, 2005.

[204] A. Chirokov, A. Gutsol, and A. Fridman, “Atmospheric pressure plasma of dielectric barrier discharges,” *Pure Appl. Chem.*, vol. 77, no. 2, pp. 487–495, 2005.

[205] T. Ma, H. Jiang, J. Liu, and F. Zhong, “Decomposition of Benzene Using a Pulse-Modulated DBD Plasma,” *Plasma Chem. Plasma Process.*, vol. 36, no. 6, pp. 1533–1543, 2016.

[206] R. Díaz, A. Márquez, D. Menéndez, and R. Pérez, “Medium frequency pulse train ozone generation,” *Ozone Sci. Eng.*, vol. 21, no. 6, pp. 635–642, 1999.

[207] P. Olszewski, J. F. Li, D. X. Liu, and J. L. Walsh, “Optimizing the electrical excitation of an atmospheric pressure plasma advanced oxidation process,” *J. Hazard. Mater.*, vol. 279, pp. 60–66, Aug. 2014.

[208] R. Barni, I. Biganzoli, E. C. Dell’Orto, and C. Riccardi, “Effect of duty-cycles on the air plasma gas-phase of dielectric barrier discharges,” *J. Appl. Phys.*, vol. 118, no. 14, p. 143301, Oct. 2015.

[209] P. Seri *et al.*, “Influence of the voltage waveform’s shape and on-time duration on the dissolved ozone produced by a DBD bubble reactor,” *Plasma Sources Sci. Technol.*, vol. 28, no. 3, p. 035001, Mar. 2019.

[210] A. Wright *et al.*, “Microbubble-enhanced dielectric barrier discharge pretreatment of microcrystalline cellulose,” *Biomass and Bioenergy*, vol. 118, pp. 46–54, Nov. 2018.

[211] A. Wright, B. Uprety, A. Shaw, G. Shama, F. Iza, and H. Bandulasena, “Effect of humic acid on E. coli disinfection in a microbubble-gas plasma reactor,” *J. Water Process Eng.*, vol. 31, p. 100881, Oct. 2019.

[212] I. a Kossyi, a Y. Kostinsky, a a Matveyev, and V. P. Silakov, “Kinetic scheme of the non-equilibrium discharge in nitrogen-oxygen mixtures,” *Plasma Sources Sci. Technol.*, vol. 1, no. 3, pp. 207–220, 1999.

[213] L. Sieck, J. Heron, and D. Green, “Chemical Kinetics Database and Predictive Schemes for Humid Air Plasma Chemistry. Part I: Positive Ion–Molecule Reactions,” *Plasma Chem. Plasma Process.*, vol. 20, no. iii, pp. 1–5, 2000.

[214] J. T. Herron and D. S. Green, “Chemical kinetics database and predictive schemes for nonthermal humid air plasma chemistry. Part II. Neutral species reactions,” *Plasma Chem. Plasma Process.*, vol. 21, no. 3, pp. 459–481, 2001.

[215] C. Riccardi and R. Barni, *Chemical Kinetics*. InTech, 2012.

[216] Y. H. Choi, J. H. Kim, and Y. S. Hwang, “One-dimensional discharge simulation of nitrogen DBD atmospheric pressure plasma,” *Thin Solid Films*, vol. 506–507, pp. 389–395, 2006.

[217] T. Murakami, K. Niemi, T. Gans, D. O’Connell, and W. G. Graham, “Afterglow chemistry of atmospheric-pressure helium–oxygen plasmas with humid air impurity,” *Plasma Sources Sci. Technol.*, vol. 23, p. 025005, 2014.

[218] W. Van Gaens and A. Bogaerts, “Argon / humid air plasma chemistry : focus on gas phase reaction kinetics,” in *21st Int. Symp. Plasma Chem.*, 2013, pp. 13–18.

[219] A. Hurlbatt *et al.*, “Concepts, Capabilities, and Limitations of Global Models: A Review,”

Plasma Process. Polym., vol. 14, no. 1–2, pp. 1–21, 2017.

[220] R. Barni, P. Esena, and C. Riccardi, “Chemical kinetics simulation for atmospheric pressure air plasmas in a streamer regime,” *J. Appl. Phys.*, vol. 97, no. 7, p. 073301, Apr. 2005.

[221] T. Shimizu, Y. Sakiyama, D. B. Graves, J. L. Zimmermann, and G. E. Morfill, “The dynamics of ozone generation and mode transition in air surface micro-discharge plasma at atmospheric pressure,” *New J. Phys.*, vol. 14, no. 10, p. 103028, Oct. 2012.

[222] D. Gardoni, A. Vailati, and R. Canziani, “Decay of Ozone in Water: A Review,” *Ozone Sci. Eng.*, vol. 34, no. 4, pp. 233–242, 2012.

[223] D. Swern, “Epoxidation and Hydroxylation of Ethylenic Compounds with Organic Peracids,” in *Organic Reactions*, Hoboken, NJ, USA: John Wiley & Sons, Inc., 2011, pp. 378–434.

[224] J. Rudolph *et al.*, “Highly Efficient Epoxidation of Olefins Using Aqueous H2O2 and Catalytic Methyltrioxorhenium/ Pyridine: Pyridine-Mediated Ligand Acceleration,” vol. 7863, no. 12, pp. 6189–6190, 1997.

[225] P. C. Page, B. R. Buckley, L. F. Appleby, and P. A. Alsters, “Highly Efficient Catalysts for Epoxidation Mediated by Iminium Salts,” *Synthesis (Stuttg).*, vol. 1, no. 19, pp. 3405–3411, 2005.

[226] P. C. B. Page, M. M. Farah, B. R. Buckley, and A. J. Blacker, “New Chiral Binaphthalene-Derived Iminium Salt Organocatalysts for Asymmetric Epoxidation of Alkenes,” *J. Org. Chem.*, vol. 72, no. 12, pp. 4424–4430, 2007.

[227] P. C. B. Page, B. R. Buckley, M. M. Farah, and A. J. Blacker, “Binaphthalene-Derived

Iminium Salt Catalysts for Highly Enantioselective Asymmetric Epoxidation," *European J. Org. Chem.*, vol. 2009, no. 20, pp. 3413–3426, 2009.

[228] C. Dai, J. Zhang, C. Huang, and Z. Lei, "Ionic Liquids in Selective Oxidation: Catalysts and Solvents," *Chem. Rev.*, vol. 117, no. 10, pp. 6929–6983, 2017.

[229] M. Selvaraj, K. S. Seshadri, A. Pandurangan, and T. G. Lee, "Highly selective synthesis of trans-stilbene oxide over mesoporous Mn-MCM-41 and Zr–Mn-MCM-41 molecular sieves," *Microporous Mesoporous Mater.*, vol. 79, no. 1–3, pp. 261–268, Apr. 2005.

[230] R. A. Sheldon, "Selective catalytic synthesis of fine chemicals: opportunities and trends," *J. Mol. Catal. A Chem.*, vol. 107, no. 1–3, pp. 75–83, May 1996.

[231] H. Xu *et al.*, "trans -Stilbene epoxidation by He+O 2 atmospheric pressure plasma: Epoxidation without oxidant waste stream," *Plasma Process. Polym.*, vol. 17, no. 1, p. 1900162, Jan. 2020.

[232] "Final Report on the Safety Assessment of Benzaldehyde," *Int. J. Toxicol.*, vol. 25, no. December 2005, pp. 11–27, 2006.

[233] D. T. Elg, I.-W. Yang, and D. B. Graves, "Production of TEMPO by O atoms in atmospheric pressure non-thermal plasma–liquid interactions," *J. Phys. D. Appl. Phys.*, vol. 50, no. 47, p. 475201, Nov. 2017.

[234] S. Schneider, J.-W. Lackmann, F. Narberhaus, J. E. Bandow, B. Denis, and J. Benedikt, "Separation of VUV/UV photons and reactive particles in the effluent of a He/O 2 atmospheric pressure plasma jet," *J. Phys. D. Appl. Phys.*, vol. 44, no. 37, p. 379501, Sep. 2011.

[235] H. Suhr, "Organic Syntheses in the Plasma of Glow Discharges and Their Preparative

Application," *Angew. Chemie Int. Ed. English*, vol. 11, no. 9, pp. 781–792, 1972.

[236] H. Suhr, "Applications and Trends of Nonequilibrium Plasma Chemistry with Organic and Organometallic Compounds," vol. 1989, no. 1, pp. 7–28, 1989.

[237] M. Sankar *et al.*, "The benzaldehyde oxidation paradox explained by the interception of peroxy radical by benzyl alcohol," *Nat. Commun.*, vol. 5, no. 1, p. 3332, May 2014.

[238] J. M. Achord and C. L. Hussey, "Determination of dissolved oxygen in nonaqueous electrochemical solvents," *Anal. Chem.*, vol. 52, no. 3, pp. 601–602, 1980.

[239] E. M. Knipping and D. Dabdub, "Modeling surface-mediated renoxification of the atmosphere via reaction of gaseous nitric oxide with deposited nitric acid," *Atmos. Environ.*, vol. 36, no. 36–37, pp. 5741–5748, 2002.

[240] E. M. Knipping, "Modeling Cl 2 formation from aqueous NaCl particles: Evidence for interfacial reactions and importance of Cl 2 decomposition in alkaline solution," *J. Geophys. Res.*, vol. 107, no. D18, p. 4360, 2002.

[241] C. Schweitzer and R. Schmidt, "Physical Mechanisms of Generation and Deactivation of Singlet Oxygen," *Chem. Rev.*, vol. 103, no. 5, pp. 1685–1758, May 2003.

[242] M. Sankar *et al.*, "The benzaldehyde oxidation paradox explained by the interception of peroxy radical by benzyl alcohol," *Nat. Commun.*, vol. 5, no. 1, p. 3332, May 2014.

[243] Engineeringtoolbox, "Engineering Toolbox," 2012. [Online]. Available: http://www.engineeringtoolbox.com/.

[244] Z. C. Liu *et al.*, "Physicochemical processes in the indirect interaction between surface air plasma and deionized water," *J. Phys. D. Appl. Phys.*, vol. 48, no. 49, p. 495201, Dec.

2015.

[245] A. Yang, X. Wang, M. Rong, D. Liu, F. Iza, and M. G. Kong, “1-D fluid model of atmospheric-pressure rf He+O 2 cold plasmas: Parametric study and critical evaluation,” *Phys. Plasmas*, vol. 18, no. 11, p. 113503, Nov. 2011.

[246] R. Sander, “Compilation of Henry ’ s Law Constants for Inorganic and Organic Species of Potential Importance in Environmental Chemistry,” *Database*, vol. 20, no. 1, p. 107, 1999.

[247] J. Golda *et al.*, “Concepts and characteristics of the ‘COST Reference Microplasma Jet,’” *J. Phys. D. Appl. Phys.*, vol. 49, no. 8, p. 084003, Mar. 2016.

[248] A. von Keudell, V. Schulz-von der Gathen, D. Ellerweg, J. Benedikt, and N. Knake, “Characterization of the effluent of a He/O 2 microscale atmospheric pressure plasma jet by quantitative molecular beam mass spectrometry,” *New J. Phys.*, vol. 12, no. 1, p. 013021, 2010.

[249] S. K. Kang, H. Y. Kim, G. S. Yun, and J. K. Lee, “Portable microwave air plasma device for wound healing,” *Plasma Sources Sci. Technol.*, vol. 24, no. 3, p. 035020, 2015.

[250] J. F. Friedrich, R. Mix, R. D. Schulze, A. Meyer-Plath, R. Joshi, and S. Wettmarshausen, “New plasma techniques for polymer surface modification with monotype functional groups,” *Plasma Process. Polym.*, vol. 5, no. 5, pp. 407–423, 2008.

[251] A. L. Rosen and G. M. Hieftje, “Inductively coupled plasma mass spectrometry and electrospray mass spectrometry for speciation analysis: Applications and instrumentation,” *Spectrochim. Acta - Part B At. Spectrosc.*, vol. 59, no. 2, pp. 135–146, 2004.

[252] E. Newman J and K. Thomas-Alyea, *Electrochemical Systems*, 3rd ed. New York: Wiley,

2004.

[253] B. Pastina and J. A. LaVerne, “Effect of molecular hydrogen on hydrogen peroxide in water radiolysis,” *J. Phys. Chem. A*, vol. 105, no. 40, pp. 9316–9322, 2001.

[254] A. Poisson and A. Papaud, “Diffusion coefficients of major ions in seawater,” *Mar. Chem.*, vol. 13, no. 4, pp. 265–280, 1983.

[255] J. Solórzano-López, R. Zenit, and M. A. Ramírez-Argáez, “Mathematical and physical simulation of the interaction between a gas jet and a liquid free surface,” *Appl. Math. Model.*, vol. 35, no. 10, pp. 4991–5005, Oct. 2011.

[256] D. Muñoz-Esparza, J.-M. Buchlin, K. Myrillas, and R. Berger, “Numerical investigation of impinging gas jets onto deformable liquid layers,” *Appl. Math. Model.*, vol. 36, no. 6, pp. 2687–2700, Jun. 2012.

[257] A. Bhattacharya and P. Ray, “Studies on surface tension of poly(vinyl alcohol): Effect of concentration, temperature, and addition of chaotropic agents,” *J. Appl. Polym. Sci.*, vol. 93, no. 1, pp. 122–130, 2004.

[258] M. Sato, N. Kudo, and M. Saito, “Surface tension reduction of liquid by applied electric field using vibrating jet method,” *IEEE Trans. Ind. Appl.*, vol. 34, no. 2, pp. 294–300, 1998.

[259] A. Bateni, S. Laughton, H. Tavana, S. S. Susnar, A. Amirfazli, and A. W. Neumann, “Effect of electric fields on contact angle and surface tension of drops,” *J. Colloid Interface Sci.*, vol. 283, no. 1, pp. 215–222, 2005.

[260] L. S. Chang and J. C. Berg, “The effect of interfacial tension gradients on the flow structure of single drops or bubbles translating in an electric field,” *AIChE J.*, vol. 31, no.

4, pp. 551–557, 1985.

[261] M. Sega, G. Horvai, and P. Jedlovszky, “Two-dimensional percolation at the free water surface and its relation with the surface tension anomaly of water,” *J. Chem. Phys.*, vol. 141, no. 5, p. 054707, Aug. 2014.

[262] MIT, “Marangoni Flows,” *Lect. notes*, pp. 1–5, 1985.

[263] C. W. J. Berendsen, E. M. Van Veldhuizen, G. M. W. Kroesen, and A. A. Darhuber, “Marangoni flows induced by atmospheric-pressure plasma jets,” *J. Phys. D. Appl. Phys.*, vol. 48, no. 2, p. 025203, Jan. 2015.

[264] T. Yan, X. Zhong, A. E. Rider, Y. Lu, S. A. Furman, and K. (Ken) Ostrikov, “Microplasma-chemical synthesis and tunable real-time plasmonic responses of alloyed Au x Ag 1−x nanoparticles,” *Chem. Commun.*, vol. 50, no. 24, pp. 3144–3147, 2014.

[265] T.-D. Luong, V.-N. Phan, and N.-T. Nguyen, “High-throughput micromixers based on acoustic streaming induced by surface acoustic wave,” *Microfluid. Nanofluidics*, vol. 10, no. 3, pp. 619–625, 2011.

[266] P. K. Sahu, A. Golia, and A. K. Sen, “Investigations into mixing of fluids in microchannels with lateral obstructions,” *Microsyst. Technol.*, vol. 19, no. 4, pp. 493–501, 2013.

[267] S. R. Abd Shukor and S. N. A. Ahmad Termizi, “CFD analysis of mixing element of SSIMM: The effect of inlet velocity toward mixing intensity,” *J. Eng. Sci. Technol.*, vol. 10, no. Spec.issue3, pp. 60–67, 2015.